UNIVERSITÉ DU QUÉBEC À CHICOUTIMI

DÉPARTEMENT DES SCIENCES APPLIQUÉES

Corrosion resistant superhydrophobic nanoparticles-incorporated-anodized-aluminum alloys surfaces

Ph.D. Candidate: Ying Huang

Permanent Code: HUAY16528602

Director: Prof. D. K. Sarkar

Co-director: Prof. X. Grant Chen

May, 2016

ABSTRACT

Corrosion on metal surfaces usually leads to severe safety and appearance issues, particularly in automotive applications. Majority of corrosion behaviors occur in a humid environment. Superhydrophobic surface coating significantly reduces contact area between metal surface and liquid due to the non-wetting layer. Therefore, a superhydrophobic surface is valuable to be fabricated in order to prevent corrosion.

In this project, superhydrophobic aluminum alloy surfaces were fabricated by electrophoretic deposition (EPD) of stearic acid (SA) functionalized zinc oxide (ZnO) nanoparticle. The deposited thin film shows a water contact angle of ~155^{o} with rolls off properties. The intensity of x-ray diffracted (XRD) peaks of ZnO and hence the thickness of the ZnO films increases with the increase of the bath temperatures. The activation energy of electrophoretic deposition of stearic-acid-functionalized ZnO nanoparticles was calculated to be 0.5 eV from the Arrhenius plot between bath temperature and the XRD peak area. The superhydrophobic SA-functionalized ZnO thin film has a slightly improved corrosion resistance property (polarization resistance of 55 k$\Omega \cdot cm^2$) as

compared with as-received Al alloy (polarization resistance of 50 $k\Omega \cdot cm^2$).

In order to better improve the anti-corrosion property, a modified electrodeposition process was performed to transform the as-received aluminum alloy substrates to superhydrophobic. In the process, the aluminum alloy surface was electrodeposited in the electrolytic solution containing zinc nitrate and stearic acid at 20 V DC. The optimum of molar ratio at (Zn^{2+}/SA) of 0.225 was found to provide a high surface rms roughness of 7.11 ± 0.42 μm and contact angle (CA) of 159 ± 1°. The corrosion resistance of superhydrophobic substrates prepared by electrodeposition was found to be much higher than that of as-received substrate and the superhydrophobic substrates prepared by EPD process.

Anodized aluminum has good robust and corrosion resistance properties. Based on the knowledge of electrodeposition process on the as-received aluminum substrate, aluminum alloy was firstly anodized, followed by the electrodeposition process using the electrolyte of zinc nitrate mixing with stearic acid. The formation of low surface energy micro-nanostructured zinc stearate electrodeposition transformed the anodic aluminum

oxide (AAO) surface to superhydrophobic, having water contact angle of 160°. The corrosion current densities of the anodized and aluminum alloy surfaces are found to be 200 and 400 nA/cm^2, respectively. In comparison, superhydrophobic anodic aluminum oxide (SHAAO) shows a much lower value of 88 nA/cm^2. Similarly, the charge transfer resistance, R_{ct}, measured by electrochemical impedance spectroscopy show that the R_{ct} value of SHAAO substrate was found to be 200 times larger than that of as-received aluminum alloy substrate. These results indicate that the superhydrophobic surfaces created on anodized surface remarkably improve the corrosion resistance performance of aluminum alloy.

RÉSUMÉ

La corrosion sur des métaux peut conduire à des problèmes de sécurité graves dans la vie de tous les jours. La plupart des comportements de corrosion se produisent dans un environnement humide. Les revêtements superhydrophobes, une surface enduites d'une couche non mouillanble, réduit la zone de contact à l'interfacesolide et liquide. Par conséquent, les surfaces superhydrophobes peuvent être fabriquées de manière à éviter que les comportements de corrosion.

Dans ce projet, les surfaces en alliage d'aluminium superhydrophobes ont été fabriqués par dépôt électrophorétique (EPD) d'acide stéarique (SA) de nanoparticules d'oxyde de zinc fonctionnalisé (ZnO). Le film mince déposée présente un angle de contact de l'eau de 155°. L'intensité de rayons X diffracté (XRD) des pics de ZnO et, partant, l'épaisseur des films de ZnO augmente avec l'augmentation des températures de bain. L'énergie d'activation de dépôt électrophorétique des nanoparticules de ZnO fonctionnalisé à l'acide stéarique- a été calculée à 0,5 eV à partir du tracé d'Arrhenius entre la température du bain et la surface du pic de XRD. Le film de ZnO superhydrophobe a une petite amélioration de la propriété de résistance à la corrosion (résistance de polarisation 55 kΩ/cm^2) par rapport aux telle que reçue alliage Al (résistance de polarisation 50 kΩ/cm^2).

Afin de mieux améliorer la propriété anticorrosion, un processus d'électrodéposition

modifié a été effectuée dans le projet de transformer les substrats en alliage d'aluminium telle que reçue à superhydrophobe. Dans le procédé, la surface en alliage d'aluminium par électrolyse est effectuée dans une solution électrolytique contenant du nitrate de zinc et d'acide stéarique à 20 V DC. La valeur optimaledu rapport molaire au (Zn^{2+} / SA) de 0,225 a été trouvé pour fournir la rugosité de 7,11 ± 0,42 um et l'angle de contact (CA) de 159 ± 1 °. La résistance à la corrosion de substrats superhydrophobes préparées par électrodéposition a été jugée beaucoup plus élevée que celle du substrat telle que reçue et les substrats préparés par un procédé superhydrophobes EPD.

Il est bien connu que l'aluminium anodisé a des propriétés mécaniques élevées et résistant à la corrosion. Par conséquent, avec la compréhension du procédé d'électrodéposition sur un substrat d'alliage d'aluminium telle que reçue, l'alliage d'aluminium est tout d'abord anodisée, suivi par le procédé de dépôt électrolytique utilisant l'électrolyte de nitrate de zinc à mélanger avec de l'acide stéarique, qui est le même que sur la telle que reçue surface de l'alliage d'aluminium. La formation d’un film hybride organique-inorganique micro-nanostructuré de stéarate de zinc électrolytique transformé la surface d'oxyde d'aluminium anodique (AAO) à superhydrophobe, ayant angle de 160 ° de contact de l'eau. Les densités de courant de corrosion des surfaces

d'aluminium anodisé et d'alliages sont avérés 200 et 400 nA/cm^2, respectivement. A titre de comparaison, superhydrophobe anodique d'oxyde d'aluminium (SHAAO) représente une valeur beaucoup plus faible de 88 nA/cm^2. De même, la résistance de transfert de charge, R_{ct}, mesurée par spectroscopie d'impédance électrochimique montre que le substrat a été trouvé SHAAO être 200 fois plus grande que le substrat en alliage d'aluminium telle que reçue. Ces résultats ont prouvé que les surfaces superhydrophobes créées sur la surface anodisée ont considérablement amélioré la propriété de résistance à la corrosion de l'alliage d'aluminium.

ACKNOWLEDGEMENTS

After years of research, working with a great number of expert scientists, engineers and technicians, the project has been finally greatly valued by the scientific as well as non-scientific community. It is a great pleasure to convey my humble gratitude to all the people involved in building up this thesis.

In the first place, I would like to thank all the sponsors of this research project, namely, the UQAC/NSERC/REGAL. Thanks to their financial support.

I would like to express my sincere and special thanks to my director, Prof. Dilip Sarkar, for his patience, guidance, encouragement and support of my research work. He always has plenty of good ideas to solve problems and I have always gained a lot of knowledge whenever I talked with him. I am so proud and privileged to work with him and learn from his expertise throughout my studies.

I am extremely grateful to my co-director Prof. X.-Grant Chen, for his continuous support during my research work. Thanks to his valuable instructions technical discussions and suggestions throughout this project.

Both technical and scientific discussions with Prof. Sarkar and Prof. Grant Chen made me extremely successful in demonstrating my presentation skills in conferences, where I got two rewards of best posters from both rio tinto alcon and aluminum association of canada in national conferences such as REGAL's students day.

I would also like to thank all my colleagues, professors and technicians in Cural for their continuous support and help throughout my study. Those include Dr. Zhan Zhang, Émélie Brideau, Alexandre, Dany Racine, Kun Liu, Zhen Li, Na Xu, Zhanying Guo, Lanfeng Jin, Hezhaoye Ma, Qinfu Zhao, Jiawei Xiong, Jian Qin and Lei Pan.

I would like to specially thank Dr. Zhan Zhang, Dr. N. Saleema, Prof. Dilip. Sarkar and Prof. X.-Grant Chen for taking their precious time off to be present in my examination committee in spite of their busy schedules.

Also I sincerely appreciate Jean-Denis Brassard for his help in the French learning, during my research period and for correcting the French abstract of my thesis.

I would like to express my warmest and deepest appreciation to my dear parents, my father and my mother for their never-ending support, understanding and patience in all the situations. Whenever I came across any kind of difficulties, they always say "you can do it" to encourage me.

Cangji Shi, my beloved husband, is a very important contributor to the successful completion of my thesis. Thanks for his suggestion during the research, his encouragement, his affection, and his love. Thanks for everything he did for me.

"Best for last"... my lovely cute son Andrew Louie Shi, now 20 months... the best part of my life, of me. I only have tears and no words to thank him. He went to day care since 4 months. He has sacrificed a lot of happy moments, as all the children with their mothers. However, he gave me a lot of support and happiness. I love you Andrew.

Finally, I would like to thank everybody who was important to the successful realization of this thesis; I apologize that I could not thank them personally one by one.

TABLE OF CONTENTS

FIGURE CONTENTS

TABLE CONTENTS

EQUATION CONTENTS

CHAPTER 1 INTRODUCTION

This chapter provides an introduction to the problems posed by the corrosion behaviors and a potential solution using superhydrophobic coatings. The hypothesis and objectives of the thesis and the methodologies are outlined in the following sections.

1.1 Introduction

In our previous study, superhydrophobic surfaces can be fabricated using electrochemical deposition method, which is applied for corrosion resistance on metals. In the present work, superhydrophobic aluminum alloy surfaces are prepared by incorporation of surface anodizing and electrophoretic deposition, while their corrosion resistance property is investigated as well.

1.1.1 Superhydrophobicity

The wetting properties of the surfaces (metal, alloy, oxide, etc.) are evaluated by the water contact angle measurements on those surfaces. When the contact angle of water is less than 90^{o} the surface is termed as hydrophilic and when the contact angle is more than

90^{o} the surface is termed as hydrophobic. When the water contact angle is close to zero degree (complete wetting) the surface is called superhydrophilic; on the other hand when the contact angle on a surface is more than 150^{o} (non-wetting) this surface is termed as superhydrophobic.

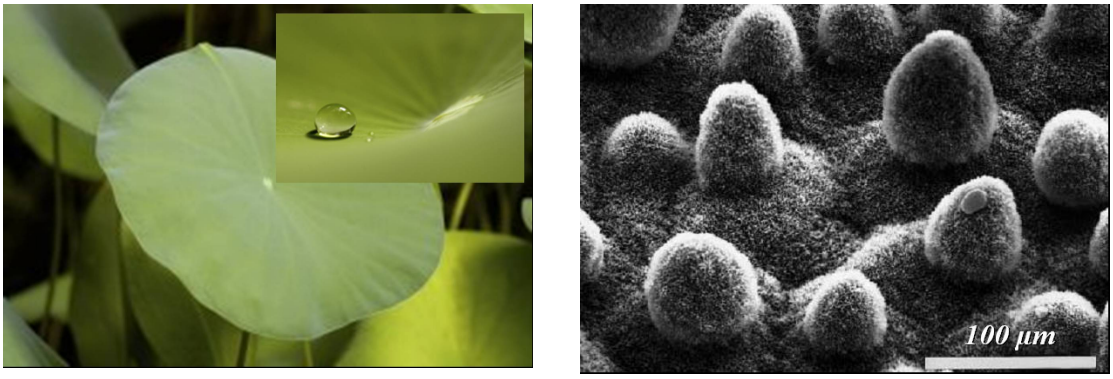

Figure 1. 1 Water drop on a lotus leaf and microstructure of a lotus leaf [1]

The superhydrophobic properties or non-wetting properties are commonly observed on surfaces of many natural plants and insects. One of the commonly cited examples is the lotus leaf. The so-called "Lotus effect" is due to the presence of a rough micro-nanostructure (Figure 1.1) covered with waxy materials with a high degree of resistance to wetting, resulting in a water contact angle slightly above 150^{o} [2].

Among several other plants, animals and insects which exhibit superhydrophobic properties, water striders are also commonly known as they can easily stand and walk on water due to the special non-wetting feature of their legs [3]. The water repellency of their legs, according to Gao and Jiang [3], is due to the legs' special hierarchical structure, as they are covered with large numbers of oriented tiny hairs (microsetae) with fine nanogrooves coated with waxy materials.

The rough structure allows for large amounts of air to be trapped between the gaps of the micro/nanostructure, resulting in a heterogeneous surface composite, where air and the waxy tissue provide very low surface energy enhancing the contact angle of the rough structured surface. Learning from nature, superhydrophobicity can be obtained by creating a surface with optimum roughness followed by passivation with a low-surface-energy coating. As the contact area of water on a superhydrophobic solid surface is negligible, such surfaces would effectively reduce the contact area water and hence reduce corrosion, a deleterious effect caused mostly due to constant contact of surfaces with wet and humid environment.

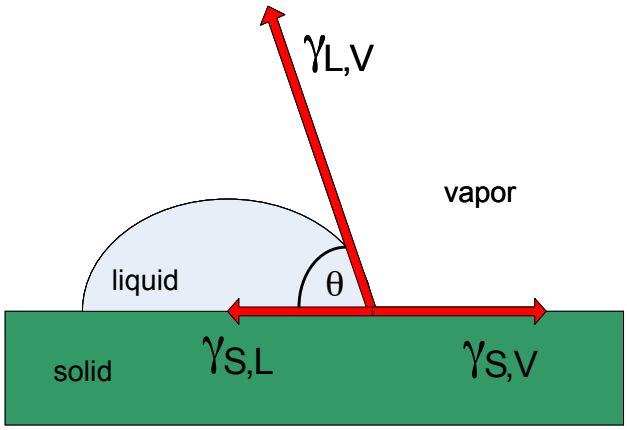

Figure 1. 2 A water drop in equilibrium state on a surface, as presented by Young [4]

A very basic and commonly used relation (Equation 1.1) describing wettability with respect to the contact angle of a drop in equilibrium with a solid surface was given by Young [4]**.** It relates the interfacial free energies of the three interfaces the drop comes into contact with, when placed on a solid surface, namely the solid/liquid (γ_{SL}), solid/vapor (γ_{SV}), and liquid/vapor (γ_{LV}) interfaces. The line of contact with the three co-existing phases of the system makes an angle of contact, θ , with the surface, as shown in Figure 1.2.

$$cos\theta = \frac{\gamma_{SV}-\gamma_{SL}}{\gamma_{LV}} \qquad \text{(Equation 1. 1)}$$

To reach contact angle values greater than 150°, necessary for achieving superhydrophobicity, surface roughness is often added to enhance the hydrophobicity of the solid surface. The surface topography effects have been mathematically expressed by the Wenzel and the Cassie-Baxter equations [5,6]. The Wenzel equation is expressed as:

$$\cos\theta^* = R_W \cos\theta \qquad \text{(Equation 1. 2)}$$

where the roughness factor R_w is the ratio of the true to the apparent surface areas. Figure 1.3(a, b) depict the behavior of water drop based on Wenzel and Cassie-Baxter models.

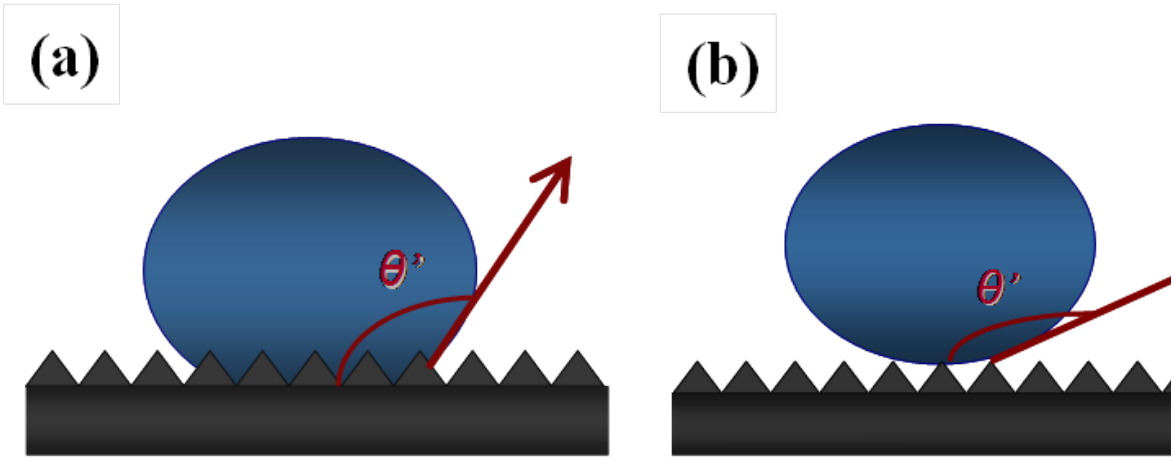

Figure 1. 3 Surface topography effects on water contact angle by (a) Wenzel Model, (b) Cassie-Baxter Model [5,6]

The Cassie-Baxter model, however, describes the effect of roughness on chemically heterogeneous structures where the apparent contact angle is mathematically derived from the Cassie equation, as follows:

$$\cos\theta' = f_1\cos\theta_1 + f_2\cos\theta_2 \qquad \text{(Equation 1. 3)}$$

where θ' is the contact angle of the composite surface consisting of two components with contact angles θ_1 and θ_2, and their corresponding area fractions f_1 and f_2. In such a composite system, f_1 is assumed to be the area fraction of the solid surface and f_2 is assumed to be that of air, where θ_2 is 180^o. As $f_1 + f_2 = 1$, Equation 1.3 can be further modified as:

$$\cos\theta' = f_1(\cos\theta_1 + 1) - 1 \qquad \text{(Equation 1. 4)}$$

This equation explains why, on a rough surface with a large amount of air entrapment in the surface irregularities, one can obtain a highly superhydrophobic surface with a very small area fraction f_1 of the surface in contact with the water drop.

The commonly used approaches to prepare superhydrophobic surfaces are lithographic and template-based techniques [7], laser ablation technique [8] and plasma treatment of the surfaces [9,10], self-assembly and self-organization [10], chemical bath deposition (CBD) [11,12], chemical vapor deposition (CVD) [13], and electrochemical deposition [14] as a first step in order to create a certain roughness on the surface. Such surfaces are usually coated with a low surface energy material as a second step to eliminate or reduce further interactions with water. Sarkar et al. [14-17] fabricated several superhydrophobic surfaces using diverse methods which demonstrated water roll-off properties [14-17]. All the above-mentioned studies involve two-step processes where in the first step a rough surface is created and in the second step, the rough surface is "passivated" by coating with low surface energy molecules or thin films. Recently, Sarkar and Paynter [18] showed the fabrication of superhydrophobic silver surfaces in one-step process by incorporating fluoroalkylsilanes (FAS) molecules in silver nitrate solution [18] where surface roughness and lowering of surface energy takes place at the same time.

1.1.2 Corrosion

Corrosion is the disintegration of an engineered material into its constituent atoms due to chemical reactions with its surroundings. In other words, corrosion is the wearing off of metals due to a chemical reaction. The metals or alloys surfaces exposed to corrosive environments (humidity, salt, acid, base, etc.) along with pollution are not stable and can result in severe damages on the surfaces due to corrosion. Aluminum alloys corrode merely from exposure to moisture in the air, but the process can be strongly affected by exposure to certain substances such as salt, acid, corrosive gas (SO_2) etc. Corrosion usually starts on the surface forming pits and cracks which propagate into the material under continued exposure to the corrosive environment, ultimately resulting in serious damages.

Surface passivation or conversion coatings are being used to reduce surface corrosion processes. However, very recently, superhydrophobicity is under research for protecting surfaces from corrosion [19-30]. Because the superhydrophobic surfaces with a non-wetting layer reduced the contact area between the superhydrophobic surfaces and

the corrosive environment.

Corrosion tests can often be done in different solutions, such as in seawater [31,32], in hydrochloric acid (HCl) [33], in chloride containing solution [34], in NaCl, Na_2HPO_4, $NaHCO_3$, KCl solution [35], deionized water et al. [36], etc., depending on the kind of intended application. In addition, corrosion resistance phenomenon can also be monitored via weight loss measurements [37] and neutron reflectivity [38]. The effects of corrosion resistance can also be seen from the potentiodynamic curves [19,31].

1.2 Hypothesis

Based on the above introduction, it is therefore plausible that a properly nanostructured material with an optimized surface roughness will reduce the contact area between the surface and corrosive environment, thereby inhibiting corrosion behavior. In this project, this hypothesis will be investigated by the deposition of passivated, nanostructured materials to ultimately preventing corrosion behavior on the aluminum alloy substrates.

1.3 Objectives

Corrosion behavior on metals are one of the most main problems in the industrial applications, which is caused mainly by their contact with wet environments can be effectively reduced or even eliminated completely by making the surfaces superhydrophobic where water wouldn't stick, thereby repelling wet corrosive substances.

The main objective of this research project is to produce a stable superhydrophobic thin films surface on aluminum alloy using anodizing and electrophoretic deposition/electrodeposition to inhibit corrosion on aluminum alloy surfaces. The main objective can be sub-categorized as follows:

- Preparation of superhydrophobic aluminum alloy substrates；

Superhydrophobic aluminum alloy substrates are fabricated by electrophoretic deposition and electrodeposition. The details of methodology of electrophoretic deposition are in chapter 3 section 3.4. The details of electrodeposition are in chapter 3 section 3.5.

- Anodization of aluminum alloy surfaces;

The anodized aluminum alloy surfaces are prepared using phosphoric acid electrolytic solution. The details of the anodizing process are in chapter 3 section 3.6.

- Electrophoretic deposition/electrodeposition of superhydrophobic thin film on anodized surface;

As the superhydrophobic aluminum alloy surfaces have been fabricated by electrophoretic deposition and electrodeposition, the superhydrophobic anodized surfaces are prepared with the same process as illustrate in chapter 3 section 3.4 and 3.5. The details are in section 3.7.

- The dynamic corrosion studies on these surfaces and surface characterization prior to and after dynamic corrosion studies.

The details of the characterization and corrosion test of the samples are shown in chapter 3 section 3.8.

1.4 Methodology

The major procedures of this research work consist of the following steps：

(i) Creating nanopatterns on the aluminum alloy substrates: Nanopatterns are created on the substrates of aluminum alloy by electrophoretic deposition, a method where the aluminum alloy substrate was immersed in the electrolytic solution containing ZnO nanoparticles in a mixture of 0.01 M stearic acid, 2-propanol and tert-butyl alcohol in the application of DC voltage.

(ii) Creating nanopatterns on the aluminum alloy substrates: Nanopatterns are created on the substrates of aluminum alloy by electrodeposition, a method where the aluminum alloy substrate was immersed in the electrolyte containing zinc nitrate ($Zn(NO_3)_2$) mixing with stearic acid in the application of 20 V DC.

(iii) Anodization of aluminum alloys. Anodization process was performed in H_3PO_4 in the constant current mode.

(iv) Creating nanopatterns on the anodized aluminum oxide substrates: The anodized aluminum oxide substrates were electrodeposited using electrolytic solution containing

zinc nitrate mixing with stearic acid.

(v) Characterizations: Surface morphology studies are performed using optical microscopy, field emission scanning electron microscopy (SEM), and optical profilometry. The surface compositional analyses are carried out using X-ray diffraction (XRD), X-ray photoelectron spectroscopy (XPS) and Fourier-transform infrared spectrometry (FTIR). Superhydrophobicity tests are performed using a contact angle goniometer. The corrosion behaviors are tested by potentiodynamic polarization as well as electrochemical impedance spectroscopy (EIS).

References

(1) Wenzel, R. N. *Industrial & Engineering Chemistry* **1936**, *28*, 988.

(2) Neinhuis, C.; Barthlott, W. *Annals of Botany* **1997**, *79*, 667.

(3) Gao, X.; Jiang L. *Nature* **2004**, *36*, 432.

(4) Young, T. *Phil. Trans. R. Soc. Lond* **1805**, *95*, 65.

(5) Wenzel, R. N. *Ind. Eng. Chem.* **1936**, *28*, 988.

(6) Cassie, A.B. D.; Baxter S. *Trans. Faraday Soc.* **1944**, *40*, 546.

(7) Thieme, M.; Frenzel, R.; Schmidt, S.; Simon, F.; Hennig, A.; Worch, H.; Lunkwitz, K.; and Scharnweber, D.*Adv. Eng. Mater.* **2001**, *3*, 691.

(8) Stelmashuk, V.; Biederman H.; Slavinska, D.; Zemek, J.; and Trchova, M. *Vacuum* **2005**, *77*, 131.

(9) Kim, S. H.; Kim, J.H.; Kang, B. K.; and Uhm, H. S. *Langmuir* **2005**, *21*, 12213.

(10) Schondelmaier, D.; Cramm, C.; Klingeler, R.; Morenzin, J.; Zilkens, C. and Eberhardt W. *Langmuir* **2002**, *18*, 6242.

(11) Hosono, E.; Fujihara, S.; I. Honma and H. Zhou *J. Am. Chem. Soc.* **2005**, *127*, 13458.

(12) Saleema, N.; Farzaneh, M. *Applied Surface Science* **2008**, *254*, 2690.

(13) Liu, H.; Zhai, J.; Jiang, L. and Zhu, D. B. *Langmuir* **2004**, *20*, 5659.

(14) Sarkar, D. K.; Farzaneh, M. *Journal of Adhesion Science and Technology* **2009**, *23*, 1215.

(15) Safaee, A.; Sarkar, D.; Farzaneh, M. *Applied Surface Science* **2008**, *254*, 2493.

(16) Sarkar, D. K.; Farzaneh, M. *Applied Surface Science* **2008**, *254*, 3758.

(17) Sarkar, D. K.; Farzaneh, M.; Paynter, R. W. *Materials Letters* **2008**, *62*, 1226.

(18) Sarkar, D. K.; Paynter, R. W. *Journal of Adhesion Science and Technology* **2010**, *24*, 1181.

(19) Liu, H.; Szunerits, S.; Xu, W.; Boukherroub, R. *ACS applied materials & interfaces* **2009**, *1*, 1150.

(20) Zhang, F.; Zhao, L.; Chen, H.; Xu, S.; Evans, D. G.; Duan, X. *Angewandte Chemie* **2008**, *47*, 2466.

(21) Yin, Y.; Liu, T.; Chen, S.; Liu, T.; Cheng, S. *Applied Surface Science* **2008**, *255*, 2978.

(22) Zhang, F.; Chen, S.; Dong, L.; Lei, Y.; Liu, T.; Yin, Y. *Applied Surface Science* **2011**, *257*, 2587.

(23) Tittarelli, F.; Moriconi, G. *Cement and Concrete Research* **2008**, *38*, 1354.

(24) Wang, P.; Zhang, D.; Qiu, R.; Hou, B. *Corrosion Science* **2011**, *53*, 2080.

(25) Ishizaki, T.; Hieda, J.; Saito, N.; Saito, N.; Takai, O. *Electrochimica Acta* **2010**, *55*, 7094.

(26) Liu, T.; Chen, S.; Cheng, S.; Tian, J.; Chang, X.; Yin, Y. *Electrochimica Acta* **2007**, *52*, 8003.

(27) Wang, J.; Li, D.; Liu, Q.; Yin, X.; Zhang, Y.; Jing, X.; Zhang, M. *Electrochimica Acta* **2010**, *55*, 6897.

(28) Wang, P.; Qiu, R.; Zhang, D.; Lin, Z.; Hou, B. *Electrochimica Acta* **2010**, *56*,

517.

(29) Milošev, I.; Kosec, T.; Bele, M. *Journal of Applied Electrochemistry* **2010**, *40*, 1317.

(30) Mojca, F.; Angela, S. Aljaz, V.; Robi, J. and Vojmir, F. *Langmuir* **2007** *23*, 5505.

(31) He, T.; Wang, Y.; Zhang, Y.; lv, Q.; Xu, T.; Liu, T. *Corrosion Science* **2009**, *51*, 1757.

(32) Liu, T.; Chen, S.; Chang, X.; and Cheng, S. *Electrochimica Acta* **2007**, *52*, 3709.

(33) Shen, G.X.; Lin, L.; Lin, C.J.; and Scantlebury, D. *Electrochimica Acta* **2005**, *50*, 5083.

(34) Barkhudarov, P.M.; Watkins, E.B.; Doshi, D.A.; Brinker, C.J. and Majewski, J. *Corrosion Science* **2008**, *50*, 897.

(35) Li, H.F.; Cheng, Y. and Zheng, Y.F. *Materials Letters* **2010**, *64*, 1462.

(36) Bentiss, F. Gengembre L. and Lagrene´e M. *Applied Surface Science* **1999**, *152*, 237.

(37) Smith, C.J.E.; Baldwin, K.R., and Hewins, M.A.H. *Institute of Materials* **1993**, *2*, 1652.

(38) Ishizaki, T.; Saito, N. *Langmuir* **2010**, *26*, 9749.

CHAPTER 2 LITERATURE REVIEW

In this chapter, the literature related to the project is organized. The literature on the fabrication of superhydrophobic surfaces, anodizing and the study of corrosion resistance are presented. Recently, various fabrication methods for superhydrophobic surfaces have been explored [1-13], such as sol-gel process [14,15], plasma treatment [16], chemical vapor deposition [17], chemical etching [3], anodizing, electrodeposition [18] and electrophoretic deposition (EPD) [19] et al.. In this project, the EPD and electrodeposition are utilized to prepare superhydrophobic surfaces. Because they are easier to operate,and not expensive in the whole process including the electrolyte, electrode system and materials et al.

2.1 Fabrication methods of superhydrophobic surfaces

When dispersed in a polar solvent or an electrolyte solution, the surface of nanoparticles develops an electrical charge via one or more of the following mechanisms: (1) preferential dissolution or (2) deposition of charges or charged species, (3) preferential reduction or (4) oxidation, and (5) adsorption of charged species such as

polymers [20]. Charged surfaces will electrostatically attract oppositely charged species (typically called counterions) in the solvent or solution. A combination of electrostatic forces, Brownian motion and osmotic forces would result in the formation of a so-called double layer structure, as schematically illustrated in Figure 2.1.

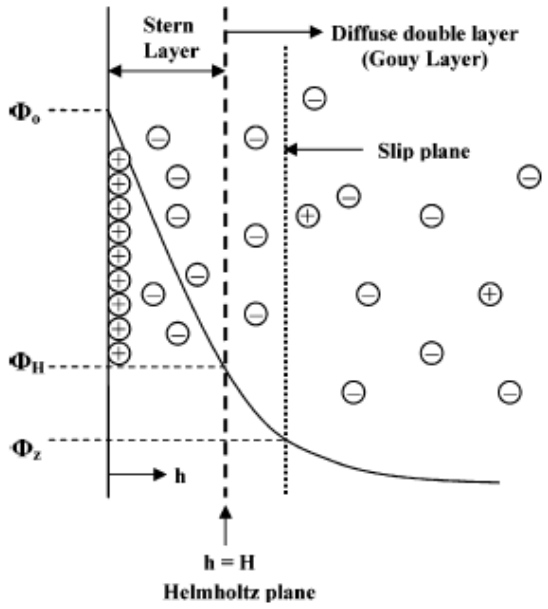

Figure 2. 1 Schematic illustrating electrical double layer structure and the electric potential near the solid surface with both Stern and Gouy layers indicated. Surface charge is assumed to be positive [20].

The Figure depicts a positively charged particle surface, the concentration profiles of negative ions and positive ions and the electric potential profile. The concentration of

counterions gradually decreases with distance from the particle surface, whereas that of charge-determining ions increases. As a result, the electric potential decreases with distance. Near to the particle surface, the electric potential decreases linearly, in the region known as the Stern layer. Outside the Stern layer, the decrease follows an exponential relationship, and the region between Stern layer and the point where the electric potential equals zero is called the diffusion layer. Together, the Stern layer and diffusion layer are called the double layer structure in the classic theory of electrostatic stabilization.

Upon application of an external electric field to a colloidal system or a sol, the constituent charged particles are set in motion in response to the electric field, as schematically illustrated in Figure 2.2.

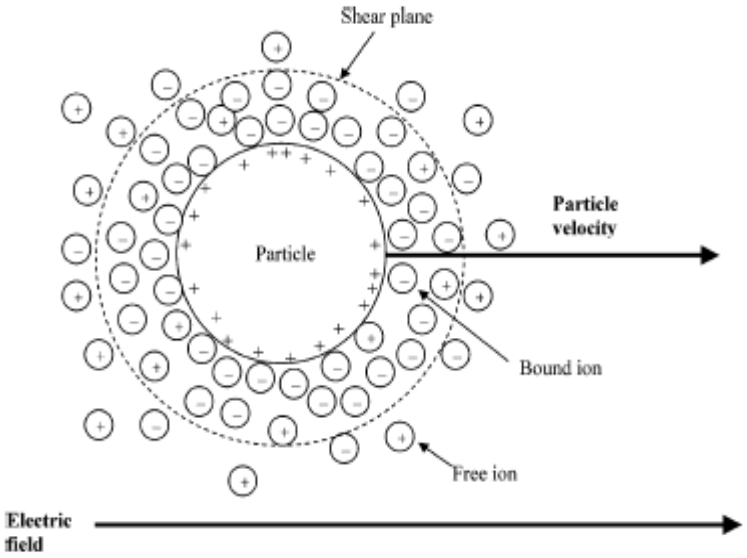

Figure 2. 2 Schematic of electrophoresis of a charged particle in a colloidal suspension, demonstrating the motion in the direction of the applied electric field. Some of the solvent or solution surrounding the particle will move with it, since this part of the solvent or solution is tightly bound to the particle and separated from the rest solvent or solution by shear plane [20].

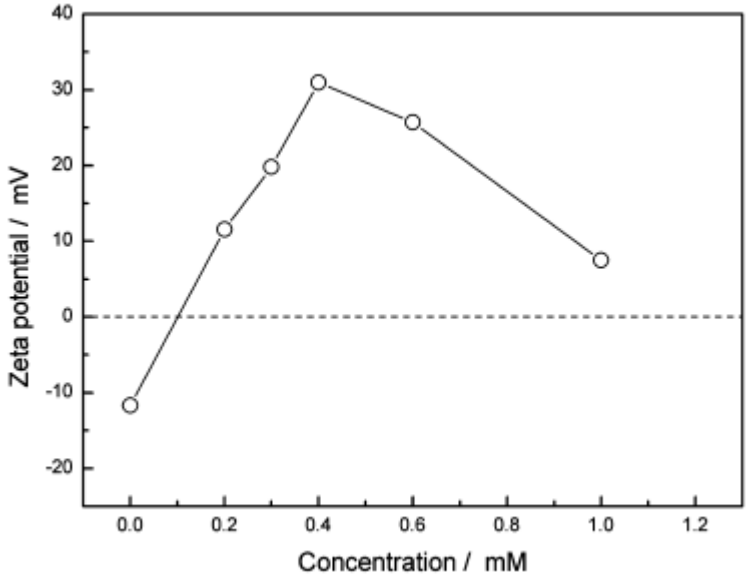

Figure 2. 3 Zeta potential of the activated-carbon suspensions with various concentrations of nickel nitrate [20].

This type of motion is referred to as electrophoresis. When a charged particle is in motion, some of the solvent or solution surrounding the particle will move with it, since part of the solvent or solution is tightly bound to the particle. The plane that separates the tightly bound liquid layer from the rest of the liquid is called the slip plane. The electric potential at the slip plane is known as the zeta potential. The zeta potential is an important parameter in determining the stability of a colloidal dispersion or a sol; a zeta potential larger than about 25 mV is typically required to stabilize a system. Generally, the higher zeta potential means the more stability.

In the study of Wu et al. [21], Ni-decorated activated-carbon film is deposited directly onto the stainless steel substrate by using one-step electrophoretic deposition (EPD) in the activated-carbon suspension containing nickel nitrate additive. The variation of zeta potential as a function of the concentrations of nickel nitrate was plotted in Figure 2.3. The zeta potential of activated-carbon suspension in the isopropanol bath without the nickel nitrate additive was measured to be about -12 mV, indicating a weakly and negatively charged surface of activated-carbon particles. It is generally believed that a

low magnitude of the zeta potential may result in a drawback in activated-carbon transport under the applied electric field. The suspension of low zeta potential in magnitude is unstable because there is no conspicuous repulsion force between the activated carbons to inhibit the agglomeration of activated carbons. The zeta potential shown in Figure 2.3 increases with increasing the concentration of nickel nitrate; it reaches a maximum value of 31mV at a concentration of 0.4 mM and then decreases with further increase in the concentration. An increase in zeta potential can be explained by the adsorption of positively charged nickel ions on the negatively charged activated-carbon particles. The higher the concentration leads to the higher the adsorption amount of nickel ion on the activated-carbon surface. Therefore, the zeta potential increases linearly with increasing the concentration of nickel ion. A decrease in zeta potential after the addition of excess amount of nickel nitrate (concentration higher than 0.4 mM) is attributed to the increased ionic strength. The ionic strength, which depends strongly on the charge type and concentration of the electrolyte, plays an important role in determining the thickness of electric double layer (EDL) and consequently affecting

the stability of activated-carbon suspension. When the ionic strength of electrolyte is high enough, the EDL may become very compact, and the charge on colloidal surface is shielded up to very short distances [21]. Under this circumstance, the activated carbons can approach quite closely before the electrostatic repulsion becomes apparent, and the van der Waals attraction between particles may be quite large. Therefore, it is reasonable to conclude that when the ionic strength is increased with increasing the concentration of nickel nitrate, the thickness of EDL decreases, leading to the precipitation of activated carbons.

Figure 2.4 shows a schematic of the proposed Ni-decorated activated-carbon deposition in the EPD process. EPD of the activated-carbon film is achieved via transport of positively charged activated carbons (adsorbed with nickel ions) toward a negative electrode and via deposition of activated carbons with charge neutralization under an applied electric field. When an activated carbon arrives at the SS substrate, nickel ions adsorbed on the surface of the activated carbon (including the interior surface of pores) are reduced electrochemically to form metallic nickel because the activated carbon has

electrical conductivity, which allows electrons to conduct from the SS substrate to the outer layer of the activated carbon. Metallic nickel appears to be appropriate as a metal binder for attaching the activated carbons because of its higher electrical conductivity compared with that of the polymer binders [22,23]. As a result, the activated carbon particles having electrically charged surfaces (because of adsorption of nickel ions) continue to deposit on the film forming a Ni-decorated activated-carbon film.

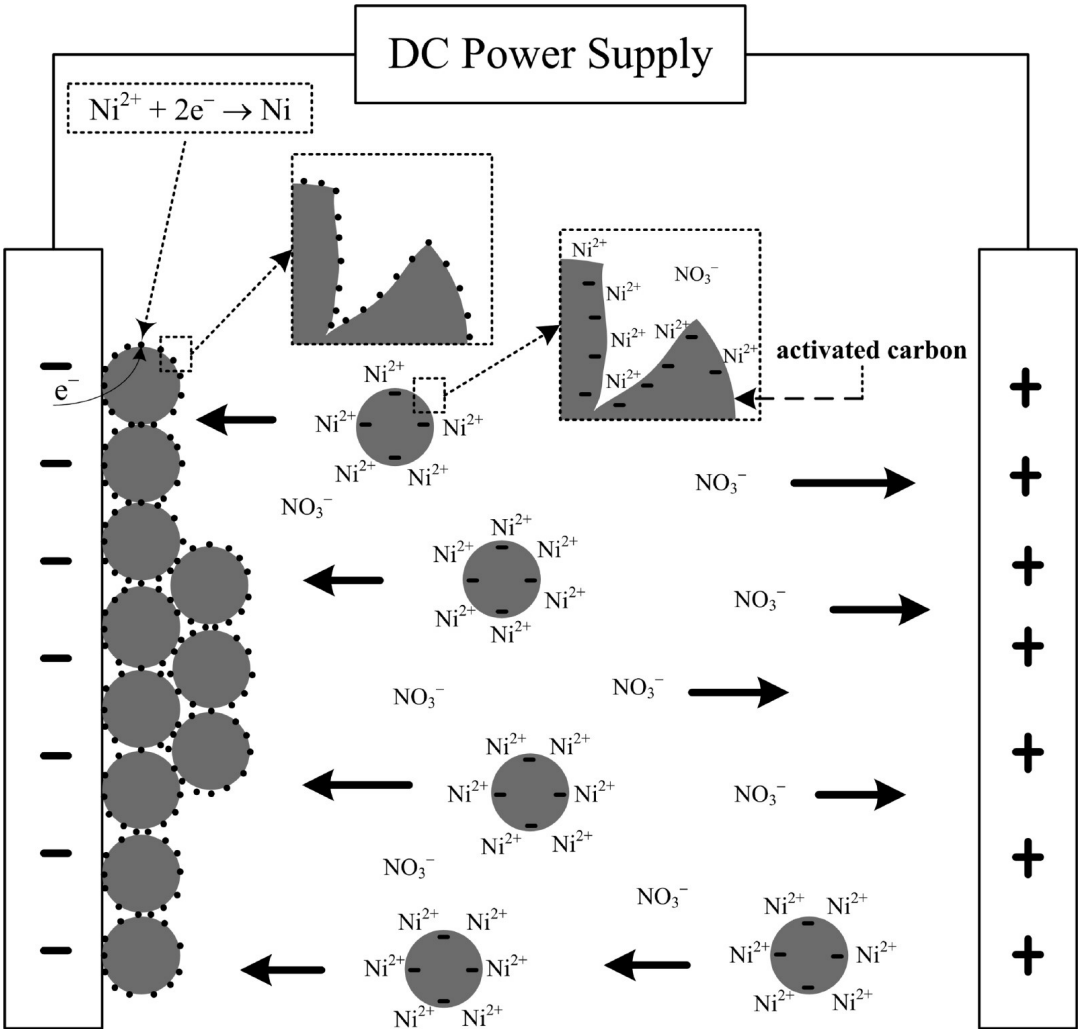

Figure 2. 4 Schematic of the proposed Ni-decorated activated-carbon deposition in the EPD process [21].

The mobility of a nanoparticle, μ, in a colloidal dispersion or a sol is dependent on the dielectric constant of the liquid medium, ϵ_r, the zeta potential of the nanoparticle, ξ, and the viscosity of the fluid, η. Several forms for this relationship have been proposed,

such as the Huckel equation [24].

$$\mu = \frac{2\epsilon_r \epsilon_0 \xi}{3\pi\eta} \qquad \text{(Equation 2. 1)}$$

Double layer stabilization and electrophoresis are extensively studied subjects. Electrophoretic deposition simply uses such an oriented motion of charged particles to grow films or monoliths by enriching the solid particles from a colloidal dispersion or a sol onto the surface of an electrode as schematically illustrated in Figure 2.5. If particles are positively charged (more precisely speaking, having a positive zeta potential), then the deposition of solid particles will occur at the cathode. Otherwise, deposition will be at the anode. At the electrodes, surface electrochemical reactions proceed to generate or receive electrons. The electrostatic double layers collapse upon deposition on the growth surface, and the particles coagulate. There is not much information on the deposition behavior of particles at the growth surface. Some surface diffusion and relaxation is expected. Relatively strong attractive forces, including the formation of chemical bonds

between two particles, develop once the particles coagulate. The films or monoliths grown by electrophoretic deposition from colloidal dispersions or sols are essentially a compaction of nanosized particles. Such films or monoliths are porous, i.e., there are voids inside. Typical packing densities, defined as the fraction of solid (also called green density) are less than 74%, which is the highest packing density for uniformly sized spherical particles [25]. The green density of films or monoliths by electrophoretic deposition is strongly dependent on the concentration of particles in sols or colloidal dispersions, zeta potential, externally applied electric field and reaction kinetics between particle surfaces. Slow reaction and slow arrival of nanoparticles onto the surface would allow sufficient particle relaxation on the deposition surface, so that a high packing density is expected.

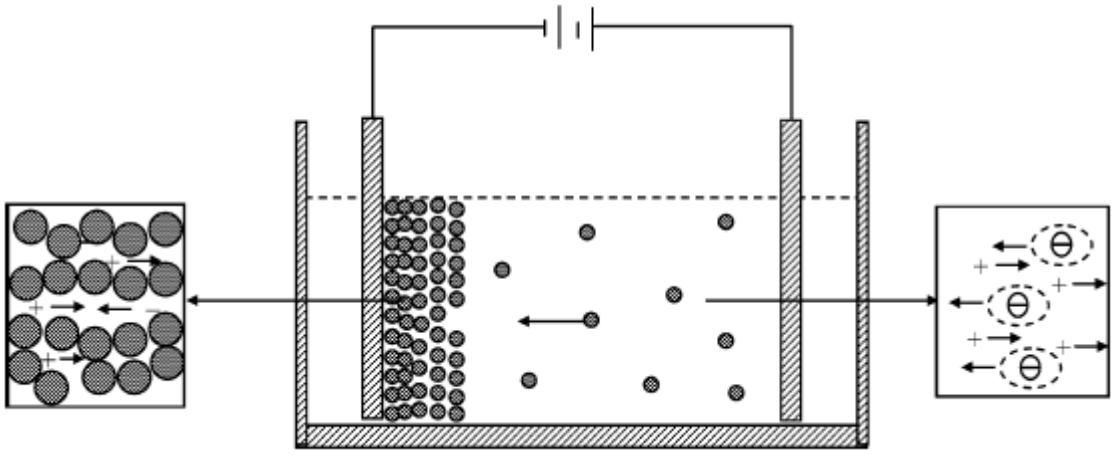

Figure 2. 5 Schematic showing the electrophoretic deposition. Upon application of an external electric field to a colloidal system or a sol, the constituent charged nanoparticles or nanoclusters are set in motion in response to the electric field, whereas the counterions diffuse in the opposite direction [21].

Many theories have been proposed to explain the processes at the deposition surface during electrophoretic deposition. The electrochemical process at the deposition surface or electrodes is complex and varies from system to system. However, in general, a current exists during electrophoretic deposition, indicating that reduction and oxidation reactions occur at electrodes and/or the deposition surface. In many cases, films or monoliths grown by electrophoretic deposition are electric insulators. However, the films or monoliths are porous and the surface of the pores would be electrically charged just

like the nanoparticle surfaces, since surface charge is dependent on the solid material and the solution. Furthermore, the pores are filled with solvent or a solution that contains counterions and charge-determining ions. The electrical conduction between the growth surface and the bottom electrode can proceed via either surface conduction or solution conduction. Since films or monoliths grown by electrophoretic deposition are porous, postdeposition sintering at elevated temperatures is usually required to form a dense material. However, considering the fact that the films or monoliths are a compaction of nanosized particles, sintering or densification is relatively easier than conventional ceramic sintering. If the initial solid particles were amorphous, sintering would also induce crystallization.

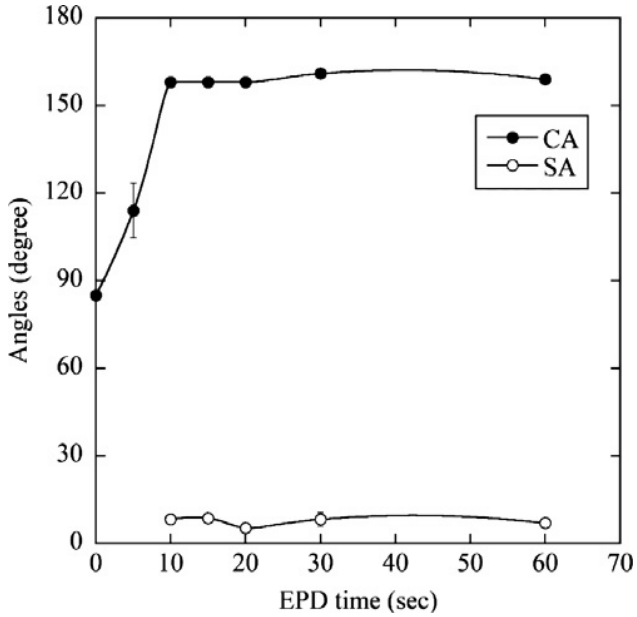

Figure 2. 6 CAs and SAs of SiO2/TMSS composite coatings on ITO plates prepared under different EPD time [26].

In the application of electrophoretic deposition (EPD), fabrication of superhydrophobic surface is one of the most important fields, in terms of the wide applications of superhydrophobicity as well as the advantages of the methodology of EPD.

Hitoshi Ogihara applied one-step electrophoretic deposition for preparation of superhydrophobic silica particle/trimethylsiloxysilicate (TMSS) composite coatings [26]. According to the study, superhydrophobic particle coatings are formed when using mildly

unstable suspensions of hydrophobic nanoparticles as EPD baths, because the appropriate surface roughness of the coatings is formed by the deposition of nanoparticle aggregates.

Figure 2.6 shows CAs of SiO_2/TMSS composite coatings prepared at different EPD times ranging from 5 to 60 s. The sharp increase of contact angle from 0-10s was observed from 85° to 160°. The value of CAs was maintained after 10s of EPD. This is reasonable tendency because the amount of both SiO_2 particles and TMSS deposited by EPD for a short time could not be sufficient to exhibit superhydrophobicity.

However, the variation of contact angle with EPD time has a different tendency in the study of Young Soo Joung [27]. In their study, low surface energy materials with high surface roughness are achieved using EPD of unstable hydrophobic SiO_2 particle suspensions. Dynamic contact angles were measured on the films produced as a function of deposition time, as shown in Figure 2.7. The difference between advancing and receding contact angles is considered a more reliable method to evaluate superhydrophobicity, since water repellent surfaces can be evaluated strictly by contact angle hysteresis. The calculated roll-off angles shown in the inset of Figure 2.6 were 3°, 2°

and 7° for 30, 60 and 90s deposition time, respectively. Roll-off angles less than 10° indicate that the surface can be regarded as superhydrophobic in terms of both static and dynamic contact angles.

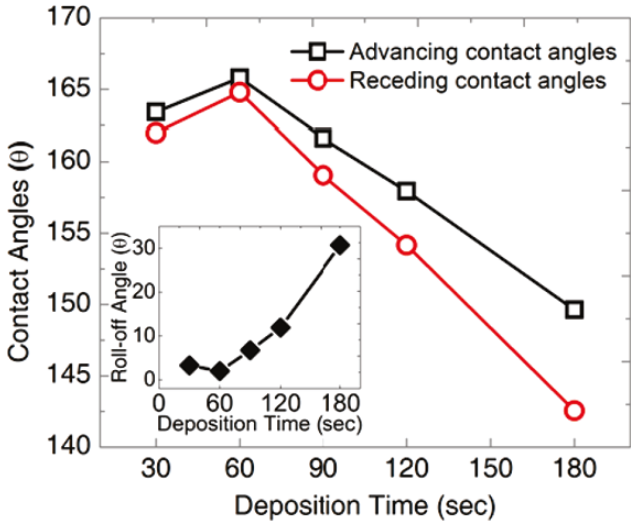

Figure 2. 7 Advancing and receding contact angles on the surfaces created at suspension pH 7.6. The inset shows roll-off angles calculated from the advancing and receding contact angles [27].

The colors of the superhydrophobic coating could be controlled by spraying a pigment nanoparticle suspension with electrophoretic deposition by Hitoshi Ogihara [28]. The pigment nanoparticles (β-type copper phthalocyanine, phthalocyanine green, disazo yellow, carbon black or cromophtal DPP red) and trimethylsiloxysilicate (TMSS)/

cyclopentasiloxane were added to ethanol to obtain different colored superhydrophobic surfaces.

As compared with electrophoretic deposition, electrodeposition is more widely used to fabricate superhydrophobic surfaces. In electrodeposition technique, two electrodes are connected with the power supply. A reaction may happen in the electrolyte and a deposition appeared on the surface of one of the electrode in the force of electricity.

Liu et al. prepared a superhydrophobic magnesium alloy surfaces by electrodeposition process [29].

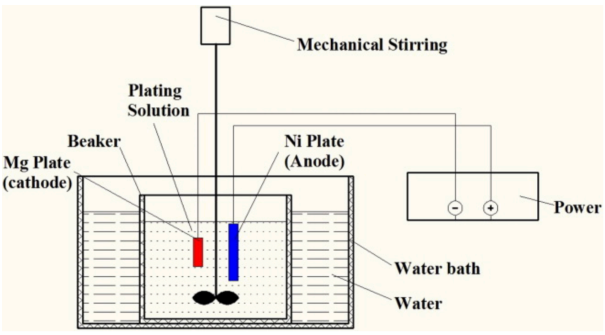

Figure 2. 8 Schematic representation of the electrodeposition [29].

In the electrodeposition process as shown in Figure 2.8, the power was connected to the anodic sample and cathodic sample in the electrolytic solution. When the power is

on, the anodic sample connects to the cathodic sample with the electrolytic solution, and the electric circuit is formed.

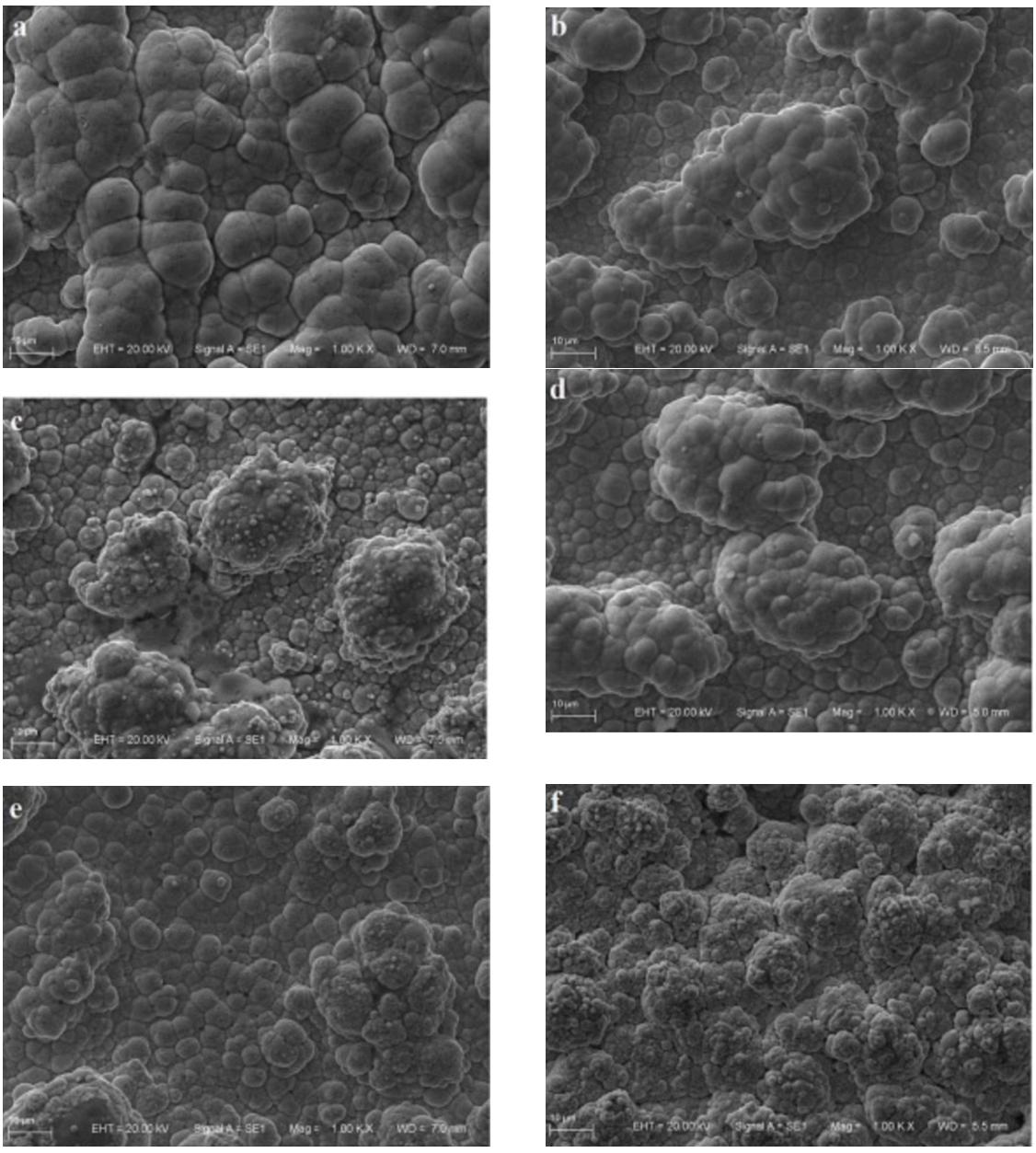

Figure 2. 9 SEM images of the sample surfaces after electroplated under the different time at for (a) 0, (b) 1, (c) 3, (d) 5, (e) 7 and (f) 10 min [29].

Figure 2.9 shows SEM images of sample surfaces under different times for (a) 0, (b) 1, (c) 3, (d) 5, (e) 7 and (f) 10 min, respectively. It is clearly concluded that the surfaces consist of three dimensional microstructures. The samples are covered by a large area of protrusive particles by electroless plating as shown in Figure 2.9(a) and the protrusive particles is uniform and tidiness. At 1 min of electrodeposition time, it can be seen clearly that the amount of protrusive particles are increased; at same time more and more particles are packed on surface and formed cauliflower-like clusters as shown in Figure 2.9(b).

The microstructure of the optimal super-hydrophobic surface is shown in Figure 2.9(c), and the water contact angles of the sample show the maximum value. It can be seen that the surface is rather rough and covered by particles, and the particles is covered with 1 to 2 μm cauliflower-like clusters. Between the particles, it can be seen that the surfaces are covered with small particles with the diameter of about 3-4 μm. By this microstructure air is trapped among the grooves formed from particles cluster, and the trapped air can reduce the water droplet touch the samples surfaces. Thus the water

cannot penetrate into the grooves. With the extension of electrodeposition time, the particles became bigger and the Ni coating became thicken as shown in Figure 2.9(d & e). The coatings become uniformly and densely covered by cauliflower-like clusters compactly at 10 min of deposition time as shown in Figure 2.9(f).

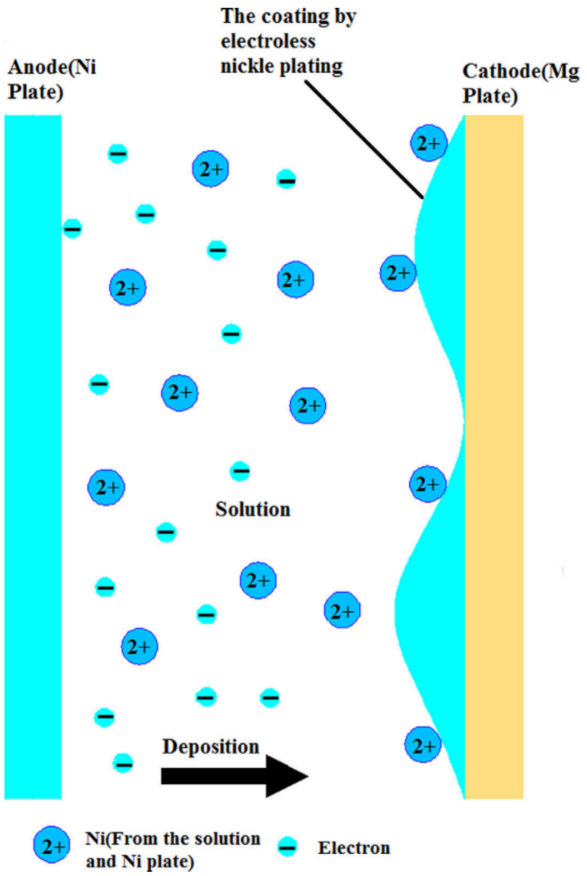

Figure 2. 10 Schematic illustration of the reaction process in the electrodeposition

Figure 2.10 shows the schematic illustration of the electrodeposition process. The Ni plate is used as anode, and as-prepared samples by electroless are applied as cathode.

When the Ni plate is applied with DC voltage as the anode, Ni ions are forced released from the Ni plate into the solution. On the other hand, some Ni ions released from the $NiCl_2$ solution, and all the Ni ions in the solution move to the cathode (Mg plate) with the electrons moving. So the Ni is deposited on the surface under the DC voltage.

A fast electrodeposition method for fabrication of lanthanum superhydrophobic surface with hierarchical micro-nanostructures has been presented by Chen et al. [30], with the electrolytic solution containing lanthanum chloride ($LaCl_3 \cdot 6H_2O$), myristic acid ($CH_3(CH_2)_{12}COOH$) and ethanol.

Figure 2.11 shows SEM images of cathodic copper surface at 0.038 M lanthanum chloride, 0.1 M myristic acid solution for different electrodeposition time. When the electrodeposition time is prolonged to 1 min, the number of particles increases and uniformity is improved. At a longer electrodeposition time, the homogeneous crystallite particle clusters are dense, and they cover the entire substrate. When the electrodeposition time is extended to 8 min, these nanostructure assemblies evolve into some small flowers, as shown in Figure 2.11(f). When the electrodeposition time is prolonged to 10 min, the

number of these small flowers becomes more (see Figure 2.11(g)). When the electrodeposition time is 15 min, all of the nanostructure assemblies evolve into the flowers, and the flower has the tendency to grow up with a larger size.

The electrodeposition reaction process is explained that when the copper electrodes are immersed in the electrolyte solution with the application of DC voltage, some La^{3+} ions near the cathode react with myristic acid, the reaction is shifted towards the formation of lanthanum myristate as protons are reduced to hydrogen around the cathodic surface. Meantime, the generation of H_2 gas stirs the electrolyte, the reaction preferentially proceeds in the vicinity of the cathode of the growing particles, where the concentration of H^+ is decreased, and the growth is mainly controlled by reaction.

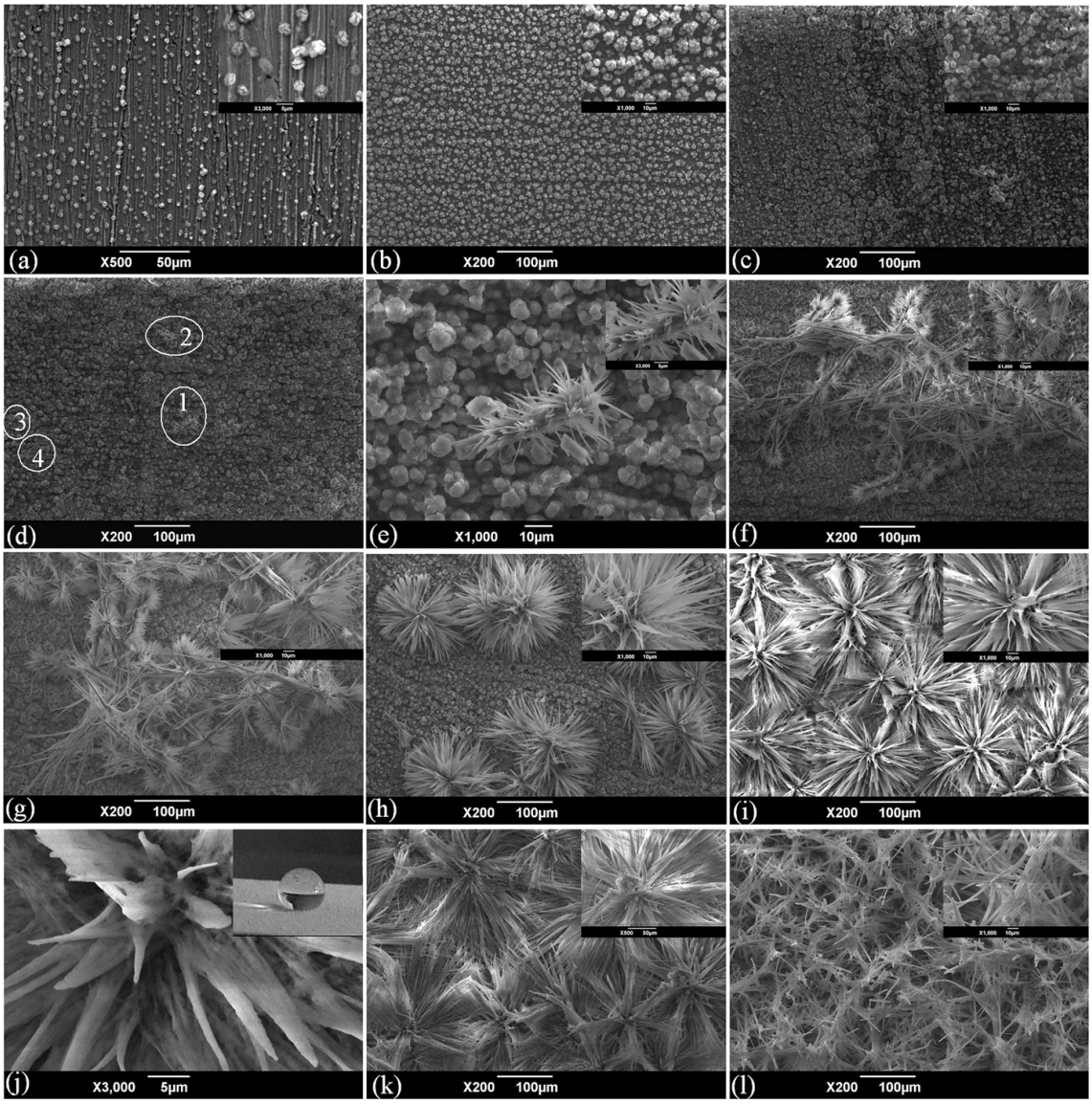

Figure 2. 11 SEM images of cathodic copper surface at 0.038 M lanthanum chloride, 0.1 M myristic acid solution with a DC voltage of 30 V for different electrodeposition times (a) 0.25 min; (b) 1 min; (c) 3 min; (d) 6 min; (e) the corresponding high magnification for 6 min; (f) 8 min; (g) 10 min; (h) 15 min; (i) 20 min; (j) the corresponding high magnification for 20 min; (k) 90 min and (l) 240 min [30].

$$La^{3+} + 3CH_3(CH_2)_{12}COOH \rightarrow La[CH_3(CH_2)_{12}COO]_3 + 3H^+ \qquad \text{(Equation 2. 2)}$$

In order to depict the wettability property of the cathodic surface, the corresponding water contact angles of surfaces with different time were tested with CCD measurement, and they were shown in Figure 2.12. When electrodeposition time is 0.25 min, the value of contact angle reaches 123˚. When deposition time increased to about 1 min, the contact angle enhances to 155˚. Thus, we can infer that the homogeneous crystallite particle clusters with low surface energy play an important role in superhydrophobicity. When deposition time is prolonged to 10 min, the contact angle is improved to 160˚. Furthermore, when deposition time becomes 20 min, the contact angle is enlarged to 162˚, and rolling angle is less than 2˚. When deposition time further increases to 240 min, the contact angle shows 165˚, and rolling angle is less than 2˚. The increasing improvement of contact angle results from the heterogeneous structures. With the deposition time evolves, the packing density of the flower-like microstructures increases, and superhydrophobicity slightly enhances, which is in agreement with the conclusion in the reference. In addition, according to C-B equation, it can be deduced that the air stored in the micro-nanostructure surface prevents a water drop from infiltrating

the surface, and it plays an important role in improving the wettability. Therefore, the surface exhibits superhydrophobicity within electrodeposition time of 1 min, and this technique has fast and facile advantages.

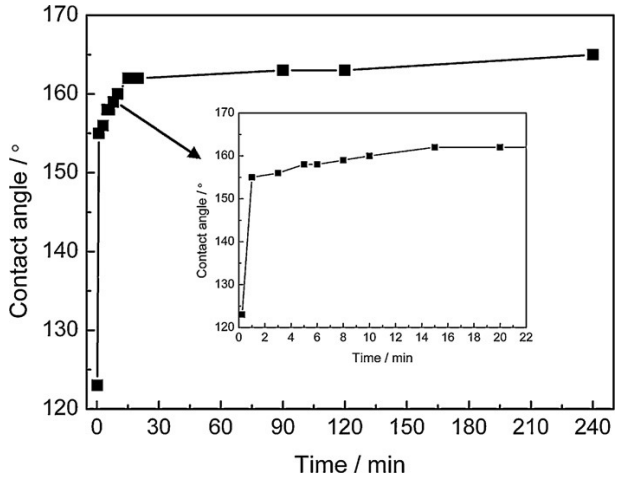

Figure 2. 12 Relation of water contact angle and electrodeposition time [30].

A similar technique has also been used to fabricate superhydrophobic copper surfaces by Chen et al. [31], using nickel chloride mixing with myristic acid as electrolytic solution in the one-step electrodeposition process

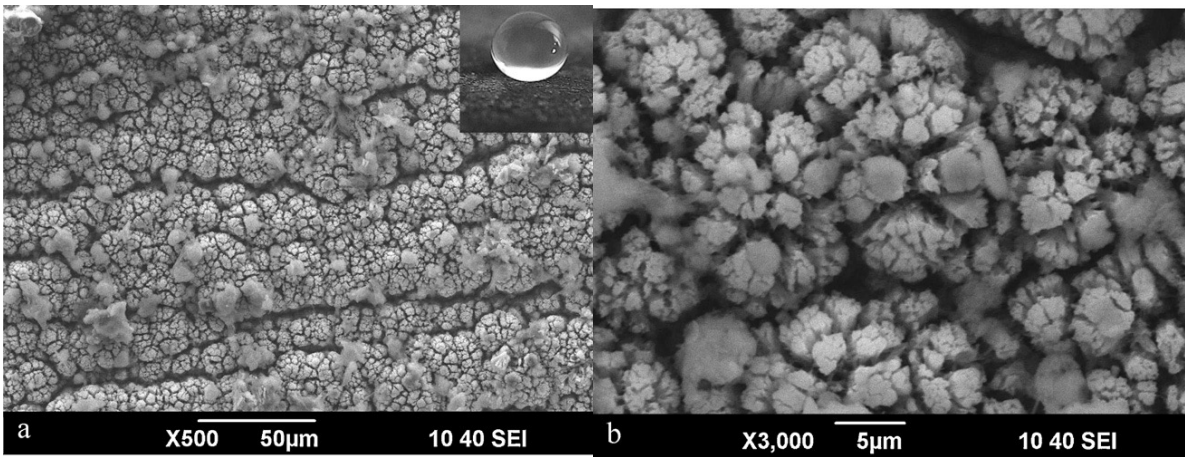

Figure 2. 13 SEM images of superhydrophobic surface on cathodic plates at 0.074 M nickel chloride and 0.080 M myristic acid with DC voltage of 30 V, for 30 min. (a) 500× and (b) 3000× [31].

The surface morphology of the as-prepared cathodic surface is clearly shown by the SEM images in Figure 2.13. Figure 2.13(a) shows the rough coating surface with the packed cauliflower-like cluster at nickel chloride, myristic acid. A reaction between nickel chloride and myristic acid in an electrolytic solution with an applied DC voltage results in the formation of cauliflower-like morphology on the cathodic surface, as shown by a high magnification SEM image in Figure 2.13(b). It further reveals that a cauliflower-like bud pattern has a diameter of about 10 µm, and a typical single

microcluster includes many nano scales structure. Furthermore, the wetting property was described with a contact angle. The contact angle is 163°, and the rolling angle is smaller than 2°. Shape of water drop on the superhydrophobic surface was shown in the inset of Figure 2.13(a).

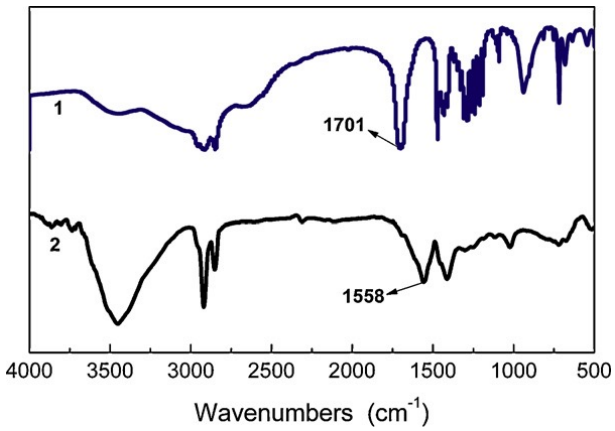

Figure 2. 14 FTIR spectrums of myristic acid (curve 1) and as-fabricated cathodic superhydrophobic surface (curve 2) [31].

Chemical composition analyses of the surfaces were studied by FTIR. Figure 2.14 plots the FTIR spectrums of the myristic acid and as-prepared cathodic surface. Curve 1 is in the presence of 1701 cm^{-1} from the free -COO band of myristic acid before the electrodeposition process. After the electrodeposition process, the free -COO band of

1701 cm^{-1} is no longer present, but a new band of 1558 cm^{-1} appears in curve 2, corresponding to coordinated -COO functional groups.

Based on FTIR analysis, it can be deduced that the cauliflower-like cluster has a composition of Ni and $Ni[CH_3(CH_2)_{12}COO]_2$. It is thought that $Ni[CH_3(CH_2)_{12}COO]_2$ crystals results from a reaction between myristic acid and nickel ions with the application of DC voltage, and its appearance confirms the presence of low surface energy methylated (CH_3 and CH_2) components on the cathodic surfaces. The corresponding mechanism was thought that when the DC voltage was applied to the two electrodes, a few of Ni^{2+} ions around the cathode plate fast get electron, and then they become pure nickel (Ni) nucleus on the cathodic surface. Meantime, the other Ni^{2+} ions near the cathodic plate react with myristic acid forming nickel myristate, and the high flux of Ni nucleus provides a good basis for the anisotropy crystal growth of nickel myristate. In addition, it was observed hydrogen was gradually released around the cathode plate during the reaction process, which leads to fabrication of the loose cauliflower-like

morphology with superhydrophobicity. The reaction processes can be formulated as follows:

$$Ni^{2+} + 2e^- \rightarrow Ni \quad \text{(Equation 2. 3)}$$

$$Ni^{2+} + 2CH_3(CH_2)_{12}COOH \rightarrow Ni[CH_3(CH_2)_{12}COO]_2 + 2H^+ \quad \text{(Equation 2. 4)}$$

$$2H^+ + 2e^- \rightarrow H_2 \quad \text{(Equation 2. 5)}$$

In another study by Chen et al. [32], superhydrophobic copper surfaces were also fabricated via the same one-step electrodeposition process, using manganese chloride mixing with myristic acid. Furthermore, Liu et al. [33] presented one-step electrodeposition process to fabricate superhydrophobic surfaces, using cerium nitrate hexahydrate ($Ce(NO_3)_3 \cdot 6H_2O$) and myristic acid [33].

In addition, the superhydrophobic surfaces have also been fabricated by other techniques, such sol-gel [2], chemical etching [4], lithography [34] et al. The general idea to fabricate superhydrophobic surfaces is to make a rough surface as well as lower the surface energy. In the study of Brassard's [2] study of fabricating superhydrophobic aluminum alloy substrates using sol-gel process, the solutions containing fluorinated

silica nanoparticles of varying sizes are prepared in the laboratory using standard Stober process. The rough structure with synthesized silica nanoparticles is further functionalized in an ethanolilc fluoroalkylsilane or FAS-17 ($C_{16}H_{19}F_{17}O_3Si$) solution. Saleema et al. [4] has used chemical etching process to prepare superhydrophobic surfaces. Aluminum alloy substrate was initially chemical etched by NaOH solution followed by passivation by low surface energy material. Moreover, in the study of Lai et al. [34] which fabricate superhydrophobic surfaces using lithography process, two step processes are performed. At the first step, the superhydrophobic TiO_2 nanotube film is fabricated through electrochemical and self-assembled techniques. And at the second step, the superhydrophobic film is selectively exposed to UV light through a photomask to locally photocatalyse the organic monolayer assembled on the TiO_2 nanotube surface.

2.2 Anodizing

The "bottom-up" methods, the piecing together of systems to give rise to grander systems, with low costs and scalable processing have been considerably widespread. Among them, a template synthesis employing anodic aluminum oxide (AAO) membranes

has proved to be an elegant, inexpensive and technologically simple approach for fabrication of various sophisticated nanoscale materials.

Anodizing is an electrolytic passivation process used to increase the thickness of the natural oxide layer on the surface of metal parts. The process is called "anodizing" because the part to be treated forms the anode electrode of an electrical circuit. Anodizing increases corrosion resistance and wear resistance, and provides better adhesion for paint primers and glues than does bare metal. Anodic films can also be used for a number of cosmetic effects, either with thick porous coatings that can absorb dyes or with thin transparent coatings that add interference effects to reflected light. Anodizing is also used to prevent galling of threaded components and to make dielectric films for electrolytic capacitors. Anodic films are most commonly applied to protect aluminum alloys, although processes also exist for titanium, zinc, magnesium, niobium, and tantalum. Iron or carbon steel metal exfoliates when oxidized under neutral or alkaline microelectrolytic conditions; i.e., the iron oxide (actually "ferric hydroxide" or hydrated iron oxide, also known as rust) forms by anoxic anodic pits and large cathodic surface, these pits

concentrate anions such as sulfate and chloride accelerating the underlying metal to corrosion. Carbon flakes or nodules in iron or steel with high carbon content (high carbon steel, cast iron) may cause an electrolytic potential and interfere with coating or plating. Ferrous metals are commonly anodized electrolytically in nitric acid, or by treatment with red fuming nitric acid, to form hard black ferric oxide. This oxide remains conformal even when plated on wire and the wire is bent.

Anodization changes the microscopic texture of the surface and changes the crystal structure of the metal near the surface. Thick coatings are normally porous, so a sealing process is often needed to achieve corrosion resistance. Anodized aluminum surfaces, for example, are harder than aluminum but have low to moderate wear resistance that can be improved with increasing thickness or by applying suitable sealing substances. Anodic films are generally much stronger and more adherent than most types of paint and metal plating, but also more brittle. This makes them less likely to crack and peel from aging and wear, but more susceptible to cracking from thermal stress.

The spontaneous reaction leading to the formation of aluminum oxide in air can be

ascribed to the large negative Gibb's free energy changes:

$$2\mathrm{Al(s)} + \frac{3}{2}\mathrm{O_2(g)} \rightarrow \alpha\mathrm{Al_2O_3(s)};\ \Delta\mathrm{G}^\circ = -1582\ \mathrm{kJ/mol} \qquad \text{(Equation 2. 6)}$$

$$2\mathrm{Al(s)} + 3\mathrm{H_2O(l)} \rightarrow \alpha\mathrm{Al_2O_3(s)} + 3\mathrm{H_2};\ \Delta\mathrm{G}^\circ = -871\ \mathrm{kJ/m} \qquad \text{(Equation 2. 7)}$$

If aluminum is electrochemically anodized, an oxide grows at the anode electrode

$$2\mathrm{Al(s)} + 3\mathrm{H_2O(l)} = \mathrm{Al_2O_3(s)} + 6\mathrm{H^+} + 6\mathrm{e^-} \qquad \text{(Equation 2. 8)}$$

And hydrogen evolves at the cathode

$$6\mathrm{H^+} + 6\mathrm{e^-} = 3\mathrm{H_2} \qquad \text{(Equation 2. 9)}$$

Assuming there are no complex anions, the Nernst equation reads

$$E = E_0 - \left(\frac{RT}{ZF}\right) ln(\frac{[red]}{[ox]}) \qquad \text{(Equation 2. 10)}$$

where R is the universal gas constant, 8.314472(15) $\mathrm{J.K^{-1}.mol^{-1}}$, T is the absolute

temperature in Kelvin, z is the charge number of the electrode reaction, and F is the Faraday constant (96,500 C mol^{-1}). The electrode potential E at the anode can be written as

$$E = -1.550 - 0.0591pH \qquad \text{(Equation 2. 11)}$$

This explains that the reaction at the anode electrode (Al) thermodynamically depends on the pH value, which is determined by electrolyte and temperature.

The current density passing across the oxide film can be written as

$$j = j_a + j_c + j_e \qquad \text{(Equation 2. 12)}$$

where j_a , j_c and j_e are the anion-contributing, cation-contributing and electron-contributing current density, respectively. Since the electronic conductivity in the aluminum oxide is very low, the ionic current density (j_i=j_a + j_c) is the predominant mode to transport the charges. The relationship between the ionic current,j_i, and the

electric field, E, can be expressed in terms of the Guntherschultze-Betz equation

$$j_i = j_0 \exp(\beta E) \qquad \text{(Equation 2. 13)}$$

where both j_0 and β are temperature- and metal-dependent parameters. For the aluminum oxide, the electric field E, j_0 and β are in the range of 10^6 to 10^7 V/cm, 1×10^{-16} to 3×10^{-2} mA/cm^2 and 1×10^{-7} to 5.1×10^{-6} V/cm, respectively.

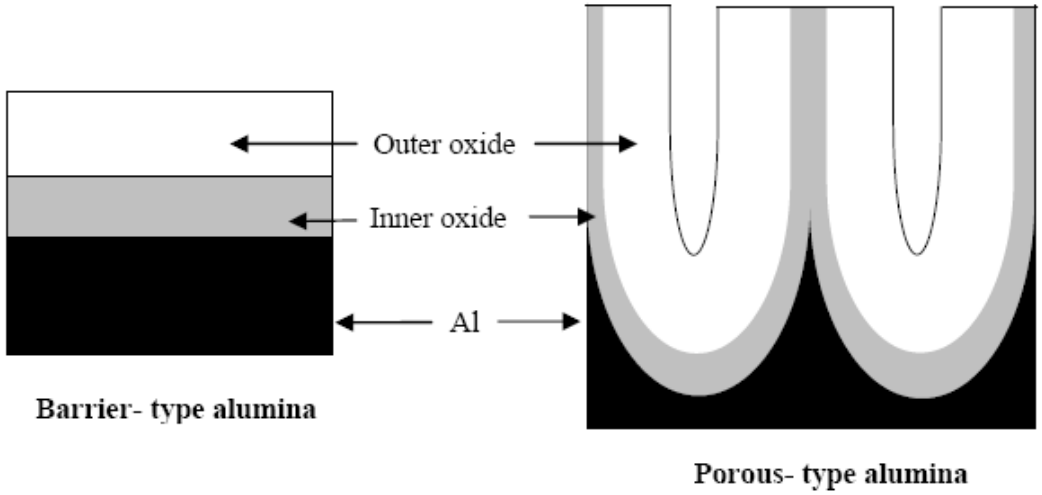

Figure 2. 15 Schematic diagram for barrier type alumina and porous type alumina. The aluminum metal, an inner oxide consisting of pure alumina and an outer oxide consisting of an anion-contaminated alumina are indicated.

As shown in Figure 2.15, both the barrier-type and the porous-type alumina films consist of an inner oxide of high purity alumina and an outer oxide layer comprised of alumina which has incorporated anions. In fact, the nomenclature of the inner and the outer oxide are determined in terms of the interfaces. The inner oxide is adjacent to the oxide/metal interface, while the outer oxide is adjacent to the electrolyte/oxide interface.

Table 2. 1 Anodizing ratios for barrier film formation on valve metals. Note that in the case of aluminum anodized in sulfuric, oxalic, phosphoric, and chromic acid, anodizing ratios of the barrier layer formed beneath the porous alumina are indicated.

Metal	Anodizing ratio ($ÅV^{-1}$)
Tantalum	16
Niobium	22
Zirconium	20-27
Tungsten	18
Silicon	4-8
Aluminum	10.0 in 15% sulfuric acid 11.8 in 2% oxalic acid 11.9 in 4% phosphoric acid 12.5 in 3% chromic acid 13-13.7 in barrier-type electrolytes

It is generally accepted that the thickness of barrier-type alumina is mainly determined by the applied voltage, even though there is a small deviation depending on the electrolytes and temperature. The anodizing ratio, which is defined as oxide thickness formed per volt, demonstrates that the barrier type films are also strongly influenced by the type of metal, which is anodized as shown in Table 2.1.

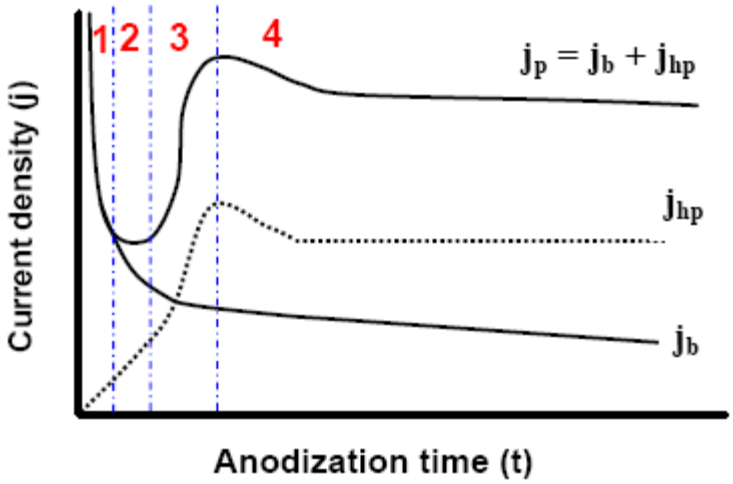

Figure 2. 16 Schematic diagram of current density curve during the initial growth (< 1h) at constant voltage. j_b and j_p indicate the current density for the barrier film and the porous film formation, respectively. j_{hp} represents a hypothetic current density, which is the difference between j_p and j_b.

The transient of the potentiostatic current density reflects the formation of barrier-type or porous type porous alumina (Figure 2.16). At the beginning of the oxide

formation, both transients have an identical behavior. However, for the barrier film formation, the current density j_b decays exponentially. Eventually, the barrier film current is dominated by an ionic current j_i. In the case of the formation of porous films, the following current density profiles are typically observed. First, the current density j_p decreases rapidly (regime 1 in Figure 2.16). Then, it passes through minimum value (regime 2 in Figure 2.16). It increases to arrive at a maximum value (regime 3 in Figure 2.16). Subsequently, it slightly decreases again. Finally, a steady current density remains (regime 4 in Figure 2.16). One can consider the current density j_p as the sum of j_b and hypothetic current density j_{hp}, which means the pure current density for creating pores. j_b is determined by the applied potential in terms of the anodizing ratio, while j_{hp} depends on the electrolyte and the temperature as well as on the applied potential. The pore formation mechanism is displayed schematically in Figure 2.17, corresponding to the four regimes of Figure 2.16. At the beginning of the anodization, the barrier film, which consists of non-conductive oxide (= $10^{10} \sim 10^{12}$ Ωcm), covers the entire surface of the aluminum (regime 1 in Figure 2.16 and Figure 2.17). The electric field is focused locally

on fluctuations of the surface (regime 2 in Figure 2.16 and Figure 2.17). This leads to field-enhanced or/and temperature enhanced dissolution in the formed oxide and thus to the growth of pores (regime 3 in Figure 2.16 and Figure 2.17). Since some pores begin to stop growing due to competition among the pores, the current decreases again as shown in regime 4 in Figure 2.16. Finally, j_p maintains an equilibrated state. In this stage, pores grow in a stable manner. However, it is very often observed that during the stable pore growth, the current density continues to decrease slightly. This is due to diffusion limits in the long pore channels.

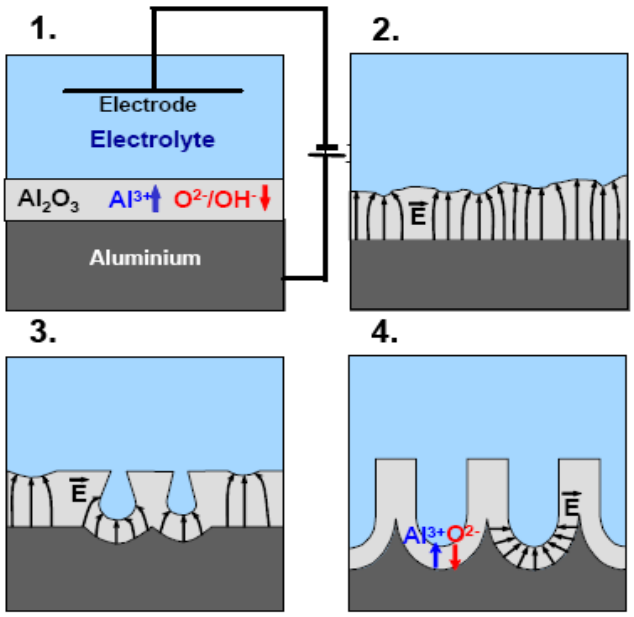

Figure 2. 17 Schematic diagram of the pore formation at the beginning of the anodization. Regime 1: formation of barrier oxide on the entire area; regime 2: local field distributions caused by surface fluctuations; regime 3: creation of pores by field-enhanced or/and temperature-enhanced dissolution; regime 4: stable pore growth.

Experimental procedures of two-step anodization are described in detail in Figure 2.18. Firstly, aluminum with a high purity (99.99%) is cleaned with acetone in an ultrasonic bath. Then, it is immersed in 100 ml of a mixture containing $HF/HNO_3/HCl/H_2O$ at a ratio of 1:10:20:69 in order to remove impurities on the surface. After cleaning with deionized (DI) water, Al is annealed for 3 h at 500 °C in N_2 to obtain large single crystalline grains. As a matter of fact, the larger the grains are, the larger are

the domains of self-ordered porous alumina (see Figure 2.18 (a)). To reduce surface roughness, electropolishing is carried out in a mixture consisting of 1/4 $HClO_4$+ 3/4 C_2H_5OH (Figure 2.18(b)). Electropolishing is a prerequisite for the formation of selfordered porous alumina with large domain size. Note that caution is needed when perchloric acid/ethanol is used due to its explosiveness at moderate temperatures. After the pretreatment, anodization is performed either at 19 V in 2 M H_2SO_4, at 25 V in 0.3 M H_2SO_4, at 40 V in 0.3 M $(COOH)_2$, at 160 V in 1 M H_3PO_4, or at 195 V in 0.1 M H3PO4 for more than 1 day (Figure 2.18(c)).

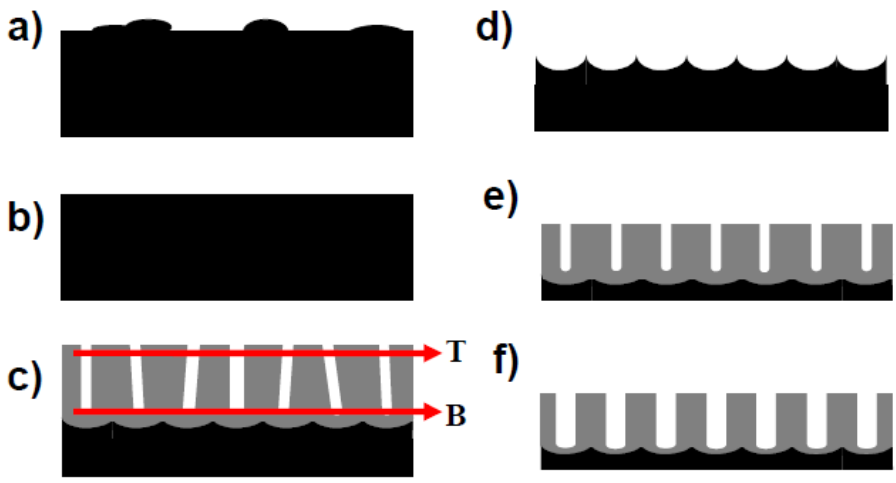

Figure 2. 18 Stages of the formation of self-ordered alumina: a) Annealing at 500 °C for 3h; b) electropolishing in a solution of 1/4 $HClO_4$ + 3/4 C_2H_5OH for 4 min at 8 V with agitation; c) first anodization (typically 1 - 2 days); d) selective dissolution of the formed oxide layer; e) second anodization under the same conditions as the first anodization; and f) isotropic etching in 1 M phosphoric acid at 30 °C to widen the pores.

Since pores are randomly created on the surface, the initial pore arrangement is very irregular (Figure 2.19(a)). However, due to the repulsive forces between neighboring pores during the long-anodization, self-organization occurs. As a result, hexagonally close-packed arrays are obtained at the interface between the porous alumina layer and the aluminum substrate (Figure 2.19 (b)). Then, the porous alumina film is selectively dissolved in a solution containing chromic acid (Figure 2.18(d)). Patterns that are replicas of the hexagonal pore array are preserved on the fresh aluminum surface. This allows the

preparation of pores with a high regularity by a subsequent second anodization under the same conditions as the first anodization (Figure 2.18(e)). If needed, the resulting pores can be isotropically widened by chemical etching with 0.5 - 1 M phosphoric acid (Figure 2.18(f)).

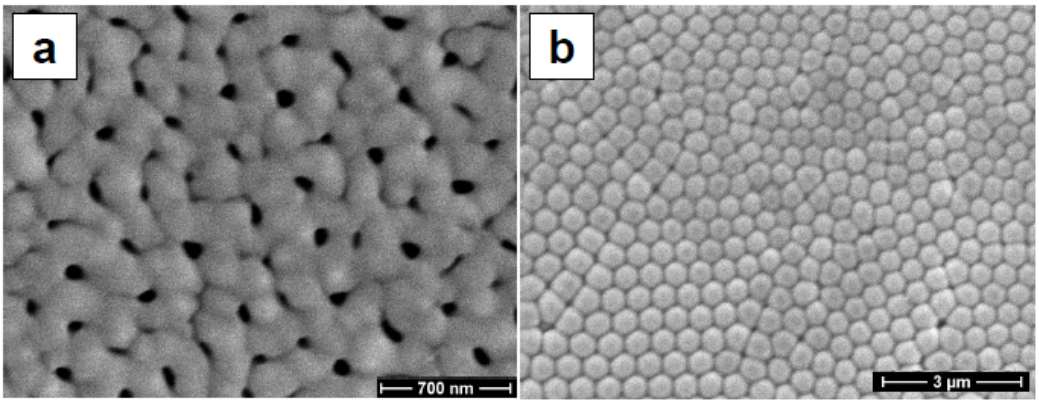

Figure 2. 19 Scanning Electron Microscopy (SEM) images of a porous alumina sample produced by a first anodization (in 0.1Mphosphoric acid at 195 V). (a) the surface, and (b) the bottom of the membrane after selective removal of Al, which correspond to T and B in Figure 2.18 (c), respectively.

The two-step anodizing is also widely applied. For example, Sulka et al. [35] studied anodic aluminum oxide (AAO) membranes with a highly ordered nanopore arrangement typically serve as ideal templates for the formation of various nanostructured materials by

two step anodizing process. Before anodizing, the high-purity annealed aluminum foil was electrochemical polishing in a 1:4 volume of $HClO_4$ and C_2H_5OH at constant current density of 500 $mAcm^{-2}$ for 1 min at 10°C. The anodic porous alumina layer was formed by two-step procedure under a constant cell voltage ranging between 30 and 65V in a 0.3 M oxalic acid at the temperature of 20, 25 and 30°C for 30 or 60min. Then the formed aluminum oxide was removed by chemical etching in a stirred mixture of 6 wt% H_3PO_4 and 1.8 wt.% H_2CrO_4 at 60°C for 60min. Immediately after the oxide removal, the aluminum sample was re-anodized for 30 or 60min under the same anodizing conditions as those used in the first anodization.

In their study, the current-time transients recorded during the first three minutes of the second anodizing step preformed in 0.3 M oxalic acid at 30°C for the anodizing potential ranging from 30 to 65 V was shown in Figure 2.20(a). The current evolution is typical for anodization of aluminum with formation of the porous oxide layer [35]. It was observed the decrease of current density during the initial period of anodization, due to the compact high-resistance oxide film formed on the aluminum substrate.

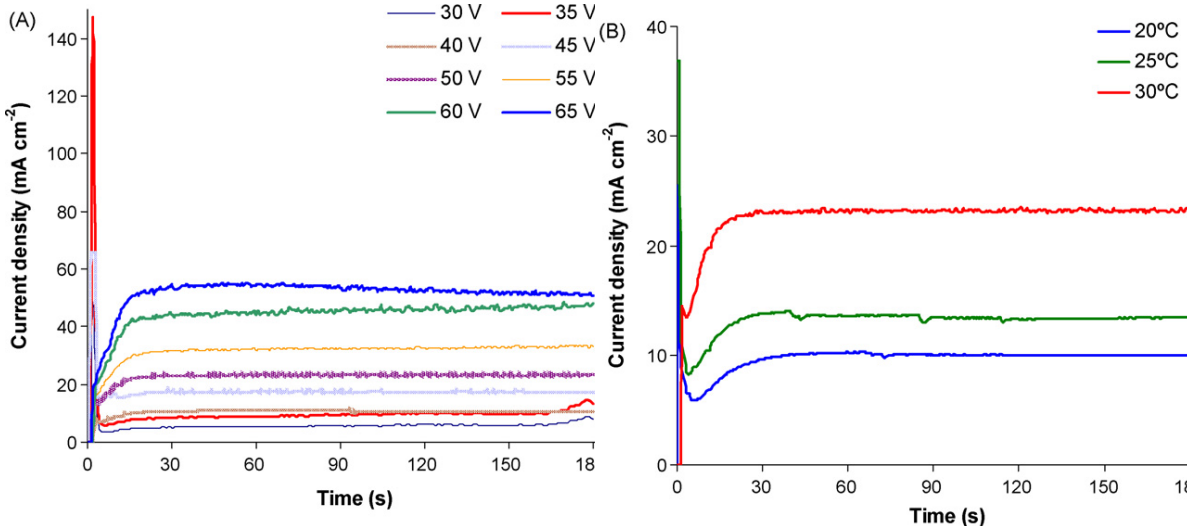

Figure 2. 20 Current density vs. anodizing time recorded for the first three minutes of the second anodizing step performed in 0.3M oxalic acid at 30 ◦C for various anodizing potentials (A) and for 50V at various anodizing temperatures (B) [35].

At the minimum of current density, a propagation of individual paths through the barrier layer begins and an increase in the current density is observed, leading to the formation of pores precursors. After reaching the maximum value, the current density does not change significantly with time and the porous oxide layer starts to grow on aluminum. It is worth noting that the anodizing current is related with the movement of oxygen containing ions (O^{2-} or OH^{-}) from the electrolyte through the barrier layer at the

pore bottoms to the oxide growth interface and with simultaneous outward drift of Al^{3+} ions across the oxide layer. A rapid increase in oxide thickness results in a significant extension of the diffusion path along the channels of porous layer and gradual decrease of the ionic current over time. Furthermore, the increase of operation temperature was found to be responsible for the increase of current density.

In the study of Zaraska et al. [36], the two-step anodizing procedure is as follow. AA1050 alloy was degreased followed by the electrochemical polishing performance in a mixture of perchloric acid (60 wt.%) and ethanol (1:4 vol.) at a constant potential of 20 V for 1 min at 10 ˚C. After rinsed with water, ethanol and dried, the first step of anodization was carried out in 0.3 M oxalic acid under a constant potential of 45 V for 60min at a temperature of 20˚C. As-prepared alumina layers were then chemically removed by immersing in a mixture of 6 wt.% H_3PO_4 and 1.8 wt.% H_2CrO_4 at 45˚C for 12h. Subsequently, the second anodization was carried out in the same experimental conditions as were used in the first step.

The reason why two-step anodization is necessary is that the pores are randomly

created on the surface by first anodizing, and the initial pore arrangement is very irregular. However, due to the repulsive forces between neighboring pores during the long-anodization, self-organization occurs. As a result, hexagonally close-packed arrays are obtained at the interface between the porous alumina layer and the aluminum substrate. Then, the porous alumina film is selectively dissolved in a solution. Patterns that are replicas of the hexagonal pore array are preserved on the fresh aluminum surface. This allows the preparation of pores with a high regularity by a subsequent second anodization under the same conditions as the first anodization.

However, the uniform pore size is still obtained by one-step anodizing process [37]. The high-purity aluminum foil was used for one-step anodization, after electropolishing with ethanolic $HClO_4$ at 20 V for 30s. The one-step anodization was performed in oxalic by hybrid pulse anodization (HPA) and DCA at environment temperatures of 5-15 ◦C. The applied hybrid pulse was constructed from a positive square wave followed by another negative square wave with the duty ratio of 1:1. The positive and negative potential of HPA are 40 V and -2V, respectively, and the period of hybrid pulse was 2s

(1s:1s). The SEM image in Figure 2.21 shows the micrographs of AAO formed by one-step HPA. The morphology of AAO by HPA method exhibits ordered pore arrangement and uniform pore size.

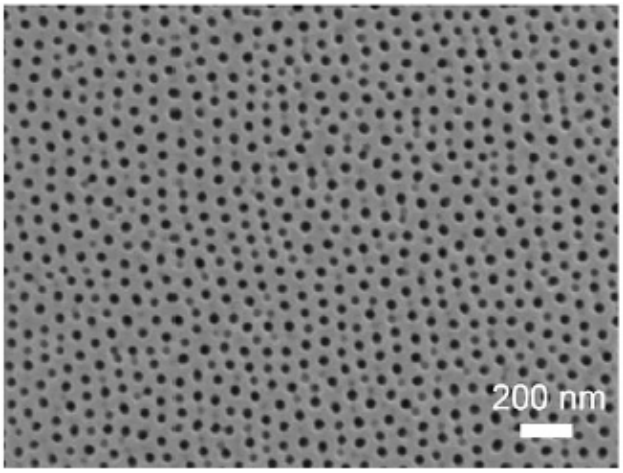

Figure 2. 21 SEM micrographs of AAO formed by one-step HPA from 99.997% Al foil in 0.5 M oxalic acid at 5 °C for 1 h and then immersed in phosphoric acid 5 wt.% for 30 min [37].

The mechanism of the hybrid pulse action on one-step AAO growth during porous anodizing is explained as follow. In general, formation and dissolution of aluminum oxide during electrochemical reaction can be expressed in formulas (1) and (2), respectively [38,39]. When the potential was applied to the electrochemical cell, both

reactions of formulas (1) and (2) reacted with the aluminum specimen and reached a balanced condition. The releasing electrons in formula (1) produce anodizing current. At the beginning of anodizing, surface fluctuation causes varied local field distributions. The dissolution of the aluminum oxide can be enhanced by local high field and pores are created first in high field region. After a period of anodizing, the AAO structures at the pore bottom become stable growth and the regularity of pores configuration is adjusted with increasing anodizing time. However, the AAO structure on the top was still rough and distorted due to these anodizing processes only occur in the barrier layer at the bottom of AAO. That is the reason for removing the first anodized alumina and performing the second anodization for better configuration in the conventional two-step anodization. In the case of HPA process, the small negative potential (−2 V) is applied after a duration of anodizing positive potential. And the hydrogen ions with positive charge are attracted to the surface at the same time as shown in the schematic diagram of Figure 2.22. The attracted hydrogen ions lead to the dissolution of AAO on the top. Therefore, the rough and distorted AAO structure can be improved. Moreover, there is no

electron in dissolution reaction of alumina so that no extra Joule's heat generates when applying negative potential. The small negative voltage resulting in the nearly zero current at the negative duration is good for the uniformity and circularity of pore distribution as mentioned previously. It is noted that too large negative potential may lead to negative current by electrical breakdown and destroy the whole AAO structure.

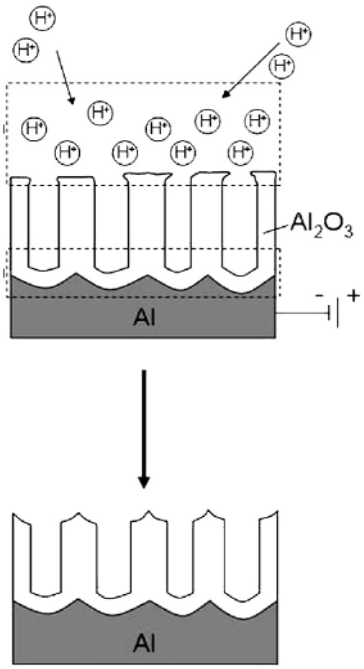

Figure 2. 22 Schematic diagram of the effect of negative potential applied in one-step HPA anodization during AAO growth. The positive hydrogen ions attracted to the surface lead to the dissolution of the top of AAO for improving the rough and distorted structure by one-step direct current anodizing (DCA).

What is also worthy to mention is that pore circularity is another important factor to determine the quality of porous AAO besides the pore size. The definition of circularity can be expressed as [40]:

$$\text{circularity} = 4\pi\left(\frac{A}{S^2}\right) \qquad \text{(Equation 2. 14)}$$

where A and S represent the area and perimeter of each pore of AAO. Generally, a circularity value of 1.0 indicates a perfect circle.

2.3 Study of corrosion behaviors

Corrosion is an electrochemical process in which a metal reacts with its environment to form an oxide or other compound. The cell which causes this process has three essential constituents: an anode, a cathode and an electrolyte (electrically conducting solution). The anode is the site at which the metal is corroded; the electrolyte is the corrosive medium; and the cathode (part of the same metal surface or of another metal

surface in contact with it) forms the other electrode in the cell and is not consumed in the corrosion process. At the anode the corroding metal passes into the electrolyte as positively charged ions, releasing electrons which participate in the cathodic reaction. Hence the corrosion current between anode and the cathode consists of electrons flowing within the metal and ions flowing within the electrolyte. The schematically image of ions movement in corrosion behavior is shown in Figure 2.23(a).

The surface of one component may become the anode and the surface of another component in contact with it the cathode. Usually, corrosion cells will be much smaller and more numerous, occurring at different points on the surface of the same component. Anodes and cathodes may arise from differences in the constituent phases of the metal itself, from variations in surface deposits or coatings on the metal, or from variations in the electrolyte. The schematically image of one component corrosion behavior is shown in Figure 2.23(b).

The metal may be immersed in an electrolyte or the electrolyte may be present only as a thin condensed or adsorbed film on the metal surface. The rate of corrosion is

influenced considerably by the electrical conductivity of the electrolyte. Pure water has poor electrical conductivity and the corrosion rate will be much lower than say an acid solution of high conductivity.

As illustrated in Figure 2.23(c), the anodic reaction of metal is as follow:

$$M \rightarrow M^{+} + e^{-} \qquad \text{(Equation 2. 15)}$$

The electron flown to cathode electrode and the cathodic reaction is as follow:

$$O_2 + 2H_2O + 4e^{-} \rightarrow 4OH^{-} \qquad \text{(Equation 2. 16)}$$

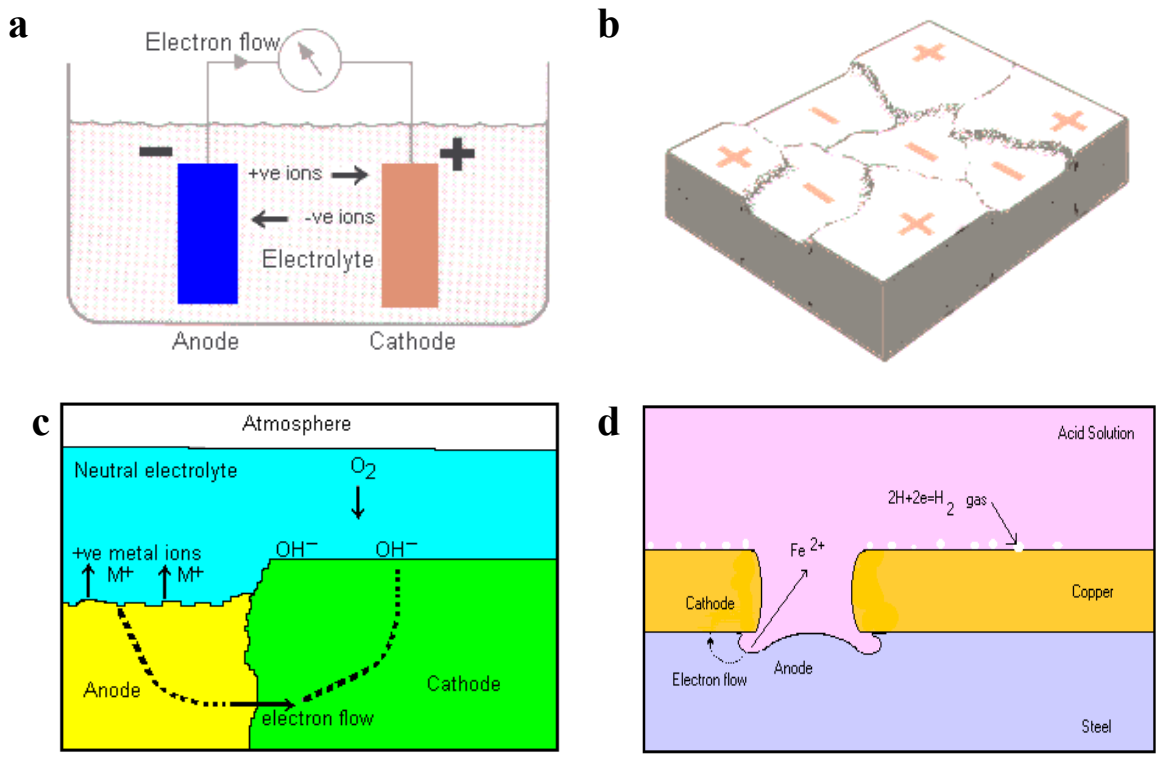

Figure 2. 23 (a) Schematically image of ions movement in corrosion behavior; (b) one component corrosion behavior; (c) Anodic and cathodic corrosion reactions and (d) an example of corrosion behavior on steel and copper as anode and cathode, respectively.

An example of a corrosion cell is provided by an imperfect coating of copper on steel immersed in dilute sulphuric acid, showing in Figure 2.23(d). The current generated passes from the copper to the steel by the path of lowest resistance and returns to the copper through the solution by the passage of ions. The steel, which has the greatest negative potential, dissolves and is called the anode; whilst the copper is called the

cathode. In such acid attack the hydrogen, which is freed as the iron dissolves, is deposited on the surface of the copper cathode and as it increases in amount two things may occur. The corrosion of the steel is either reduced because of the formation of an opposing hydrogen electrode, i.e. the cell is polarized; or the hydrogen may be evolved as bubbles which stream away, with the result that the corrosion will occur continuously. In the first case the corrosion will be accelerated by exposure to oxidizing agents (e.g. air) which remove the hydrogen from the cathode. The size of the cathode relative to the anode is important, e.g. copper rivet in a large steel plate, is quickly polarized and corrosion on the plate is small. On the other hand, a large cathode coupled to a small anode has the opposite effect, with rapid attack of the anode.

The ability of metals to resist corrosion is to some extent dependent upon their position in the electrochemical series, as shown in table 2.2.

Table 2. 2 Electrochemical series

Element	Ion	Electrode potential (V)	Hydrogen overvoltage (V)
Magnesium	Mg^{2+}	-1.87 (Base end)	0.7
Aluminum	Al^{3+}	-1.35	0.5
Zinc	Zn^{2+}	-0.76	0.7
Chromium	Cr^{2+}	-0.6	0.32
Iron	Fe^{2+}	-0.44	0.18
Cadmium	Cd^{2+}	-0.4	0.5
Cobalt	Co^{2+}	-0.29	
Nickel	Ni^{2+}	-0.22	0.15
Tin	Sn^{2+}	-0.14	0.45
Hydrogen	H^{+}	0	-
Antimony	Sb^{3+}	+0.11	0.42
Copper	Cu^{2+}	+0.34	0.25
Silver	Ag^{+}	+0.8	0.1
Gold	Au^{3+}	+1.3 (Noble end)	0.35
Oxygen	OH^{-}	+0.4	
Chlorine	Cl^{-}	+1.36	

The metal may be immersed in an electrolyte or the electrolyte may be present only as a thin condensed or adsorbed film on the metal surface. The rate of corrosion is influenced considerably by the electrical conductivity of the electrolyte. Pure water has poor electrical conductivity and the corrosion rate will be much lower than say an acid

solution of high conductivity.

There are two basic mechanisms by which metals in electrolytes corrode, electrolytic corrosion and galvanic corrosion.

Electrolytic corrosion is a result of direct current from outside sources entering and then leaving a particular metallic structure by way of the electrolyte. Where current enters the structure, that part is usually unaffected or is provided with some degree of protection. Where current leaves the structure, corrosion occurs. In underground work, this type of corrosion is often referred to as stray current corrosion and results from currents entering the soil from sources of DC such as electric railway systems or DC machinery.

Galvanic corrosion is self-generated activity resulting from differences in energy levels or potentials which develop when metal is placed in an electrolyte. These differences can arise from the coupling of dissimilar metals, variations in the electrolyte, non-homogeneity of the metal, or a combination of the above. Current will be generated when two dissimilar metals are electrically connected and immersed in an electrolyte. One of the metals will corrode. The path of the current will be from the corroding metal,

through the electrolyte (soil) to the non-corroding metal and then back through the connection (conductor) between the two metals. The corroding metal is the one where the current leaves to enter the electrolyte and is called an anode. The metal that receives the current is called the cathode.

The two metals immersed into an electrolyte forms a galvanic cell, in which the metal having lower value of electrode potential (higher position in the table of electrochemical series) will oxidize (anodic reaction) and the metal having higher value of electrode potential (more noble) provide cathodic reaction (reduction) on its surface.

The algebraic difference between the electrode potentials of the two metals determines the driving force of galvanic corrosion.

Two examples of galvanic corrosion are presented in the Figure 2.24.

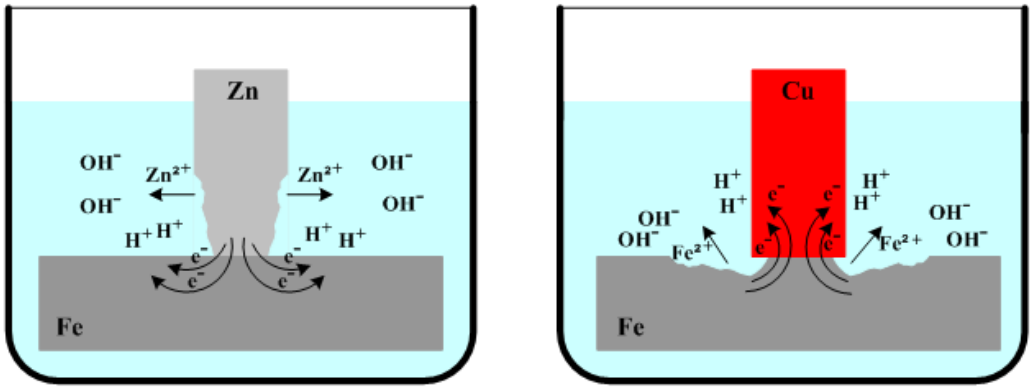

Figure 2. 24 Two examples of galvanic corrosion.

(1) System iron-zinc

The Standard electrode potentials of the metals: E^0_{Zn} = -0.763 V, E^0_{Fe} = -0.44 V. The difference: E^0_{Fe} - E^0_{Zn}= 0.323 V. The potential of Zn is lower therefore it dissolves in electrolyte according to anodic reaction: $Zn = Zn^{2+} + 2e^-$ (corrosion of zinc). The electrons given up by the anode flow to the cathode (iron) where they are discharged in the cathodic reaction: $H^+ + e^- = H$.

(2) System iron-copper

The standard electrode potentials: E^0_{Fe} = -0.44 V, E^0_{Cu} = +0.337 V. The difference: E^0_{Cu} - E^0_{Fe} = 0.777 V. Potential of iron is lower therefore it reacts anodically (dissolves)

in this system: $Fe = Fe^{2+} + 2e^-$ (corrosion of iron). Cathodic reaction of the electrons with hydrogen ions occurs on the copper surface.

The cathode may be polarized by the hydrogen atoms producing a film covering the cathode surface. The film affects corrosion kinetic: it slows down the reaction between the electrons and hydrogen ions dissolved in the electrolyte. Slowing cathodic reaction causes slowing anodic reaction, which are linked to each other. In the electrolytes with high concentration of hydrogen ions (acidic solutions) the hydrogen atoms adsorbed on the cathode surface form hydrogen gas escaping from the cathode and promoting corrosion: $2H = H_2$.

Common aqueous solutions are aerated (contain dissolved oxygen) therefore hydrogen atoms formed on the cathode surface react with oxygen: $1/2O_2+2H=H_2O$. Kinetic of the process in this case is determined by the diffusion of oxygen to the cathode surface.

Passivation is a formation of a thin film of oxidation products preventing further corrosion of the metal. The oxide passivation film may form either on exposure to air or

in electrolyte with presence of oxygen. Passivation is a formation of a thin film of oxidation products preventing further corrosion of the metal.

A damage of the passive film may cause intensive localized corrosion (pitting corrosion). Passive oxide layers are dissolved in electrolytes containing sulfates and chlorides.

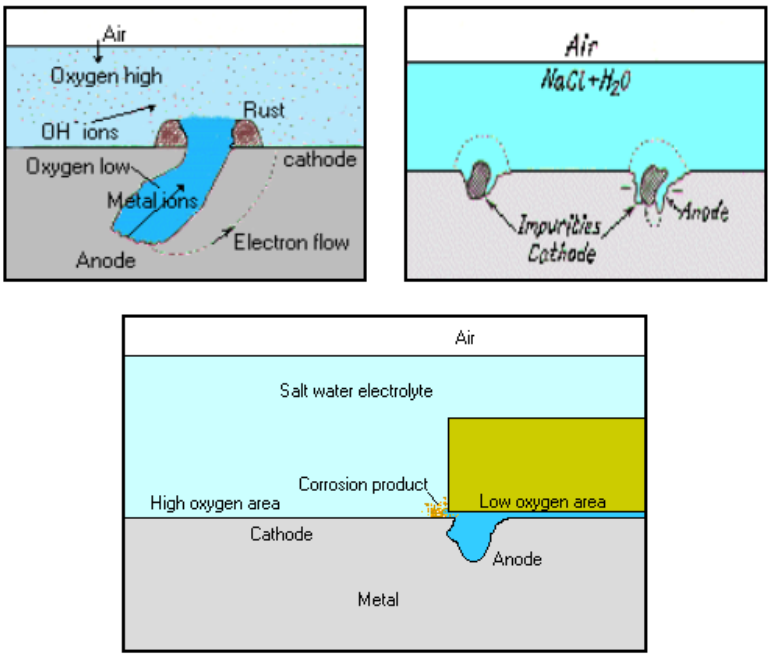

Figure 2. 25 Schematic of pitting corrosion.

Electrochemical corrosion can be stimulated from not only differences in the metal surface, but also from variations in the electrolyte. The above is effected to some degree

by this mechanism, as oxygen diffuses into the water drop a concentration gradient is set up, where the oxygen content at the extremities is the highest and the lowest being at the centre where the anode forms. Cavities in metal surfaces and metal surfaces partially covered by another material are prone to this type of attack. The diffusion of oxygen into cavities or crevices is impeded and results in these areas becoming anodic to the surrounding metal to which oxygen can easily reach (oxidation-concentration cell or differential aeration cell). The metal ions formed in the cavity migrate outwards and react with the hydroxide ions flowing in the opposite direction to form a corrosion product (rust) at the mouth of the cavity or crevice. This position of the corrosion product accentuates the corrosion by making the diffusion of oxygen to the anode more difficult, and if the cathodic area is large severe pitting may occur. Also when dry conditions prevail moisture can be trapped in the cavities allowing corrosion to continue. Pitting corrosion occurs in materials that have a protective film such as a corrosion product or when a coating breaks down. The exposed metal gives up electrons easily and the reaction initiates tiny pits with localized chemistry supporting rapid attack. Figure 2.25

shows the schematic of pitting corrosion.

In my masters study, superhydrophobic copper and aluminum alloy surfaces were fabricated by electrochemical modification and electrodeposition[18]. In this research project, superhydrophobic aluminum alloy surfaces will be fabricated via anodization of aluminum surfaces followed by electrophoretic deposition. Anodization involves electrochemical methods to grow oxide film of aluminum with well ordered pores in the dimension of micro-nanoscale. In the electrophoretic deposition (EPD) process, micro-nanoparticles are deposited on to an electrode from a colloidal suspension under the application of an electric field.

Superhydrophobic surfaces have been prepared in the application of anti-corrosion. Corrosion resistance properties were analyzed by potentiodynamic polarization and (or) electrochemical impedance spectroscopy.

The corrosion resistant performance and durability of the superhydrophobic surface on magnesium alloy coated with nanostructured cerium oxide film and fluoroalkylsilane

molecules in corrosive NaCl aqueous solution were investigated by Ishizaki et al. [41] using electrochemical and contact angle measurements.

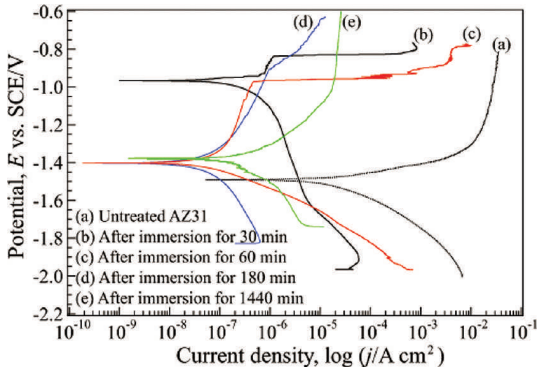

Figure 2. 26 Potentiodynamic curves of (a) untreated magnesium alloy, and superhydrophobic surface formed on magnesium alloy after immersion in 5 wt.% NaCl aqueous solution for (b) 30, (c) 60, and (d) 180 min. The scanning rate was 0.5 mV/s [41].

We investigated the corrosion resistance of the superhydrophobic surface in 5 wt.% NaCl aqueous solution from the electrochemical points of view. Figure 2.26 shows potentiodynamic polarization curves of (a) untreated magnesium alloy after immersion in 5 wt.% NaCl aqueous solution for 30 min and superhydrophobic surface formed on the magnesium alloy after immersion in 5 wt.% NaCl aqueous solution for (b) 30, (c) 60, (d) 180, and (e) 1440 min. As compared to the

corrosion current density (j_{corr}) of the untreated magnesium alloy (9.25×10^{-5} A/cm^2), that of the superhydrophobic surface formed on the magnesium alloy (2.17×10^{-7} A/cm^2) decreased by more than 1 order of magnitude. The j_{corr} values of the superhydrophobic surface formed on the magnesium alloy after immersion in the NaCl aqueous solution for 60, 180, and 1440 min were estimated to be 4.79×10^{-8}, 6.89×10^{-8}, and 2.21×10^{-7} A/cm^2, respectively. It should be noted that all the j_{corr} values for the samples after immersion in the NaCl aqueous solution for 60 to 1440 min were much lower than that of untreated magnesium alloy. This supports the conclusion that the superhydrophobic treatment is effective for improving the corrosion resistance. The corrosion potential (E_{corr}) of the AZ31 was -1510 mV. Hydrogen evolution dominates at more negative potentials than E_{corr}, resulting in an increase in the cathodic currents. At more positive potentials than E_{corr}, magnesium oxidation prevails and the metal is continuously dissolved as a result of the absence of a passivation layer, which is not formed under these conditions of high chloride concentration. On the other hand, E_{corr} of the

superhydrophobic surface is -967 mV and is considerably shifted to the positive direction compared to that of untreated magnesium alloy. The significant shift in the E_{corr} to the positive direction could be attributed to an improvement in the protective properties of the superhydrophobic surface formed on the magnesium alloy. At more positive potentials than E_{corr}, the abrupt increase in the current density at the potentials of -830 mV is clearly observed. This increase in the current density could be related to the pitting corrosion, showing that the electrolyte permeated through the film and consequently initiated pitting corrosion. This might be due to the permeation of the electrolyte through the crack in the film. A similar behavior has been reported even in aluminum alloys. The E_{corr} moved in the negative direction and the j_{corr} decreased with an increase in the immersion time of the superhydrophobic surface formed on the magnesium alloy. On the other hand, the passive region became wide. The presence of passive region suggests that the superhydrophobic surface exhibits protective properties in a solution containing Cl^- ions. In the case of the sample after immersion for 1440

min, no increase in the current density at more positive potentials than the E_{corr}, that is, passive region, can be observed in the curves, and the current density values were almost kept constant at more positive potentials than -1050 mV.

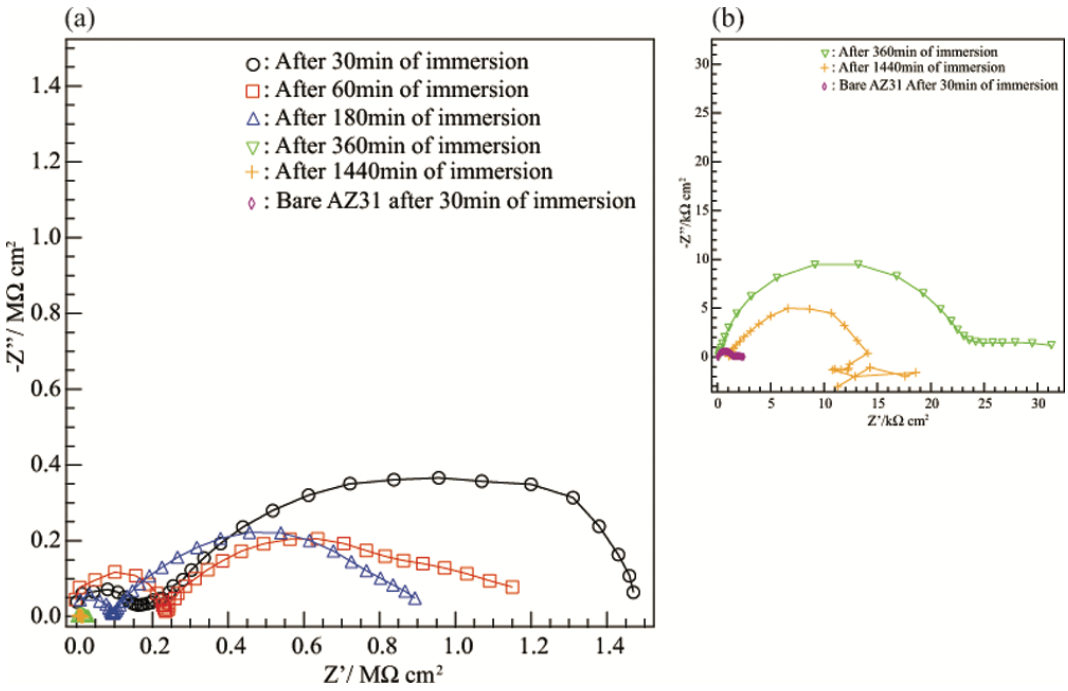

Figure 2. 27(a) Evolution of Nyquist plots of the untreated magnesium alloy and the superhydrophobic surface formed on magnesium alloy AZ31after immersion in 5 wt.% NaCl aqueous solution for 30, 60, 180, 360, and 1440 min. (b) Enlarged impedance spectra [41].

To probe the corrosion mechanism and quantify the corrosion resistant performance of the super hydrophobic surface, EIS studies were performed. Figure 2.27(a) presents the evolution of the impedance spectra of the superhydrophobic surface formed on magnesium alloy after different times of immersion in 5 wt.% NaCl solution. Figure 2.27(b) shows the enlarged impedance spectra. The impedance spectra of the untreated magnesium alloy and superhydrophobic surface after immersion in 5 wt.% NaCl solution for more than 360 min had capacitive loops at high and medium frequencies and a tail at low frequencies. The capacitive loops can be attributed to the charge transfer of the corrosion process and the tail might be associated with a diffusion process across the corrosion layer. On the other hand, when the immersion time is less than 180 min, the two capacitive loops at high and medium to low frequencies are observed as shown in Figure 2.27(a). The first loop from high to medium frequencies regions can be attributed to a protective surface film of FAS molecules and/or nanostructured cerium oxide, and the double layer capacitance at the electrode surface, while the second one from medium to low frequencies might be attributed to the charge transfer (corrosion) resistance. The

capacitive loops decreased gradually with an increase in the immersion time. This indicates that the anticorrosion performance of the superhydrophobic surface formed on magnesium alloy is reduced gradually with immersion time.

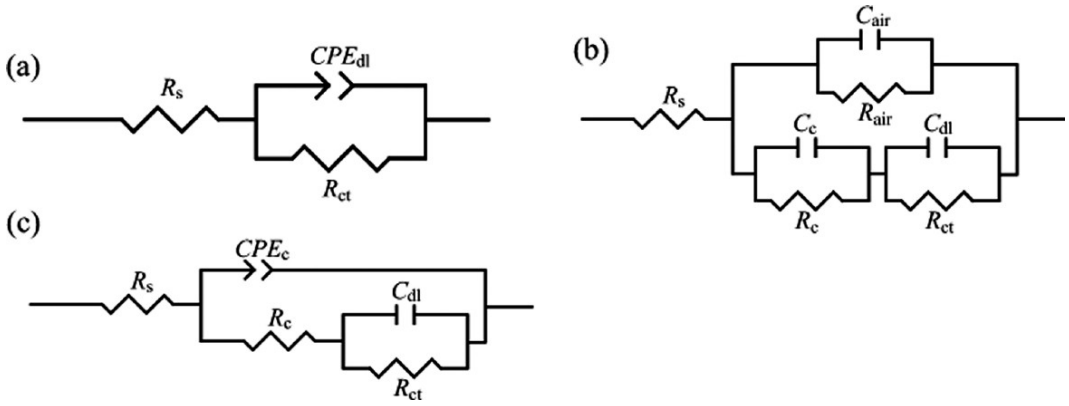

Figure 2. 28 Equivalent circuit models of the studied system for (a) untreated magnesium alloy, (b) superhydrophobic surface after immersion in 5 wt.% NaCl aqueous solution within 360 min, and (c) superhydrophobic surface after immersion in 5 wt.% NaCl aqueous solution for 1440 min [41].

The two equivalent circuit models are shown in Figure 2.28. Figure 2.28(a) shows the equivalent circuit model representing the electrochemical behavior of the untreated AZ31 surface, which shows one time constant. In this circuit, R_{ct} means the charge transfer resistance, CPE_{dl} is the constant phase element of the electrical double layer, and

R_s is the solution resistance. The R_{ct} value is an indicative of total corrosion resistance performance. The constant phase element (*CPE*) is often used as a substitute for the capacitor in the equivalent circuit to fit the impedance behavior of the electrical double layer more accurately. In the case of the superhydrophobic surface, the equivalent circuit model should have two time constants in the corresponding impedance spectra, since our fabricated superhydrophobic surface has a rough surface with many minute pores that could trap air at the solid-liquid interface. C_C would normally be assigned to the capacitance of a surface film, which is based on various factors such as film thickness and defect structure. The $R_{ct}||C_{dl}$ elements in Figure 2.28(b) show the impedance with the interface reaction between the film and substrate. The parallel combination of R_c and C_c represents impedance with the interface reaction between the electrolytic solution and the film. R_{air} and C_{air} are typically associated with the resistance and capacitance of air within a minute pore, respectively. The $R_{air}||C_{air}$ elements were arranged in parallel to the above-mentioned two elements with considering that the many minute pores would be filled with air. By applying this equivalence circuit model in Figure 2.28(b) to the

impedance spectra for superhydrophobic surface formed on magnesium alloy, better fitting results could be obtained. Moreover, we applied the equivalent circuit model as shown in Figure 2.28(c) to the super- hydrophobic surface after immersion in 5 wt.% NaCl aqueous solution for 1440 min. This model is often used in the case of a protection film formed on metal substrate. The reason we used the model is that the water contact angles on the superhydrophobic surface after immersion in 5 wt.% NaCl aqueous solution for 1440 min show hydrophilic properties and the air layer formed between many minute pores does not exist.

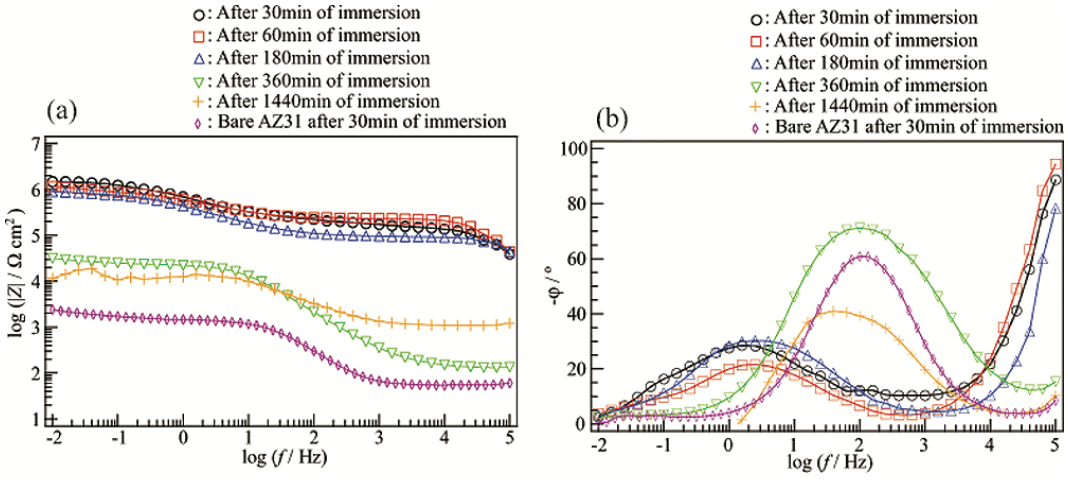

Figure 2. 29 Evolution of Bode plots of the untreated magnesium alloy and superhydrophobic surface after immersion in 5 wt.% NaCl for different time [41].

The bode plots are shown in Figure 2.29, because the phase angle, j, is a sensitive parameter for indicating the presence of additional time constants in the impedance spectra and the whole impedance data are presented explicitly. Figure 2.29 shows the bode plots of the untreated and superhydrophobic treated magnesium alloy. One well-defined time constant can be observed in the EIS spectra of untreated magnesium alloy at around 100 Hz. This relaxation process is associated with electrochemical activity of the untreated magnesium alloy surface immersed in the NaCl aqueous solution and can be ascribed to the capacitance of electrochemical double layer on the solid/electrolyte interface. The resistive response at low frequencies corresponds to the polarization resistance. The EIS spectra of the superhydrophobic surface after immersion in 5 wt.% NaCl solution for more than 360 min show one phase maximum at medium frequency and exhibit similar behavior to untreated magnesium alloy, while those of the superhydrophobic surface after immersion in 5 wt.% NaCl solution within 180 min have two phase maxima at relatively low and high frequencies (Figure 2.29(b)). The high

frequency time constant, at around 10^5 Hz, is related to the superhydrophobic surface formed on the magnesium alloy. Another time constant at around 3 Hz can be ascribed to the capacitance of double layer and is shifted to lower frequency than the time constant of untreated magnesium alloy because of good barrier properties of the superhydrophobic surface which sup- press the penetration of the NaCl aqueous solution to the magnesium alloy surface. In addition, the impedance behaviors of the superhydrophobic surface after immersion in 5 wt.% NaCl solution within 180 min show a similar shape (Figure 2.29(a)). Such a shape is related to porosity phenomena with paint layers. The impedance level decreases monotonically with an increase in the immersion time. In the low frequency region, a coincidence of the spectra is observed for the superhydrophobic surface after immersion in 5 wt.% NaCl solution within 180 min. The impedance behaviors in the low frequency region depend on the properties of the protective layer. The high impedance level evidences that our superhydrophobic surface shows high corrosion resistance due to the superhydrophobic property if the immersion time is within 180 min. However, in the case where the immersion time is more than 360 min, different impedance behavior can

be observed. The increase of immersion time causes different chemical and/or physical changes in the superhydrophobic surface formed on magnesium alloy. Due to the changes in the surface states, the |Z| values of the superhydrophobic surface gradually approach that of the untreated magnesium alloy with an increase in immersion time. However, the |Z| values at low frequency of the superhydrophobic surface formed on the magnesium alloy after immersion in 5 wt.% NaCl aqueous solution for 24 h are estimated to be about 7.2×10^{3} $\Omega\cdot cm^{2}$, 5 orders of magnitude higher than that of untreated magnesium alloy. This indicates that our superhydrophobic film retards the formation of the corrosion products considerably due to a synergistic effect of superhydrophobicity based on the FAS coating and protective property of the nanostructured cerium oxide film.

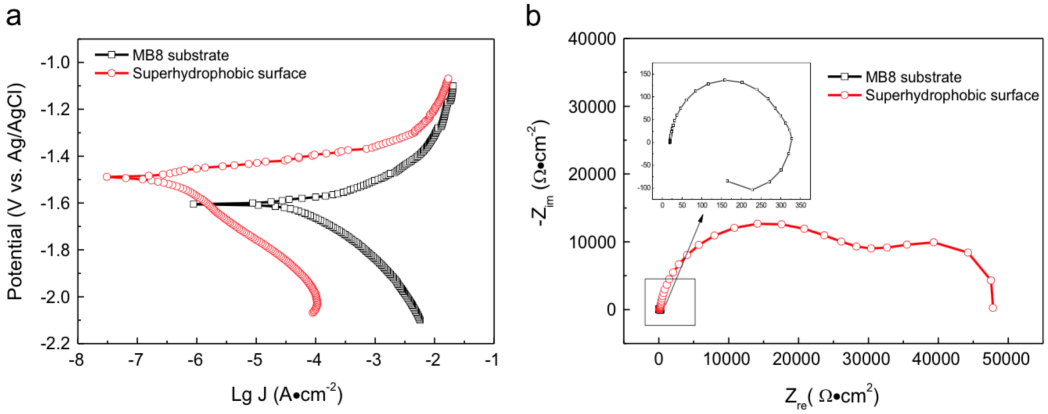

Figure 2. 30 Electrochemical measurements of the substrate and superhydrophobic surfaces: (a) polarization curves and (b) Nyquist plots [33].

Superhydrophobic surfaces have been prepared by Liu et al., using electrolytic solution containing cerium nitrate hexahydrate ($Ce(NO_3)_3 \cdot 6H_2O$) and myristic acid via one-step electrodeposition process [33]. Figure 2.30 shows the polarization curves using the Tafel extrapolation method. The corrosion potential (E_{corr}) positively increases from -1.596 V of the substrate to -1.489 V of the superhydrophobic surface. Accordingly, the corrosion current density (I_{corr}) of the superhydrophobic surfaces is 1.42×10^{-7} A/cm^2, which decreases by more than 2 orders of magnitude compared to that of the substrate (2.48×10^{-5} A/cm^2). Increasing of E_{corr} and decreasing of I_{corr} reveal that the superhydrophobic surface significantly improves the corrosion resistance of MB8. Figure

2.30(b) shows the Nyquist plots for the EIS studies. The plot of the substrate displays one capacitive loop ascribed to the charge transfer resistance (R_{ct}) in high frequency and one inductive loop associated with the dissolution of the metal substrate in low frequency. While the plot for superhydrophobic surface displays two capacitive loop in both high and low frequencies. The high frequency loop is also related to R_{ct} and the lower frequency one is ascribed to diffusion process through the superhydrophobic surface. It is well known that the diameter of the capacitive loop related to R_{ct} in the Nyquist plots represents the impedance of the samples. The value of R_{ct} for the superhydrophobic surface (13 kΩ) is about 100 times larger than that of the substrate surface (137 Ω), which indicates the superhydrophobic film has largely improved the corrosion properties.

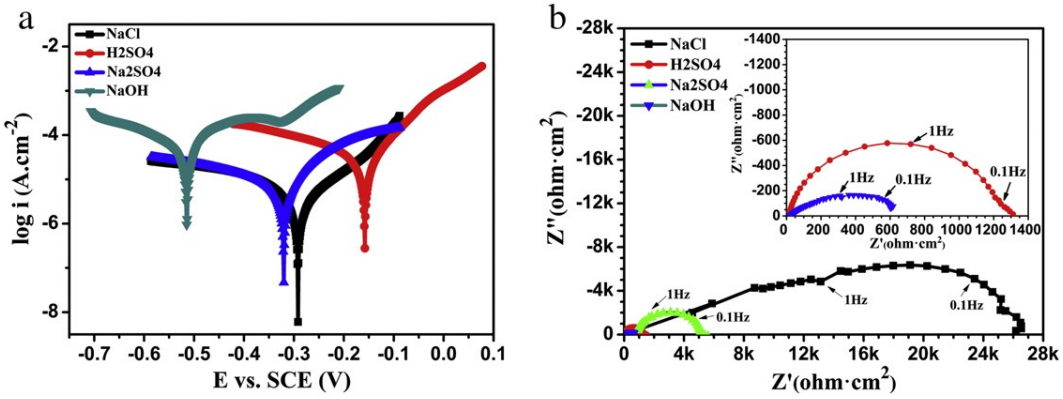

Figure 2. 31 (a) Potentiodynamic polarization curves and (b) Nyquist plots of the superhydrophobic Ce coating deposited at 50 V for 10 min in different corrosive solutions [42].

Different corrosive solutions have been applied in Cansen Liu's study [42]. In their work, the superhydrophobic surfaces are fabricated using electrodeposition process, using cerium chloride mixing with myristic acid electrolytic solution. To broaden the applications of the as-prepared Ce coating under different environments, the electrochemical corrosion properties were tested in different corrosive solutions. Potentiodynamic polarization curves and Nyquist plots of the superhydrophobic surface tested in different corrosive solution are shown in Figure 2.31(a) and (b), respectively. The relevant electrochemical parameters, such as Tafel slopes (β_a and β_c), corrosion current density (I_{corr}), corrosion potential (E_{corr}) and corrosion rate, are shown in Table

2.3. The electrochemical parameters are obtained by fitting the potentiodynamic polarization curves (Figure 2.31(a)) via the Corrview software. As shown in Figure 2.31(a), the superhydrophobic Ce coating displayed the best corrosion resistance in neutral 3.5 wt.% NaCl solution, followed by in 0.6 M Na_2SO_4 and then in 0.5 M H_2SO_4 solutions. The coating tested in 0.6 M NaOH solution exhibited the worst corrosion resistance because of its highest I_{corr} and lowest E_{corr} value. The corrosion rate of the coating tested in 3.5 wt.% NaCl was tested in 0.6 M NaOH solution.

Table 2. 3 Tafel slopes (β_a and β_c), corrosion current (I_{corr}), corrosion potential (E_{corr}) and corrosion rate of the superhydrophobic Ce coating measured in different corrosive solution (3.5 wt.% NaCl, 0.5 M H_2SO_4, 0.6 M NaOH and 0.6 M Na_2SO_4).

Corrosive solution	βa (mV)	βc (mV)	i_{corr} ($\times 10^{-6}$ A cm^{-2})	E_{corr} (mV)	Corrosion rate (mm y^{-1})
NaCl	198.9	334.2	6.94 ± 0.347	−291.7 ± 14.6	0.118 ± 0.00354
Na_2SO_4	181.2	2171.9	18.2 ± 0.908	−321.3 ± 16.1	0.307 ± 0.0123
H_2SO_4	102.1	283.6	33.1 ± 1.65	−158.9 ± 7.95	0.561 ± 0.0168
NaOH	529.8	1876.4	329.3 ± 16.5	−514.8 ± 25.7	5.58 ± 0.279

Nyquist plots had a good agreement with the potentiodynamic polarization curves, as shown in Figure 2.31(b). These results suggested that the superhydrophobic Ce coating is not suitable for applications in the solution with strong alkalinity. At the same time, Table 2.3 displays that the corrosion rate of the sample tested in Na_2SO_4 was slightly higher than that in the NaCl solution, which might be attributed to the different cerium salts formed in these two solutions during the electrochemical corrosion process. The cerium sulfate solution was less efficient for blocking the oxygen reduction reaction in the cathodic process than cerium chloride solution, which approximately 2.11% of the one corresponded to the slightly higher corrosion rate of the resulting Ce coating in the Na_2SO_4 solution than in the NaCl solution.

When the corrosion and superhydrophobicity to prevent corrosion, it is necessary to mention conversion coatings. Conversion coatings are coatings for metals where the part surface is converted into the coating with a chemical or electro-chemical process. Examples include chromate conversion coatings [43], phosphate conversion coatings [44], bluing, black oxide coatings on steel, and anodizing. They are used for corrosion

protection, to add decorative color and as paint primers. As compared with superhydrophobic coating for preventing corrosion, conversion coatings are more complex to operate. Furthermore, in most of the cases, the corrosion resistance property by conversion coatings is not as good as superhydrophobic coating.

References

(1) Huang, Y.; Sarkar, D. K.; Chen, X. G.; Advanced Materials Research: 2012; Vol. 409, p 497.

(2) Brassard, J. D.; Sarkar, D. K.; Perron, J. *ACS Appl Mater Inter* **2011**, *3*, 3583.

(3) Saleema, N.; Sarkar, D. K.; Gallant, D.; Paynter, R. W.; Chen, X. G. *ACS Applied Materials & Interfaces* **2011**, *3*, 4775.

(4) Saleema, N.; Sarkar, D. K.; Paynter, R. W.; Chen, X. G. *ACS Applied Materials & Interfaces* **2010**, *2*, 2500.

(5) Brassard, J.D.; Sarkar, D.K.; Perron J. *Appl. Sci.* **2012**, *2*, 453.

(6) Safaee, A.; Sarkar, D.; Farzaneh, M. *Applied Surface Science* **2008**, *254*, 2493.

(7) Sarkar, D. K.; Farzaneh, M.; Paynter, R. W. *Applied Surface Science* **2010**, *256*, 3698.

(8) Sarkar, D. K.; Farzaneh, M. *Journal of Adhesion Science and Technology* **2009**, *23*, 1215.

(9) Sarkar, D. K.; Paynter, R. W. *Journal of Adhesion Science and Technology* **2010**, *24*, 1181.

(10) Huang, Y.; Sarkar, D. K.; Chen, X. G. *Materials Letters* **2010**, *64*, 2722.

(11) Sarkar, D. K.; Farzaneh, M.; Paynter, R. W. *Materials Letters* **2008**, *62*, 1226.

(12) Huang, Y.; Sarkar D. K.; Chen, X.G. *Nano-micro letters* **2011**, *3(3)*, 160.

(13) Sarkar, D. K.; Saleema, N. *Surface and Coatings Technology* **2010**, *204*, 2483.

(14) Ramezani, M.; Vaezi, M. R.; Kazemzadeh, A. *Applied Surface Science* **2014**, *317*, 147.

(15) Brassard, J.D.; Sarkar, D. K.; Perron, J. *ACS Applied Materials & Interfaces* **2011**, *3*, 3583.

(16) Marchand, D. J.; Dilworth, Z. R.; Stauffer, R. J.; Hsiao, E.; Kim, J.-H.; Kang, J.-G.; Kim, S. H. *Surface and Coatings Technology* **2013**, *234*, 14.

(17) Zheng, Z.; Gu, Z.; Huo, R.; Ye, Y. *Applied Surface Science* **2009**, *255*, 7263.

(18) Huang, Y.; Sarkar, D. K.; Chen, X. G. *Nano-Micro Letters* **2011**, *3*, 160.

(19) Huang, Y.; Sarkar, D. K.; Chen, X. G. *Applied Surface Science* **2015**, *327*, 327.

(20) Cao, G.Z. *The Journal of Physical Chemistry B* **2004**, *108*, 19921.

(21) Rieger P.H. *Electrochemistry* **1994**, *Chapman&Hall: New york*.

(22) Wu. M.S., H. C. Y., Jow J.J. *Electrochem. Commun.* **2009**, *11*, 779.

(23) Wu, M. S., Huang, C. Y., Lin, K. H. *Electrochem. Solid-State Letter* **2009**, *12*, A129.

(24) Hunter, R. J. *Zeta potential in colloid science: Principles and Applications*; Academic press: London, 1981.

(25) Callister, W. D. New york, 1997.

(26) Ogihara, H.; Okagaki, J.; Saji, T. *Chemistry Letters* **2009**, *38*, 132.

(27) Joung, Y. S.; Buie, C. R. *Langmuir* **2011**, *27*, 4156.

(28) Ogihara, H.; Okagaki, J.; Saji, T. *Langmuir* **2011**, *27*, 9069.

(29) Liu, Y.; Yin, X.; Zhang, J.; Yu, S.; Han, Z.; Ren, L. *Electrochimica Acta* **2014**, *125*, 395.

(30) Chen, Z.; Hao, L.; Chen, A. *Colloids and Surfaces A: Physicochemical and Engineering Aspects* **2012**, *401*, 1.

(31) Chen, Z.; Hao, L.; Chen, A.; Song, Q.; Chen, C. *Electrochimica Acta* **2012**, *59*, 168.

(32) Chen, Z.; Li, F.; Hao, L.; Chen, A.; Kong, Y. *Applied Surface Science* **2011**, *258*, 1395.

(33) Liu, Q.; Kang, Z. *Materials Letters* **2014**, *137*, 210.

(34) Lai, Y.; Lin, C.; Wang, H.; Huang, J.; Zhuang, H.; Sun, L. *Electrochemistry*

Communications **2008**,*10*, 387.

(35) Sulka G.D. *Nanostructured Materials in Electrochemistry,* **2008**, *Wiley-VCH*, 1.

(36) Zaraska, L.; Sulka, G. D.; Jaskuła, M. *Surface and Coatings Technology* **2010**, *205*, 2432.

(37) Chung, C. K.; Chang, W. T.; Liao, M. W.; Chang, H. C. *Thin Solid Films* **2011**, *519*, 4754.

(38) Chung, C.K.; Zhou R. X.; Liu, T.Y.; Chang W.T. *Nanotechnology* **2009**, *055301*, 20.

(39) Wu, Z.; Richter C.; Menon, L *J. Electrochem. Soc.* **2007**, *E8*, 154.

(40) Yang, W.B.; Tang X.H. *Mater. Sci. Forum* **2011**, *272*, 663.

(41) Ishizaki, T.; Masuda, Y.; Sakamoto, M. *Langmuir* **2011**, *27*, 4780.

(42) Liu, C.; Su, F.;Liang, J.; Huang, P. *Surface and Coatings Technology* **2014**, *258*, 580.

(43) Pommiers-Belin, S.; Frayret, J.; Uhart, A.; Ledeuil, J.; Dupin, J.; Castetbon, A.; Potin-Gautier, M. *Applied Surface Science* **2014**, *298*, 199.

(44) Zeng, R.; Hu, Y.; Zhang, F.; Huang, Y.; Wang, Z.; Li, S.; Han, E. *Transactions of Nonferrous Metals Society of China* **2016**, *26*, 472.

CHAPTER 3 EXPERIMENTS

In this chapter, the details of experiments including the property of the materials, the experimental procedural and the material characterization et al. Furthermore, the facilities in the experiments is presented in this chapter.

3.1 Selection of materials

Due to the light weight and the Mg-Si rich composition, the *6xxx* aluminum alloy series are widely used in many important structures such as aircrafts, marine, automobiles, constructions and buildings. The most commonly used AA 6061 alloy will be principally investigated in this project. The composition of AA6061 alloy is as follow: Mg 1.08 wt.%, Si 0.63 wt.%, Mn 0.52 wt.%, Cu 0.32 wt.%, Fe 0.17 wt.%, Ti 0.02 wt.%, V 0.01 wt.%, Al remainder.

3.2 Substrate cleaning

The mechanically polished and as-received aluminum alloys substrates will be

degreased by ultrasonication in dilute LIQUINOX solution (1 wt.%) for 15 minutes followed by rinsing in de-ionized water for two times of 5 minutes.

3.3 Passivation of ZnO nanoparticles by Stearic acid

ZnO nanoparticles (1 g) in evaporating dish are put in 70 °C in an oven for 10 h. The dried ZnO nanoparticles are then put in ethanolic stearic acid solution, followed by stirring for 20 minutes and ultrasonic for 20 minutes, respectively. The well mixed solution is then put in centrifuge for 5minutes to obtain stearic acid passivated ZnO nanoparticles. They are then put in 70 °C for 10 h. The X-ray diffraction is then used to analyze the crystal structure of the dried passivated nanoparticles. The passivation of ZnO nanoparticles by stearic acid is schematically shown in Figure 3.1.

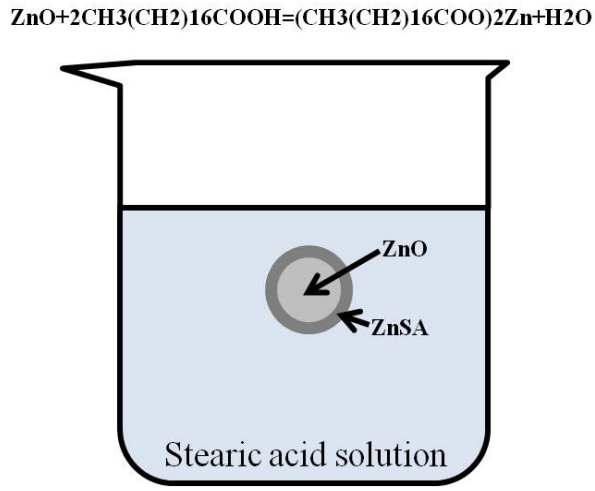

Figure 3. 1 The model of the reaction between stearic acid and ZnO nanoparticles

3.4 Preparation of superhydrophobic aluminum alloy surfaces by electrophoretic deposition (EPD)

The thin films growth mechanism by EPD will be studied on bare aluminum alloy substrates, and the EPD process will further be used to incorporate the passivated nanoparticles in the anodized pores of the anodized aluminum alloy surfaces later on.

EPD method consists following steps:

The deposition process by EPD is presented schematically in Figure 3.2. Hydrophilic ZnO particles (average particle diameter of 30 nm) will be put in a mixture of 0.01 M stearic acid, 2-propanol and tert-butyl alcohol (vol. = 1:2:4), followed by

ultrasonication for 1 h.

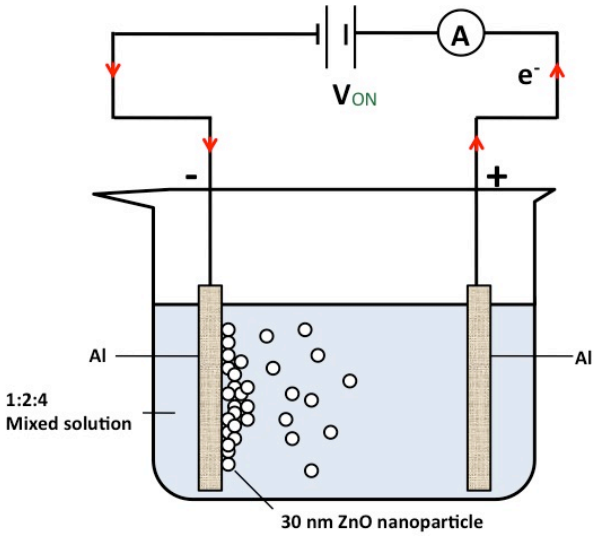

Figure 3. 2 The schematic image of electrophoretic deposition.

A pair of aluminum alloy substrates is vertically immersed in the prepared suspension solution. With the application of a DC voltage under varied range of bath temperature, the positive charged suspended particles will be deposited as a film on the cathodic electrode. The evolution of the morphological feature as well as the chemical compositional changes will be studied with respect to the variation of electric field and deposition time.

3.5 Preparation of superhydrophobic aluminum alloy substrates via electrodeposition process

Due to the insufficient corrosion resistance property of superhydrophobic aluminum alloy substrates fabricated by EPD process, a new one-step electrodeposition process was created. 0.01 M zinc nitrate ($Zn(NO_3)_2$) and 0.01 M stearic acid (SA) solution with different molar ratio (Zn^{2+}/SA) was mixing followed by stirring for 1 hour. The cleaned AA 6061 aluminum alloy substrate as cathode was deposited in the $Zn(NO_3)_2$ and SA mixing electrolytic solution at 20 V for 10 min.

3.6 Anodization of aluminum alloy surfaces

The pretreatment of aluminum alloy surfaces will be performed by chemical etching with 1 M NaOH (100 ml) in ultrasonication at 55°C for 3 minutes and then clean it with distilled water for 1 minute and put it in 1 L distilled water for 10minutes. The aluminum alloy substrates will be then immersed in 10 vol.% HNO_3 solution for 1.5 minutes and clean it with distilled water for 1 minute and put it in 1 L distilled water for 10 minutes.

Etched aluminum alloy surfaces will be anodized in 3 vol.% H_3PO_4 solution at DC current ranging from 2.5 mA/cm^2 to 10 mA/cm^2 for 2 h at different operating temperature. The schematic of anodized aluminum alloy surface is shown in Figure 3.3.

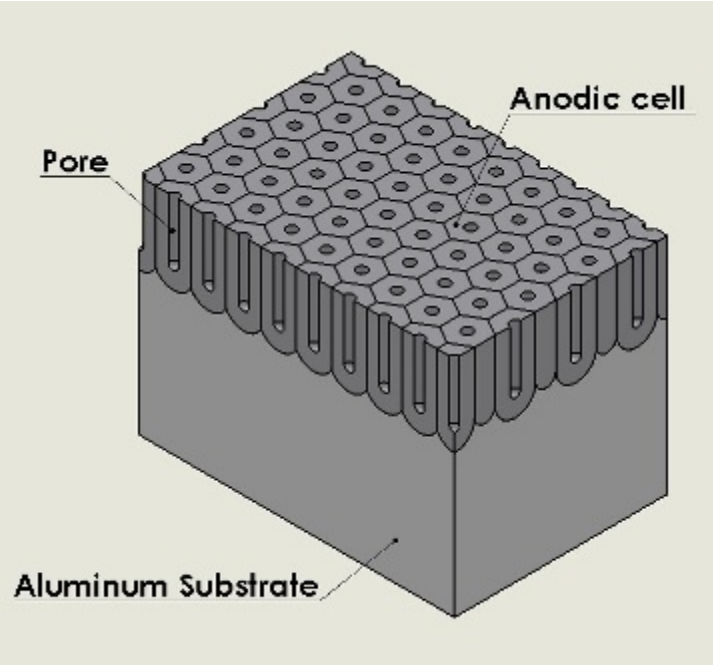

Figure 3. 3 Schematics of anodized aluminum alloy surface.

3.7 Incorporation of electrodeposition in the anodized pore to obtain superhydrophobic surfaces

The superhydrophobic anodized aluminum alloy surfaces will be obtained by further

electrophoretic deposition with ZnO nanoparticles under the same condition as EPD process illustrated in section 3.5. In addition, the anodized aluminum alloy surfaces were also modified to superhydrophobic by electrodeposition process, which is the same process as illustrated in section 3.6.

3.8 Characterization: Structural, morphological, chemical compositional analysis, superhydrophobicity and corrosion behavior analysis

The following techniques available in CURAL, UQAC; ATC-NRC, Chicoutimi; and in INRS-ÉMT, Varennes will be used in collaboration:

(i) Microstructural characterization by scanning electron microscopy (SEM) and optical profilometry as shown in Figure 3.4 and 3.5, respectively.

Figure 3. 4 Instrument of scanning electron microscopy (SEM).

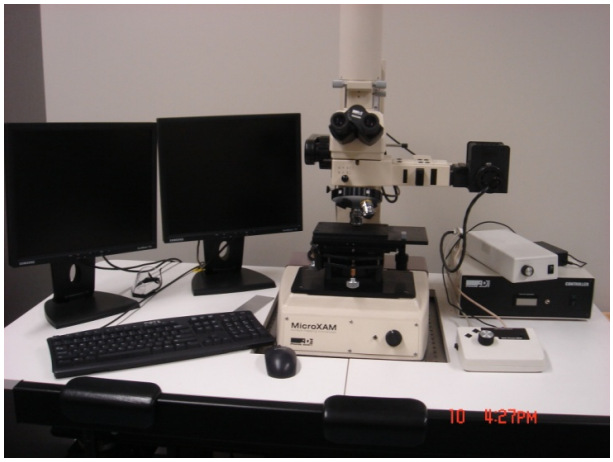

Figure 3. 5 Instrument of optical profilometry.

(ii) X-ray diffraction (XRD) for verification of crystalline properties of the modified surfaces (Figure 3.6).

Figure 3. 6 Instrument of X-ray diffraction (XRD).

(iii) Attenuated total reflection-Fourier transform infrared spectroscopy (ATR-FTIR) (in collaboration with ATC-NRC, Chicoutimi) to analyze stearic acid modified metal surfaces for chemical information (Figure 3.7).

Figure 3. 7 Instrument of Fourier transform infrared spectroscopy (FTIR)

(iv) X-ray photoelectron spectroscopy (XPS) (in Figure 3.8) studies (in collaboration with R. W. Paynter, INRS-ÉMT, Varennes) in order to evaluate the surface chemistry with higher resolution than ATR-FTIR.

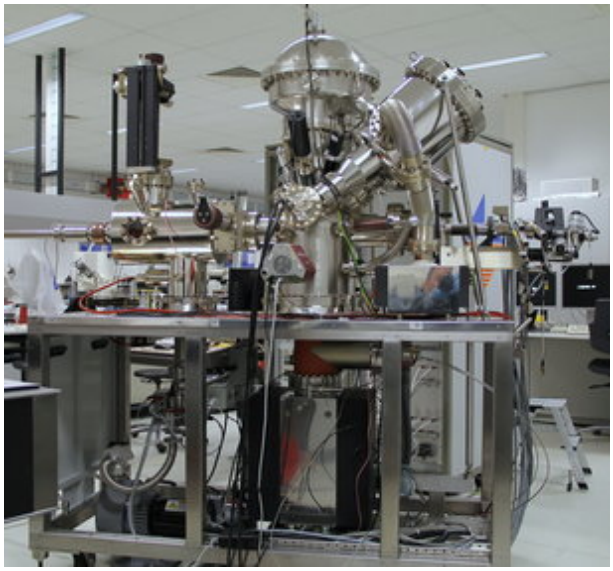

Figure 3. 8 Instrument of X-ray photoelectron spectroscopy (XPS).

(v) The wetting behaviour of the stearic acid modified surface will be analyzed using the contact angle measurement facilities at GRTB (in Figure 3.9).

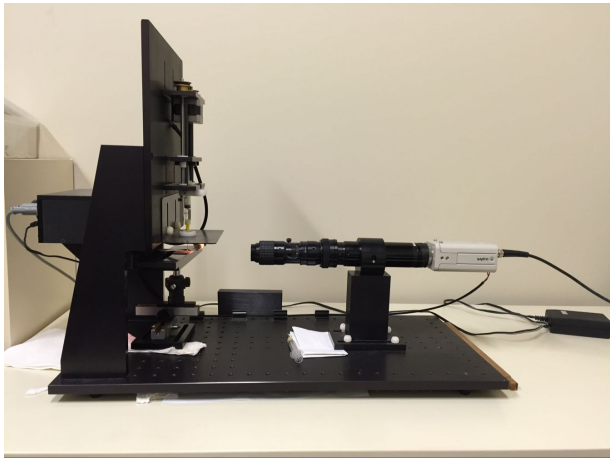

Figure 3. 9 Instrument of contact angle goniometer.

The corrosion resistance performance of the samples was investigated via both potentiodynamic polarization experiments as well as electrochemical impedance spectroscopy (EIS). The instrument of corrosion test is shown in Figure 3.10. Electrochemical experiments were performed using a PGZ100 potentiostat and a 300 cm^3 - EG&G PAR flat cell (London Scientific, London, ON, Canada), equipped with a standard three-electrode system with an Ag/AgCl reference electrode, a platinum (Pt)

mesh as the counter electrode (CE), and the sample as the working electrode (WE). For the potentiodynamic polarization experiments, the potential was scanned from -250 mV to +1000 mV of OCP value in a 0.5 M (3 wt.%) NaCl solution. The electrochemical impedance spectroscopy (EIS) technique was performed in the frequency ranges between 0.01 Hz and 100 kHz with sine-wave amplitude of 10 mV at room temperature. SEM/EDX, XRD, ATR-FTIR and XPS studies will be carried out to monitor surface property changes following exposure to the corrosive environments.

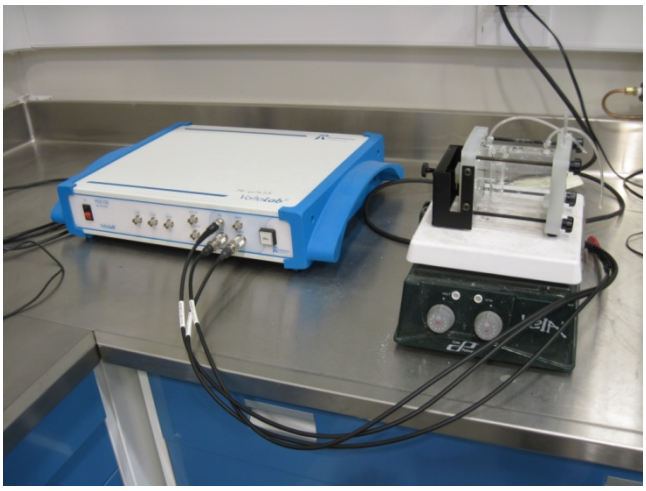

Figure 3. 10 Instrument of corrosion test.

CHAPTER 4. SUPERHYDROPHOBIC ALUMINUM ALLOY SUBSTRATE PREPARED BY CHEMICAL ETCHING PROCESS AND THEIR CORROSION RESISTANCE PROPERTY

In the previous study, the chemical etching process was initially studied to prepare superhydrophobic aluminum alloy surfaces. However, the effect of the passivation time on the superhydrophobic properties and their corrosion resistance property was not investigated. Therefore, in this section, the superhydrophobic aluminum alloy substrates prepared by chemical etching process and their corrosion resistance properties are studied, for the completeness and better understanding of the master study as well as being the reference comparing with the superhydrophobic surfaces prepared in the Ph.D. work. The article titled “Superhydrophobic aluminum alloy substrate prepared by chemical etching process and their corrosion resistance property” has been published in journal of applied

surface science.

4.1 Introduction

Superhydrophobicity is the property that describes the non-wetting characteristics of material surfaces. Superhydrophobic surfaces are attracting ever increasing attention from the scientists and engineers due to wide applications in corrosion resistance and anti-sticking of snow and ice and potential incorporation into eyeglasses, windows, self-cleaning automobile windshields, and other technologies [1-3]. Recently, various fabrication methods for superhydrophobic surfaces have been explored [4-16]. These methods are guided by the common principles of optimizing topography and lowering surface energy. In other words, both the surface geometrical structure and the chemical composition control the wettability of the solid surface.

Chemical etching process is the process of removing a layer on a metal surface through a chemical reaction and is an effective method for obtaining rough surfaces. It has been widely used to fabricate superhydrophobic aluminum alloy surfaces [6,7,17-21]. Sarkar *et al.* obtained superhydrophobic aluminum surfaces by chemical etching followed

by coating with an ultrathin rf-sputtered Teflon film [14]. Saleema *et al.* used a one-step etching process to obtain a superhydrophobic aluminum alloy substrate with a NaOH and fluoroalkylsilane (FAS-17) mixed solution [6,7]. Ruan *et al.* utilized HCl mixed with HF as an etchant on an aluminum alloy substrate followed by passivation with different modifiers such as dodecyl mercaptan (DDM), lauric acid, myristic acid and palmitic acid [17]. Similarly，HCl was also used by Escobar *et al.* in a chemical etching process, together with passivation employing dodecanoic acid, to obtain superhydrophobic aluminum alloy substrates [18]. In addition, Liao *et al.* fabricated superhydrophobic aluminum alloy substrates by copper assisted chemical etching with HCl solution followed by passivation with hexadecyltrimethoxysilane [19].

A number of investigations have been performed on other superhydrophobic surfaces (apart from aluminum alloy substrates) obtained by chemical etching, such as superhydrophobic silicon etched by HF mixed with $AgNO_3$ followed by passivation with trimethoxysilane [22], superhydrophobic titanium etched by NaCl followed by passivation with tridecafluoroctyltriethoxysilane [23], superhydrophobic

zinc (Zn) etched by $NaCl/NaNO_3$ followed by passivation with fluorinated polymer [24], superhydrophobic magnesium etched by H_2SO_4/H_2O_2 followed by passivation with stearic acid (SA) [25] and superhydrophobic copper etched by HNO_3 followed by passivation with 1H,1H,2H,2H-perfluorodecyltriethoxysilane (FDTES) [26].

It is well known that the contact of metals with water triggers corrosion; therefore, one may consider using superhydrophobic surfaces to repel water and thus prevent corrosion. The corrosion resistance properties of superhydrophobic aluminum alloy substrates have been studied in the literature [3,27-29]. He *et al.* investigated the corrosion resistance of superhydrophobic aluminum alloy substrates, prepared by anodizing followed by passivation with myristic acid, via potentiodynamic polarization experiments as well as electrochemical impedance spectroscopy (EIS) [3]. A similar method for preparing superhydrophobic aluminum alloy substrates has also been used by Liu *et al.*, and the reduced microbiologically influenced corrosion of superhydrophobic aluminum alloy substrates was investigated using EIS, polarization as well as scanning electron microscopy (SEM) [28]. Furthermore, Liang *et al.* developed a facile sol–gel method, with

tetraethylorthosilicate (TEOS) and vinyltriethoxysilane (VTES) as co-precursors at room temperature, to create a superhydrophobic aluminum alloy substrate [27], the authors then characterized the corrosion resistance and durability of the superhydrophobic silica-based surface formed on the aluminum substrate in a corrosive NaCl solution via EIS measurements [27]. In another study by Liu *et al.* [29], the corrosion resistance properties of a superhydrophobic aluminum alloy substrate, fabricated by graphene spin-coated on the surface, were investigated and compared with those of the as-received aluminum alloy substrate.

In our previous study, superhydrophobic copper surfaces were fabricated by a one-step electrochemical modification process with ethanolic stearic acid solution using a DC voltage [13]. Furthermore, the corrosion resistance of the superhydrophobic copper substrates was investigated by potentiodynamic polarization experiments [30]. The decrease of corrosion current density (I_{corr}) as well as the increase of polarization resistance (R_p) obtained from the polarization curves revealed that the superhydrophobic film on the copper surfaces improved the corrosion resistance of the copper substrate. In a recent

study from our group, anti-corrosion and anti-icing superhydrophobic steel coatings were achieved by electrodeposition of Zn on steel followed by functionalization of Zn using an ultra-thin film of commercial silicone polymer [31].

In the present study, superhydrophobic aluminum alloy substrates were prepared by chemical etching using alkaline NaOH solution followed by passivation with ethanolic stearic acid (SA) solution. Chemical etching has the technological advantages of being both cost-effective and easy to scale up. The fabricated superhydrophobic aluminum alloy substrates were analyzed using both potentiodynamic polarization and electrochemical impedance spectroscopy (EIS) to evaluate their corrosion properties.

4.2 Experiments

As starting materials, rolled sheets of AA 6061 aluminum alloy were chemically etched using 1 M alkaline NaOH solution (pH of 14) in an ultrasonic bath. After cleaning with distilled water, the etched aluminum alloy substrate was dried at 70 °C in a closed oven for more than 10 hr. The passivation process was performed by immersing the etched aluminum alloy substrate at room temperature in 0.01 M ethanolic SA solution for

a range of passivation times. The morphological analyses of the samples were performed using a scanning electron microscope (SEM, JEOL JSM-6480 LV). The wetting characterization of the sample surfaces was carried out by measuring static and dynamic contact angles using a First Ten Angstrom contact angle goniometer (the static contact angle has been abbreviated as CA and the dynamic contact angle has been abbreviated as contact angle hysteresis (CAH)). The adhesion of the superhydrophobic aluminum alloy substrates was carried out according to the ASTM D3359 standard test method using a Cross Hatch Cutter, model Elcometer 107. The corrosion resistance properties of the samples were investigated via both potentiodynamic polarization experiments as well as electrochemical impedance spectroscopy (EIS). Electrochemical experiments were performed using a PGZ100 potentiostat and a 300 cm^3-EG&G PAR flat cell (London Scientific, London, ON, Canada), equipped with a standard three-electrode system with an Ag/AgCl reference electrode, a platinum (Pt) mesh as the counter electrode (CE), and the sample as the working electrode (WE) [6]. For the potentiodynamic polarization experiments, the open-circuit potential was scanned from -250 mV to +1000 mV in a 3.5

wt.% NaCl solution. An attempt was made to perform EIS measurements using 3 wt.% NaCl, as 3.5 wt.% was more reactive, in the frequency ranges between 0.01 Hz and 100 kHz with a sine-wave amplitude of 10 mV at room temperature.

4.3 Surface characterization

Figure 4.1(a) shows the SEM image of the surface of an as-received aluminum rolled sheet, which had a surface root-mean-square (rms) roughness of 0.45 μm and water contact angle (CA) of 87 ± 3° (inset of the Figure). The surface of rolled aluminum sheets generally exhibits the rolled lines and therefore will have a certain inherent roughness [32]. The CA of the SA passivated aluminum alloy substrate was found to be only 110 ± 1°. Therefore, a pretreatment of chemical etching using a 1 M alkaline NaOH solution was performed to modify the surface of the as-received aluminum alloy substrate. The morphology of the etched aluminum alloy substrate is shown in Figure 4.1(b). The NaOH etched aluminum alloy substrate (Figure 4.1(b)) was found to be rougher compared with the as-received aluminum alloy substrate (Figure 4.1(a)). Consequently, the surface roughness of the etched aluminum alloy substrate was increased to 1.38 ± 0.17 μm from

0.45 ± 0.03 μm of the as-received aluminum alloy substrate. The CA on the NaOH etched aluminum alloy substrate was decreased to 34 ± 4°, which can be attributed to the increase of surface area as well as the possible change of surface composition. The Wenzel model and its mathematical equation (Equation (4.1)) [33] can be used to explain the decrease of CA assuming no change of surface composition due to chemical etching.

$$\cos\theta^* = R_W \cos\theta \qquad \text{(Equation 4. 1)}$$

where θ is the CA of a smooth surface and θ^* is the CA of a rough surface without any alteration of surface composition, the roughness factor R_w is the ratio of the true to the apparent surface areas. It is evident that R_w is always more than 1 as true surface area is larger than the apparent surface area due to the presence of roughness; therefore, as the CA of the as-received aluminum alloy substrate (assumed to be smooth) is 87 ± 3°, the CA of the etched rough surface would be smaller than 87 ± 3°. As the CA of the NaOH etched aluminum alloy substrate was 34 ± 4°, the R_w associated with the roughness of the etched substrate was calculated to be 15.84.

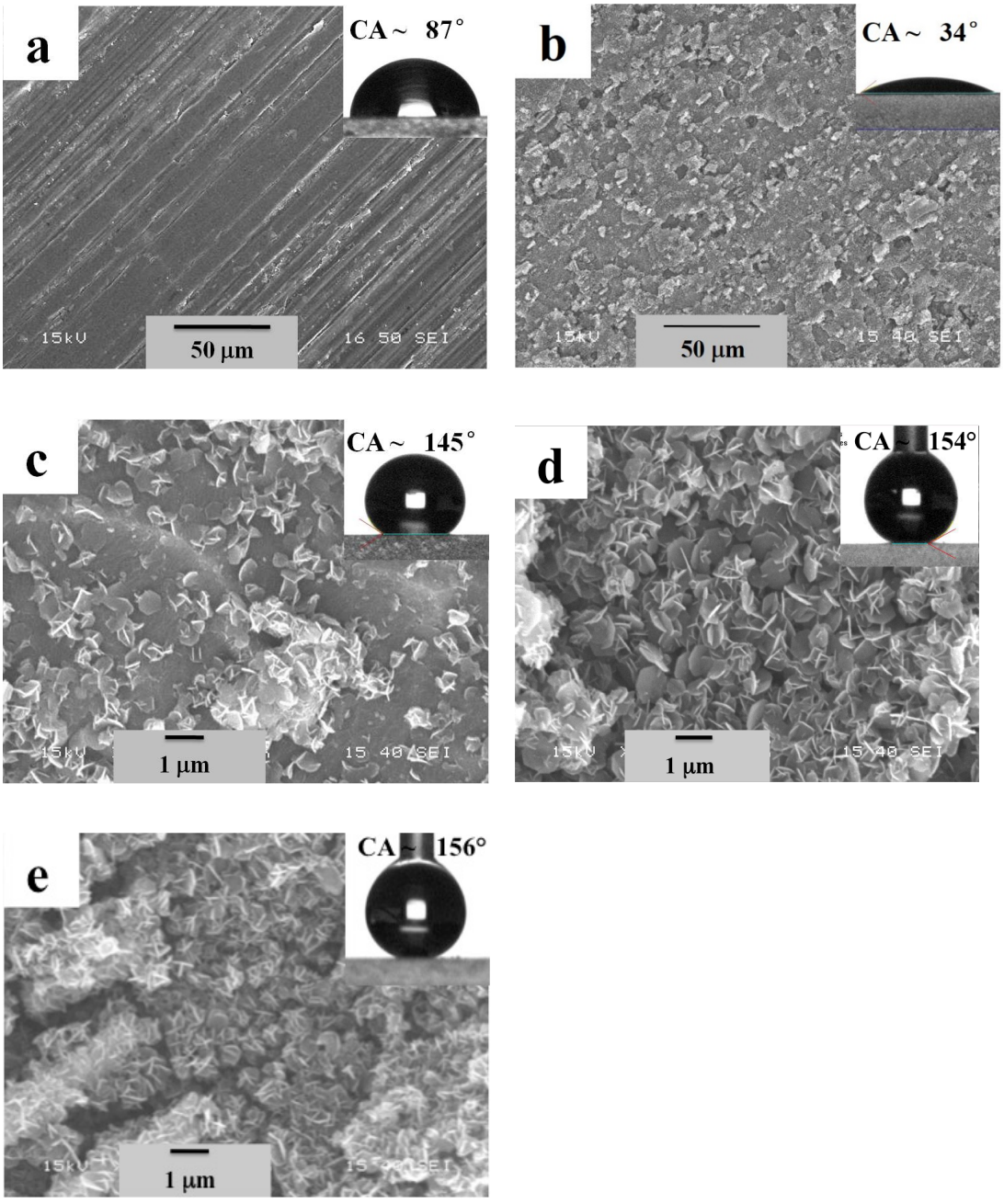

Figure 4. 1 SEM images of the surface of (a) as-received aluminum alloy substrate; (b) NaOH etched aluminum alloy substrate; (c-e) 5 s-, 1 min- and 24 min-SA passivated NaOH etched aluminum alloy substrates. The insets of Figure 4.1(a-e) show the water drops and CA

on the respective surfaces.

However, it was not evident from the surface morphology that the surface area of the etched substrate could be 15 times more than that of as-received aluminum alloy. Therefore, the change of chemical composition due to the chemical etching process also played a role in the change of CA on the etched aluminum alloy substrate. We will see further that the SA passivation can modify the morphology of the NaOH etched aluminum alloy substrate but is unable to modify the as-received aluminum alloy substrate, which may due to the surface composition of the latter.

The NaOH etched aluminum alloy substrate was then passivated by SA for a range of passivation times varying from couple of seconds to a maximum of an hour. Figure 4.1(c-e) shows the morphologies of the NaOH etched aluminum alloy substrates followed by SA passivation for 5 s, 1 min and 24 min. The flake-like micro-nanostructure features appeared on the etched surface after SA passivation for 5 s as shown in Figure 4.1(c). The inset of Figure 4.1(c) shows the image of a water drop with a CA of 145 ± 2°. The enhancement of the CA was due to the formation of low surface energy aluminum

stearate (AlSA). The chemical analysis of these flake-like molecules is given in Figure 4.2(a). The number density of these flake-like micro-nanostructures increased by increasing the SA passivation time to 1 min, as shown in Figure 4.1(d). Consequently, the surface of etched substrate is nearly covered with these flake-like structures just after 1 min of SA passivation. In this situation, the CA of this surface further increased to 154 ± 2°, as shown in the inset of Figure 4.1(d). The compactness of these structures was further increased on the surface by increasing the SA passivation time to 24 min, as shown in Figure 4.1(e). However, the CA did not increase much as shown in the inset of Figure 4.1(e), yielding a value of 155 ± 1°. Because the surface morphology from 60 min-SA passivation on etched aluminum alloy is very similar to that from 24 min-SA passivation, the SEM image of that surface is not presented.

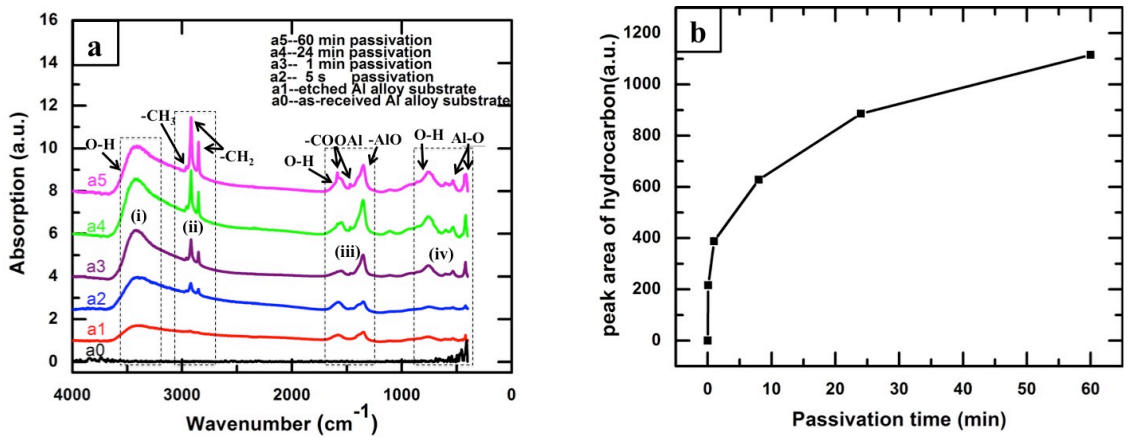

Figure 4. 2 (a) FTIR spectra of (a0) as-received aluminum alloy substrate, (a1) NaOH etched aluminum alloy substrate, and (a2) 5 s-, (a3) 1 min-, (a4) 24 min- and (a5) 60 min-SA passivated NaOH etched aluminum alloy substrates. (b) depicts the variation in the area under the hydrocarbon (–CH_2 and -CH_3) peaks as a function of the SA passivation time.

The infrared spectra of the as-received aluminum alloy substrate, the NaOH etched aluminum alloy substrate, and the SA passivated NaOH etched aluminum alloy substrates for a range of passivation times are shown in Figure 4.2(a). The four main infrared absorption zones were observed in all spectra. These zones are (i) a broad absorption peak between 3000-3500 cm^{-1}, (ii) two sharp absorption peaks at 2856 and 2917 cm^{-1}, (iii) an absorption zone approximately 1500 cm^{-1}, and (iv) a peak approximately 750 cm^{-1}.

The broad absorption peak at 3420 cm^{-1} in zone (i) is assigned to -OH bonding on the NaOH etched aluminum alloy substrate, as shown in Figure 4.2(a1). As is evident in comparing with the spectrum of the as-received aluminum alloy substrate (Figure 4.2(a0)), the presence of –OH bonding at the surface of the NaOH etched aluminum alloy substrate may be due to possible –OH bond formation during the reaction of NaOH with the aluminum alloy substrate, as shown below using Equations (4.2-4.5):

$$2Al + 2NaOH + 6H_2O \rightarrow 2NaAl(OH)_4 + 3H_2 \quad \text{(Equation 4. 2)}$$

$$NaAl(OH)_4 \rightarrow NaAlO_2 + 2H_2O \quad \text{(Equation 4. 3)}$$

$$Al_2O_3 + 2NaOH \rightarrow 2NaAlO_2 + H_2O \quad \text{(Equation 4. 4)}$$

$$NaAlO_2 + H_2O \rightarrow Al(OH)_3 + NaOH \quad \text{(Equation 4. 5)}$$

A similar reaction mechanism based on Equations 4.2 and 4.3 have been presented by Saleema *et al.* [6], who studied how to obtain superhydrophobic properties through a one-step process on aluminum alloy substrates using an alkaline NaOH solution containing FAS-17 molecules. However, they did not specify that the sodium aluminate ($NaAlO_2$) further hydrolyzed in the continuing reaction to produce $Al(OH)_3$ and NaOH.

Furthermore, the presence of native oxides on aluminum alloy substrates most likely consists of aluminum oxide (Al_2O_3). Al_2O_3 on the surface of the aluminum alloy substrate can react with NaOH and form sodium aluminate ($NaAlO_2$), which can then hydrolyze to $Al(OH)_3$ and NaOH, as presented in Equation 4.4-4.5. Therefore, the above chemical reactions show that the aluminum alloy substrates will be covered with a layer of $Al(OH)_3$ after chemical etching with NaOH. Evidently, the appearance of the –OH peak in the IR spectrum (Figure 4.2 (a1)) of the NaOH etched aluminum alloy substrate is in good agreement with the chemical reactions.

It was observed from the IR spectra of Figure 4.2(a) that the intensity of the –OH peak increased with the time of SA passivation. The formation of aluminum stearate (AlSA) ($CH_3(CH_2)_{16}COOAl(OH)_2$) (in Equation 4.6) as a reaction product between $Al(OH)_3$, present on the aluminum alloy substrates after NaOH etching, and SA was what led to the enhancement of the –OH peak after SA passivation (Figure 4.2(a2-a5)). The schematic illustration of the formation of AlSA on NaOH etched aluminum alloy substrates, engrafted with $Al(OH)_3$, is shown in Figure 4.3.

$$Al(OH)_3 + CH_3(CH_2)_{16}COOH \rightarrow CH_3(CH_2)_{16}COOAl(OH)_2 + H_2O \quad \text{(Equation 4. 6)}$$

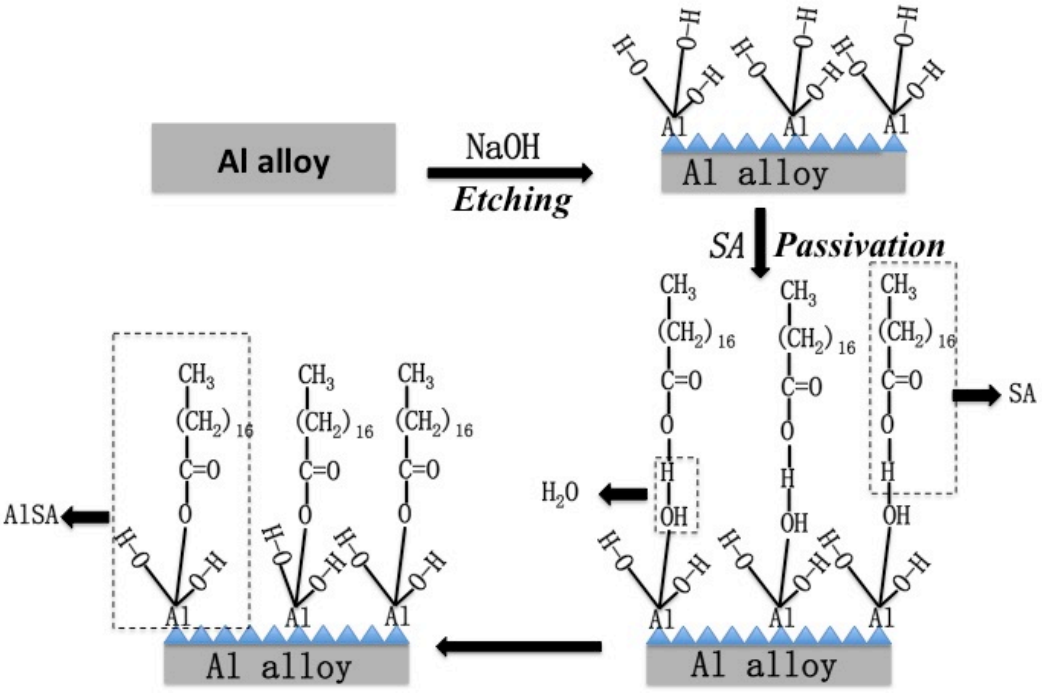

Figure 4. 3 Schematic illustration of the formation of the superhydrophobic surface prepared by SA passivation on NaOH etched aluminum alloy substrate.

It should be mentioned that, the appearance of –OH bonding on the NaOH etched aluminum alloy substrate is responsible for the formation of a superhydrophobic aluminum alloy substrate. However, the as-received aluminum alloy substrate without –OH bonding was unable to be passivated by SA solution, where it shows a maximum CA of 110 ± 1°

Furthermore, the peaks at 414, 536 and 607 cm^{-1} in zone (iv) may have appeared due to the Al-O bonding. The peaks at 1582 cm^{-1} in zone (iii) as well as 750 cm^{-1} in zone (iv) have also been assigned to the bending absorption mode of –OH, and the intensity of the peaks was also found to increase with the SA passivation time. The increasing intensity of the –OH peak as well as $–CH_2$ bonding with increasing passivation time indicate that greater AlSA formation took place, or, in other words, more amounts of SA molecules were adsorbed on the NaOH etched aluminum alloy substrates during the passivation process. Furthermore, in zone (iii), the infrared absorption peaks at 1586 and 1466 cm^{-1} were arising from –COOAl bonding; these peaks are more distinct on the IR spectrum of the samples passivated for 24 min (Figure 4.2(a5)). This is also in line with the analysis from SEM images (Figure 4.1(c-e)), where an increasing SA passivation time led to a thicker deposition of flake-like micro-nanostructures.

Compared with the –COOZn bonding at 1550 cm^{-1} presented in our recent publication on the superhydrophobic aluminum alloy substrate by SA-functionalized ZnO nanoparticles [32], the –COOAl bonding has shifted towards higher a wavenumber of 1586

cm^{-1} due to the lower atomic number of Al compared to that of Zn.

In addition, the two main sharp absorption peaks in zone (ii), which appeared at 2917 and 2851 cm^{-1}, are ascribed to the asymmetric, symmetric C-H stretching modes, respectively, of $–CH_2$ groups on the AlSA molecules. Additionally, a very small peak at 2956 cm^{-1} was present in the spectrum due to the asymmetric in-plane C-H stretching mode of the $–CH_3$ group on the AlSA molecules.

The presences of absorption bands from –OH, –COOAl, $-CH_2$ as well as $–CH_3$ confirmed the engrafting process of SA on NaOH etched aluminum alloy substrates, as modeled in Figure 4.3. The model illustrates how hydrophilic components, such as –COO and –OH, bonding with the aluminum alloy substrates kept the hydrophobic components, such as $–CH_2$ and $–CH_3$, away from the surface, which effectively reduced the surface energy; hence, they are responsible for the superhydrophobic properties. In our previous study, $-CH_2$, $-CH_3$ and –COO absorption peaks were also observed in the spectrum of superhydrophobic copper surfaces fabricated by one-step electrochemical modification [30]. It should be mentioned that unlike copper stearate (CuSA), which does not have any –OH

bonds [13], AlSA has two –OH bonds [34].

Because the intensity of the IR absorption peak of a molecule is proportional to its quantity, the peak area of $–CH_2$ peak was monitored with the SA passivation time. It was observed that the intensity of the $–CH_2$ peak of the passivated SA molecules increased with increasing SA passivation time, as shown in Figure 4.2(a2-a5). Figure 4.2(b) depicts the variation of the peak areas of the $–CH_2$ and $–CH_3$ peaks as a function of the SA passivation time. Initially, a fast and almost linear increase in the peak area was observed. The peak area was calculated to be 216 for the sample with 5 s-SA passivation; the peak area increased to 388 for the sample with 1 min-passivation; the peak area further increased to 886 for the sample with 24 min-SA passivation. Further increase of the peak area to 1115 was also observed for the sample with 60 min-passivation. These observations are consistent with the morphological analysis by SEM, where an increase in the SA passivation time led to an increase in the density and thickness of AlSA flake-like micro-nanostructures.

Both XRD and XPS have been carried out to complement the observation of

FTIR and validate the model on the formation of aluminum stearate. Figure 4.4 shows the low angle XRD between 2-12° and high angle XRD between 12-70° for both NaOH etched aluminum alloy substrate and SA passivated NaOH etched aluminum alloy substrates.

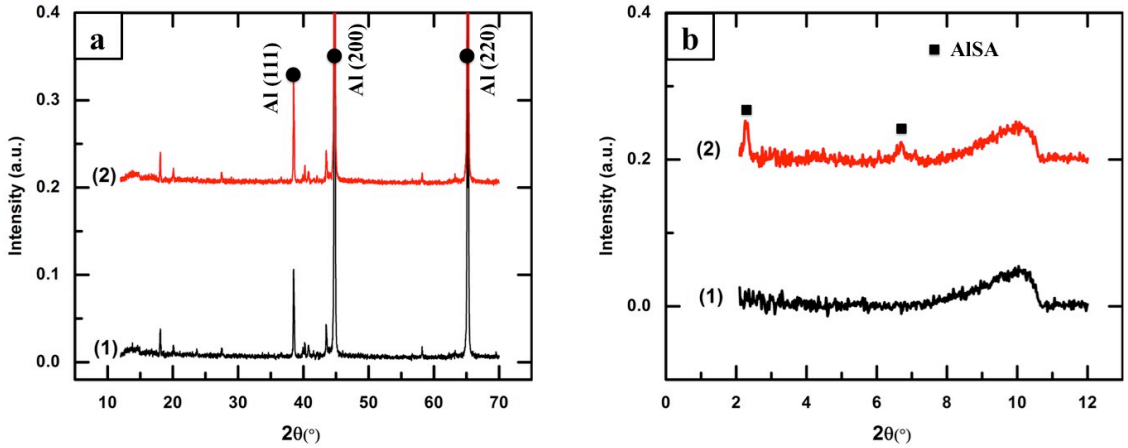

Figure 4. 4 X-ray diffraction (XRD) patterns of (1) chemical etched aluminum alloy substrate and (2) stearic acid (SA) passivation on NaOH etched aluminum alloy substrate in the 2θ range of (a) 12-70° and (b) 2-12°. (Aluminum stearate is abbreviated as AlSA).

The X-ray diffraction (XRD) patterns of (1) chemical etched aluminum alloy substrate and (2) stearic acid (SA) passivation on NaOH etched aluminum alloy substrate are presented in Figure 4.4. As evident from the patterns at higher 2θ range of 12-70° in Figure 4.4(a), the characteristic peaks of Al (111), Al (200) and Al (220) at 38.47°, 44.72°

and 65.1°, respectively, come from as-received aluminum alloy substrate. Furthermore, two weak peaks in the low 2θ of 2.26° and 6.68° are found in Figure 4.4(b), which is in good agreement with the characteristic peak of aluminum stearate (AlSA). It is also complementary with the FTIR spectra of the SA-passivated NaOH etched aluminum alloy substrate, where the formation of aluminum stearate (AlSA) is discussed.

Figure 4.5(a) shows the survey spectrum of the SA passivated NaOH etched aluminum alloy substrate. Two strong peaks of C 1s and O 1s are accompanied with a small peak of Al 2p. The Figure 4.5(b) shows the high resolution peak of C 1s that composed of a strong peak at 285 eV corresponds to C-C or C-H bonds and a tiny peak at 288.6 eV due to the –COO peak due to the formation of aluminum stearate. The ratio of the peaks area of –COO and C-C is found to be the 0.06 which is the finger print on the engrafting of stearic acid on a metal surface. Similar observations are reported on interaction of stearic acid with zinc [35,36]. Figure 4.5(c) shows the O 1s peak that composed to two peaks having binding energy 530.2 eV and 531.9 eV corresponds to the bonding of Al-O and Al-OH [36].

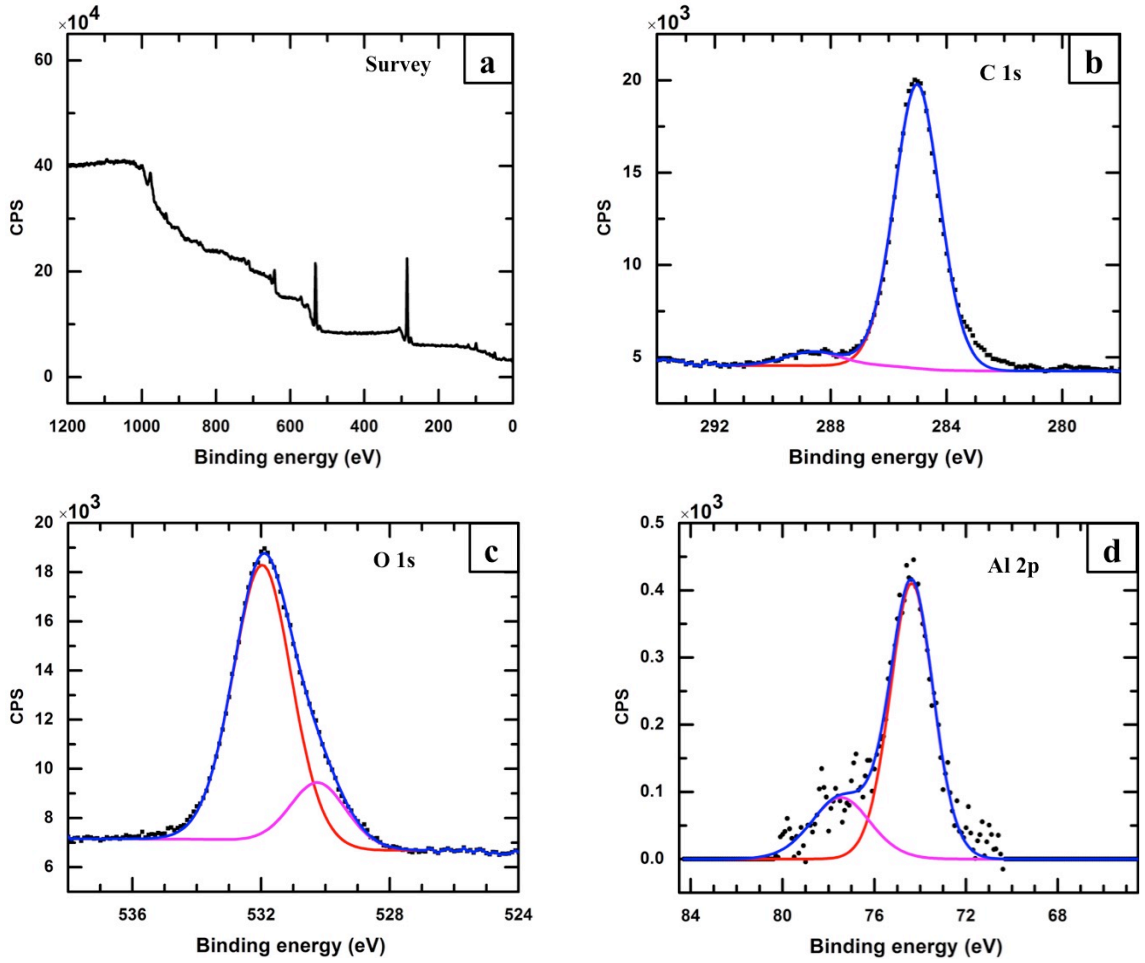

Figure 4. 5(a) shows the survey spectrum of the SA passivated NaOH etched aluminum alloy substrates (a) survey, (b) C 1s, (c) O 1s, (d) Al 2p.

Figure 5(d) shows the Al 2p has two distinct peaks at 74.4 eV and 77.5 eV due to the bonding of Al-O and Al-OH [37]. The high resolution XPS analysis on the C 1s, O 1s and Al 2p confirm the presence of –COO, C-H (or C-C) as well as Al-O and Al-OH as found by FTIR in Figure 4.2 and proposed in the model in Figure 4.3.

Figure 4.6(a-c) depict the variation of surface rms roughness, CA and CAH as a function of SA passivation time on the NaOH etched aluminum alloy substrates. The substrate has a surface rms roughness of 1.38 ± 0.17 μm and a CA of 34 ± 4°. The surface rms roughness and CA of the 5 s-SA passivated NaOH etched aluminum alloy substrate increased to 2.23 ± 0.18 μm and 145 ± 2°, respectively, due to the formation of flake-like micro-nanostructures of AlSA. The transition from a hydrophilic surface, i.e., the NaOH etched aluminum alloy substrate, to superhydrophobic surfaces occurred at the 1 min-SA passivation time mark, with a surface rms roughness of 2.29 ± 0.2 μm, a CA of 154 ± 2° and a CAH of 1.88 ± 0.4°. The appearance of surface superhydrophobicity was due to the formation of low surface energy AlSA, evident from the FTIR spectra in Figure 4.2(a), as well as the presence of a micro-nanorough flake-like morphology, evident from the SEM images in Figure 4.1(d). The surface rms roughness remained constant from 1 min- to 24 min-SA passivation time but there was a slight tendency towards reduced roughness for SA passivation longer than 24 min. This reduction might be an indicator of the compactness of the passivated AlSA formation on the NaOH etched aluminum alloy

substrates. On the other hand, the CA and CAH of the surfaces prepared by SA passivation were observed to remain constant with SA passivation times between 1 min to 60 min. The CA variation with SA passivation time has been reported in the literature [17,38]. Ruan *et al.* prepared a superhydrophobic aluminum alloy substrate via chemical etching with HCl/HF solution followed by passivation with a different fatty acid. An optimum modified time of 1.5 h on the etched aluminum alloy substrate (with a CA of 167.6°) was observed by using lauric acid as the modifier, and the CA reduced to 155.2° for 2 h passivation [17]. The authors mentioned that the appearance of the optimum CA might have resulted from the change of surface morphology and microstructure due to different etching and modification parameters. However, the change of the surface morphology or the chemical composition with passivation time in their study was not investigated as performed here using SEM and FTIR. In the study by Kim *et al.*, a superhydrophobic substrate with a CA of 153° was produced by using a reactive ion etching process combined with hydrophobic coatings with PTFE [38]. The variation of the morphology with PTFE passivation time was found to contribute to the variation of the

CA. However, the chemical composition, one of the most important factors in superhydrophobicity, was not analyzed in their study. In the literature, NaOH as an etchant has been utilized to prepare superhydrophobic aluminum alloy substrates utilizing both one- and two-step processes [6,21,39].

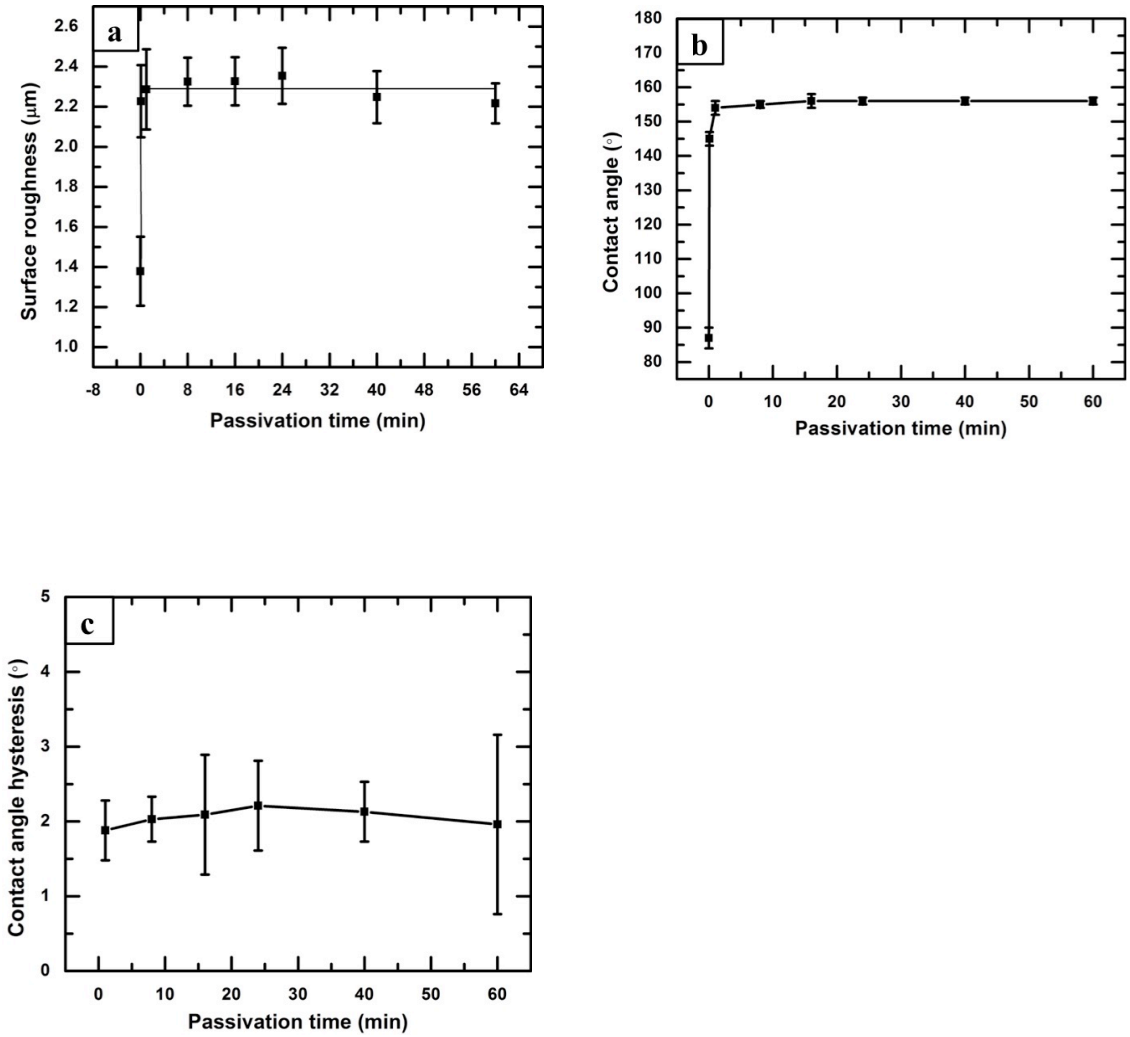

Figure 4. 6(a) Surface root-mean-square (rms) roughness; (b) CA and (c) CAH variation as a function of SA passivation time on NaOH etched aluminum alloy substrates.

We have recently reported the formation of superhydrophobic aluminum alloys substrates, fabricated by electrodeposition of copper on aluminum alloy substrates followed by electrochemical modification using SA organic molecules, which provided similar CA [15]. Furthermore, Sarkar *et al.* (including one of the current authors) also studied superhydrophobic properties of ultrathin rf-sputtered Teflon films coated HCl etched aluminum alloy substrates [14]; the authors reported the effect of the etching time on the aluminum alloy substrates. A maximum CA of 164 ± 3° was observed on the ultrathin rf-sputtered Teflon coated aluminum substrates that were HCl etched for 2.5 min. Another study in our group fabricated superhydrophobic aluminum alloy substrates by monodispersive silica nanoparticles spin coating [40].

4.4 Corrosion resistance property of superhydrophobic surfaces by chemical etching process

Figure 4.7(a) shows the potentiodynamic polarization curves of the as-received aluminum alloy substrate, NaOH etched aluminum alloy substrate, and 5 s-, 1 min-, and 24 min-SA passivated NaOH etched aluminum alloy substrates. I_{corr} was calculated from

the extrapolation of the cathodic curves [41]. R_p was calculated by the Stern-Geary equation, given by

$$R_p = \frac{\beta_a \beta_c}{2.3 I_{corr}(\beta_a + \beta_c)} \quad \text{(Equation 4. 7)}$$

where β_a and β_c are the anodic and cathodic Tafel slopes, respectively.

The I_{corr} and R_p of as-received aluminum alloy substrate were found to be 2.89 ± 0.8 μA/cm^2 and 3.79 kΩ·cm^2, respectively. The NaOH etched aluminum alloy substrate exhibited a larger I_{corr} of 16.29 ± 2.8 μA/cm^2 as well as a smaller R_p of only 2.24 kΩ·cm^2. This could be explained by the increase of surface area as well as the loss of the protective oxide layer during the chemical etching process. This is consistent with the existing literatures, where it has been shown that the increase of surface roughness leads to similar trends in I_{corr} and R_p [42-44]. For example, in the study by Walter *et al.* [43], different surface roughness of AZ91 magnesium alloy, were obtained by polishing with different grits of silicon carbide (SiC) and 3 μm diamond paste, measured using atomic force microscopy (AFM). Consequently, it was observed that the I_{corr} of the AZ91 alloy in

potentiodynamic polarization tests increased from 2.19 μA/cm^2 to 6.92 μA/cm^2 with an increase in the surface roughness from 0.08 μm to 0.43 μm.

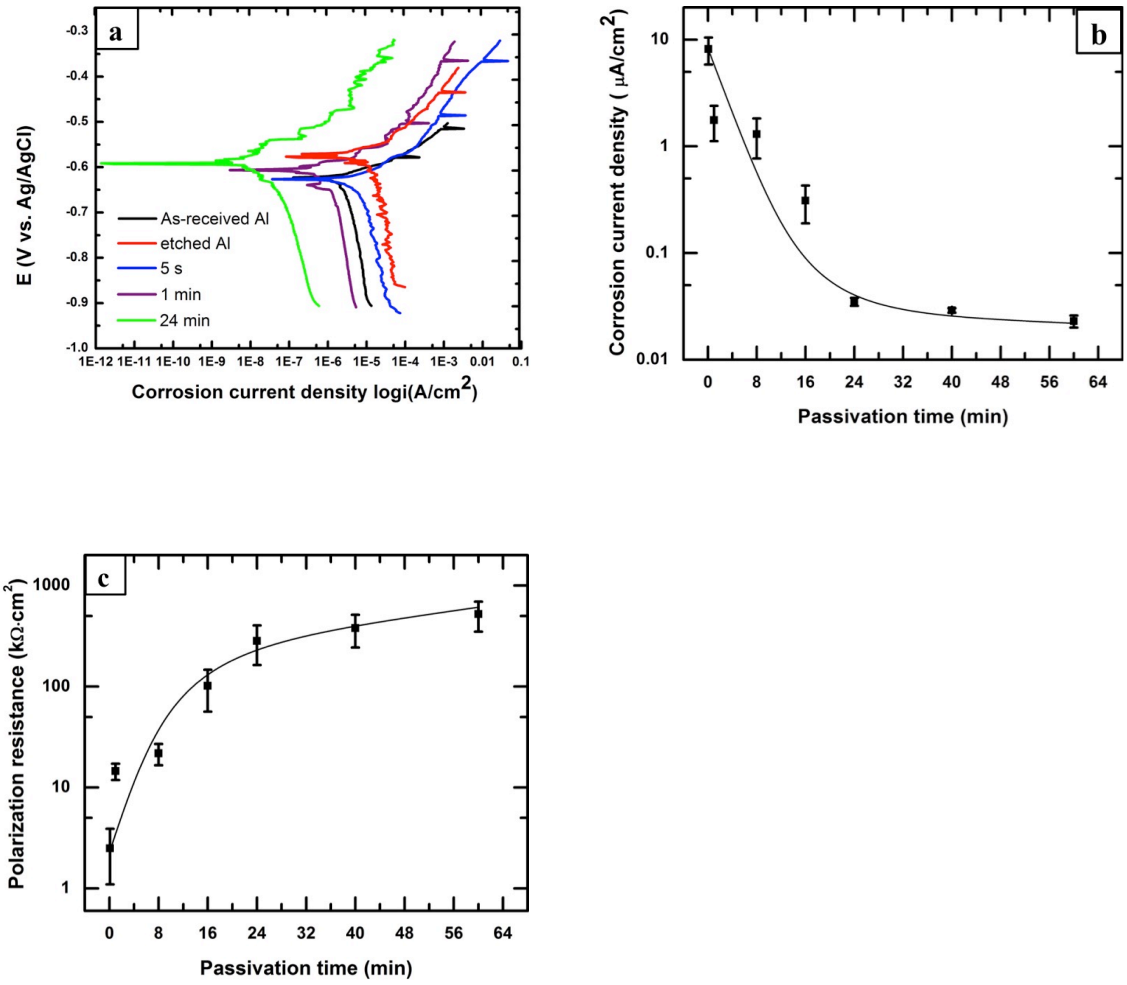

Figure 4. 7(a) Potentiodynamic polarization curves of as-received aluminum alloy substrate, NaOH etched aluminum alloy substrate, and 5 s-, 1 min-, and 24 min-SA passivated etched aluminum alloy substrates. Variation of (b) I_{corr} and (c) R_p as a function of the SA passivation time on NaOH etched aluminum alloy substrates.

Table 4. 1 CA and CAH values and their respective I_{corr} and R_p values calculated by the Stern-Geary equation, as extracted from Figures 4.6 and 4.7 for SA passivation on NaOH etched aluminum alloy substrates for a range of passivation times.

Sample condition/SA passivation time	Contact angle CA (°)	Contact angle hysteresis CAH (°)	Corrosion current density I_{corr} ($\mu A/cm^2$)	Polarization resistance R_p ($k\Omega \cdot cm^2$)
As-received Al	87 ± 3	-	2.89 ± 0.8	3.79 ± 1.8
Etched Al	34 ± 4	-	16.29 ± 2.8	2.24 ± 0.98
5 s	145 ± 2	-	8.16 ± 2.3	2.50 ± 1.4
1 min	154 ± 2	1.88 ± 0.4	1.76 ± 0.64	14.53 ± 2.72
8 min	155 ± 1	2.03 ± 0.3	1.30 ± 0.53	21.83 ± 5.16
16 min	156 ± 2	2.09 ± 0.8	0.31 ± 0.12	101.59 ± 45
24 min	156 ± 1	2.21 ± 0.6	0.035 ± 0.003	283.28 ± 120
60 min	156 ± 1	1.96 ± 1.2	0.023 ± 0.003	521.59 ± 171

In our case, the hydrophobic aluminum alloy substrate, prepared by 5 s-SA passivation on a NaOH etched aluminum alloy substrate, exhibited a lower value of I_{corr} of 8.16 ± 2.3 μA/cm^2 and a higher R_p of 2.5 kΩ·cm^2 compared with the aluminum alloy substrate treated with only NaOH etching, implying that the hydrophobic substrate inhibits corrosion of the substrate. However, these results are still inferior to that of the as-received aluminum alloy substrate, indicating that the hydrophobic surface having a water CA of 145 ± 2° is not resistant enough to prevent chemical attack from a corrosive environment.

However, both the anodic and cathodic current densities of superhydrophobic substrates, prepared with SA passivation longer than 1 min on NaOH etched alloy substrates, were significantly reduced, as observed in Figure 4.7(a). This reduction is due to a restricted supply of oxygen, as well as due to water-limiting oxygen and water reduction [45]. It is generally believed that the air trapped on the superhydrophobic surfaces behave as a dielectric for a parallel plate capacitor, which inhibits the electron transfer between the aluminum alloy substrate and the electrolyte and hence protects the substrate.

The reduction in anodic current density of the superhydrophobic aluminum alloy substrates indicated that the anodic dissolution process was inhibited or postponed compared with the as-received aluminum alloy substrate [46]. Table 4.1 and Figure 4.7(b-c) show the variation of I_{corr} and R_p of the prepared samples. It should be mentioned that the 1 min-passivated NaOH etched aluminum alloy substrate, exhibiting a CA of 154 ± 2°, had a much lower I_{corr} of 1.76 ± 0.64 μA/cm^2 and a higher R_p of 14.53 kΩ·cm^2 compared with the as-received aluminum alloy substrate. With increasing SA passivation time up to 8 min and 16 min, I_{corr} values of the superhydrophobic aluminum alloy substrates reduced to 1.3 ± 0.53 μA/cm^2 and 0.31 ± 0.12 μA/cm^2, and R_p values increased to 21.83 kΩ·cm^2 and 101.59 kΩ·cm^2, respectively. The I_{corr} further decreased notably to 0.035 ± 0.003 μA/cm^2 and R_p increased to 283.28 kΩ·cm^2 for 24 min-SA passivation on NaOH etched aluminum alloy substrate. The R_p was found to increase as high as 521.59 kΩ·cm^2 after 60 min-SA passivation. It can be concluded that the I_{corr} value for the superhydrophobic aluminum alloy substrates were much lower than that of the as-received sample, and I_{corr} was found to decrease gradually with the increase of SA

passivation time; on the other hand, the R_p values increased with the extended SA passivation time. Both the reduced I_{corr} and the enhanced R_p indicate that preparation by chemical etching followed by SA passivation process is effective for improving the corrosion resistance properties. It has been further shown that the corrosion inhibition of superhydrophobic surfaces by longer SA passivation times is superior to that of shorter passivation times.

It was observed that the corrosion potential (E_{corr}) increased as a function of the SA passivation time, from -0.627 V for 5 s-SA passivation to -0.578 V for 60 min-passivation on NaOH etched aluminum alloy substrates. This also suggests increasing corrosion resistance of the samples with extended passivation time. The more positive E_{corr} indicated that the surface could better prevent corrosion owing to the increasing density of AlSA molecules formed on the etched aluminum alloy substrates. Brassard *et al.* [31] has discussed the variation of E_{corr} on different Zn coated steel substrates followed by passivation with RTV-silicone and showed that superhydrophobic surfaces had higher E_{corr} compared to as-received aluminum alloy substrates. In our case,

however, the E_{corr} increased with an increasing number density of AlSA molecules, that is, the E_{corr} still increased even when the CA remained constant on the superhydrophobic substrates prepared by different SA passivation times on the NaOH etched aluminum alloy substrates.

In the present study, another method was applied for calculating R_p, namely from the slope of the linear potential-current (E-I) curves by varying the potential ±10 mV around the corrosion potential (E_{corr}) and using Ohm's law (as shown in Figure 4.8(a))

$$R_P = \frac{\Delta E}{\Delta I} \qquad \text{(Equation 4. 8)}$$

where E and I are the potential and current, respectively.

The R_p calculated by Ohm's law (R_p1) values versus the R_p calculated by Stern-Geary equation (R_p2) values are plotted in Figure 4.8(b). As can be observed, there is excellent agreement between the R_p values calculated by the two methods. Furthermore, to evaluate the difference between R_p1 and R_p2, the relative error between them can be expressed as follows:

$$\text{Relative error} = \left|\frac{R_P2 - R_P1}{R_P2}\right| \times 100\% \qquad \text{(Equation 4. 9)}$$

According to the calculation, the relative error associated with corresponding R_p1 and R_p2 values is in the range of 10-20%, which indicates a good agreement between the R_p calculated by both Ohm's law and the Stern-Geary equation. The presence of small differences between the R_p values may be due to the differences in the Tafel slopes (β_a and β_c) and the slope of $\Delta E/\Delta I$ chosen in the analysis of the polarization curves. In this article (as well as in Table 4.1), the presented R_p was calculated using Stern-Geary equation (Equation 4.7).

The corrosion inhibition mechanism of superhydrophobic substrates by NaOH etching and SA passivation is similar to that in our previous study on the corrosion properties of superhydrophobic copper surfaces [30]. In that study, the superhydrophobic copper surfaces, fabricated by one-step electrochemical modification in an ethanolic SA solution, demonstrated improved corrosion resistance properties with increasing electrochemical modification time. In the present study, the corrosion properties of the

etched and passivated substrates are significantly improved compared to the as-received substrate. The presence of the superhydrophobic AlSA flake-like morphology on the aluminum alloy substrate acted as a physical barrier to retard electrolyte penetration, as demonstrated by the gradual reduction of I_{corr} as well as enhanced R_p for longer SA passivation times. The corrosion test performed by Saleema *et al.* on a superhydrophobic aluminum alloy substrate prepared by a one-step process using a mixture of NaOH and FAS-17 solution did not provide any polarization data [6]; however, the superhydrophobic substrates formed corrosion pits after the polarization experiment. In the published literature, polarization curves have been widely used to analyze the corrosion resistance of superhydrophobic substrates; however, the R_p of superhydrophobic substrates compared with those of the as-received substrates were not presented in these studies [3,47-49]. On the other hand, superhydrophobic coatings have been fabricated using myristic acid with cerium chloride solution on copper substrates [50]. In this study, polarization curves were presented to quantify the corrosion properties of Ce deposited superhydrophobic coatings, which had better corrosion resistance than the bare copper

substrate. As the authors did not present the R_p of their coatings, we have used their values for β_a, β_c and I_{corr} to calculate the R_p of superhydrophobic Ce coatings in NaCl solution (3.5 wt.%) using the Stern-Geary equation (Equation 4.7): the calculated value of R_p was found to be 7.81 $k\Omega \cdot cm^2$. This calculated R_p value of for the Ce coated superhydrophobic copper substrate is much less than those for our fabricated superhydrophobic substrates. Evidently, the R_p value of our superhydrophobic substrate prepared by 60 min-SA passivation after NaOH etching is 66 times more than that of the superhydrophobic copper substrate with Ce coating.

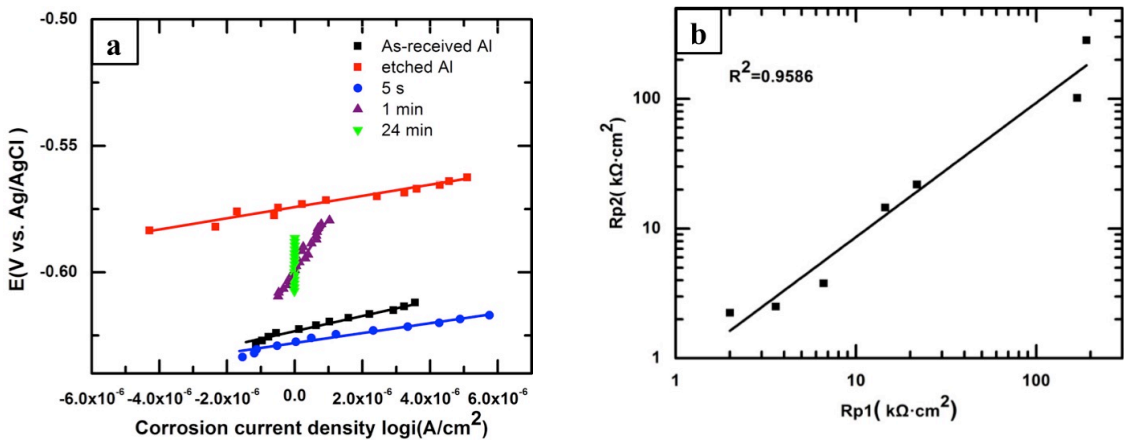

Figure 4. 8(a) Potential-current (E-I) curves from varying the potential ±10 mV around the corrosion potential (*Ecorr*) for calculating *Rp* by Ohm's law; (b) Correlation between *Rp* calculated by (i) Ohm's law (*Rp*1) and (ii) the Stern-Geary equation (*Rp*2). R2 quantifies a measure of the goodness-of-fit of the linear regression.

Figure 4.9 shows the morphological and chemical composition changes of the hydrophobic substrates prepared by 5 s-SA passivation and of superhydrophobic substrate that was prepared by 24 min-SA passivation after corrosion tests. Compared with the image of the hydrophobic substrate before corrosion testing, (Figure 4.9(a)), the SEM image of hydrophobic aluminum alloy substrate after corrosion testing clearly indicates the formation of corrosion pits as marked by arrows in Figure 4.9(c); additionally, the CA was found to decrease from 145 ± 2° to 124 ± 6° after the corrosion

test. The intensities of the $–CH_2$, $-CH_3$ and -COO peaks in the FTIR spectrum of the hydrophobic substrate after corrosion were found to clearly decrease, as shown in the inset of Figure 4.9(e). However, the surface morphology of superhydrophobic substrate remained the same before and after the corrosion test, as shown in Figure 4.9(b, d)). Furthermore, no discernible variation in the intensities of the $–CH_2$, $-CH_3$ and -COO peaks in the FTIR spectrum of the superhydrophobic substrate were found before and after the corrosion test, as shown in Figure 4.9(f)). The inset images of water drops also indicate the wetting properties remained the same. These results are consistent with those from the polarization curves, which indicated that the superhydrophobic aluminum alloy substrates had superior corrosion resistance as compared with both the as-received and hydrophobic aluminum alloy substrates.

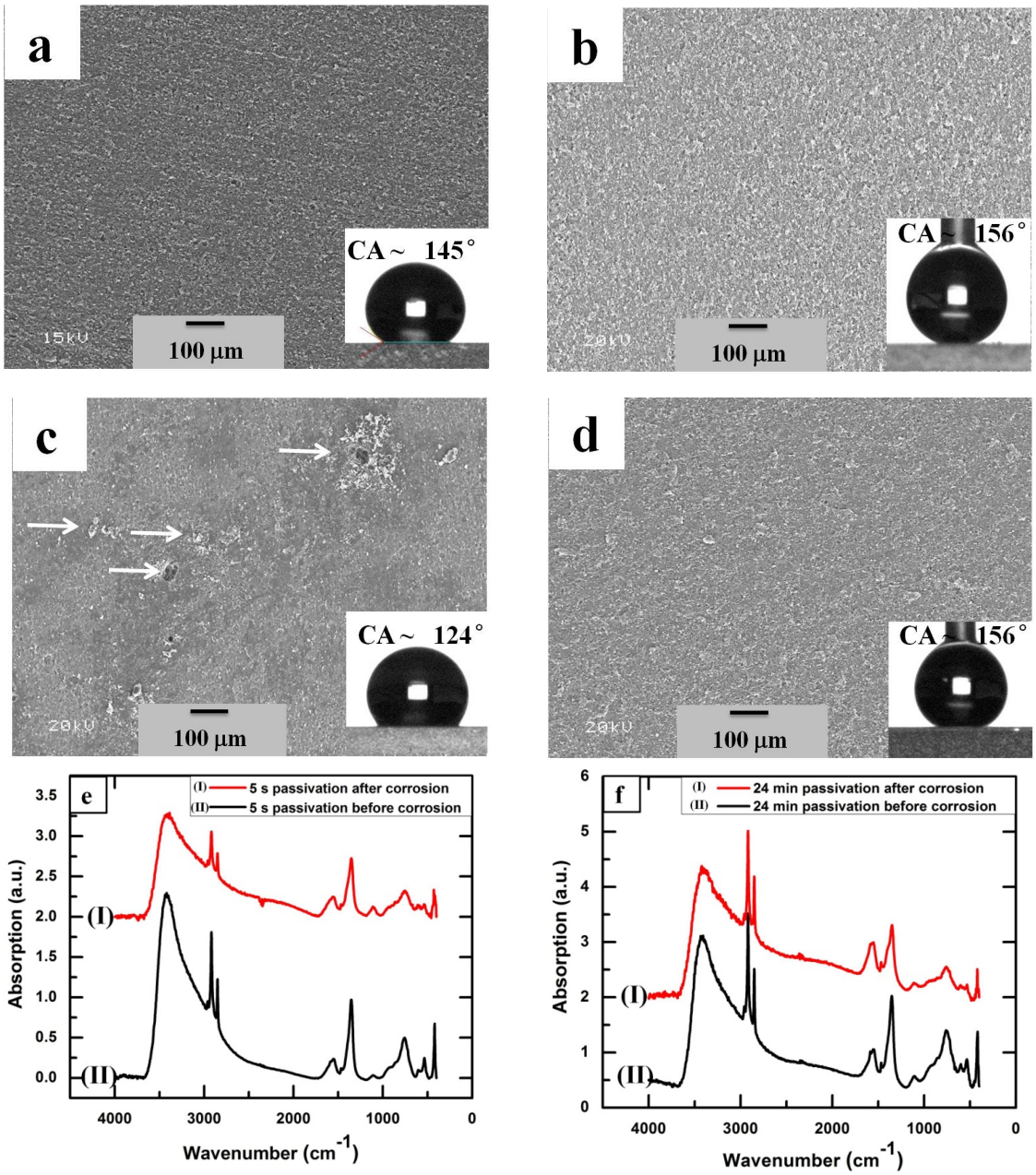

Figure 4. 9 SEM images of the surfaces of the (a) 5 s- and (b) 24 min-passivated NaOH etched aluminum alloy substrates before corrosion, and (c-d) the surfaces after corrosion testing, respectively. The inset images show the water drops on the corresponding surfaces. Figure 4.9(e-f) shows FTIR spectra of the 5 s- and 24 min-passivated NaOH etched aluminum alloy substrates before (I) and after (II) corrosion, respectively.

As mentioned before, in the study by Saleema *et al.* on the corrosion resistance property of superhydrophobic aluminum substrates prepared by chemical etching [6], a poor corrosion resistance was observed in the superhydrophobic substrates, where a number of pits formed after corrosion testing. Several other studies have also reported on the corrosion resistance properties of superhydrophobic substrates [51-53]; however, until the current study, other works have not reported on the variations in morphological, compositional and wetting properties of superhydrophobic substrates.

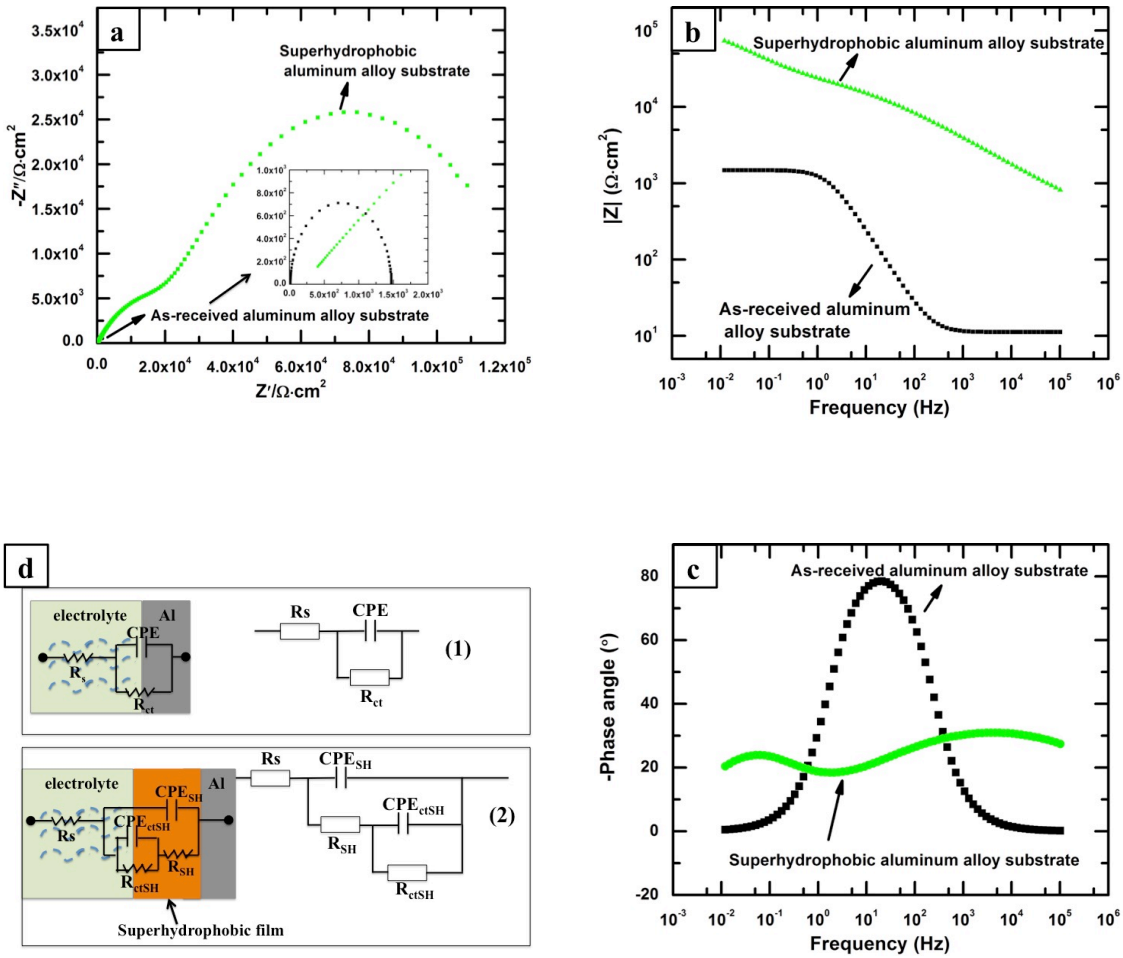

Figure 4. 10(a) Nyquist plots, (b) Bode modulus diagrams and (c) Bode phase angle diagrams of as-received aluminum alloy substrate and superhydrophobic aluminum alloy substrate. (d) Electrical equivalent circuits for EIS of (d1) as-received aluminum alloy substrate and (d2) superhydrophobic aluminum alloy substrate. The insets image in (a) shows the enlargement of the high frequency region of the plots.

An attempt has been made to evaluate the corrosion resistance of superhydrophobic surfaces using electrochemical impedance spectroscopy (EIS) as a complementary tool to

polarization resistance. EIS was performed after immersing the samples in a salt solution for approximately 10 hr. The EIS data have been analyzed in light of the analysis presented on the superhydrophobic surfaces prepared on aluminum alloy substrates by Liu *et al.* [29] and Liang *et al.* [27]. Figure 4.10 shows the Nyquist and Bode plots as well as the equivalent electrical circuits for the EIS data from the as-received aluminum alloy substrate and the superhydrophobic aluminum alloy substrate prepared by 24 min-SA passivation. The graphs were plotted from the fitted data based on the equivalent electrical circuit (see the supporting information for both original and fitted EIS plots). Specifically, Figure 4.10(a) shows the Nyquist plots, which present the real component of impedance (Z_{real} or Z') versus the imaginary component ($Z_{imaginary}$ or Z'') on a linear scale. Additionally, Figure 4.10 shows the Bode plots, (b) modulus of impedance (|Z|) vs. frequency and (c) phase angle vs. frequency. The diameter of the semicircle in the Nyquist plot signifies the charge transfer resistance (R_{ct}) of the double layer formed at the interface between the sample surface and the corrosive medium. The semicircle diameter of the Nyquist plot of the as-received aluminum alloy substrate was found to be 1.46

$k\Omega \cdot cm^2$ and is presented as an inset in Figure 4.10(a). On the other hand, two semicircles were observed on the Nyquist plot of the superhydrophobic aluminum alloy substrate, as shown in Figure 4.10(a). Among them, the smaller semicircle with a diameter of 29 $k\Omega \cdot cm^2$ at higher frequency (close to the coordinate origin) represents the resistance of the superhydrophobic thin films (R_{SH}), and the second large semicircle with a diameter of 95 $k\Omega \cdot cm^2$ represents charge transfer resistance (R_{ctSH}) of the double layer at the interface between the superhydrophobic surface and the salt solution. The large value of impedance of the superhydrophobic film compared to the as-received aluminum alloy surfaces shows that the superhydrophobic surfaces are more resistant against corrosion.

The top of Figure 4.10(b) shows the Bode plot of the superhydrophobic substrate, and bottom portion shows the Bode plot of the as-received aluminum alloy substrate. As observed in the bottom part of Figure 4.10(b), the as-received aluminum alloy substrate had a |Z| value of only 11.6 $\Omega \cdot cm^2$ at the high frequency of 10^4 Hz, in good agreement with the results presented by Liu *et al.* [29] and Liang *et al.* [27]. However, the superhydrophobic substrate exhibited a |Z| value of 1.74 $k\Omega \cdot cm^2$, which is nearly 150

times larger than that of the as-received aluminum alloy substrate at the same frequency. Similarly, at the low frequency of 0.01 Hz, the |Z| value of the as-received aluminum alloy substrate was found to be 1.06 $k\Omega \cdot cm^2$. In contrast, it was as high as 73.4 $k\Omega \cdot cm^2$ on the superhydrophobic aluminum alloy substrate. In general, AC impedance at high frequencies is the response of coatings with the solution and, at low frequency, reflects R_{ct} and the double-layer capacitance [54]. It is well known that the larger value of |Z| in the low frequency region signifies a better barrier in the thin film [52]. Therefore, according to the analysis of the Bode plots, the superhydrophobic substrate was found to have better corrosion resistance as compared with the as-received aluminum alloy substrate. It agrees well with the results from the polarization experiments, where R_p of the superhydrophobic surface was larger than that of the as-received aluminum alloy substrate, as shown in Table 4.1. This is comparable to the study by Liu *et al*. [29], where it was concluded, based on results from Bode plots, that the corrosion resistance of the graphene coated aluminum alloy was an order of magnitude higher than that of the uncoated aluminum alloy substrate. In the present study, compared with the as-received

substrate, the corrosion resistance of the superhydrophobic aluminum alloy substrate was close to two orders of magnitude higher at low frequencies. This indicates that our superhydrophobic aluminum alloy substrate has better corrosion resistance than the graphene coated substrate [29]. This difference may be due to differences in the physical properties of graphene, in the case of Liu *et al*., and aluminum stearate, in the current case.

Recently, Liang *et al*. fabricated silica-based superhydrophobic coatings on aluminum alloy substrates and performed EIS analysis [27]. In their work, the |Z| at 10 kHz of the superhydrophobic aluminum alloy substrate with a silica-based film, immersed for 30 minute in a salt solution, was reported to be 100 $\Omega \cdot cm^2$; the |Z| of the same sample was reported to be 2.5 $\Omega \cdot cm^2$ after increasing the immersion time to 24 hr. This reported |Z| value is even lower than those of their as-received aluminum alloy substrates. While comparing the impedance at 0.01 Hz, the |Z| value of the 30 min-immersed silica-based film coated superhydrophobic samples was reported to be 560 $k\Omega \cdot cm^2$, which further reduced to 16 $k\Omega \cdot cm^2$ after 8 hr of immersion. This value is very similar to that from our

observations.

The Bode phase plot of the superhydrophobic substrate exhibits the two time constants, as shown in Figure 4.10(c). At the frequency of 25 Hz, the phase angle of the as-received aluminum alloy substrate arrived at the maximum value of 78°. However, the phase angle of the superhydrophobic surface exhibited the minimum value of 18.4° at a similar frequency. It is comparable with the study of Liu *et al*., where two time constants were observed on the superhydrophobic aluminum alloy substrate fabricated by graphene spin coating [29]. The authors observed that the maximum phase angle value for the AA2024 aluminum alloy substrate was 75° and the lowest phase angle value of for the sample with the superhydrophobic graphene coating was 40° at the same frequency. It is well known that phase angle (ϕ) is defined by the expression in Equation 4.10.

$$\varphi = arctan(\frac{|Z_{imaginary}|}{|Z_{real}|}) \qquad \text{(Equation 4. 10)}$$

Thus, a smaller phase angle indicates a larger value of Z_{real} (or Z'), which

corresponds to a large diameter in the Nyquist plot. In the current results from the Bode plots, the obtained phase angle of 18.4° for the superhydrophobic substrate is much smaller than that of 40° as reported by Liu et al., suggesting our superhydrophobic surface has better corrosion resistance than samples from the latter.

Figure 4.10(d1) shows the equivalent electrical circuit of the as-received aluminum alloy surface in reaction with the salt solution, as modeled by EIS. In this circuit, R_s is the resistance of the solution; R_{ct} and *CPE* are the charge transfer resistance and the constant phase element associated with the double layer formed at the interface between the aluminum surface and salt solution, respectively. In the case of superhydrophobic coatings on the aluminum surface, an extra resistance R_{SH} and constant phase element CPE_{SH} have been included in the circuit due to the dielectric nature of the superhydrophobic coating. As the interaction of the salt with the superhydrophobic surface will be different compared to that with untreated aluminum, the charge transfer resistance and constant phase element associated with the double layer at the interface have been presented by R_{ctSH} and CPE_{ctSH}. The assumption of this model is well supported

by the observation of two time constants in the Bode plot.

Finally, the mechanical properties of the superhydrophobic substrate are very important for its uses against surface erosion, friction and corrosion [30]. The adhesion strength of all surfaces prepared by SA passivation after NaOH etching was found to be 5B, tested according to the ASTM D3359 standard.

4.5 Summary

Chemical etching of aluminum alloy substrates by NaOH followed by stearic acid (SA) passivation was used to prepare superhydrophobic aluminum alloy surfaces, and their corrosion resistance properties were investigated. The SA passivation process produces flake-like aluminum stearate micro-nanostructures on NaOH etched aluminum alloy substrates. The number density of these flake-like structures is observed to increase with the extension of SA passivation time. Investigations into the wetting properties of these surfaces demonstrated water contact angles of more than 150° after 1 min of SA passivation, which remained constant to 60 min of passivation time. However, the polarization resistance determined from polarization curves increases gradually from 3.79

to 521.59 $k\Omega \cdot cm^2$ for the as-received aluminum alloy substrates and the superhydrophobic surface prepared SA passivation for 60 min, respectively. Electrochemical impedance spectroscopy (EIS) shows that the moduli of impedance |Z| at lower frequencies for the as-received aluminum substrate and superhydrophobic aluminum substrate are 1.06 $k\Omega \cdot cm^2$ and 73.4 $k\Omega \cdot cm^2$, respectively. The higher values of the polarization resistance and modulus of impedance of the superhydrophobic aluminum surfaces with respect to the as-receive aluminum alloy surface demonstrate that the superhydrophobic surfaces prepared by chemical etching followed by SA passivation have superior corrosion resistance properties.

4.6 Supporting information

Table 4.2: The electrical components (parameters) obtained from simulation of EIS data of as-received aluminum alloy substrate and superhydrophobic aluminum alloy substrate

		Double layer			Film		
Sample	*Rs* ($\Omega \cdot cm^2$)	*CPE/CPE$_{ctSH}$* ($\mu F/cm^2$)		*R_{ct}/R_{ctSH}* ($k\Omega \cdot cm^2$)	*CPE_{SH}* ($\mu F/cm^2$)		*R_{SH}* ($k\Omega \cdot cm^2$)
		Y/Y_{ctSH}	n/n_{ctSH}		Y_{SH}	n_{SH}	
As-received Al	11.6	70	0.98	1.46	-	-	-
Superhydrophobic Al	192.3	40	0.6	95	7.16	0.4	29

CPE, Y, n and R_{ct} are due to the double layer between surface of aluminum and NaCl electrolyte.

CPE_{ctSH}, $Y_{ctSH,}$ n_{ctSH} and R_{ctSH} are due to the double layer between surface of superhydrophobic aluminum and NaCl electrolyte.

CPE_{SH} , Y_{SH}, , n_{SH}, *and* R_{SH} are due to the superhydrophobic aluminum thin film.

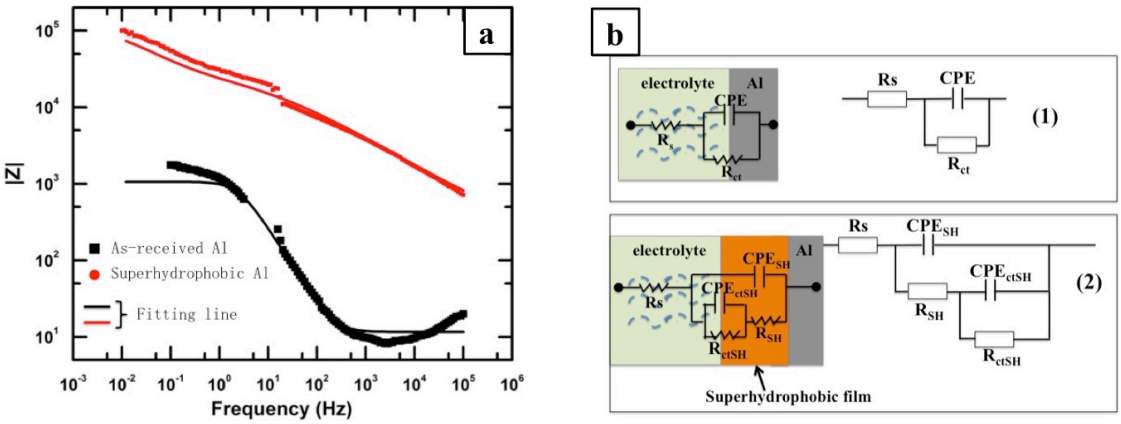

Figure 4. 11(a) shows the original and fitted Bode modulus plots of as-received aluminum alloy substrate and superhydrophobic aluminum alloy substrate. (b) The equivalent circuit used to fit the EIS data. This figure has been included in the manuscript as Figure 4.10(d) Electrical equivalent circuits for EIS of (d1) as-received aluminum alloy substrate and (d2) superhydrophobic aluminum alloy substrate.

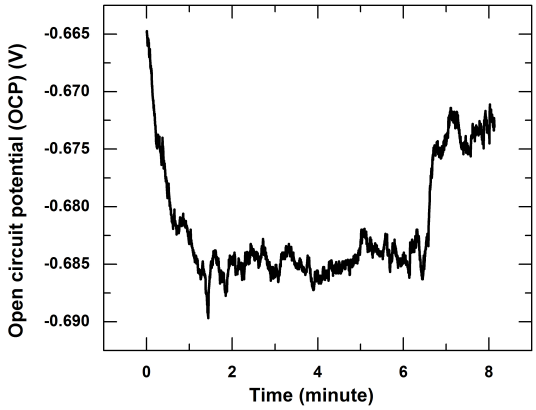

Figure 4. 12 Open circuit potential (OCP) value of superhydrophobic aluminum alloy substrate as a function of time.

Figure 4.12 shows the open circuit potential (OCP) value of superhydrophobic aluminum alloy substrate as a function of time. The initial polarization potential of -0.922

V, which is -0.25V lower than the OCP value of -0.672 mV, indicating the OCP value is matching with the polarization curve.

Reference

(1) Neinhuis, C.; Barthlott, W. *Annals of Botany* **1997**, *79*, 667.

(2) Genzer, J.; Efimenko, K. *Biofouling* **2006**, *22*, 339.

(3) He, T.; Wang, Y.; Zhang, Y.; lv, Q.; Xu, T.; Liu, T. *Corrosion Science* **2009**, *51*, 1757.

(4) Huang, Y.; Sarkar, D. K.; Chen, X. G.; Advanced Materials Research: 2012; Vol. 409, p 497.

(5) Brassard, J. D.; Sarkar, D. K.; Perron, J. *ACS Appl Mater Inter* **2011**, *3*, 3583.

(6) Saleema, N.; Sarkar, D. K.; Gallant, D.; Paynter, R. W.; Chen, X. G. *ACS Applied Materials & Interfaces* **2011**, *3*, 4775.

(7) Saleema, N.; Sarkar, D. K.; Paynter, R. W.; Chen, X. G. *ACS Applied Materials & Interfaces* **2010**, *2*, 2500.

(8) Brassard, J.D.; Sarkar, D. K.; Perron, J. *Appl. Sci.* **2012**, *2*, 453.

(9) Safaee, A.; Sarkar, D.; Farzaneh, M. *Applied Surface Science* **2008**, *254*, 2493.

(10) Sarkar, D. K.; Farzaneh, M.; Paynter, R. W. *Applied Surface Science* **2010**, *256*, 3698.

(11) Sarkar, D. K.; Farzaneh, M. *Journal of Adhesion Science and Technology* **2009**, *23*, 1215.

(12) Sarkar, D. K.; Paynter, R. W. *Journal of Adhesion Science and Technology* **2010**, *24*, 1181.

(13) Huang, Y.; Sarkar, D. K.; Chen, X. G. *Materials Letters* **2010**, *64*, 2722.

(14) Sarkar, D. K.; Farzaneh, M.; Paynter, R. W. *Materials Letters* **2008**, *62*, 1226.

(15) Huang, Y.; Sarkar, D. K.; Chen, X.G. *Nano-micro letters* **2011**, *3(3)*, 160.

(16) Sarkar, D. K.; Saleema, N. *Surface and Coatings Technology* **2010**, *204*, 2483.

(17) Ruan, M.; Li, W.; Wang, B.; Luo, Q.; Ma, F.; Yu, Z. *Applied Surface Science* **2012**, *258*, 7031.

(18) Escobar, A. M.; Llorca-Isern, N. *Applied Surface Science* **2014**, *305*, 774.

(19) Liao, R.; Zuo, Z.; Guo, C.; Yuan, Y.; Zhuang, A. *Applied Surface Science* **2014**, *317*, 701.

(20) Zuo, Z.; Liao, R.; Guo, C.; Yuan, Y.; Zhao, X.; Zhuang, A.; Zhang, Y. *Applied Surface Science* **2015**, *331*, 132.

(21) Bernagozzi, I.; Antonini, C.; Villa, F.; Marengo, M. *Colloids and Surfaces A: Physicochemical and Engineering Aspects* **2014**, *441*, 919.

(22) He, Y.; Jiang, C.; Yin, H.; Chen, J.; Yuan, W. *J Colloid Interface Sci* **2011**, *364*, 219.

(23) Lu, Y.; Xu, W.; Song, J.; Liu, X.; Xing, Y.; Sun, J. *Applied Surface Science* **2012**, *263*, 297.

(24) Sun, J.; Zhang, F.; Song, J.; Wang, L.; Qu, Q.; Lu, Y.; Parkin, I. *Applied Surface Science* **2014**, *315*, 346.

(25) Wang, Y.; Wang, W.; Zhong, L.; Wang, J.; Jiang, Q.; Guo, X. *Applied Surface Science* **2010**, *256*, 3837.

(26) Pan, L.; Dong, H.; Bi, P. *Applied Surface Science* **2010**, *257*, 1707.

(27) Liang, J.; Hu, Y.; Wu, Y.; Chen, H. *Surface and Coatings Technology* **2014**, *240*, 145.

(28) Liu, T.; Dong, L.; Liu, T.; Yin, Y. *Electrochimica Acta* **2010**, *55*, 5281.

(29) Liu, Y.; Zhang, J.; Li, S.; Wang, Y.; Han, Z.; Ren, L. *RSC Adv.* **2014**, *4*, 45389.

(30) Huang, Y.; Sarkar, D. K.; Gallant, D.; Chen, X. G. *Applied Surface Science* **2013**, *282*, 689.

(31) Brassard, J. D.; Sarkar, D. K.; Perron, J.; Audibert-Hayet, A.; Melot, D. *Journal of Colloid and Interface Science* **2015**, *447*, 240.

(32) Huang, Y.; Sarkar, D. K.; Chen, X. G. *Applied Surface Science* **2015**, *327*, 327.

(33) Wenzel, R. N. *Industrial & Engineering Chemistry* **1936**, *28*, 988.

(34) Osmond, G.; Boon, J. J.; Puskar, L.; Drennan, J. *Applied Spectroscopy* **2012**, *66*, 1136.

(35) Johansson, E.; Nyborg, L. *Surface and Interface Analysis* **2003**, *35*, 375.

(36) Rittermeier, A.; Miao, S.; Schroter, M. K.; Zhang, X.; van den Berg, M. W. E.; Kundu, S.; Wang, Y.; Schimpf, S.; Loffler, E.; Fischer, R. A.; Muhler, M. *Physical Chemistry Chemical Physics* **2009**, *11*, 8358.

(37) Maldonado, C.; De la Rosa, J.; Lucio-Ortiz, C.; Hernández-Ramírez, A.; Barraza, F.; Valente, J. *Materials* **2014**, *7*, 2062.

(38) Kim, B.; Seo, S.-B.; Bae, K.; Kim, D.-Y.; Baek, C.-H.; Kim, H.-M. *Surface and Coatings Technology* **2013**, *232*, 928.

(39) Xie, D.; Li, W. *Applied Surface Science* **2011**, *258*, 1004.

(40) Brassard, J.-D.; Sarkar, D. K.; Perron, J. *ACS Applied Materials & Interfaces* **2011**, *3*, 3583.

(41) Y. Han, D. G., X.-G. Chen *Corrosion* **2011**, *67*, 115005.

(42) Yoo, B.; Shin, K. R.; Hwang, D. Y.; Lee, D. H.; Shin, D. H. *Applied Surface Science* **2010**, *256*, 6667.

(43) Walter, R.; Kannan, M. B. *Materials & Design* **2011**, *32*, 2350.

(44) Shahryari, A.; Kamal, W.; Omanovic, S. *Materials Letters* **2008**, *62*, 3906.

(45) Liu, H.; Szunerits, S.; Xu, W.; Boukherroub, R. *ACS Appl Mater Inter* **2009**, *1*, 1150.

(46) Xiao, W.; Man, R.; Miao, C.; Peng, T. *Journal of Rare Earths* **2010**, *28*, 117.

(47) Cheng, Y.; Lu, S.; Xu, W.; Wen, H. *RSC Advances* **2015**, *5*, 15387.

(48) Fan, Y.; Chen, Z.; Liang, J.; Wang, Y.; Chen, H. *Surface and Coatings Technology* **2014**, *244*, 1.

(49) Liu, Q.; Kang, Z. *Materials Letters* **2014**, *137*, 210.

(50) Liu, C.; Su, F.; Liang, J.; Huang, P. *Surface and Coatings Technology* **2014**, *258*, 580.

(51) Wang, P.; Zhang, D.; Qiu, R.; Hou, B. *Corrosion Science* **2011**, *53*, 2080.

(52) Zhang, F.; Chen, S.; Dong, L.; Lei, Y.; Liu, T.; Yin, Y. *Applied Surface Science* **2011**, *257*, 2587.

(53) Yin, B.; Fang, L.; Tang, A.-q.; Huang, Q.-l.; Hu, J.; Mao, J.-h.; Bai, G.; Bai, H. *Applied Surface Science* **2011**, *258*, 580.

(54) Shen, G. X.; Chen, Y. C.; Lin, L.; Lin, C. J.; Scantlebury, D. *Electrochimica Acta* **2005**, *50*, 5083.

CHAPTER 5 SUPERHYDROPHOBIC NANOSTRUCTURED ZNO THIN FILMS ON ALUMINUM ALLOY SUBSTRATES BY ELECTROPHORETIC DEPOSITION PROCESS

Superhydrophobic aluminum alloy substrate has been prepared by chemical etching process, as illustrated in chapter 4. The corrosion resistance property was also investigated by both EIS and polarization techniques. The superhydrophobic aluminum alloy substrate prepared by chemical etching process has a polarization resistance value of 521 $k\Omega \cdot cm^2$ in 3 wt.% NaCl corrosive solution. In the master study, the superhydrophobic copper surfaces have been fabricated via one-step electrochemical modification process. The R_p value of copper was increased from 1 $k\Omega \cdot cm^2$ to 1220 $k\Omega \cdot cm^2$ after modification. We realized that the superhydrophobic aluminum alloy substrate might be able to have a better anti-corrosion property using some other

techniques. Therefore, in this project, the electrophoretic deposition process is utilized to fabricate superhydrophobic aluminum alloy substrate, and a journal article titled as "Superhydrophobic nanostructured ZnO thin films on aluminum alloy substrates by electrophoretic deposition process" has been published in journal Applied Surface Science. It is presented in section 5.1.

5.1 Effect of temperature on superhydrophobic aluminum alloy surfaces in EPD process

5.1.1 Introduction

A surface that provides non-wetting characteristics with water contact angle higher than 150° is termed as a superhydrophobic surface. After the discovery of superhydrophobic surfaces in nature [1, 2], many artificial superhydrophobic coatings have been fabricated by mimicking nature [3, 4]. In order to create superhydrophobic surfaces, it is observed that creation of a certain micro-nanoroughness structures promotes the entrapment of the air in the space between the rough features. In addition, lowering the surface energy helps to reduce the affinity of water drops with a surface thereby

weakening the water-surface interaction.

Zinc oxide (ZnO) is widely use in solar cells [5], gas sensors [6], transistors [7], ultraviolet lasers [8], UV detectors [9] etc. Superhydrophobic ZnO thin films have been successfully synthesized by many synthetic routes, e.g., physical vapor deposition [10], chemical bath deposition (CBD) [11], electrodeposition [12, 13], etc [14-16]. The literatures show ZnO thin films can be superhydrophobic without any low surface energy passivation layers [10, 14, 15]. However, most of the cases an extra layer was incorporated to reduce the surface energy of ZnO to obtain superhydrophobic properties [12, 13, 16].

Electrophoretic deposition (EPD) is a wet-deposition process in which colloidal charged particles suspended in a liquid medium migrate under the influence of an electric field and get deposited on the surface of the electrode. When a sufficient electric field is applied to a colloidal suspension, they get deposited on the oppositely charged electrodes [17, 18]. A review on the fundamentals and applications of electrophoretic deposition (EPD) describes the effects of time, applied potential, concentration of solid in suspension, etc., [18]. Recently, EPD process has been used to prepare superhydrophobic surfaces by

fabricating rough structures with low surface energy materials. Joung and Buie fabricated superhydrophobic surfaces using electrophoretic deposition (EPD) of hydrophobic SiO_2 particle suspension modified by polydimethylsiloxane (PDMS) at room temperature [19]. Ogihara *et al*. prepared superhydrophobic SiO_2 particle/silicone resin composite coatings by EPD at room temperature [20]. They have also fabricated superhydrophobic colored films by EPD of hydrophobic pigment particles on substrates [21]. However, the effect of bath temperature on the EPD process to prepare thin films as well as fabricate superhydrophobic surfaces is not found in the literatures. Recently, we have used electrochemical modification and electrodeposition techniques to prepare superhydrophobic copper and aluminum alloy substrates [3, 4, 22]. In the present study, we develop the one-step electrophoretic deposition (EPD) process to fabricate superhydrophobic ZnO thin films on aluminum alloy substrates using stearic acid (SA)-functionalized ZnO nanoparticles suspension. The effects of the bath temperatures on the characteristics of deposited ZnO thin films and its superhydrophobic properties have been studied.

5.1.2 Experiments

In electrophoretic deposition process to prepare superhydrophobic ZnO thin films on aluminum alloy substrates, as-purchased hydrophilic ZnO particles (average particle diameter of 30 nm from MKNano, Ontario, Canada) were added in a mixture of 0.01 M ethanolic stearic acid (SA), 2-propanol and tert-butyl alcohol (vol. = 1:2:4) [23], followed by ultrasonication for one hour. In the case of preparing non-functionalized ZnO thin films on aluminum alloy substrates, ethanol, 2-proponal and tert-butyl alcohol mixed solution with the same ratio was applied. Though the concentration of nanoparticles were varied from 0.14 g/L to 1.4 g/L, the results of 1.4 g/L were only given in this manuscript. As-rolled aluminum alloy sheets, having rolled lines, have been used as aluminum alloy substrates for more efficient in economical and time-saving point of view instead of using polished aluminum alloy substrates. A pair of cleaned AA6061 aluminum alloy substrates was vertically immersed in the suspension and kept at a distance of 1.5 cm and a 30 V DC was applied for 10 minutes at the bath temperature ranging from 10-50 °C. The bath temperature was controlled using a thermal bath normally used for cooling the solution

for anodization of aluminum alloy substrates. The morphological and elemental analyses were performed using a scanning electron microscope (SEM, JEOL JSM 6480 LV) equipped with energy dispersive x-ray spectrometer (EDX). A thin gold layer was sputtered on the modified surfaces with Polaron sputter coater (SC7640) for improving the resolution of non-conducting samples during SEM and EDX studies. The chemical composition of surfaces was analyzed by X-ray diffraction (XRD, D8 discover with Cu K_{α} wavelength 0.154 nm) and infrared reflection absorption spectroscopy (IRRAS, Nicolet 6700FT-IR). As-purchased and SA-functionalized ZnO nanoparticles were analyzed by making pellets with KBr powder and using Fourier Transform Infrared (FTIR, Perkins Elmer Spectrum One) spectroscopy. The roughness of surfaces was measured using an optical profilometer (MicroXAM-100 HR 3D surface profilometer). The wetting characteristics of the sample surfaces were carried out by measuring static contact angles (abbreviated as CA) using a First Ten Angstrom contact angle goniometer. Furthermore, the dynamic contact angle (abbreviated as CAH) of the superhydrophobic surface was also measured by holding the water drop with a stationary needle in contact

with the superhydrophobic surface and moving the goniometer stage in one direction. CAH is defined as the difference between the advancing and receding contact angle as published before [3, 4, 24].

5.1.3 Surface characterizations

Figure 5.1(a) shows the x-ray diffraction (XRD) patterns of (aI) as-received AA6061 aluminum alloy substrate, and (aII) thin film of SA-functionalized ZnO electrophoretically deposited at bath temperature of 50 °C on the AA6061 aluminum alloy substrate in the 2θ scan range of 30-70°. The XRD pattern (aII) shows the characteristic peaks of ZnO (100), (002), (101) and (110) at 31.82°, 34.47°, 36.19° and 56.78° [25], respectively, confirming the ZnO deposition on aluminum alloy substrate. It also shows the peaks at 38.47°, 44.72° and 65.1°, respectively, which are in good agreement with the characteristic peaks of Al (111), (200) and (220) in as-received aluminum alloy substrate pattern (aI) [26]. The crystal size of the deposited ZnO at 50 °C bath temperature was calculated by the Debye-Scherrer's formula with the help of full width at half maximum (FWHM) of the XRD peak.:

$$D = \frac{0.9\,\lambda}{\beta \cos\theta} \qquad \text{(Equation 5. 1)}$$

Where λ is the wavelength (0.154 nm) and β is full width in radian at half maximum of the peak and θ is the Bragg's angle of the XRD peak. The crystallite size of ZnO deposited on aluminum alloy substrate at 50 °C is calculated to be 26 nm, which is consistent with the average diameter of 30 nm of as purchased ZnO nanoparticles.

Fourier Transform Infrared spectroscope (FTIR) and Infrared reflection absorption spectroscopy (IRRAS) were used to analyze the atomic bonding in (bI) ZnO nanoparticles and (bII) the SA-functionalized ZnO thin film on aluminum alloy substrate in Figure 5.1(b), respectively. ZnO nanoparticles were analyzed by FTIR as powder pellets with KBr. The bands centered at 1506 cm^{-1} and 1400 cm^{-1} were observed both in the IRRAS spectrum ((bII)) as well as FTIR spectra ((bI)) are due to the ZnO [27]. Furthermore, the peak at 560 cm^{-1} also comes from ZnO stretching mode. The observation of ZnO peaks is consistent with that of XRD pattern of SA-functionalized

ZnO electrophoretically deposited alloy in Figure 5.1(a). The peaks at 2850 cm^{-1}, 2919 cm^{-1} and 2962 cm^{-1}, which appeared in the spectrum of SA-functionalized ZnO thin film on alloy surface rather than ZnO spectrum, are from $–CH_2$ and $-CH_3$ vibrations as shown in (bII).

The appearance of these bands confirm the presence of low surface energy components of methylated in the coatings [28]. It is to be mentioned that, a low intense new peak at 1550 cm^{-1} is due to the -COOZn bonds appeared in the spectra of SA-functionalized ZnO thin film surface [26]. The infrared studies confirm the formation of zinc stearate hence the functionalization of zinc oxides by stearic acid and their thin film formation by EPD process as presented in the Figure 5.1(b). IRRAS was used to evaluate the thin films on the aluminum alloy substrates as IR does not pass through metals. The overall objectives were to evaluate both the as-received ZnO nanoparticles and as well as the thin films on aluminum alloy substrates. However, the intensity of the peaks can't be compared between these two different analyzing methods.

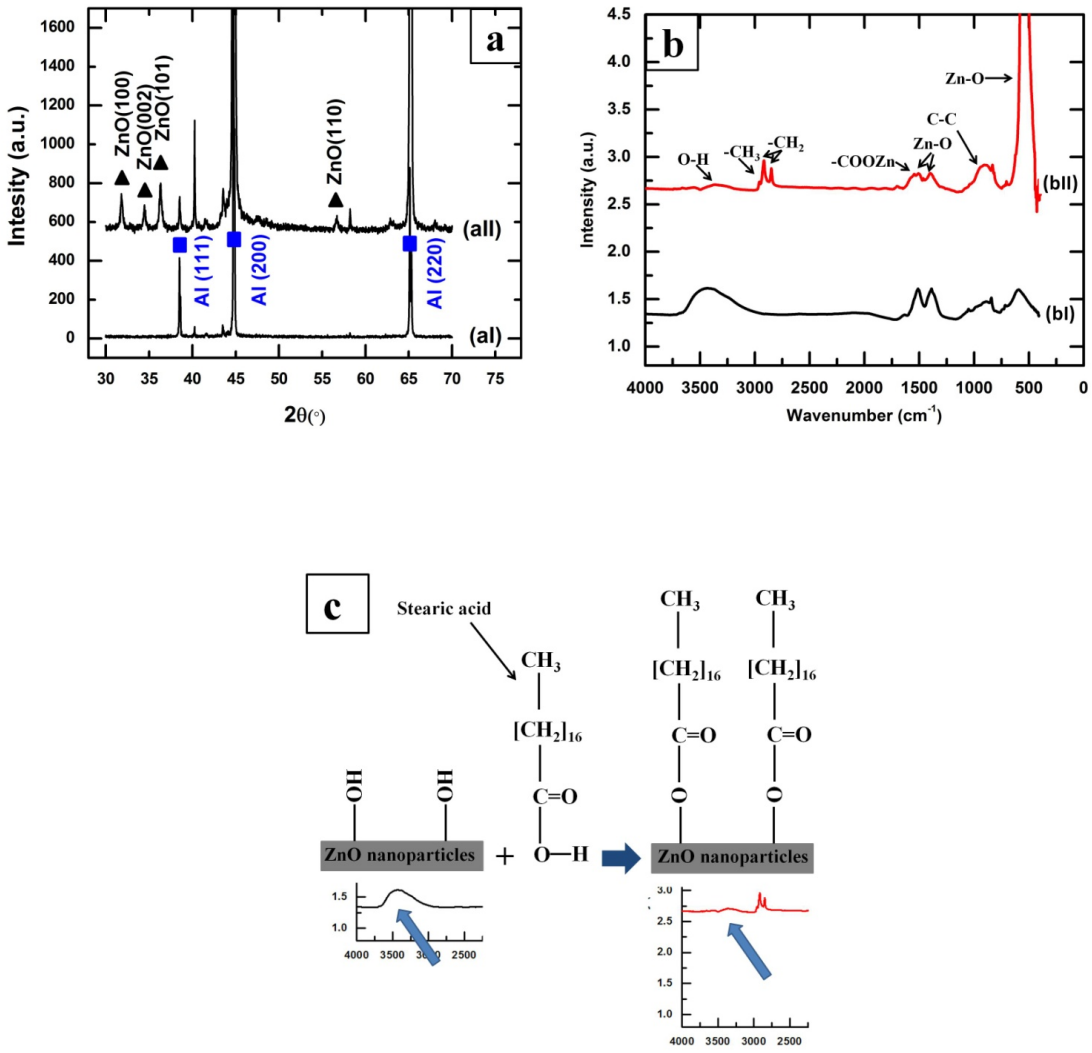

Figure 5. 1(a) XRD patterns of (aI) aluminum alloy substrate and (aII) electrophoretic deposited SA-functionalized ZnO thin film on the aluminum alloy substrate; (b) FTIR spectrum of (bI) the palette of as-received ZnO nanoparticles with KBr powder and (bII) IRRAS spectrum of SA-functionalized ZnO film on aluminum alloy substrate; (c) The schematic graph of interaction between SA and ZnO.

Figure 5.1(c) shows the schematic graph of the interaction between SA and ZnO. It shows that the ZnO surface was functionalized by SA molecules, with the formation of

zinc stearate. The –OH bonding on ZnO surface was replaced by –COOZn in the interaction between ZnO and SA, which explained the disappearance of –OH after ZnO functionalized by SA molecules in Figure 5.1(b).

Table 5.1 summarizes the properties of SA-functionalized ZnO thin films deposited by EPD process at varying bath temperatures. Figure 5.2(a) shows the SEM image of the surface of as-received aluminum alloy substrate, which has a surface roughness of 0.45 μm and water contact angle of 87 ± 3° (inset of the Figure). Anyone must be aware that rolled sheets generally shows the rolled lines on its surfaces and therefore, will have a certain roughness inherently. Figure 5.2(b) shows the thin films of SA-functionalized ZnO deposited at the bath temperature of 10 °C. It is clear from the Figure that the formation a few white microdots on the aluminum alloy substrate. Interestingly the contact angle of water on this surface is increased to 101 ± 4° while the surface roughness remaining almost the same as untreated aluminum alloys substrate (0.48 μm).

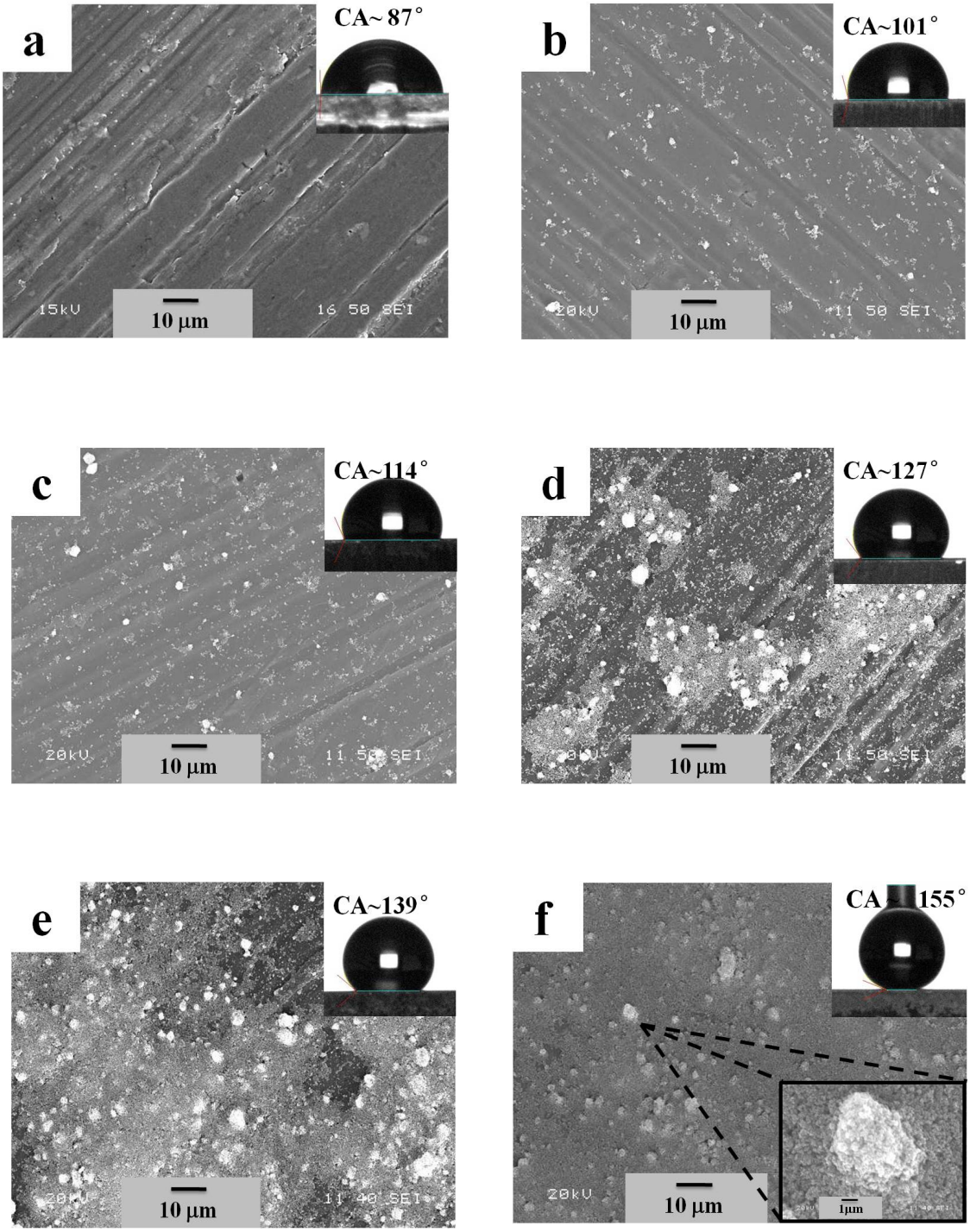
a
CA~ 87°
15kV
10 µm
16 50 SEI
b
CA~101°
20kV
10 µm
11 50 SEI
c
CA~114°
20kV
10 µm
11 50 SEI
d
CA~127°
20kV
10 µm
11 50 SEI
e
CA~139°
20kV
10 µm
11 40 SEI
f
CA 155°
20kV
10 µm
1µm

Figure 5. 2 SEM images of (a) the surface of as-received aluminum alloy substrate; (b-f) the SA-functionalized ZnO thin film on aluminum alloy substrates at bath temperature of EPD process (b) 10 °C, (c) 20 °C, (d) 30 °C, (e) 40 °C and (f) 50 °C. The insets of SEM images show the images of water drop on respective surfaces. Also, the inset of down-right-corner of (f) shows the magnified image of a cluster.

This increase of water contact angle is due to the presence of SA-functionalized ZnO, as stearic acid (SA) reduces the surface energy due to the presence of $-CH_2$ and $-CH_3$ radicals. Furthermore, the number density of microdots increases slightly with the increase bath temperature of 20 °C from 10 °C as shown in Figure 5.2(c). Evidently, a slight increase of surface roughness from 0.48 μm to 0.64 μm is observed. It has been observed that the contact angle also increases from 101 ± 4° to 114 ± 4° due to the increase of roughness of the thin films associated with the increase of the bath temperatures. Moreover, increasing bath temperatures to 30 °C and 40 °C lead to the more amounts of deposits and higher coverage of SA-functionalized ZnO microdots on the aluminum alloy substrates as evident from Figure 5.2(d) and (e). The roughness and the water contact angle of the films deposited at 30 °C and 40 °C are 0.81 μm and 127 ± 2°

and 2.72 μm and 139 ± 2°, respectively. The similar microdots structure formations were also reported in the literatures [29-31]. A thin film with complete coverage is observed when the bath temperature is increased to 50 °C as shown in Figure 5.2(f). The higher magnification micronanostructure is shown in the inset of Figure 5.2(f). The morphology of the SA-functionalized ZnO thin films deposited at bath temperature of 50 °C is similar to the morphology of the flower-like micro-nanostructures on the superhydrophobic copper surfaces in our previous study by electrochemical modification using ethanolic stearic acid [3], which is comparable to that of the lotus leaves morphology [32].

The combination of micro-nanorough clusters of ZnO nanoparticles with the low-surface-energy stearic acid molecules transforms the aluminum alloy substrates to superhydrophobic. The films deposited at 50 °C have a surface roughness of 4.54 μm providing a high contact angle of 155 ± 3°, as shown in the inset of Figure 5.2(f), as well as a contact angle hysteresis of 5 ± 2°. Stearic acid (SA) passivated flat ZnO surface prepared by sol-gel process shows a CA of 60°. Therefore, the thin films prepared by SA-functionalized ZnO nanoparticles follow the Cassie-Baxter model [33].

The thin films were prepared using as-received ZnO nanoparticles to compare the wetting properties with the thin films prepared with the SA-functionalized ZnO nanoparticles. The morphologies of the thin films prepared by EPD process using as-received (in other words non-functionalized) ZnO nanoparticles are shown in Figure 5.3. The morphologies are very similar as found for the thin films prepared from the SA-functionalized ZnO nanoparticles. The wetting properties of these films are presented in the inset of the images as well as the down graph of Figure 5.4(b). It is found that the CA of the films reduces with the increase of the bath temperature that might be due to the increase of roughness of the films associated with the size of the cluster [34]. The contact angle is found be as low as 9° when the film was deposited at 50 °C bath temperature.

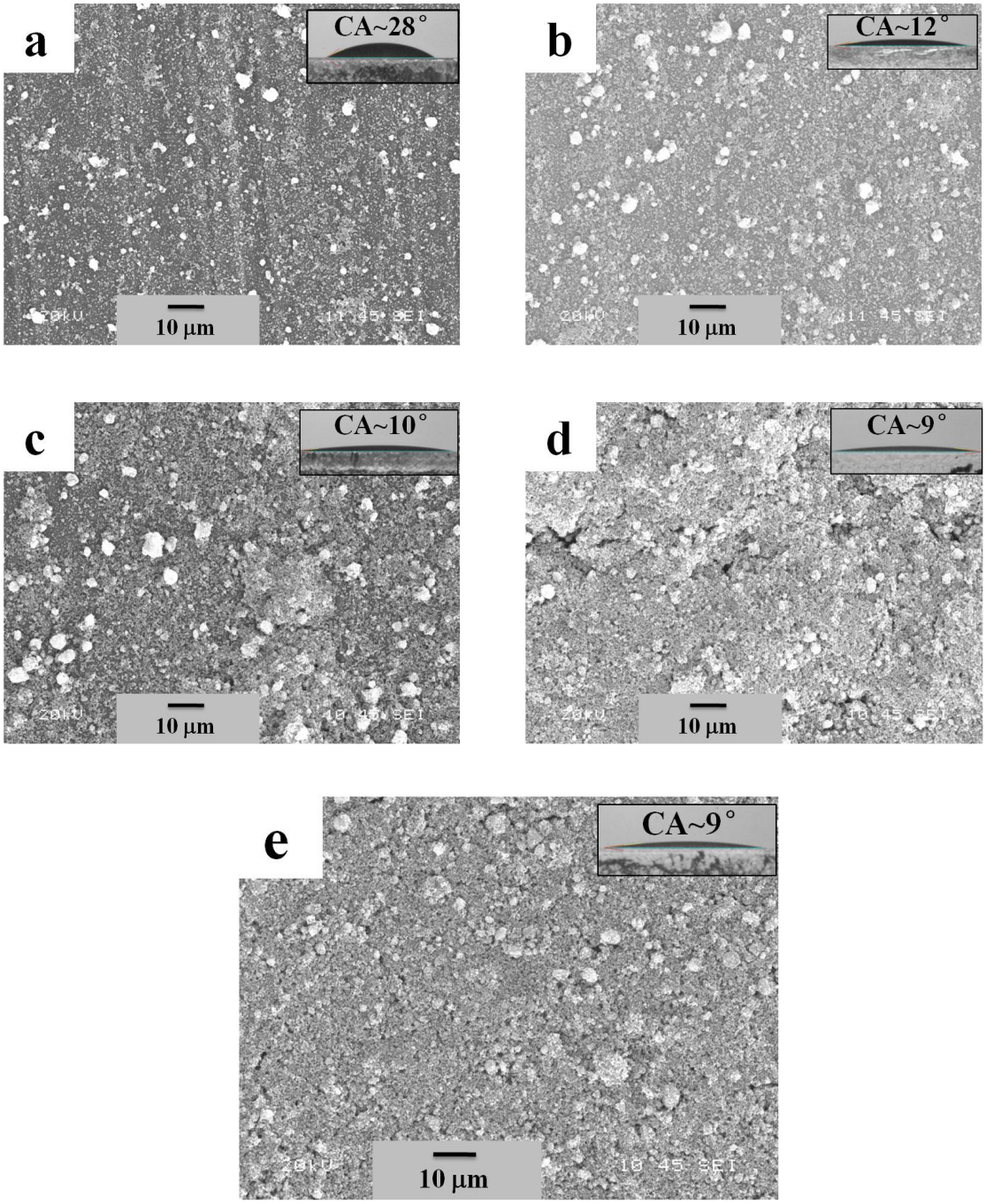

Figure 5. 3 SEM images showing the morphologies of the thin films prepared by EPD process using as-received (in other words non-functionalized) ZnO nanoparticles: (a) 10 °C, (b) 20 °C, (c) 30 °C, (d) 40 °C and (e) 50 °C. The insets of SEM images show the images of water drop on respective surfaces.

The reduction of the contact angle (CA) due to the wetting of the surface according to the Wenzel model [35] as a smooth ZnO thin films gives a water contact angle of 27° prepared by sol-gel process (see the supplementary material). However, it has been reported that some cases the ZnO thin films can be superhydrophobic without any passivation [10, 14, 15] but most of the cases a layer of low surface energy films or monolayers were used to obtain superhydrophobic properties [12, 13, 16] as in our case. Compared with the morphologies of petal, tube or wire structures, as reported in the literatures [36, 37] spherical cluster of SA-functionalized ZnO particles observed in the present studies. The formation of spherical cluster is more probable as it requires minimum Gibbs free energy barrier to form as compared to other forms like, cube, petal or wire. As reported by Laurenti [10], ZnO nanowires were grown by hydrothermal method on ZnO seed layer. However, in our case, ZnO nanoparticles (either as-received or SA-functionalized) were deposited on the aluminum alloy substrates (possible having a native oxide layer) by EPD process. Due to the dissimilar properties of the substrate and deposited materials, their surface energies are not the same; the expected growth mode

would be Volmer-Weber (island growth). Evidently, we have observed the formation of islands of ZnO or SA-functionalized ZnO on aluminum alloy substrates. Recently, our group has shown that superhydrophobic ZnO thin films can be deposited by chemical bath deposition process. The SA-functionalized ZnO thin films were produced by the reaction between $Zn(NO_3)_2$, NH_4OH and stearic acid in an ethanolic solution driven by thermal energy. However, in the present study we have used as-purchased 30 nm hydrophilic ZnO nanoparticles and chemically modified them by SA and used EPD process to prepare superhydrophobic thin films driven by electrical energy.

Table 5. 2 Properties of SA-functionalized ZnO thin films deposited by EPD process at varying bath temperatures.

Bath temperature	Atomic percentage of Zn (%) by EDX	Surface roughness (μm)	Contact angle (°)	Intensity of XRD peak of ZnO (101) plan (a.u.)
As-received Al alloy substrate	Not applicable	0.45 ± 0.03	87 ± 3	0
10 °C	Non detected	0.48 ± 0.02	101 ± 4	17 ± 0.4
20 °C	Non detected	0.64 ± 0.09	114 ± 2	17 ± 0.7
30 °C	4	0.81 ± 0.10	127 ± 2	18 ± 0.9
40 °C	25	2.72 ± 0.17	139 ± 2	30 ± 1.0
50 °C	70	4.54 ± 0.23	155 ± 3	65 ± 4.5

Figure 5.4 shows the variation of surface roughness and water contact angle of the films prepared with the increase of bath temperatures. It is found that the surface roughness increases with the increase of bath temperature and have a sudden jump at 40 and 50 °C (Figure 5.4(a)). The increase of roughness with the increase of deposition temperature may be due to the increase size and density of the micro-clusters of ZnO as seen in the SEM. On the other hand the contact angle of SA-functionalized ZnO thin films is found to increase linearly with the increase of bath temperature (Figure 5.4(b)).

According to Cassie-Baxter model, a surface with higher roughness can entrap more air between the water drop and rough surface, resulting increase in contact angle hence leads to the superhydrophobic properties. The variation of surface roughness and contact angle with the size of the fluorinated silica nanoparticles in the film deposited on aluminum alloy substrate have also been discussed in the study of Brassard et al. [34]; where we have presented that the water contact angle as well as the surface roughness of the thin films increases with the increase of the size of the fluorinated silica nanoparticles.

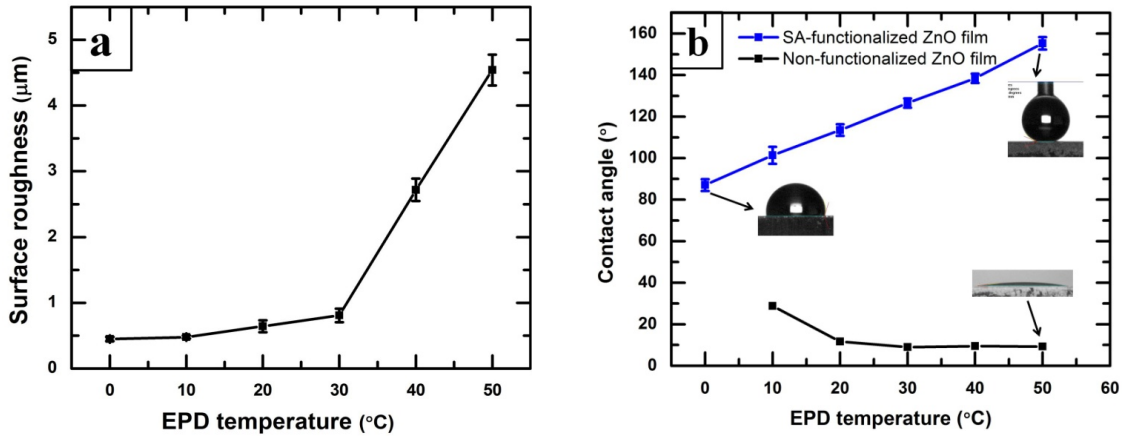

Figure 5. 4(a) The variation of surface roughness thin films prepared from SA-functionalized ZnO nanoparticles at different bath temperature. (b) The variation of water contact angle of thin films prepared from (top) SA-functionalized ZnO nanoparticles (bottom) as received ZnO nanoparticles at different bath temperatures.

Figure 5.5(a) compares energy dispersive x-ray microanalysis (EDX) spectra of SA-functionalized ZnO thin films deposited on aluminum alloy substrates at various bath temperature of the electrophoretic deposition (EPD) process. The peak Au M_{α} at 2.14 is observed, due to the thin layer of gold on the SA-functionalized ZnO thin films for improving the resolution by eliminating the charging effect of non-conducting samples during EDX analyses. The appearance of characterized x-ray peaks of Zn L_{α}, K_{α} and K_{β} at 1.01 keV, 8.63 keV and 9.56 keV, respectively, confirms the presence of Zn. Similarly, the characteristics x-ray peak of O K_{α} at 0.52 keV is observed as the thin films composed of ZnO. This result is complementary with the analysis using XRD and FTIR as presented in Figure 5.1(a) and (b). Figure 5.5(a) also depicts that the intensity of the x-ray peaks of Zn as well as O increases with the increase of bath temperature. The atomic percentage of Zn has been calculated from the EDX data and presented in Figure 5.5(b). It is found that the atomic percentage of Zn increases with the increase of bath temperature. It can be conferred from this results that the thickness of the SA-functionalized ZnO thin films also increases with the increase of bath temperatures. It

can be seen in the Figure 5.5(a) that the x-ray peak of Al K_α at 1.48 keV, coming for the aluminum alloy substrates, reduces drastically due to the enhance thickness of the SA-functionalized ZnO thin films grown at the bath temperature of 50°C. The results are also summarized in the Table 5.1.

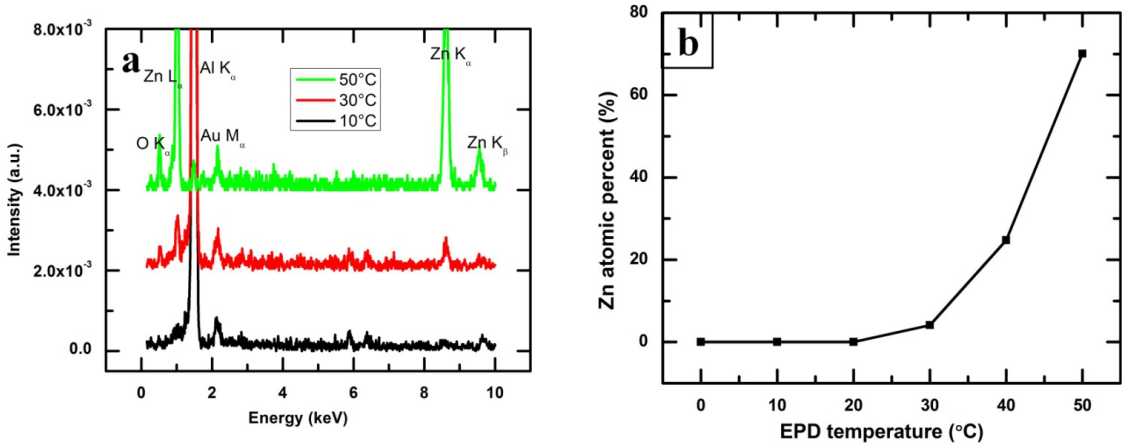

Figure 5. 5(a) EDX spectra of SA-functionalized ZnO thin films as a function of bath temperature of EPD process; (b) Atomic percentage of Zn in the SA-functionalized ZnO thin films deposited at various bath temperature of EPD process as measured by EDX.

Figure 5.6(a) shows the variation of the XRD peak area of ZnO (101) situated at 2θ of 36.2° for the thin films of SA-functionalized ZnO nanoparticles prepared by EPD process at varying bath temperature of 30-50°C. The systematic increase of the XRD peak area indicates that the thickness of the deposited thin films of SA-functionalized ZnO nanoparticles increases with the increase of the bath temperature of the EPD process,

which is complementary with the observation in the SEM images (Figure 5.2(b-f)) as well as the EDX analyses in Figure 5.5(b).

The colloidal nanoparticles in liquid suspension always undergo Brownian motion depending on their bath temperature. The constant thermal motion of the individual nanoparticles leads to collisions between them. The higher electrophoretic temperature, having a faster Brownian motion and collisions, decreases the sedimentation at the bottom of the bath due to the presence of less number of agglomerated particles. Therefore, more nanoparticles in suspension that enhances the deposition of nanoparticles on a substrate under the sufficient electric field [38].

Figure 5.6(b) shows the variation of the logarithm of the XRD peak areas (A) as a function of the reciprocal of the bath temperatures (T). It is found that the logarithm of peak area decreases linearly as a function of the reciprocal of operating temperature (1/T), following the Arrhenius type of behavior as shown in Figure 5.6(b) and presented in Equation as follow:

$$A = a_0 \exp\left(-\frac{E}{kT}\right) or\ \ln A = -\frac{E}{k}\left(\frac{1}{T}\right) - \ln(a_0) \qquad \text{(Equation 5. 2)}$$

where a_0 is a constant, E is the activation energy and k is the Boltzmann constant.

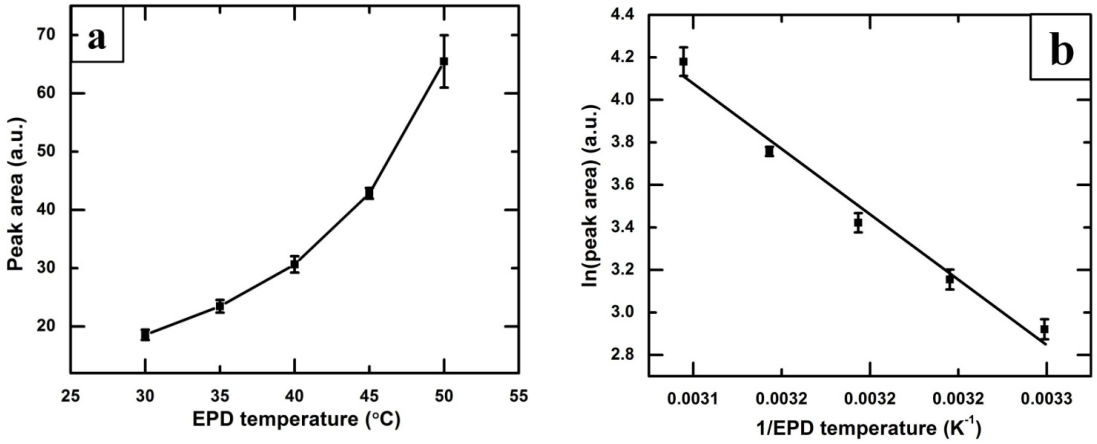

Figure 5. 6(a) Variation of the area under the XRD peaks at 2θ of 36.19° of SA-functionalized ZnO thin films as a function of the EPD bath temperature. (b) Arrhenius plot of logarithm of the peak area vs. reciprocal of EPD temperature.

The activation energy for electrophoretic deposition of SA-functionalized ZnO nanoparticle is calculated to be 0.50 eV from Figure 5.6(b). Saleema et al. [28] reported that the thermal desorption of stearic acid on superhydrophobic zinc oxide nanotowers on silicon substrates. The activation energy for desorption of SA from the ZnO surface is

calculated to be 0.34 eV in the temperature range of 130-350 °C by those authors [28].

5.2 Effect of the deposition time on superhydrophobic properties in EPD process

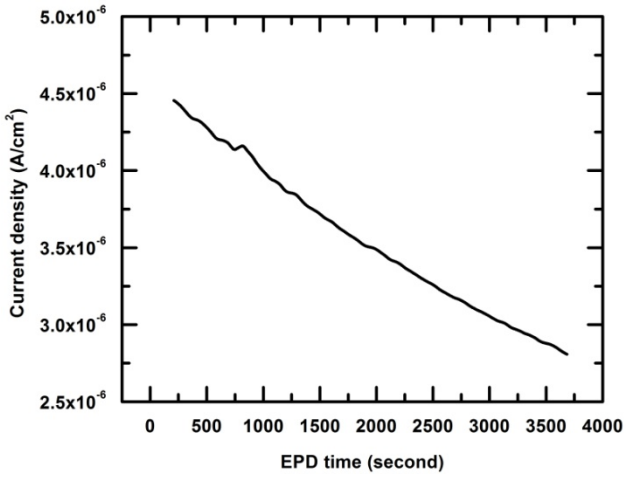

Figure 5. 7 Variation of current density as a function of time during the SA-functionalized ZnO nanoparticle electrophoretic deposited on aluminum alloy surface process at 30 V DC in the bath temperature of 50 °C.

Figure 5.7 shows the variation of current density as a function of time during the SA-functionalized ZnO nanoparticle electrophoretic deposited on aluminum alloy surface process at 30 V DC in the bath temperature of 50°C. The current density is found to decrease linealy from 4.5×10^{-6} A/cm^2 to 2.8×10^{-6} A/cm^2 in 1 h EPD process. The decrease

of current density during EPD process with time may happen due to the continuous growth of the SA-functionalized ZnO insulated layer thickness on as-received aluminum alloy surface with higher electrical resistance. Therefore, the current density reduced according to the Ohm's law.

Figure 5.8 shows the XRD patterns in the angle of 2θ range of 30-70° of SA-functionalized ZnO nanoparticles thin film on aluminum alloy surfaces for different EPD time. The three distinct peaks appearing at 31.82°, 34.47° and 36.19° are assigned to be ZnO [39], due to its positive charged nanoparticles deposited on cathodic aluminum alloy surfaces in colloidal suspensions under electric field. Furthermore, it is observed that the ZnO peak intensity increased with the elongation of EPD time, indicating the amount of ZnO deposition on the surfaces increase with the increased time. It is complementary with the analysis on current density variation with time, where the increased SA-functionalized ZnO layer deposited on alloy surface may be responsible for the decreased current density with EPD time. In addition, The XRD patterns show two characteristic peaks at 38.47°, 44.72° and 65.1° of Al (111), Al (200) and Al(220) planes,

respectively arising from the aluminum substrate. It is to be mentioned that, the origin of the two peaks at 40.22° and 58.18° in XRD patterns (Figure 5.1(b)) are due to the diffraction from Al (200) and Al (220) caused by Cu K_β radiation of wavelength 0.139 nm, whereas Cu K_α is 0.154 nm.

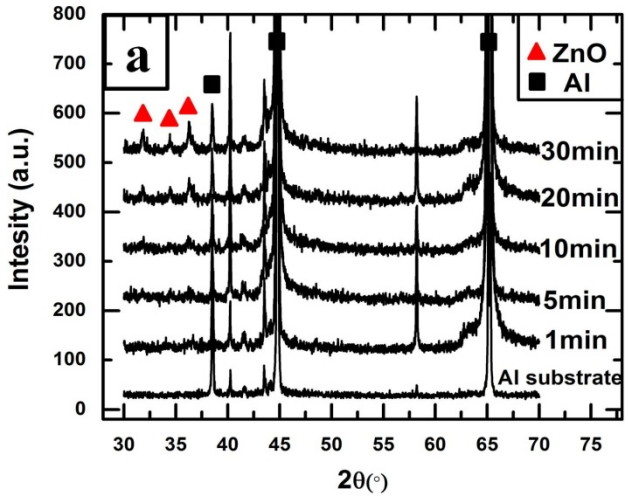

Figure 5. 8 XRD patterns of aluminum alloy substrate and electrophoretic deposited SA-functionalized ZnO thin film with different EPD time.

Figure 5.9 presents the SEM images of aluminum alloy substrates (Figure 5.9(a)) and SA-functionalized ZnO nanoparticle thin film on aluminum alloy surfaces for different EPD time ranging from 1 to 30 min (Figure 5.9(b-f)), respectively.

The scratch on AA6061 aluminum alloy surface in Figure 5.9(a) is due to the rolling

process, and the aluminum alloy substrate has a very low contact angle of 78°, as shown in the inset of Figure 5.9(a). Figure 5.9(b) shows the SA-functionalized ZnO nanoparticle thin film on alloy surface for only 1 min. According to the analyses of XRD patterns in Figure 5.8, abundant isolated micro-nanosized SA-functionalized ZnO particles are decorated loosely on the alloy substrate, having a CA of 126° and a CAH of 55° presented in the insets of Figure 5.9(b). The increase of CA on modified alloy surface as compared with as-received alloy surface is due to deposition of SA-functionalized ZnO brings higher surface roughness with those micro-nanosized ZnO cluster and lower the surface energy with SA. The number density of SA-functionalized ZnO structures increases slightly on alloy surface after 5 min EPD time in Figure 5.9(c) with a higher CA of 131° as well as lower CAH of 47°, indicating the amount and density of SA-functionalized ZnO particles deposited on alloy surfaces for a short EPD time would not be sufficient to exhibit superhydrophobicity.

With the increased EPD time, the deposited SA-functionalized ZnO nanoparticles starts to aggregate. The formation of SA-functionalized ZnO particle clusters with

features revealing micro-nanostructure of ~30-40 μm appeared on surface when EPD time was elongated to 10 min as evident from Figure 5.9(d). It is resulted in the SA-functionalized ZnO nanoparticles would like to agglomerate together during 5 - 10 min electrophoretic deposition in order to reduce the surface free energy of individual nanoparticles. It is well known that CA more than 150° as well as CAH less than 10° indicates that the surfaces can be regarded as superhydrophobic in terms of both static and dynamic contact angles. The combination of low surface energy material as well as the formation of micro-nanorough SA-functionalized ZnO thin film plotted in Figure 5.9(b) leads to the appearance of superhydrophobicity on the surface, having a CA of 156° and CAH of 3°.

It is however, 20 min electrophoretic deposition leads to the slightly decrease of CA of 155° as well as the increase of CAH of 5°, and this tendency is more serious for longer deposition time of 30 min on modified alloy surface with a CA of 155° and CAH of 8°, as shown in Figure 5.9(e & f) respectively. It is well known that the superhydrophobicity is determined by the contact angles of the composite structure of smooth

SA-functionalized ZnO film and the trapped air between micro-nanoparticles. The Cassie-Baxter equation is written as:

$$\cos\theta = f_1\cos\theta_1 + f_2\cos\theta_2 \qquad \text{(Equation 5. 3)}$$

where θ is the contact angle of the composite coating consisting of two components with contact angles θ_1 and θ_2 and corresponding area fractions f_1 and f_2. In such a composite system if f_2 is assumed to be air where θ_2 is 180° and as f_1+f_2=1, Equation 5.3 can be further modified as:

$$\cos\theta = \cos\theta_1 - f_2(\cos\theta_1 + 1) \qquad \text{(Equation 5. 4)}$$

The composite of air was decreased due to the smaller relative height of SA-functionalized ZnO thin film, as schematically shown in Figure 5.10. According to Equation 5.4 that the contact angle (θ) was decreased by reducing the air composite (f_2).

The mechanism of variation morphologies with the elongation of EPD time would be explained as follow. It is known that the SA-functionalized ZnO insulated film grows

on the alloy surface with the increased EPD time. Due to its nonuniform deposition, the current is focused locally on the thinner insulator, because the electrical resistance between alloy substrates and charged SA-functionalized ZnO nanoparticles in the suspension is smaller in those regions [40]. During the electrophoretic deposition process less than 10 minutes, the amount of deposited SA-functionalized ZnO nanoparticles is not large enough to fulfill the alloy surface. However, when the deposition time is higher than 10 minutes, the deposited SA-functionalized ZnO micro-nanostructures acting as a very important role to obtain superhydrophobicity were embedded gradually by further deposition of ZnO nanoparticles, therefore forming a more compact morphology as compared with that of 10 min in Figure 5.9(d).

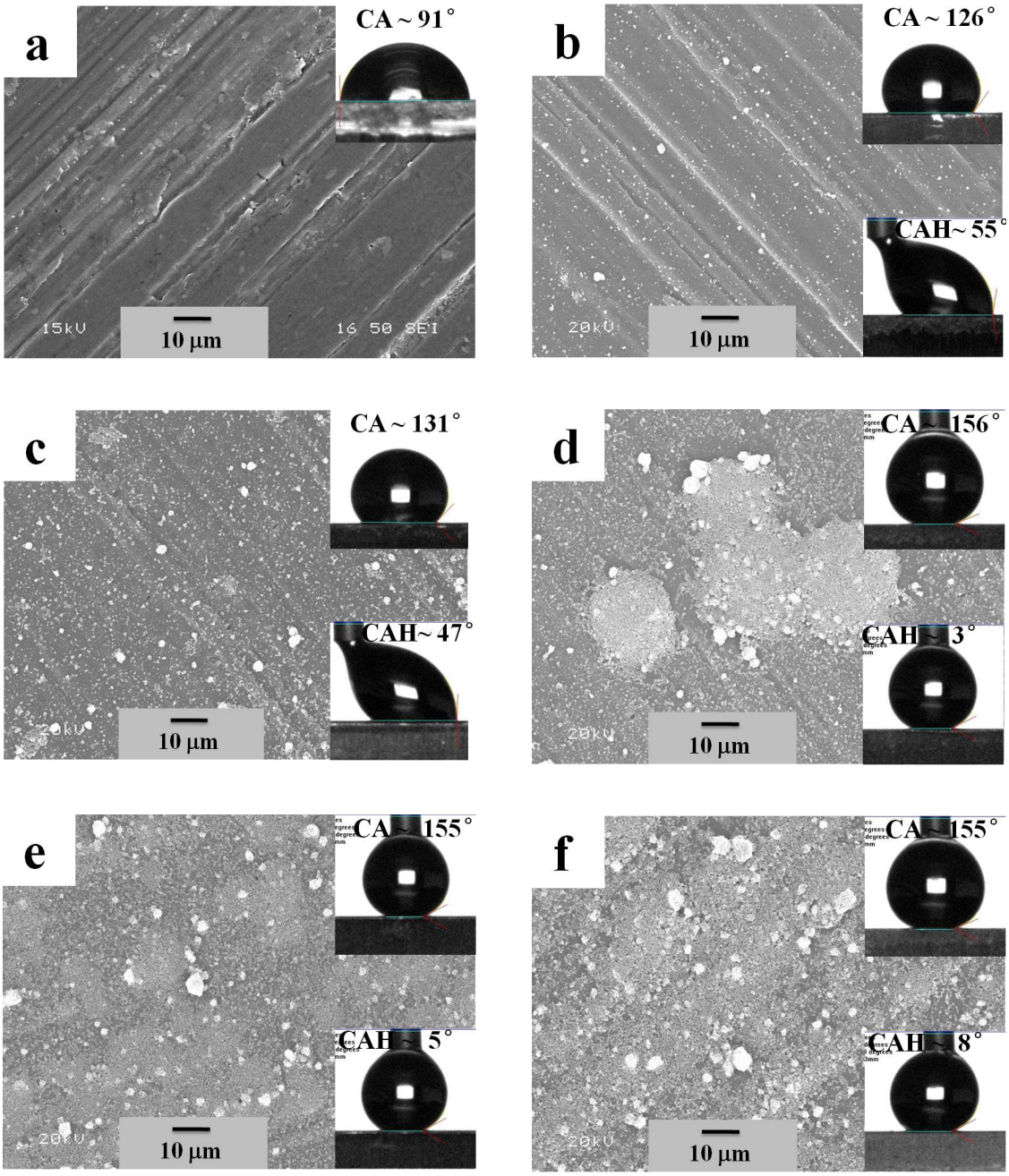

Figure 5. 9 SEM images of (a) aluminum alloy substrate and cathodic surfaces of AA6061 aluminum alloy after the electrophoretic deposition at 30 V in SA-functionalized ZnO suspension at 50°C for (b) 1 min, (c) 5 min, (d) 10 min, (e) 20 min and (f) 30 min, respectively. The inset images show the contact angle (up) and contact angle hysteresis (bottom) on the respect surfaces.

Resembled to the present study, Young Soo Joung et al. [19] fabricated superhydrophobic titanium surfaces using electrophoretic deposition with SiO_2 particles at different pH for a range of time, the optimum dynamic contact angle of as low as 2° was obtained after 60 sec EPD.

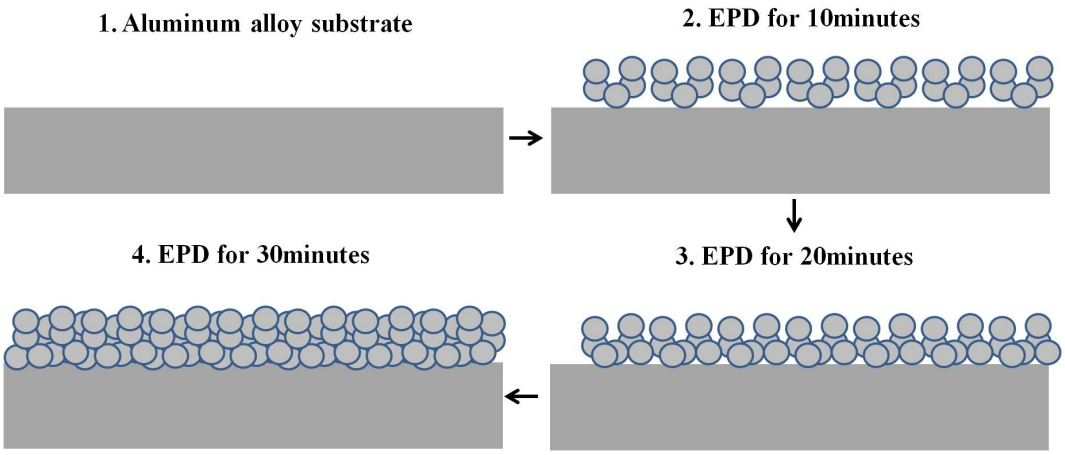

Figure 5. 10 Scheme of electrophoretic deposition of ZnO nanoparticle suspensions on aluminum alloy surfaces with the increase of EPD time.

5.3 Effect of molar ratio (ZnO/SA) on superhydrophobic properties in EPD process

In the previous study, the effect of bath temperature in EPD process on surface

superhydrophobicity has been discussed in section 5.2.1, and the mechanism of EPD process with increasing time has been discussed in section 5.2.2. The deposition of SA-functionalized ZnO nanoparticles enhanced the surface roughness and lowered the surface energy in the same EPD process, which leads to the surface exhibiting superhydrophobic properties. It should also be noticed that the amount of ZnO nanoparticles with fixed amount of SA molecules in suspension solution is also a very important parameter in the EPD process. Therefore, the variation of amount of ZnO nanoparticles in suspension solution on the electrophoretic deposition behavior and the surface superhydrophobicity after deposition is discussed in this section.

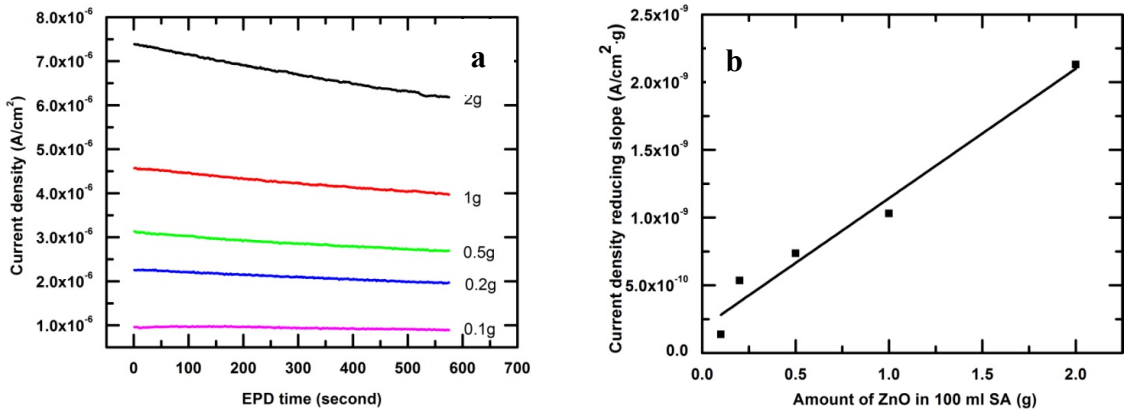

Figure 5. 11 (a) Variation of current density as a function of EPD time with different amount of ZnO in 100 ml SA included suspension solutions from 0.1 g to 2 g at 30 V DC in the bath temperature of 50°C. (b) Current density reducing slope for Figure 5.11 (a) as a function of amount of ZnO in 100 ml SA included suspension solutions.

Figure 5.11(a) shows the current density variation as a function of EPD time on cathodic aluminum alloy surfaces at 30 V DC in the bath temperature of 50°C, respectively. The ZnO nanoparticles in suspensions varied from 0.1 g to 2 g in 100 ml SA included EPD solution. It is found that the current density varied in the range of 9.6×10^{-7} A/cm^2 to 8.9×10^{-7} A/cm^2 with 0.1 g ZnO in suspensions, however, the higher amount of ZnO in suspensions leads to the higher current density appeared during EPD process. It is due to the movement of charged ZnO nanoparticles affects the variation of current density, and the more charged nanoparticles migrate in the system leads to the higher

system current density. Furthermore, the current was found to change in the range of 7.4×10^{-6} A/cm^2 to 6.2×10^{-6} A/cm^2 with 2 g ZnO nanoparticles in suspensions, several times higher than that of 0.1 g ZnO nanoparticles applied. Figure 5.11(b) shows the current reducing slopes in Figure 5.11(a) as a function of the amount of ZnO nanoparticles applied in the suspensions. It is clear to observe that the reducing current slope increased linearly as a function of the amount of ZnO nanoparticles in the suspension, indicated current reduced more markedly with higher amount of ZnO in the suspension. It is consistent with the analysis in the effect of bath temperature on electrophoretic deposition of SA-functionalized ZnO nanoparticles. In that study, the higher bath temperature in EPD process leads to a higher current and more deposition of SA-functionalized ZnO nanoparticles, because the higher electrophoretic temperature, having a faster Brownian motion and collisions, decreases the sedimentation at the bottom of the bath due to the presence of less number of agglomerated particles. Therefore, more nanoparticles in suspension enhance the deposition of nanoparticles on a substrate under the sufficient electric field. In the present study under the same bath

temperature, the higher amount of ZnO nanoparticles in suspensions decreased the distance between nanoparticles and increased the agglomeration, therefore, more clusters would like to sedimentate during the EPD process, leading to the current decreased faster with higher amount of ZnO nanoparticles in the suspensions. On the other hand, higher amount of ZnO in suspensions results in the more movement and deposition of SA-functionalized ZnO insulated layer deposited on alloy surfaces (which can be confirmed by SEM images in Figure 5.12), which is the other reason to explain the current decreased faster with higher amount of ZnO in 100 ml SA included suspension solutions.

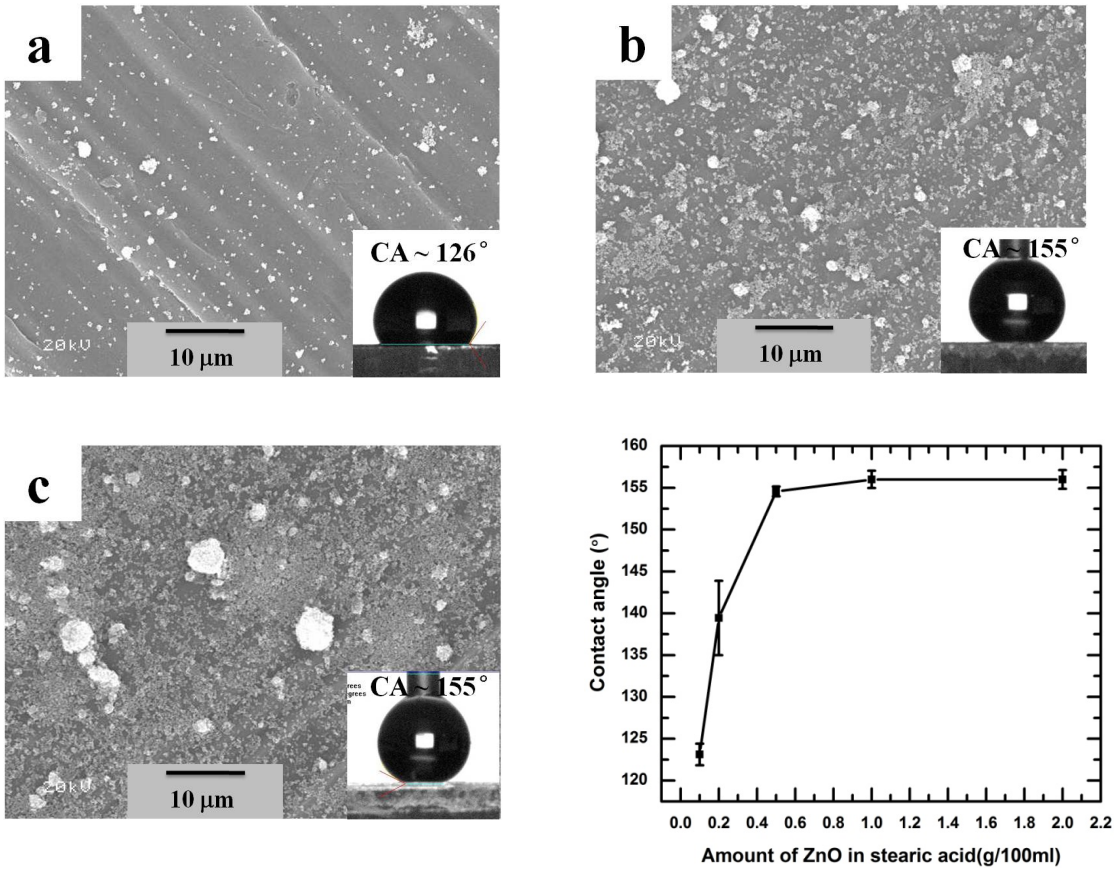

Figure 5. 12 SEM images of SA-functionalized ZnO nanoparticles electrophoretic deposited on aluminum alloy surface at 30V in the bath temperature of 50°C for 1 min with (a) 0.1 g, (b) 0.5 g and (c) 1 g ZnO in 100 ml SA.

Figure 5.12 shows the SEM images of aluminum alloy surfaces after electrophoretic deposition with SA-functionalized ZnO nanoparticles in the bath temperature of 50°C at 30 V for 1 min with (a) 0.1 g, (b) 0.5 g and (c) 1 g. More amount of micro-nanoparticles were observed to deposit on as-received alloy surface with in Figure 5.12(c) as compared

with (a & b). It confirmed the analysis of current variation with different amount of ZnO in suspensions that the higher insulated layer thickness on the surface with more amount of ZnO nanoparticles resulted in the faster decrease of current. Furthermore, the larger size of micro-nanoclusters appeared on the surface with 1 g ZnO nanoparticles applied in suspensions in Figure 5.12(c). It is complementary with the analysis of current, where the more agglomeration of ZnO by applying more nanoparticles in suspensions leads to the faster decrease of current during EPD process.

Figure 5.12(d) shows the variation of CA as a function of the applied amount of ZnO nanoparticles in suspensions. The CA on electrophoretic deposited aluminum alloy surface with 0.1 g nanoparticles is 126°. 0.5 g ZnO nanoparticles are necessary in suspensions in electrophoretic deposition process to obtain superhydrophobic on aluminum alloy surface, where the CA higher than 150°. The increase of coverage of low surface energy micro-nanostructures is responsible for the increase of surface contact angle after electrophoretic deposition process. The CA remains constant with the further increase of the amount of ZnO nanoparticles in suspensions, as shown in Figure 5.12(d).

The water drop on respect surfaces was shown in the inset of Figure 5.12(a-c).

5.4 Corrosion resistance property of superhydrophobic surfaces prepared by EPD process

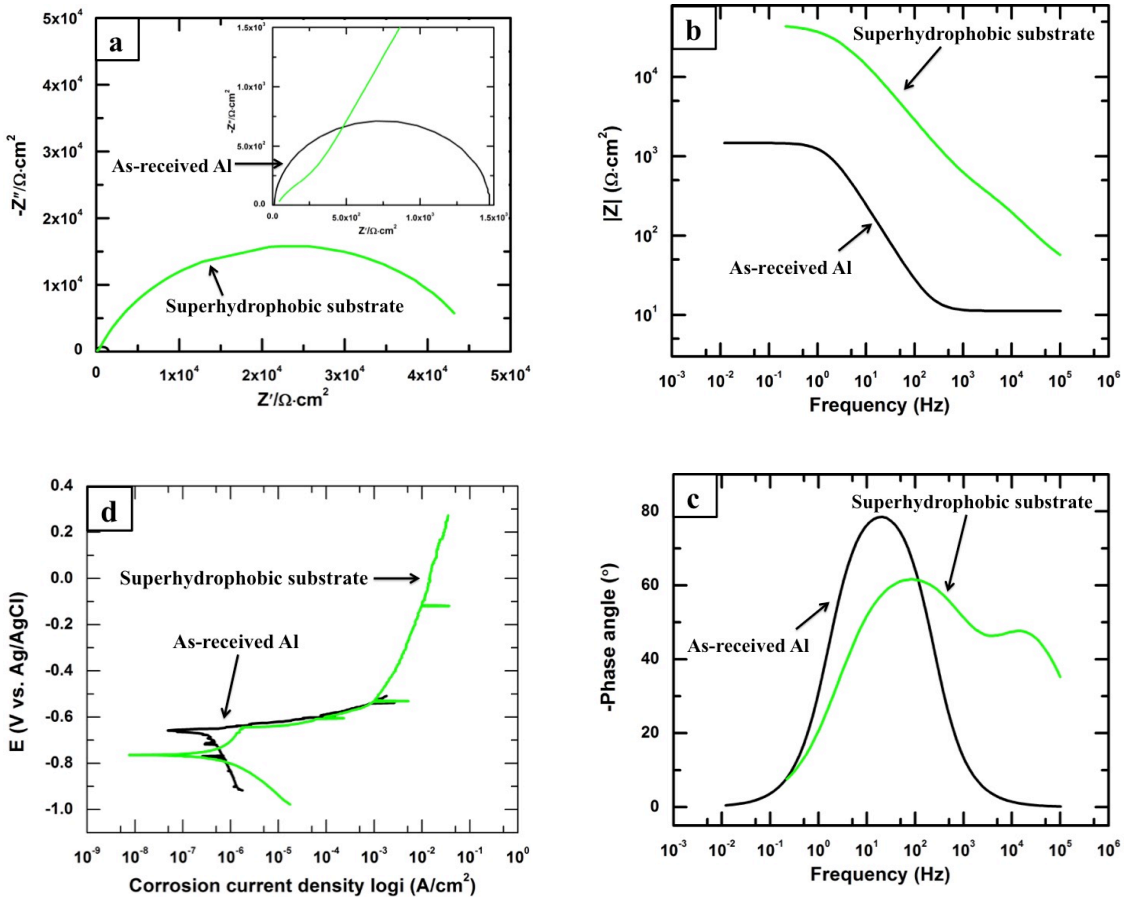

Figure 5. 13(a) Nyquist plots, (b) Bode modulus diagrams and (c) Bode phase angle diagrams of as-received aluminum alloy substrate and superhydrophobic aluminum alloy substrate prepared by EPD process. (d) Potentiodynamic polarization of as-received aluminum alloy and superhydrophobic aluminum alloy substrate.

Electrochemical impedance spectroscopy (EIS) and polarization experiments were carried out to evaluate the corrosion performance of the samples. Figure 5.13 shows the (a) Nyquist and (b & c) Bode plots for the EIS data from the as-received aluminum alloy substrate and the superhydrophobic aluminum alloy substrate prepared by EPD process. The graphs were plotted from the fitted data based on the equivalent electrical circuit (which is the same circuit of superhydrophobic aluminum alloy substrate as prepared by chemical etching process as shown in Chapter 4, Figure 4.8(d)). The charge transfer resistance (R_{ct}) of as-received aluminum alloy substrate is found to be 1.46 $k\Omega \cdot cm^2$, but the superhydrophobic aluminum alloy substrate prepared by EPD process is as high as 73.4 $k\Omega \cdot cm^2$. Further, the modulus $|Z|$ value of as-received aluminum alloy substrate is enhanced from 1.06 $k\Omega \cdot cm^2$ to 43.6 $k\Omega \cdot cm^2$. The Bode phase plot of the superhydrophobic substrate exhibits the two time constants, as shown in Figure 5.13(c), similar as the superhydrophobic aluminum alloy substrate prepared by chemical etching process. It is evident that R_{ct} and modulus $|Z|$ value of superhydrophobic aluminum alloy substrate is higher than that of the as-received aluminum alloy substrate. The impedance

in the low frequency region is reported to depend on the properties of protective layer, and a higher |Z| value corresponds with a higher corrosion resistance. Therefore, the corrosion resistance of the superhydrophobic aluminum alloy substrate is better than the as-received substrate.

In the polarization experiment in Figure 5.13(d), the as-received aluminum alloy substrate exhibited a corrosion current density (I_{corr}) of 400 nA/cm^2 and polarization resistance (R_p) of 50 kΩ·cm^2. The superhydrophobic aluminum alloy substrate displays a similar R_p of 55 kΩ·cm^2. It indicated that the superhydrophobic surfaces prepared by EPD process didn't increase the corrosion resistance property as compared with the as-received aluminum alloy substrate.

5.5 Summary

The one-step electrophoretic deposition (EPD) process has been developed to prepare superhydrophobic thin films on aluminum alloy substrates using stearic acid functionalized ZnO nanoparticles.

In the study of effect of bath temperature on the superhydrophobicity, the thickness

of the thin films increased with the increase of the EPD bath temperature. XRD and FTIR studies confirmed the presence of stearic-acid-functionalized ZnO particles in the thin films. The surface morphology of the thin film shows large number of micro-nanorough clusters of SA-functionalized ZnO nanoparticles and their intensity increases with the increase of bath temperatures. The water contact angle of 155 ± 3° with roll-off property has been observed on the film that was grown at bath temperatures of 50°C. Furthermore, the activation energy for electrophoretic deposition of SA-functionalized ZnO nanoparticle is calculated to be 0.50 eV.

In the study of effect of time on the superhydrophobicity, the amount of ZnO nanoparticles deposited on aluminum alloy surfaces was found to increase with the elongation of EPD time. The superhydrophobicity of modified aluminum alloy surfaces was found to increase when the EPD time less than 10min but decrease with the further elongation of EPD time in terms of both static and dynamic contact angles. 10 minutes was found to be the optimum EPD time to obtain superhydrophobic aluminum alloy surface with SA-functionalized ZnO nanoparticles suspensions, showing a contact angle

of 156° and contact angle hysteresis of 3°.

Furthermore, in the study of effect of the amount ZnO on the superhydrophobicity, the amount of deposited ZnO was found to increase as a function of the concentration of ZnO, and the contact angle of the modified surfaces was increased up to 158° with the increased concentration, and being stable with the further increasing concentration of 0.5 g-2 g.

In the study of corrosion resistance study of superhydrophobic aluminum alloy substrate prepared by EPD process, the polarization resistance of as-received aluminum alloy substrate was found to increase from 50 to 55 $k\Omega \cdot cm^2$ after transforming it to superhydrophobic, indicating that the anti-corrosion property of superhydrophobic aluminum alloy substrate didn't increase obviously as compared with as-received substrate.

References

(1) Barthlott, W.; Neinhuis, C. *Planta*, **1997**, *202*, 1.
(2) Gao, X. *Nature*, **2004**, 432, 36.
(3) Huang, Y.; Sarkar, D.K.; Chen, X.G. *Materials Letters*, **2010**, 64, 2722.

(4) Huang, Y.; Sarkar, D.K.; Chen, X.G. *Nano-micro letters*, **2011**, 3, 160.

(5) Paul, G.K.; Ghosh, R.; Bera, S.K.; Bandyopadhyay, S.; Sakurai, T.; Akimoto, K. *Chemical Physics Letters*, **2008**, 463, 117.

(6) Gurav, K.V.; Fulari, V.J.; Patil, U.M.; Lokhande, C.D.; Joo, O.-S. *Applied Surface Science*, **2010**, 256, 2680.

(7) Goldberger, J.; Sirbuly, D.J.; Law, M.; Yang, P. *The Journal of Physical Chemistry B*, **2004**, 109, 9.

(8) Ding, M.; Yao, B.; Shulin, E.; Guo, Z.; Zhang, L.; Shen D. *Optics express*, **2012**, 20, 13657.

(9) Basak, D.; Amin, G.; Mallik, B.; Paul, G.K.; Sen, S.K. *Journal of Crystal Growth*, **2003**, 256, 73.

(10) Laurenti, M.; Cauda, V.; Gazia, R.; Fontana, M.; Rivera, V.F.; Bianco, S.; Canavese, G. *European Journal of Inorganic Chemistry*, **2013**, 2013, 2520.

(11) Siddaramanna, A.; Saleema, N.; Sarkar, D.K. *Applied Surface Science*, **2014**, 311, 182.

(12) Li, M.; Liu, H.; Song, Y.; Jiang, L.; Zhu, D. *Journal of Physical Chemistry*, **2003**, 107, 9954.

(13) Lee, T.-C.; Wang, W.-J.; Han, T.-Y. *Journal of Adhesion Science and Technology*, **2009**, 23, 1799.

(14) Tarwal, N.L.; Patil, P.S. *Applied Surface Science*, **2010**, 256, 7451.

(15) Tarwal, N.L.; Rajgure, A.V.; Inamdar, A.I.; Devan, R.S.; Kim, I.Y.; Suryavanshi, S.S.; Ma, Y.R.; Kim, J.H.; Patil, P.S. *Sensors and Actuators A: Physical*, **2013**, 199, 67.

(16) Mondal, C.; Ganguly, M.; Sinha, A.K.; Pal, J.; Pal, T. *RSC Advances*, **2013**, 3, 5937.

(17) Yang, S.; Cai, W.; Yang, J.; Zeng, H. *Langmuir*, **2009**, 25, 8287.

(18) Besra, L.; Liu, M. *Progress in Materials Science*, **2007**, 52, 1.

(19) Joung, Y.S.; Buie, C.R. *Langmuir*, **2011**, 27, 4156.

(20) Ogihara, H.; Katayama, T.; Saji, T. *Journal of Colloid and Interface Science*, **2011**, 362, 560.

(21) Ogihara, H.; Okagaki, J.; Saji, T. *Chemistry Letters*, **2009**, 38, 132.

(22) Huang, Y.; Sarkar, D.K.; Chen, X.G. *Advanced Materials Research*, **2012**, 497.

(23) Yin, X.O.; Liu, X.Z.; Wang, L.; Liu, B. *Electrochemistry Communications*, **2010**, 12 1241.

(24) Huang, Y.; Sarkar, D.K.; Gallant, D.; Chen, X.G. *Applied Surface Science*, **2013**, 282, 689.

(25) ZnO JCPDS # [00–003–0888].

(26) Al JCPDS # [01-085-1327].

(27) Mohammadi, M.R.; Ordikhani, F.; Fray, D.J.; Khomamizadeh, F. *Particuology*, **2011**, 9, 161-169.

(28) Saleema, N.; Farzaneh, M. *Applied Surface Science*, **2008**, 254, 2690.

(29) Ogihara, H.; Okagaki, J.; Saji, T. *Langmuir*, **2011**, 27, 9069.

(30) Chen, H.W.; Lin, C.Y.; Lai, Y.H.; Chen, J.G.; Wang, C.C.; Hu, C.W.; Hsu, C.Y.; Vittal, R.; Ho, K.C. *Journal of Power Sources*, **2011**, 196, 4859.

(31) Verde, M.; Peiteado, M.; Caballero, A.C.; Villegas, M.; Ferrari, B. *Journal of Colloid and Interface Science*, **2012**, *373*, 27.

(32) Rodak, D.E.; Cheng, Y.T. *Applied Physical Letter*, **2005**, *86*, 144101.

(33) Cassie, A.B.D.; Baxter S. *Transactions of the Faraday Society*, **1944**, *40,* 546.

(34) Brassard, J.D.; Sarkar, D.K.; Perron, J. *ACS applied materials & interfaces*, **2011**, *3*, 3583.

(35) Wenzel, R.N. *Industrial & Engineering Chemistry*, **1936**, *28*, 988.

(36) Xu, L.; Liao, Q.; Zhang, J.; Xu, D. *The journal of physical chemistry. B.*, **2005**, *109* 13519.

(37) Badre, C.; Pauporté, T.; Turmine, M.; Lincot, D. *Nanotechnology*, **2007**, *18*, 365705.

(38) Gebauer, J.S.; Treuel, L. *Journal of Colloid and Interface Science*, **2011**, *354*, 546-554.

(39) ZnO JCPDS # [00–003–0888].

(40) Cao, G. *Journal of Physical Chemistry* **2004**, *108* 19921.

CHAPTER 6 SUPERHYDROPHOBIC ALUMINUM ALLOY SUBSTRATES PREPARED BY ONE-STEP ELECTRODEPOSITION PROCESS

Due to the corrosion resistance properties of superhydrophobic aluminum alloy substrates prepared by chemical etching and EPD process were not that remarkable, a new approach is developed. In the previous study, superhydrophobic copper surfaces have been fabricated via a one-step electrochemical modification process at a constant DC voltage of 30 V. However, the aluminum alloy surfaces were not able to transform to superhydrophobic by the same method. Therefore, in the previous study, copper microdots were electrodeposited on as-received aluminum alloy surface followed by electrochemical modification with stearic acid with the same process as modification for superhydrophobic copper surfaces.

In the recent study, a modified one-step electrodeposition process has been created for preparing superhydrophobic aluminum alloy surfaces, that is, ethanolic zinc nitrate ($Zn(NO_3)_2$) added in stearic acid as the electrolytic solution was used in one-step electrodeposition at 20 V DC. The result is shown in the section.

6.1 Introduction

Superhydrophobic surfaces, having water repellent property with water contact angle (CA) higher than 150°, have been attracted much increasing attention due to their interesting properties and important applications in fundamental research and industrial application, such as corrosion resistance [1], anti-ice [2], self-cleaning [3], non-adhesion [4] et al.

Recently, various methods have been explored to fabricate superhydrophobic substrates, such as sol-gel process [5, 6], plasma treatment [7], chemical vapor deposition [8], chemical etching [9], electrodeposition [10], et al.. Generally, most of the methods usually require two steps: roughening a surface and lowing its surface energy. In the previous study, a one-step electrochemical process has been developed to fabricate

superhydrophobic copper surfaces with ethanolic stearic acid (SA) solution [11]. However, due to the aluminum alloy substrate cannot be modified with the same technique, therefore, a modified two-step process was applied to prepare superhydrophobic aluminum alloy substrate, that is, electrodeposition of copper on aluminum alloy substrates followed by electrochemical modification using ethanolic stearic acid solution [10]. Furthermore, to simplify the process, the one-step electrophoretic deposition (EPD) has been presented to prepare superhydrophobic aluminum alloy substrates, via SA-functionalized zinc oxide (ZnO) deposited on cathodic substrate as a function of EPD temperature [12]. In the recent study, a new one-step electrodeposition is used to fabricate superhydrophobic aluminum alloy substrates with electrolytic solution of SA mixing with zinc nitrate ($Zn(NO_3)_2$).

In the literature, some authors have used the fatty acids mixing with some inorganic salts as the electrolyte in the electrodeposition process to prepare superhydrophobic surfaces in the application of DC voltage [13-17]. Superhydrophobic cerium substrates have been fabricated with cerium chloride ($CeCl_3 \cdot 7H_2O$) mixing with myristic acid

($CH_3(CH_2)_{12}COOH$) in the application of 10-60 V DC voltage [13]. Similarly, Liu et al. [14] studied the superhydrophobic coating on magnesium alloy substrate with cerium nitrate hexahydrate ($Ce(NO_3)_3 \cdot 6H_2O$) and myristic acid at 30 V for 10 min. Moreover, superhydrophobic copper or steel substrates were fabricated by electrodeposition in an electrolyte solution containing ethanolic manganese chloride ($MnCl_2 \cdot 4H_2O$) and myristic acid [15]. Their group has also studied the superhydrophobic copper substrates by using nickel chloride ($NiCl_2 \cdot 6H_2O$) and myristic acid as the electrolyte in the one-step electrodeposition process [16]. In a similar study from their group, the electrolyte was containing ethanolic lanthanum chloride ($LaCl_3 \cdot 6H_2O$) and myristic acid for preparing superhydrophobic surfaces [17]. However, neither of them mentioned the importance of the molar ratio between the salt and the fatty acid.

In the recent study, a slight adding of $Zn(NO_3)_2$ in ethanolic SA as the electrolyte in the one-step process for preparing superhydrophobic aluminum alloy substrates, and a varied molar ratio (Zn^{2+}/SA) was found to be a important factor to the superhydrophobic properties. Furthermore, the corrosion resistance property of the modified aluminum

alloy substrates at different molar ratio (Zn^{2+}/SA) was investigated as compared with the as-received aluminum alloy substrate by potentiodynamic polarization technique as well as electrochemical impedance spectroscopy (EIS).

6.2 Experiments

0.01 M zinc nitrate ($Zn(NO_3)_2$) and 0.01 M stearic acid (SA) solution with different molar ratio (Zn^{2+}/SA) was mixing followed by stirring for 1 hour. The cleaned AA 6061 aluminum alloy substrate as cathode was deposited in the $Zn(NO_3)_2$ and SA mixing solution at 20 V for 10 min. The morphological analyses of the samples were performed using a Scanning Electron Microscope (SEM, JEOL JSM-6480 LV). Surface roughness was measured using optical profilometer. The chemical composition is analyzed using Fourier Transform Infrared Spectroscopy (FTIR) as well as X-ray diffraction (XRD). The wetting characteristics of the sample surfaces were carried out by measuring static contact angles and dynamic contact angle using a First Ten Angstrom contact angle goniometer. The static contact angle has been abbreviated as CA and the dynamic contact angle has been abbreviated as contact angle hysteresis (CAH). The corrosion resistance

performance of the samples was investigated via both potentiodynamic polarization experiments as well as electrochemical impedance spectroscopy (EIS). Electrochemical experiments were performed using a PGZ100 potentiostat and a 300 cm^3 - EG&G PAR flat cell (London Scientific, London, ON, Canada), equipped with a standard three-electrode system with an Ag/AgCl reference electrode, a platinum (Pt) mesh as the counter electrode (CE), and the sample as the working electrode (WE). For the potentiodynamic polarization experiments, the potential was scanned from -250 mV to +1000 mV of OCP value in a 0.5 M (3 wt.%) NaCl solution. The electrochemical impedance spectroscopy (EIS) technique was performed in the frequency ranges between 0.01 Hz and 100 kHz with sine-wave amplitude of 10 mV at room temperature.

6.3 Results and discussion

6.3.1 Material characterizations

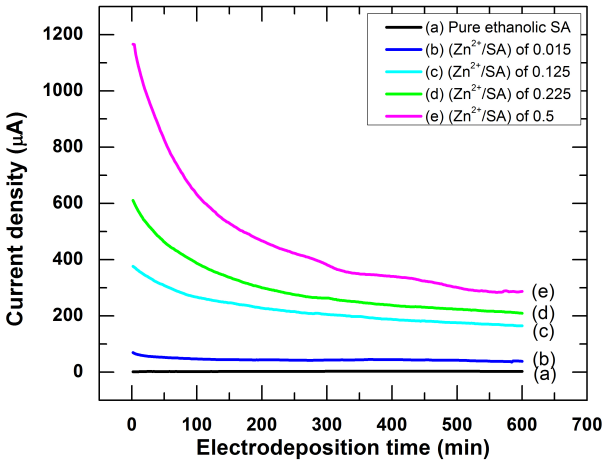

Figure 6. 1 Current density variation as a function of deposition time with (a) pure ethanolic SA and (b-e) molar ratios (Zn^{2+}/SA) of 0.015, 0.125, 0.225, 0.5, respectively, in the one-step electrodeposition process at 20 V for 10 min.

In the electrodeposition process, the pure ethanolic SA solution or the ethanolic SA mixing with $Zn(NO_3)_2$ at molar ratios (Zn^{2+}/SA) from 0.015 to 0.5 was utilized as electrolytic solution in the one-step electrodeposition process at 20 V DC. The resulting current density–time curves are shown in Figure 6.1. The current density in the electrodeposition process with pure ethanolic SA electrolyte (curve a) stabilized at 1 μA

in 10 min electrodeposition time, indicating the electrode didn't have a big difference in the electrodeposition process. However, when the electrodeposition is carried out with SA mixing with $Zn(NO_3)_2$ electrolytic solution, the initial current density (curve b-e) was found to increase to 69, 376, 610 and 1165 μA at molar ratios (Zn^{2+}/SA) of 0.015, 0.125, 0.225 and 0.5, respectively. It is important to note that the appearance of Zn^{2+} ions in the electrolytic solution is responsible for the large increase of the current density, as compared with the pure SA electrolyte. It is also observed that the current density at different molar ratios (Zn^{2+}/SA) decreased gradually in the electrodeposition process, which indicated that the electrode is changing to be more insulating. In other word, an insulating layer is forming on the electrode during the electrodeposition in SA mixing with $Zn(NO_3)_2$ electrolytic solution.

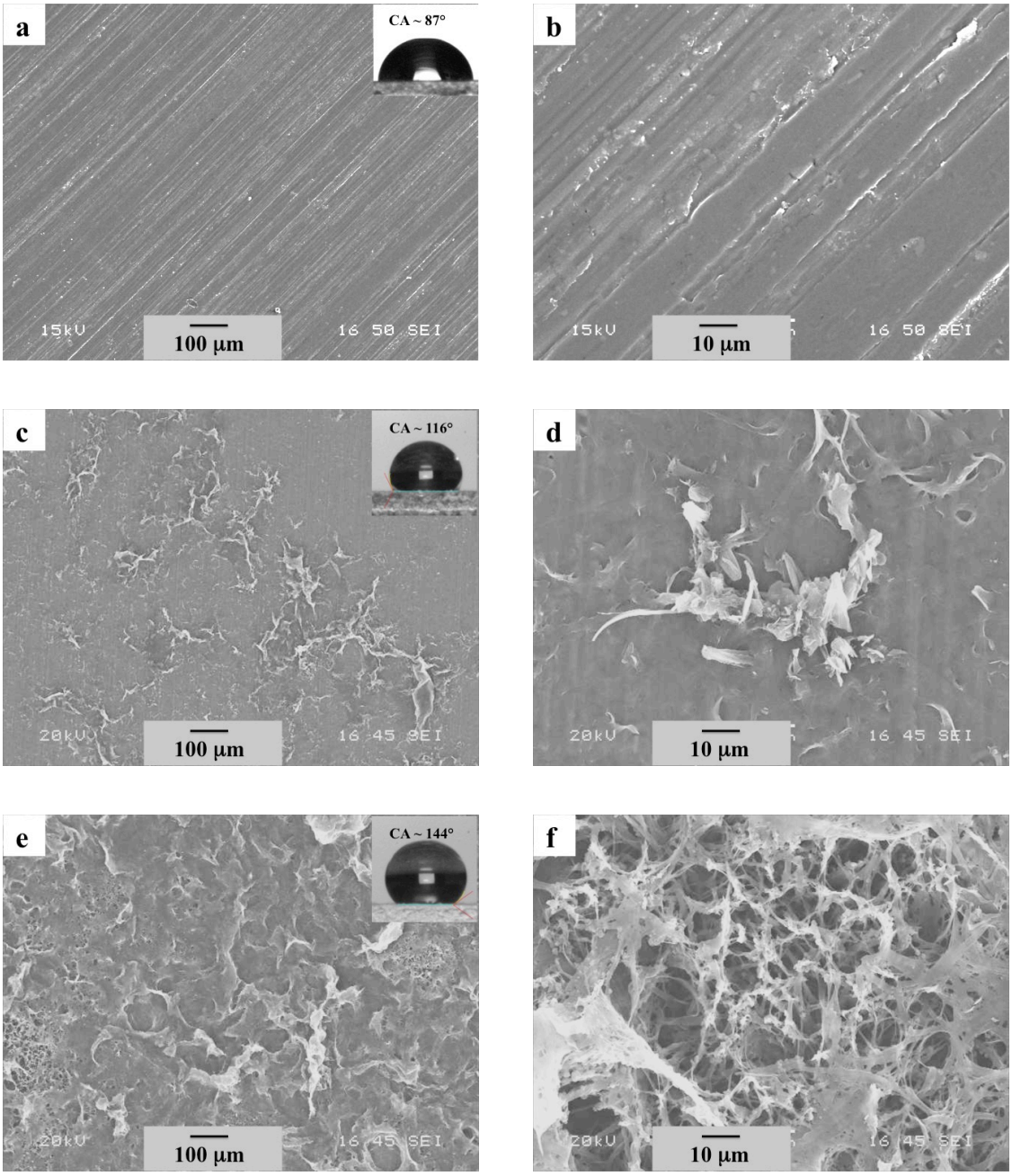
a
CA ~ 87°
15kV
100 µm
16 50 SEI
b
15kV
10 µm
16 50 SEI
c
CA ~ 116°
20kV
100 µm
16 45 SEI
d
20kV
10 µm
16 45 SEI
e
CA ~ 144°
20kV
100 µm
16 45 SEI
f
20kV
10 µm
16 45 SEI

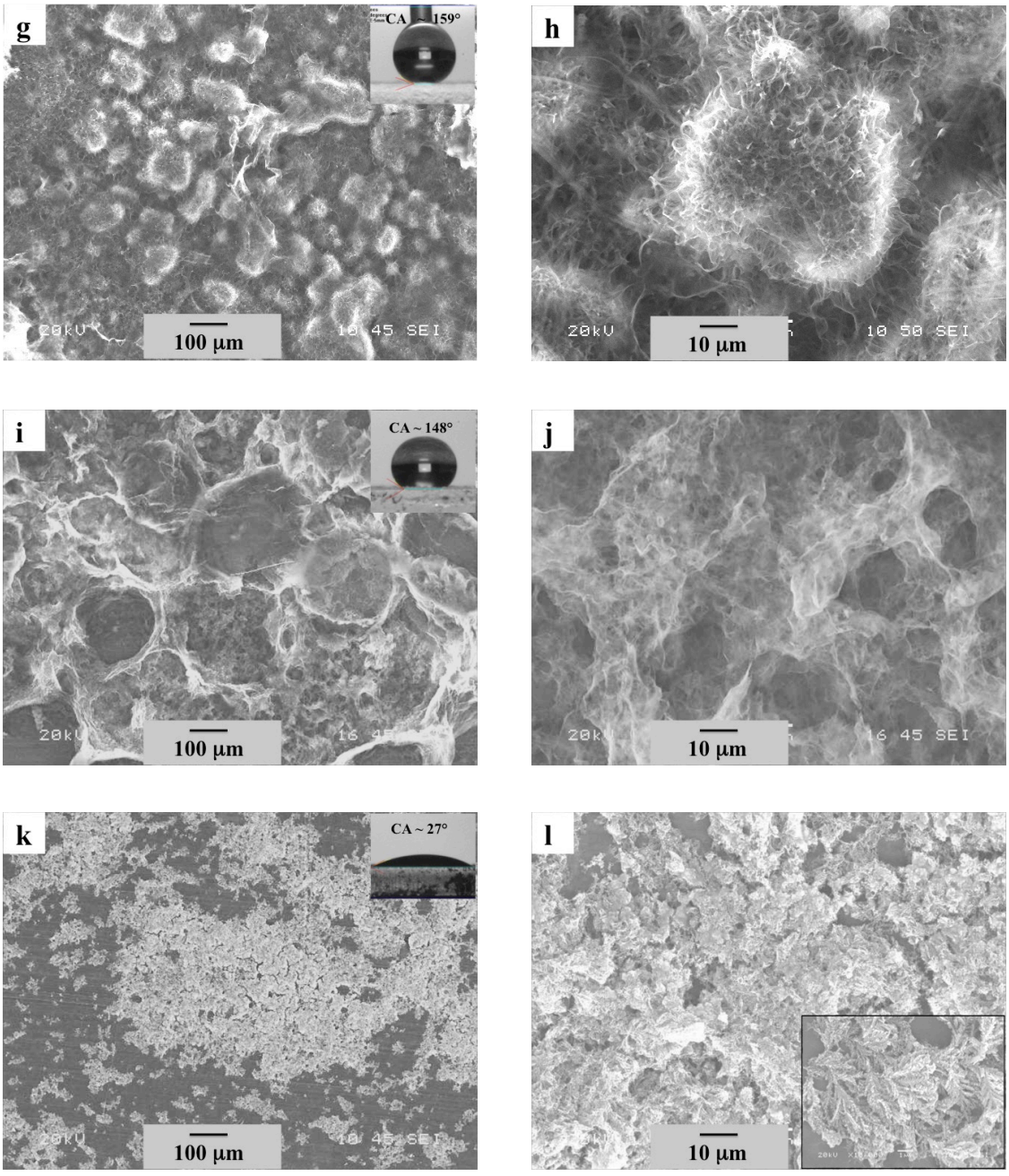

Figure 6. 2 Low and high magnification of SEM images of the surfaces of (a & b) as-received aluminum alloy substrate and the modified substrates at molar ratio (Zn^{2+}/SA) of (c & d) 0.015; (e & f) 0.125; (g & h) 0.225, (i & j) 0.5 and (k & l) infinite at 20V for 10 minutes. The inset images show the water contact angle of the respective surfaces.

Figure 6.2(a & b) shows the surface of as-received aluminum alloy substrate in low and high magnifications by SEM, respectively. The rolled sheets generally show the rolled lines on its surface and therefore, will have a certain surface rms roughness of 0.45 ± 0.03 μm and CA of 87 ± 3° in Figure 6.2(a & b). The pure ethanolic SA electrolytic solution cannot modify the aluminum alloy substrate as copper substrate [11], which has a CA of 105 ± 2°. Therefore, a modified one-step process, $Zn(NO_3)_2$ was added in SA electrolyte at different molar ratio (Zn^{2+}/SA) to prepare superhydrophobic aluminum alloy substrates. The morphology of modified aluminum alloy substrate at molar ratio (Zn^{2+}/SA) of 0.015 has been shown in Figure 6.2(c & d), where the sparse formation of micro-nanofibres was observed, with an increasing rms roughness and CA of 0.5 ± 0.15 μm and 117 ± 1°, respectively. The increase of CA is due to increased surface roughness as well as the presence of zinc stearate (ZnSA), which reduces the surface energy due to the presence of $-CH_2$ and $-CH_3$ radicals (as discussed in Figure 6.3). Furthermore, the number density of the micro-nanofibres was found to increase, and the porous net-like structure was formed associated with the increasing molar ratio (Zn^{2+}/SA) of 0.125.

Evidently, a dramatic increased rms roughness from 0.5 ± 0.15 μm to 4.48 ± 0.22 μm, resulted from the variation of the surface morphology, and the CA was found to increase from 117 ± 1° to 144 ± 4°.

It is however, evident from Figure 6.2(g & h) that the increase of the molar ratio (Zn^{2+}/SA) to 0.225 resulted in the formation of a rougher surface with features revealing flower-like micro-nanostructures (Figure 6.2(h)). The net-like structures clustered together to resemble a flower, by increasing the molar ratio (Zn^{2+}/SA) from 0.125 to 0.225. The appearance of the flower-like structures leads to a large surface rms roughness of 7.11 ± 0.42 μm as well as a high CA of 159 ± 1° in Figure 6.4. In the previous study, copper stearate flower-like structure was also fabricated on copper substrate in the electrochemical modification process with ethanolic SA solution at 30 V, having a CA of 153° [11]. The flower-like structures are comparable to that of the lotus leaves promoting entrapment of air beneath a water drop placed on its surface [18]. However, the morphology changed to cloud-like structures at the molar ratio (Zn^{2+}/SA) of 0.5 in Figure 6.2(i & j), which is resulted from the more Zn^{2+} in the electrolyte. A decreased surface rms

roughness of 5.2 ± 0.62 μm is responsible for the decrease of the air fraction on the surface without flower-like structures, and thereby decreased the surface CA 148 ± 4° combined with the less low surface energy material SA. To investigate the effect of Zn^{2+} in the electrodeposition process, the morphology of the modified aluminum alloy substrate at molar ratio (Zn^{2+}/SA) of infinite (with pure $Zn(NO_3)_2$) was presented in Figure 6.2(k & l). The feature-like structure was formed on the surface non-uniformly, and the CA decreased to only 27°.

In the electrodeposition of lanthanum myristate copper substrate for preparing superhydrophobic copper substrates by Chen et al. [17], the effect of electrodeposition time on the superhydrophobicity was studied. The single flower-like structure composed of many nanopetals with 1-4 μm wide and several tens of micrometers long was found to form in electrodeposition for 15 min at 30 V DC, and a high CA of 160° was obtained on the modified surface, similar as our optimum CA at molar ratio (Zn^{2+}/SA) of 0.225. Moreover in their study, the flower size became narrower and the interconnected flowers cover the copper surface at a longer electrodeposition time of 90 min, and finally, the

narrower flower-like structures merge together to form many nanorods, completely covered the copper substrate. In another study of them, a one-step process is used to fabricate superhydrophobic copper substrate in an electrolyte solution containing manganese chloride and myristic acid. The microstructures of the modified surface with different electrodeposition time by SEM were presented in their study [15]. The small particles for 1 min electrodeposition were found to stack together forming the bigger clusters when the electrodeposition time to 10 min, and the CA of the modified substrate increased from 152° to 163°. However, by further increasing the electrodeposition time to 25 min, the clusters merge to large-scale structures above 50 μm, and the CA decreased to 153°. The decrease of CA was because that the formed structures are too large to suppose the water drop.

The effect of applied potential of electrodeposition was investigated by Liu et al. [13], in the one-step electrodeposition of cerium myristate on the copper substrate. At the low DC voltage of 10 V, a few stalk-like particles were sparsely distributed on the copper substrate, where has a CA of 132°. When the electrodeposition voltage was increased to

30 V, the stalk-like structure evolved into the blossoming flower-like structure, and the CA of the modified substrate increased to around 150°. Furthermore, the flower-like pattern became more uniform at a higher DC voltage of 50 V, and a highest CA of 162° was observed on the modified substrate.

In the study of Chen, the electrolytic solution was containing nickel chloride and myristic acid for preparing superhydrophobic copper substrate in the electrodeposition process [16]. The variation of CA as a function of the concentration of nickel chloride revealed that the concentration of 0.074 M of nickel chloride with 0.08 M myristic acid contributed the optimum CA of 164°. However, the surface morphologies of the modified surfaces with different concentration were not presented.

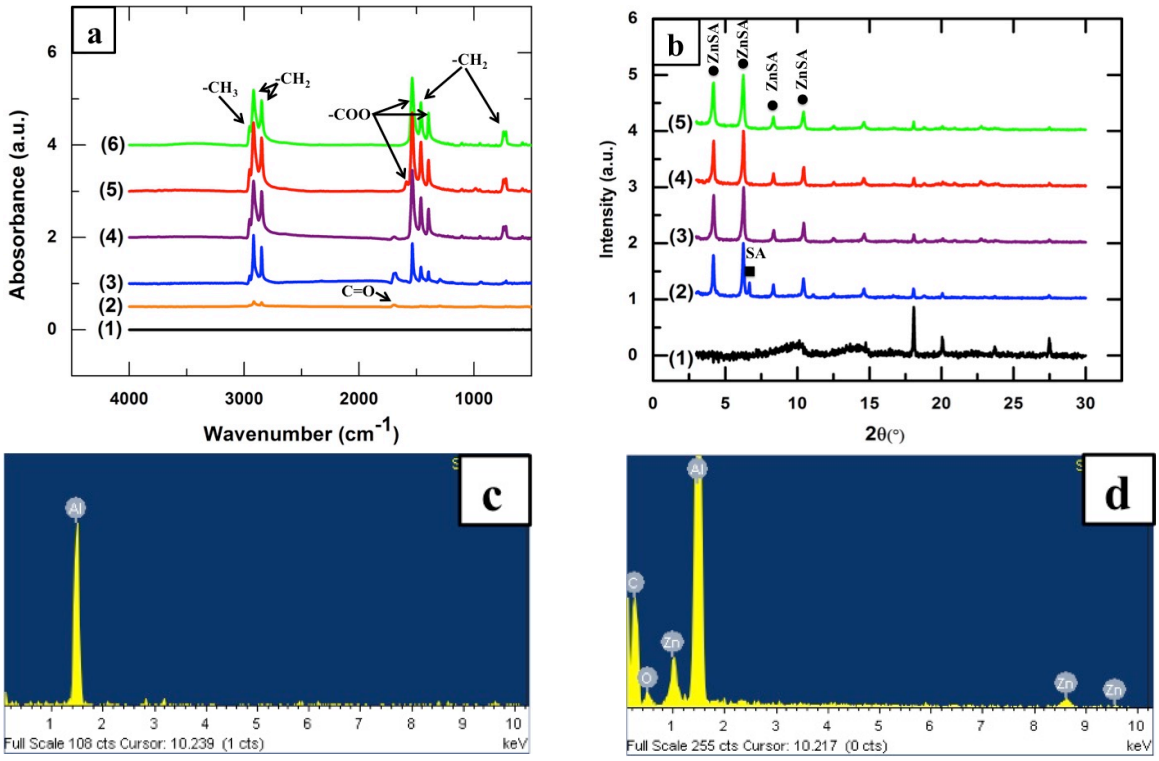

Figure 6. 3 FTIR spectra of the (a1) as-received aluminum alloy substrate, (a2) SA prepared by 10 layers drop coating of 0.01 M SA solution on as-received aluminum alloy substrate, (a3-a6) the modified aluminum alloy substrates at molar ratio (Zn^{2+}/SA) of 0.015, 0.125, 0.225 and 0.5, respectively. (b) XRD patterns of (b1) the as-received aluminum alloy substrate and (b2-b5) the modified aluminum alloy substrates at molar ratio (Zn^{2+}/SA) of 0.015, 0.125, 0.225 and 0.5, respectively. (c & d) EDX spectrum of as-received aluminum alloy substrate and modified aluminum alloy substrates at molar ratio (Zn^{2+}/SA) of 0.225, respectively.

Figure 6.3(a1) shows the FTIR spectrum of as-received aluminum alloy substrate, and no distinct peak was observed on the spectrum of the as-received aluminum alloy

substrate. However, in the spectrum of SA, prepared by 10 layers drop coating of 0.01 M SA solution on as-received aluminum alloy substrate, the antisymmetric and symmetric stretching vibrations (ν_aCH_2 and ν_sCH_2) at 2922 and 2850 cm^{-1}, which are comparable with those of the antisymmetric at 2962 cm^{-1} methyl stretching bands (ν_aCH_3), respectively [12]. Those three peaks are more visible in the spectra of modified aluminum alloy substrates at different molar ratio (Zn^{2+}/SA) as shown in Figure 6.3(a3-a6). Furthermore, another band observed in the spectrum of SA at 1700 cm^{-1} is assigned to the C=O stretching vibration in the unionized carboxylic group. However, the proton exchange between carboxylic acid and metal salt was proceeded gradually with the increase of molar ratio (Zn^{2+}/SA), since the intensity of C=O stretching band of SA at about 1700 cm^{-1} decreased with an increasing molar ratio (Zn^{2+}/SA) and finally disappeared in the spectrum at molar ratio (Zn^{2+}/SA) of 0.225.

In the FTIR spectra of modified aluminum alloy substrates at different molar ratio (Zn^{2+}/SA) in Figure 6.3(a3-a6), some more peaks were found. The absorption bands at 1540 and 1398 cm^{-1} are, respectively, assigned to antisymmetric and symmetric

stretching vibrations of the –COO group because the carboxylic acid group was ionized and metal Zn^{2+} ions were introduced into the film. Furthermore, another weak peak at 1588 cm^{-1} was found to be the carboxylate vibrations ν_{as}(COO) for the molar ratio (Zn^{2+}/SA) of 0.225 [19]. The bands at 1460 cm^{-1}, 722 cm^{-1} and 740 cm^{-1} ascribed to the -CH_2 vibrations of the stearic groups [19, 20]. The peak at 1106 cm^{-1} is arising from C-O bonding [21].

The appearance of –COOZn peaks for the modified aluminum alloy substrates at different molar ratio (Zn^{2+}/SA) is in good agreement with the FTIR spectrum of the superhydrophobic aluminum alloy substrate fabricated by electrophoretic deposition (EPD) process using SA-functionalized zinc oxide (ZnO) nanoparticles in the previous study [12]. It is also in good agreement of that of ZnSA observed by Serdar et al., indicated the formation of ZnSA on the modified aluminum alloy substrates in one-step electrodeposition process [22]. Furthermore, it is found that the intensity of the peaks –COO, -CH_2 and –CH_3 was increased with the increasing molar ratio (Zn^{2+}/SA). An optimum intensity was appeared at molar ratio (Zn^{2+}/SA) of 0.225, and the peak intensity slightly

decreased at molar ratio (Zn^{2+}/SA) of 0.5. It is worthy to note that, the presence of the weak peak of –COO at 1588 cm^{-1} appeared only in the spectrum at molar ratio (Zn^{2+}/SA) of 0.225, which further confirmed the optimum peak intensity of -COO at molar ratio (Zn^{2+}/SA) of 0.225.

Figure 6.3(b) shows the X-ray diffraction (XRD) patterns of (b1) as-received aluminum alloy substrate and (b2-b5) the modified aluminum alloy substrates at molar ratio (Zn^{2+}/SA) of 0.015, 0.125, 0.225 and 0.5 in the 2θ scan range of 3–30°. As compared with the pattern of as-received aluminum alloy substrate, the characteristic peaks of ZnSA at 4.2°, 6,26°, 8.3° and 10.4° were observed on the patterns of the modified aluminum alloy substrates [22], respectively, confirming the ZnSA deposition on the modified aluminum alloy substrates, which is complementary with the FTIR spectra in Figure 6.3(a3-a6). It is to be mentioned that, the characteristic peak of SA at 6.68° in the pattern of molar ratio (Zn^{2+}/SA) of 0.015. It appeared due to the excess volume of SA in the mixture solution of SA and $Zn(NO_3)_2$, which disappeared with the increased molar ratio (Zn^{2+}/SA). It is in good agreement with the FTIR observation, where the C=O peak

was observed in the spectrum of SA (Figure 6.3(a2)) but disappeared at the molar ratio (Zn^{2+}/SA) of 0.225. Furthermore, an optimum intensity of four ZnSA peaks at low angle was found at the molar ratio (Zn^{2+}/SA) of 0.225. It is also in good agreement with the FTIR result, where an optimum intensity of –COO, -CH_2 and-CH_3 bonding were observed at molar ratio (Zn^{2+}/SA) of 0.225.

Figure 6.3(c & d) presents the as-received aluminum alloy substrate and EDX spectrum of modified aluminum alloy substrates at molar ratio (Zn^{2+}/SA) of 0.225, respectively. The Al peak in both spectra of as-received substrate and modified substrate comes from the aluminum alloy substrate. As compared with as-received substrate, the appearance of Zn, C and O after electrodeposition process confirmed the formation of ZnSA on the substrate. It is complementary with the FTIR and XRD results.

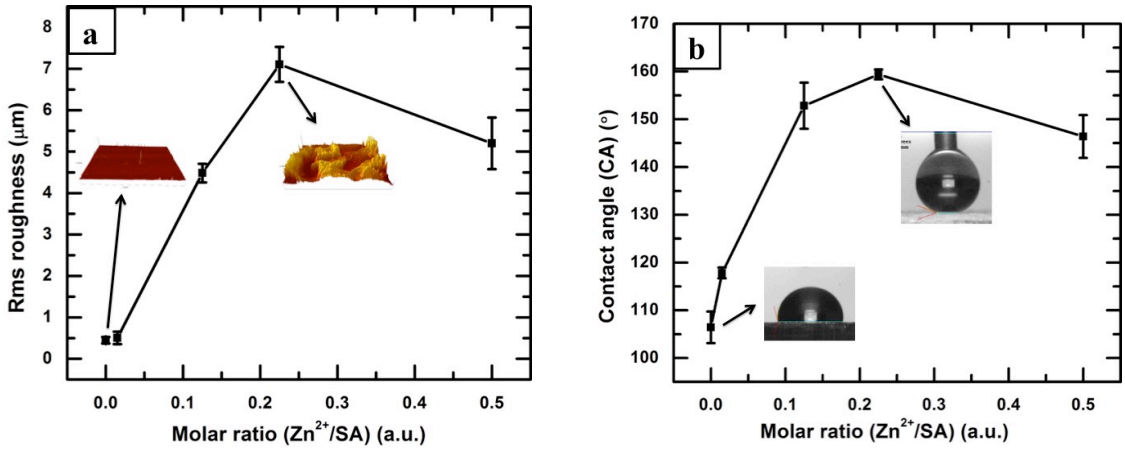

Figure 6. 4(a) Surface rms roughness and (b) CA variation as a function of the molar ratio (Zn^{2+}/SA) in the one-step electrodeposition process. The inset images show (a) 3D images of the rough surfaces and (b) the images of water drops at molar ratio (Zn^{2+}/SA) of 0 and 0.225.

Therefore, the air fraction was increased due to the water cannot fill the rough surface which was covered by low surface energy material ZnSA. This results in a superhydrophobic surface having an optimum contact angle of 159°. However, a decreased tendency was observed when the molar ratio (Zn^{2+}/SA) more than 0.225. The molar ratio (Zn^{2+}/SA) of 0.5 provides the surface rms roughness of 5.2 μm and CA of 146°. The decrease in the surface rms roughness is due to the disappearance of flower-like micro-nanostructures as evidence in SEM images (Figure 6.2(g & i)) for an increase in the molar ratio (Zn^{2+}/SA) from 0.225 to 0.5. A decreased surface rms

roughness is responsible for the decrease of the air fraction of the rough surface, and thereby decreased the surface CA combined with the less low surface energy material SA. Siddaramanna et al. studied the different molar ratio between stearic acid and ZnO in the preparation of SA-functionalized ZnO superhydrophobic surfaces [23]. The surface rms roughness was found to decrease from 6 ± 1.0 μm to 4 ± 0.9 μm due to the reduced particle size from 2.21 μm to 0.64 μm formed on the surface at the molar ratio (SA/Zn^{2+}) from 0.0125 to 0.125. As a result, the CA decreased from 165 ± 1.6° to 155 ± 2.1°.

6.3.2 Corrosion resistances of the superhydrophobic surfaces

To evaluate corrosion resistance performance of the superhydrophobic aluminum alloy surface fabricated by the electrodeposition process, corrosion tests were carried out using electrochemical impedance spectroscopy (EIS) and potentiodynamic polarization experiments. According to the results above, the optimum superhydrophobic sample prepared at molar ratio (Zn^{2+}/SA) of 0.225 for 10 minutes were chosen.

Figure 6.5 illustrates the variation of open circuit potential (OCP) with the prolongation of time on superhydrophobic aluminum alloy substrate prepared by

electrodeposition process. In Figure 6.5(a), when the sample was initially put in the corrosive solution, the OCP value shifted between -562 mV to -868 mV into 3.5 h immersion time. It is quite unstable during this period. From 3.5 to 27 h of immersion time, the OCP value varied from -662 mV to -715 mV. It can be seen that the fluctuation of OCP voltage reduces with time and stabilized nearly after 3.5 h. In contrast, the surface of aluminum alloy substrate gets stabilized within 30 minutes of immersion time in the salt solution. The OCP fluctuations of superhydrophobic substrate may be due to the poor wetting as well as protective properties of the superhydrophobic surface with the salt solution. Therefore, The EIS and polarization experiments were performed after 27 h of immersion of the superhydrophobic surface in the salt solution while monitoring the OCP continuously. Figure 6.5(b) shows the variation of OCP value after the first round of EIS test. The OCP value varies from -608 mV to -705 mV into 78 min, and then stabilizes at around -670 mV from 78 min to 700 min. After stabilization, the second round EIS was performed. Then Figure 6.5(c) shows the OCP after the second round of EIS experiment. Figure 6.5(d) shows the OCP values after the third round of EIS

experiment. It is found that, the OCP is always unstable during the initial time. Further, the OCP value didn't change greatly even after around 2 days immersion, which indicated the superhydrophobic substrate was relatively stable without losing all of the coating film.

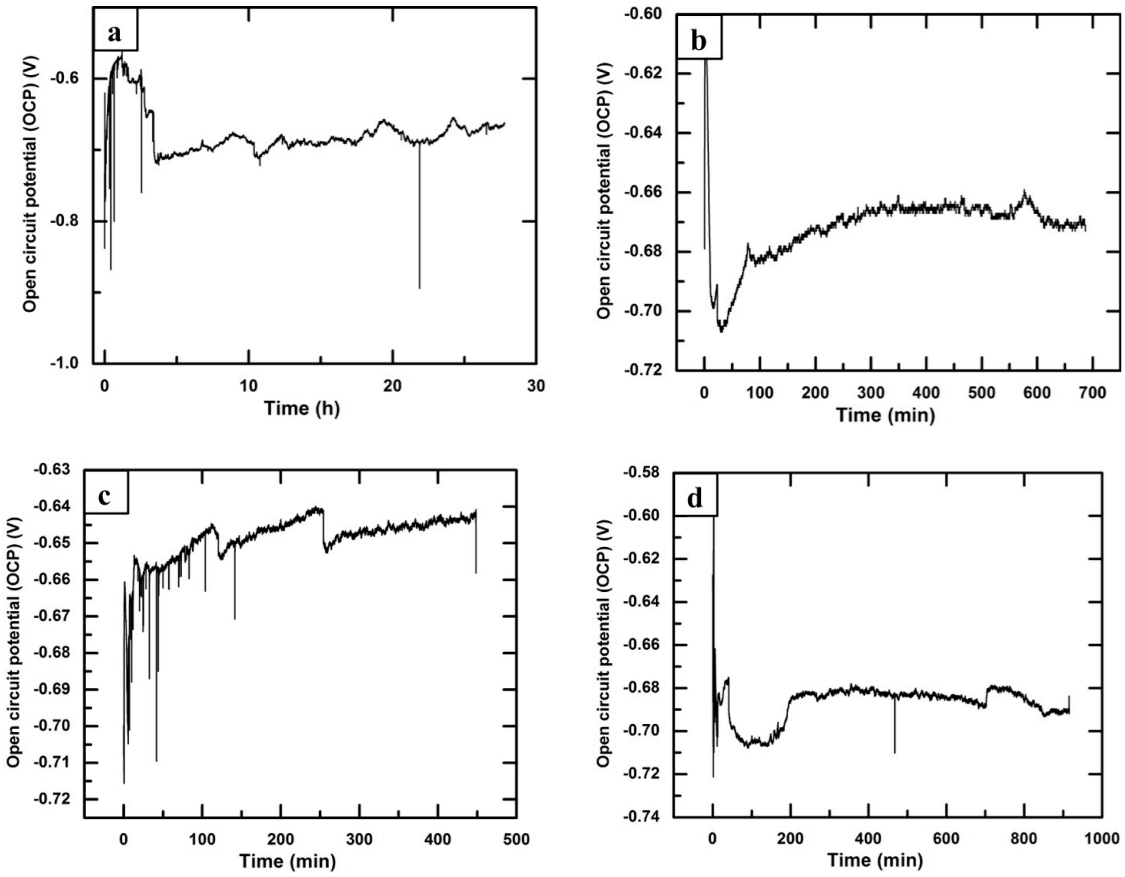

Figure 6. 5 Variation of open circuit potential (OCP) as a function of time on superhydrophobic aluminum alloy substrate prepared by electrodeposition. (a) 27 h OCP as a function of time before the first round EIS test. (b) 12 h OCP time before the second round EIS test. (c) 8 h OCP time before the third round EIS test. (d) 16 h OCP time before the fourth round EIS test.

To evaluate corrosion resistance performance of the superhydrophobic aluminum alloy surface fabricated by the electrodeposition process, corrosion tests were carried out using polarization as well as electrochemical impedance spectroscopy (EIS) after OCP for 27 h.

Figure 6.6(a) shows the polarization curves of as-received aluminum alloy substrate and the modified aluminum alloy substrates at molar ratio (Zn^{2+}/SA) of 0.015, 0.125, 0.225 and 0.5. The electrochemical parameters of corrosion current density (I_{corr}), corrosion potential (E_{corr}) and polarization resistance (R_p) for different samples are presented in Table 6.1. The I_{corr} and R_p of as-received aluminum alloy substrate are 0.4 μA/cm^2 and 50 kΩ·cm^2. The I_{corr} of modified aluminum alloy substrate at molar ratio (Zn^{2+}/SA) of 0.015, 0.125 and 0.225 was decreased to 0.0308, 0.0042 and 0.0025 μA/cm^2, respectively, and R_p increased to 1.38×10^3, 2.72×10^3 and 7.72×10^3 kΩ·cm^2, as presented in Figure 6.6(a) and Table 6.1. It refers the modified aluminum alloy substrates had a better corrosion resistance than the substrate, and the corrosion resistance property was improved with the increase of the molar ratio (Zn^{2+}/SA). However, the modified

aluminum alloy substrate at molar ratio (Zn^{2+}/SA) of 0.5 exhibited a worse corrosion resistance because of its higher I_{corr} of 0.065 μA/cm^2 and a lower R_p of 9.12×10^2 kΩ·cm^2. It happened due to the missing water repellent property at molar ratio (Zn^{2+}/SA) of 0.5, which confirmed by the reduced surface CA (146°) as compared with that of the optimum molar ratio (Zn^{2+}/SA) of 0.225 (159°). It is clear that the CA was proportional related to their corrosion resistance properties. In other words, the superhydrophobicity having a higher CA favored the enhancement of the corrosion resistance for the samples.

Figure 6.6(b) shows Nyquist plots of the as-received aluminum alloy substrate and the modified aluminum alloy substrates at molar ratio (Zn^{2+}/SA) of 0.015, 0.125, 0.225 and 0.5. The individual Nyquist plots are presented in the supporting information (Figure 6.8). Generally, the plot of the substrate represents one capacitive loop ascribed to charge transfer resistance (R_{ct}) in high frequency and one inductive loop associated with the dissolution of the metal substrate in low frequency [14]. The diameter of the capacitive loop related to R_{ct} in the Nyquist plots exhibits the impedance of the samples. The modified aluminum alloy substrates were observed to have higher R_{ct} values as compared with the

as-received aluminum alloy substrate, as presented in Figure 6.6(b) and Table 6.1. It is complementary to the polarization curves, where the I_{corr} of as-received aluminum alloy substrate decreased after modification at different molar ratio (Zn^{2+}/SA). Furthermore, the modified aluminum alloy substrates displayed an increasing R_{ct} values from 52.4 to 1.03×10^4 kΩ·cm^2 at the increasing molar ratio (Zn^{2+}/SA) from 0.015 to 0.225. However, the impedance value was noticed to decrease at the molar ratio (Zn^{2+}/SA) of 0.5. It is in great agreement with the result of the polarization curves, where the modified substrate at molar ratio (Zn^{2+}/SA) of 0.225, having a highest CA of 159°, exhibits a better corrosion resistance property, compared with the other molar ratios (Zn^{2+}/SA) of 0.015, 0.125 and 0.5. It indicates the superhydrophobicity corresponded to the higher corrosion resistance property. It is well known that, the air could be trapped in the groove of the superhydrophobic surfaces. As shown in Figure 5.2(g & h), the flower-like micro-nanostructures consisted of large hills and small papillae, which can easily trap the air within the valley between the hills and form the air packet [4]. The trapped air reduced the actual area of the surface in contact with the water. Due to the presence of the air

layer, it is difficult for the corrosive liquid to contact the substrate. It is in the same schematic of the lotus effect, where the air was filled with gaps and prevents the water drop from the infiltrating the lotus surface.

However, interestingly, the Nyquist plot of the superhydrophobic aluminum alloy substrate at molar ratio (Zn^{2+}/SA) of 0.225 displays two capacitive loops in both high and low frequencies. The plot of the substrate presents one capacitive loop ascribed to R_{ct} in high frequency and one inductive loop associated with the dissolution of the metal substrate in low frequency. It is comparable with the result from Ishizaki et al. [24], who fabricated superhydrophobic magnesium alloy substrate coated with nanostructured cerium oxide film and fluoroalkylsilane molecules. In their corrosion resistance study, the Nyquist plots of superhydrophobic substrates after immersing a range of time were presented. The diameter of the capacitive loop after 24 h was found to be 7.2 k$\Omega \cdot cm^2$, 1430 times smaller than our superhydrophobic aluminum alloy substrate modified at molar ratio (Zn^{2+}/SA) of 0.225, which has an R_{ct} value of 10.3 k$\Omega \cdot cm^2$. It indicated our superhydrophobic substrate shows a better corrosion resistance property. However, it is

to be mentioned that they utilized 5 wt.% NaCl solution in the corrosion tests, higher than ours. It might be one of the reasons of their less corrosion resistance property as compared with ours.

Figure 6.6(c & d) shows the Bode plots of as-received aluminum alloy substrates and the modified aluminum alloy substrates at molar ratio (Zn^{2+}/SA) of 0.015, 0.125, 0.225 and 0.5. Figure 6.7(c) shows the |Z| value as a function of molar ratio (Zn^{2+}/SA) at different frequency. Two phase maxima at relative low and high frequencies were observed on the plot of superhydrophobic aluminum alloy substrates modified at (Zn^{2+}/SA) of 0.225. The high frequency time constant, at round 380 Hz, is related to the superhydrophobic surface formed on the aluminum alloy substrate. Another time constant at around 0.05 Hz can be ascribed to the capacitance of double layer and is shifted to lower frequency than the time constant of as-received aluminum alloy substrate, due to the good barrier properties of the superhydrophobic substrate which suppress the penetration of the NaCl solution to the as-received aluminum alloy substrate. Moreover, the impedance level increased with an increase of the molar ratio (Zn^{2+}/SA) in Figure

6.7(c). The impedance (|Z|) behaviors in the low frequency region depend on the properties of the protective layer. The higher |Z| value of the modified aluminum alloy substrates at higher molar ratio (Zn^{2+}/SA) represents higher corrosion resistance. The |Z| value of modified aluminum alloy substrate at molar ratio (Zn^{2+}/SA) of 0.015 is 52.7 $k\Omega \cdot cm^2$ at low frequency of 0.01 Hz, and it increased to 4.6×10^3 and 6.3×10^4 $k\Omega \cdot cm^2$ at molar ratio (Zn^{2+}/SA) of 0.125 and 0.225, more than 3 and 4 orders of magnitude higher than that of as-received aluminum alloy substrate, respectively. However, the impedance value was reduced to 1.5×10^2 $k\Omega \cdot cm^2$ at the low frequency of 0.01 Hz at the molar ratio (Zn^{2+}/SA) of 0.5, which meant its less corrosion resistance property compared with the polarization curves in Figure 6.6(a). It indicates that our superhydrophobic film retards the formation of the corrosion products considerably due to the water repellent property of the flower-like micro-nanostructures formed on as-received aluminum alloy substrates.

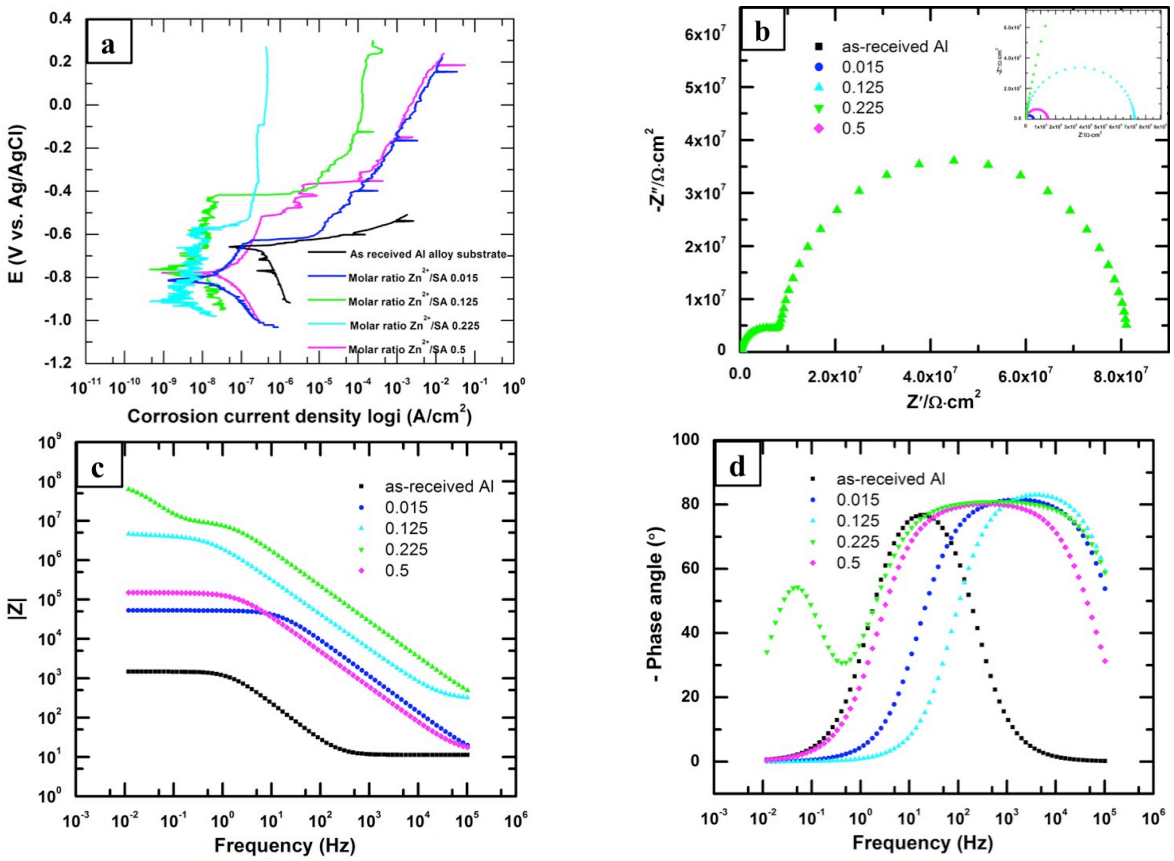

Figure 6. 6(a) Polarization, (b) Nyquist plot and (c & d) Bode plot of as-received aluminum alloy substrate and the modified aluminum alloy substrate at molar ratio (Zn^{2+}/SA) of 0.015, 0.125, 0.225 and 0.5 at 20 V for 10 min.

For a more quantitative insight into the electrochemical phenomena that leads to this improvement, electrical equivalent circuits were used to analyze the impedance data. Figure 6.7(d1) shows the equivalent circuit model of the as-received aluminum alloy substrate and hydrophobic substrate modified at the molar ratio (Zn^{2+}/SA) of 0.015, 0.125 and 0.5, the one time constant is shown in the electrochemical behavior.

In this equivalent circuit, the electrolytic resistance is represented by R_s. R_{ct} is the charge transfer resistance, and *CPE* is the constant phase element. The value of R_{ct} reveals the total corrosion resistance performance. However, in the case of superhydrophobic aluminum alloy substrate modified at the molar ratio (Zn^{2+}/SA) of 0.225, due to the presence of two phase maxima in the Bode plot, two time constants should be considered in the equivalent circuit, as shown in Figure 6.7(d2). In the equivalent circuit, R_s is the solution resistance, R_1 refers to the charge transfer resistance, the coating capacitance is represented by CPE_1, the coating capacitance is represented by CPE_2, and R_2 is associated with the impedance of the film, while electrical double layer capacitance is represented by a constant phase element.

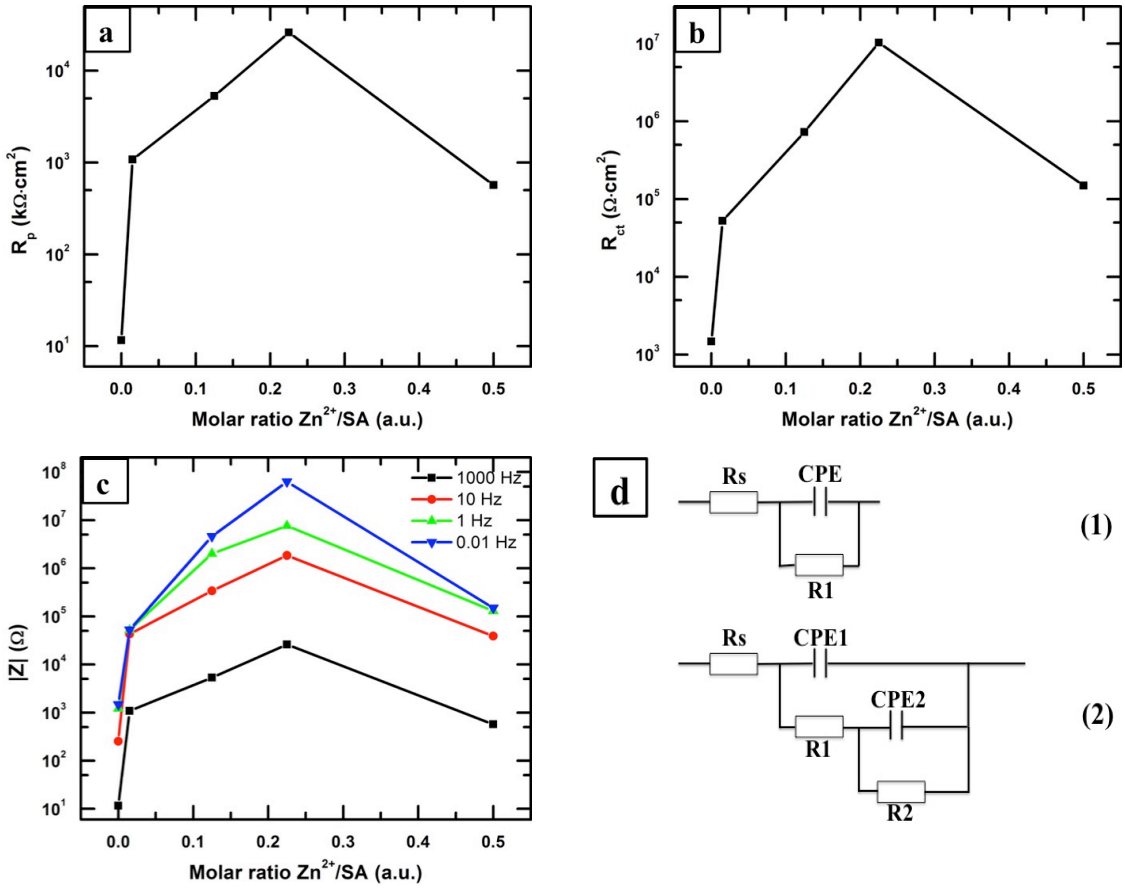

Figure 6. 7 Variation of (a) R_p, (b) R_{ct} and (c) |Z| at different frequency as a function of molar ratio (Zn^{2+}/SA). (d) Electrical equivalent circuit for evaluating the impedance of the samples.

Table 6. 1 Rms roughness, CA values and their respective I_{corr}, R_p values from polarization curves and R_{ct} values from EIS for different samples.

Molar ratio (Zn^{2+}/SA)	Rms roughness (μm)	CA (°)	I_{corr} (μA/cm^2)	R_p (Ω·cm^2)	R_{ct} (Ω·cm^2)
As-received Al	0.45 ±0.03	87 ± 3	4E-01	5E04	1.47E03
0.015	0.5 ± 0.15	117 ± 1	3.08E-02	1.38E06	6.3E04
0.125	4.48 ± 0.22	144 ± 4	4.20E-03	2.72E06	7.27E05
0.225	7.11 ± 0.42	159 ± 1	2.5E-03	7.72E06	1.03E07
0.5	5.2 ± 0.62	148 ± 4	6.5E-02	9.12E05	1.49E05

6.4 Summary

The corrosion resistant performance of superhydrophobic aluminum alloy substrates prepared by electrodeposition technique was investigated by polarization experiments and EIS tests in corrosive NaCl solution. The amount of zinc stearate (ZnSA) deposited on the surfaces was found to increase with an increasing molar ratio (Zn^{2+}/SA) from 0.015 to 0.5. The flower-like micro-nanostructures were observed at the molar ratio (Zn^{2+}/SA) of 0.225 for 10 minutes, with the optimum rms roughness and contact angle

(CA) of 7.11 ± 0.42 μm and CA of 159 ± 1°, respectively. The anticorrosion resistance of the superhydrophobic aluminum alloy substrates was estimated by polarization experiment and EIS measurement. The EIS measurement revealed that the impedance of the superhydrophobic aluminum alloy substrate was 60000 times higher than that of as-received aluminum alloy substrate. In the polarization experiment, the polarization resistance (R_p) of superhydrophobic substrate was found to be 7.72×10^3 kΩ·cm^2, much higher than that of as-received aluminum alloy substrate (50 kΩ·cm^2). Both EIS and polarization results indicated the superhydrophobic aluminum alloy substrate has an excellent corrosion resistance property as compared with as-received aluminum alloy substrate.

6.5 Supporting information

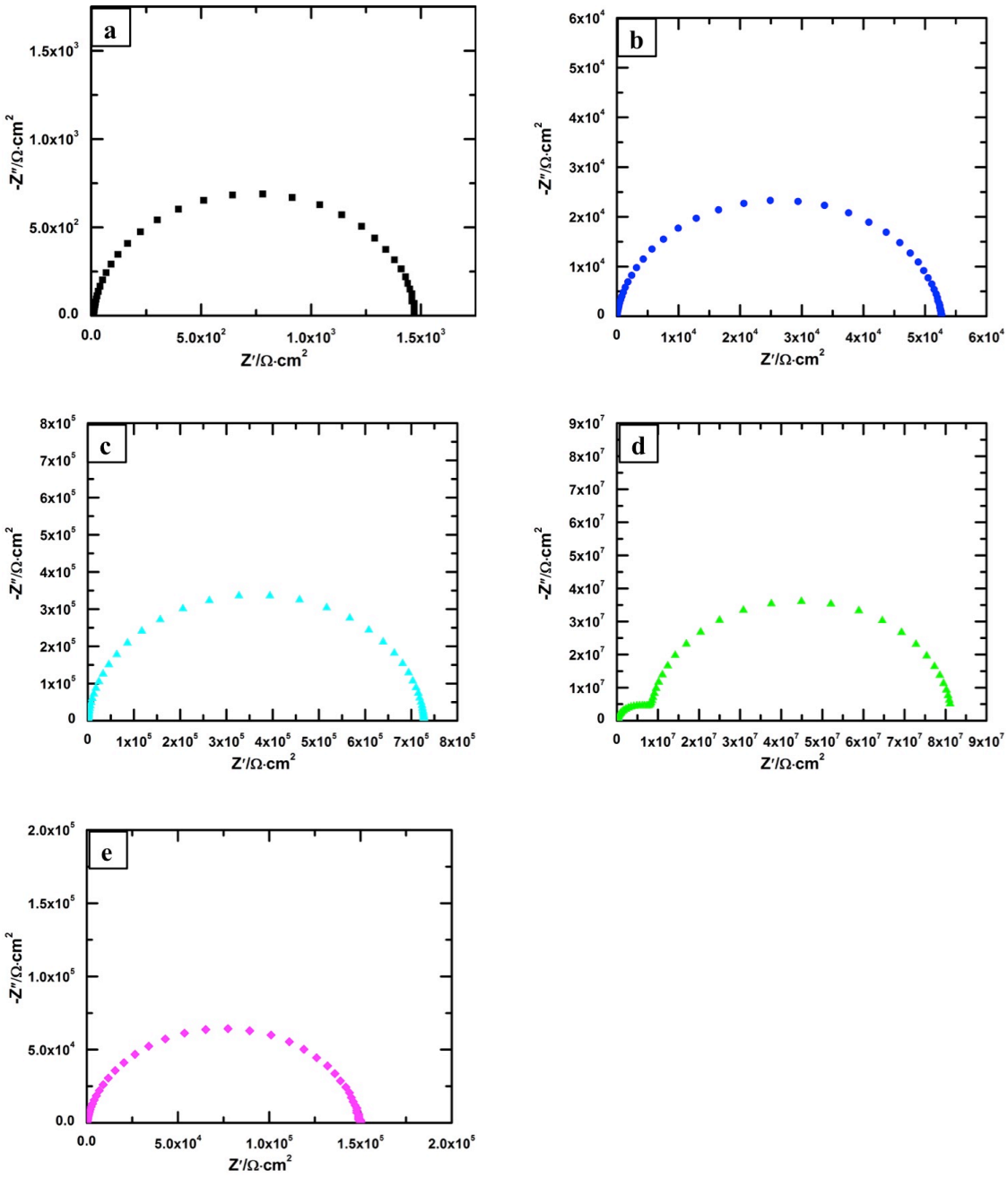

Figure 6. 8 Nyquist plots of (a) as-received aluminum alloy substrate, (b-e) modified aluminum alloy substrates at molar ratio (Zn^{2+}/SA) of (b) 0.015, (c) 0.125, (d) 0.225 and (e) 0.5.

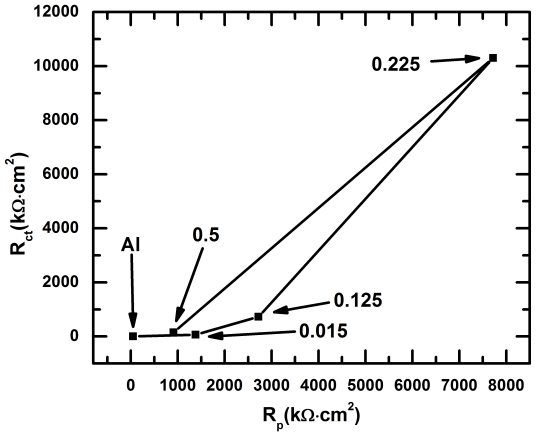

Figure 6. 9 Relationship between R_p and R_{ct}.

Table 6. 2 Information of OCP time, R_{ct} and R_p values in corrosion tests of superhydrophobic aluminum alloy substrates prepared by chemical etching, EPD and electrodeposition techniques.

	Chemical etching	EPD	Electrodeposition
OCP time	10 h	1 h	24 h
R_{ct}	95	44	10300
R_p	521	55	7720

Table 6.2 compares the OCP time, R_{ct} and R_p values in corrosion tests of superhydrophobic aluminum alloy substrates prepared by chemical etching, EPD and electrodeposition techniques. It can be seen from Table 6.2 that the superhydrophobic aluminum alloy substrate exhibits a much better anti-corrosion property, even it has been immersed a longer time in the corrosive environment.

Reference

(1) Huang, Y.; Sarkar, D.K.; Gallant, D.; Chen, X.G. *Applied Surface Science*, **2013**, 282, 689.

(2) Brassard, J.D.; Sarkar, D.K.; Perron, J.; Audibert-Hayet, A.; Melot, D. *Journal of Colloid and Interface Science*, **2015**, 447, 240.

(3) Wang, F.; Shen, T.; Li, C.; Li, W.; Yan, G. *Applied Surface Science*, **2014**, 317, 1107.

(4) Liu, Y.; Li, S.; Zhang, J.; Wang, Y.; Han, Z.; Ren, L. *Chemical Engineering Journal*, **2014**, 248, 440.

(5) Ramezani, M.; Vaezi, M.R.; Kazemzadeh, A. *Applied Surface Science*, **2014**, 317, 147.

(6) Brassard, J.-D.; Sarkar, D.K.; Perron, J. *ACS Applied Materials & Interfaces*, **2011**, 3, 3583.

(7) Marchand, D.J.; Dilworth, Z.R.; Stauffer, R.J.; Hsiao, E.; Kim, J.-H.; Kang, J.-G.; Kim S.H. Surface and Coatings Technology, **2013**, 234, 14.

(8) Zheng, Z.; Gu, Z.; Huo, R.; Ye, Y. *Applied Surface Science*, **2009**, 255, 7263.

(9) Saleema, N.; Sarkar, D.K.; Gallant, D.; Paynter, R.W.; Chen, X.G. *ACS Applied Materials & Interfaces*, **2011**, 3, 4775.

(10) Huang, Y.; Sarkar, D.K.; Chen, X.G. *Nano-Micro Letters*, **2011**, 3, 160.

(11) Huang, Y.; Sarkar, D.K.; Chen, X.G. *Materials Letters*, **2010**, 64, 2722.

(12) Huang, Y.; Sarkar, D.K.; Chen, X.G. *Applied Surface Science*, **2015**, 327, 327.

(13) Liu, C.; Su, F.; Liang, J.; Huang, P. *Surface and Coatings Technology*, **2014**, 258, 580.

(14) Liu, Q.; Kang, Z. *Materials Letters*, **2014**, 137, 210.

(15) Chen, Z.; Li, F.; Hao, L.; Chen, A.; Kong, Y. *Applied Surface Science*, **2011**, 258, 1395.

(16) Chen, Z.; Hao, L.; Chen, A.; Song, Q.; Chen, C. *Electrochimica Acta*, **2012**, 59, 168.

(17) Chen, Z.; Hao, L.; Chen, C. Colloids and Surfaces A: Physicochemical and Engineering Aspects, **2012**, 401, 1.

(18) Barthlott, W.; Neinhuis, C. Planta, **1997**, 202, 1.

(19) Rittermeier, A.; Miao, S.; Schröter, M.K.; Zhang, X.; Berg, M.W.E.v.d.; Kundu, S.; Wang, Y.; Schimpf, S.; Löffler, E.; Fischer, R.A.; Muhler, M. *Physical Chemistry Chemical Physics*, **2009**,11.

(20) Ghotbi, M.Y.; Bagheri, N.; Sadrnezhaad, S.K.; *Journal of Alloys and Compounds*, **2011**, 509, 2441.

(21) Wang, R.; Sivakumar, V.; Johnson, T.W.; Hastings, G. *Biophysical Journal*, **2004**, 86, 1061.

(22) Ozturk, S.; Balkose, D.; Okur, S.; Umemura, J. *Colloids and Surfaces A: Physicochemical and Engineering Aspects*, **2007**, 302, 67.

(23) Siddaramanna, A.; Saleema, N.; Sarkar, D.K. *Applied Surface Science*, **2014**, 311, 182.

(24) Ishizaki, T.; Masuda, Y.; Sakamoto, M. *Langmuir*, **2011**, 27, 4780.

CHAPTER 7 ANODIZATION OF ALUMINUM ALLOYS

7.1 Introduction

The porous anodic aluminum oxide (AAO) film is one of the most well-known templates for growing the nano-materials because it simply can offer self-ordered nanostructures by means of the effective electrochemical method. It is also well known that, the anodized aluminum alloy can be applied to prevent corrosion behavior. Therefore, in this project, the aluminum is anodized as shown in Chapter 7, and then, the anodized surface is modified by electrodeposition process to transform to superhydrophobicity, as shown in Chapter 8.

7.2 Experiments

The anodizing process of anodic aluminum alloy substrate was performed in 3 vol.% H_3PO_4 solution with varied applied DC current at varied temperature for 2 h. The potential variation as well as the anodized surface morphologies will be investigated in

this section.

7.3 Results and discussion

Figure 7.1 shows the potential vs. time curves for the anodizing process performed at a constant DC current of 2.5 mA/cm^2, 5 mA/cm^2, 7.5 mA/cm^2 or 10 mA/cm^2. When a constant current is applied between two aluminum electrodes for anodizing process, the potential rises linearly with time until the local maximum is reached, and then decreases gradually to the steady-state-forming potential. During the initial period of anodization, the linear increase in potential is associated with a linear growth of high-resistant oxide film (barrier film) on aluminum. Further anodizing results in the propagation of individual paths (pores precursors) through the barrier film. At the maximum of potential, the breakdown of the tight barrier film occurs and porous structure begins to be built. Finally, the steady-state growth of porous alumina proceeds and a forming potential is almost unchanged. It is also observed the higher DC current leads to a higher potential. Figure 7.2 shows the surface morphologies of anodized aluminum alloy surface at DC current of (a) 2.5 mA/cm^2 and (b) 10 mA/cm^2. The porous diameter was observed to

increase from ~100 nm at 2.5 mA/cm^2 to ~200 nm at 10 mA/cm^2, due to the higher applied DC current enhanced the reaction between the acid and alumina during anodizing process.

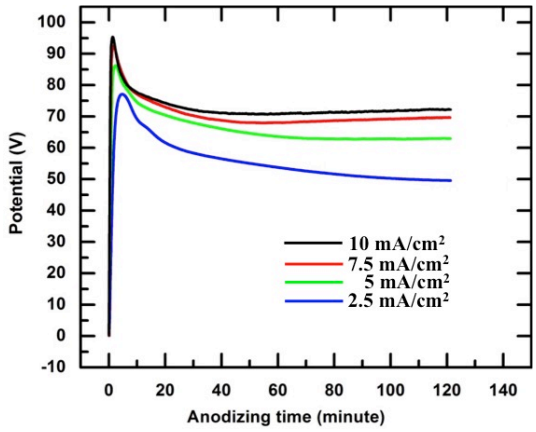

Figure 7. 1 Potential variation as a function of anodized time at different DC current from 2.5 mA/cm^2 to 10 mA/cm^2 at 10°C bath temperature.

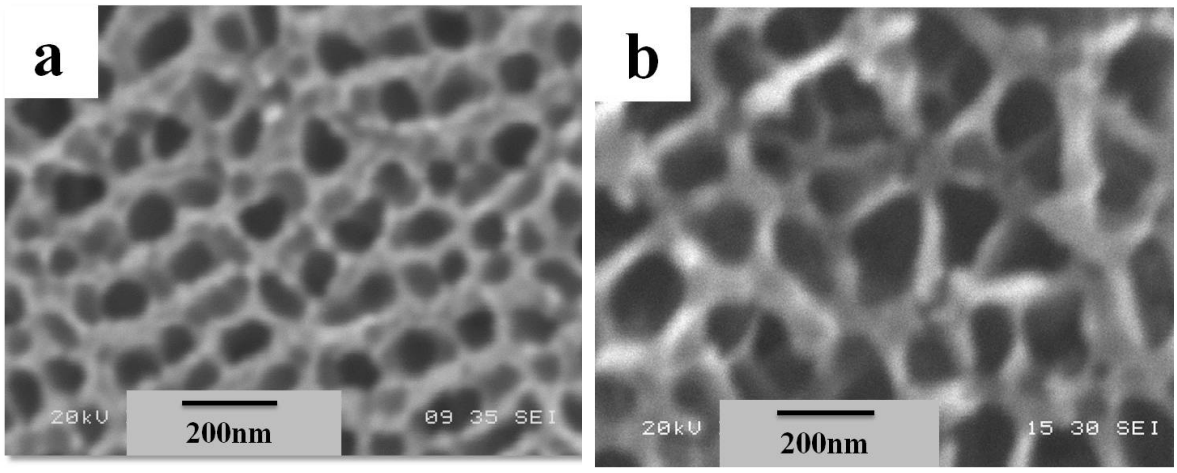

Figure 7. 2 SEM images of anodized surfaces at (a) 2.5 mA/cm^2 and (b) 10 mA/cm^2 at 10°C bath temperature for 2 h.

7.4 Summary

In the anodizing process, the potential was found to increase with higher applied DC current during anodizing process at 10°C for 2 h. Furthermore, the porous size was found to increase with higher applied DC current after anodizing process at 10°C for 2 h.

CHAPTER 8 INCORPORATION OF ELECTRODEPOSITION IN THE ANODIZED PORE TO OBTAIN SUPERHYDROPHOBIC SURFACES

As illustrated in Chapter 6 and 7, the electrodeposition process is now used on anodized surface to make a superhydrophobic anodized surface. A journal article has been applied in the journal of Metal. In this chapter, this article is presented.

8.1 Introduction

Aluminum (Al) and its alloys are naturally abundant engineering materials with extensive applications in daily life. In recent years, nanoporous anodic aluminum oxide (AAO) prepared by electrochemical anodization has multitude of applications, such as catalysis [1], drug delivery [2], biosensing [3], template synthesis [4], molecular and ion separation [5], corrosion resistance [6] and so forth. The formation of AAO on aluminum

alloy surface would act as the corrosion barrier. The formation of AAO was limited to a certain extent due to its hydrophilic behavior. Therefore, it is necessary to transform the AAO to superhydrophobicity in order to improve the corrosion resistance properties.

Superhydrophobicity, exhibiting excellent water-repellent property, is characterized by the contact angle above 150°. Creating rough surface as well as reducing the surface energy is attributed to the modification of superhydrophobicity. In the last decades a large effort has been devoted to the realization of superhydrophobic surfaces, due to their applications in biology [7, 8], anti-corrosion [9, 10], anti-icing [11], self-cleaning [12], etc. Recent publications show the anodized surface can be made superhydrophobic by passivation with organic molecules [13-16]. Recently, Vengatesh and Kulandainathan fabricated superhydrophobic anodic aluminum oxide (SHAAO) surfaces by passivation with organic molecules and show these surfaces having corrosion resistance properties indicated by potentiodynamic polarization [13]. Despite this, the fabrication as well as corrosion resistance properties of the electrodeposited hybrid organic-inorganic superhydrophobic surfaces on AAO have not been shown in the literature.

In this letter we have described the method to prepare the hybrid organic-inorganic superhydrophobic surfaces on AAO by electrodeposition process and describe their corrosion resistance properties both using potentiodynamic polarization and electrochemical impedance spectroscopy (EIS).

8.2 Experiments

The AA6061 aluminum alloy substrates were anodized using 3 vol.% H_3PO_4 aqueous solution at 10°C at 0.01 A/cm^2 for 2 h. The superhydrophobic anodic aluminum oxide (SHAAO) surface was prepared by electrodeposition process in an ethanolic solution containing 0.01 M stearic acid (SA) and 0.01 M zinc nitrate ($Zn(NO_3)_2$) by applying 20 V for 10 min. Microstructural examination were conducted using a Scanning Electron Microscope (SEM, JEOL JSM-6480 LV). Surface roughness was measured using an optical profilometer. Chemical composition of the samples was analyzed by means of X-ray diffraction with a scan range of 3-70°, Fourier Transform Infrared spectroscopy (FTIR, Perkins Elmer Spectrum One) and Energy Dispersive X-ray Spectrometer (EDX). Wetting characteristics of sample surfaces were evaluated by

measuring static contact angles (CA) [17, 18]. Electrochemical experiments were performed using a PGZ100 potentiostat and a 300 cm^3-EG&G PAR flat cell (London Scientific, London, ON, Canada), equipped with a standard three-electrode system with an Ag/AgCl reference electrode, a platinum (Pt) mesh as the counter electrode (CE), and the sample as the working electrode (WE) [19]. Before the test, the open circuit potential (OCP) was monitored for more than 20 h for stabilization by immersing the sample surface in 3 wt.% NaCl aqueous solution. The electrochemical impedance spectroscopy (EIS) was tested in the frequency range between 10 mHz and 100 kHz with a sine-wave amplitude of 10 mV. For the potentiodynamic polarization experiments, the potential was scanned from -250 mV to +1000 mV with respect to the OCP voltage at a scan rate of 2 mV/s.

8.3 Results and discussion

8.3.1 Material characterization

The anodized surface was then electrodeposited with electrolytic solution containing stearic acid (SA) mixing with zinc nitrate ($Zn(NO_3)_2$) at 20 V DC for a range of time. The electrodeposition process could be analyzed by monitoring the current density during the

process as well as the analysis of morphologies, chemical composition and surface wettability. Figure 8.1(a) shows the variation of current density in the electrodeposition process. It can be seen that the current density was reduced in electrodeposition process, which is correlated to the evolution of different morphological features at varying time, namely, 1 min, 5 min, 10 min, 20 min and 30 min as shown in Figure 8.1(b–f). At the beginning of electrodeposition (1 minute in Figure 8.1(b)), only a few micro-sized branch-like structure of zinc stearate (ZnSA) (identified by XRD and FTIR shown in Figure 8.2) is distributed loosely on the AAO surface. The current density was found to reduce sharply into 1 minute of electrodeposition process. It happened due to the non-conductive coating deposited on the anodized surface, which increased the surface resistance. As a result, the electric current was prevented to pass through the surface.

Furthermore, it can be seen that a closely packed uniform coating obtained on the anodized surface prepared by 5 min electrodeposition time. Due to the continuous deposition of insulating coating into 5 min, the current density was further reduced in this region. Furthermore, evident from the inset higher magnified SEM image, the

micro-sized coating was formed by the nano-wire structures clustering with each other on the anodized surface.

Figure 8.1(d) shows that the 10 min electrodeposition process resulted in the appearance of a porous network microstructure thin film on the anodized substrate. This thin film has the building block of micro-nano fibers cluster connected with each other as presented in the inset of Figure 8.1(d). It can be also observed that these micro-nanoporous structures are distributed uniformly on the anodized surface, resulting in a micro-nanorough surface. As compared with the surface for 5 min electrodeposition (Figure 8.1(c)), the coating on the anodized surface is getting thicker and denser, which is responsible for the continuous decrease of the current density in this period.

However, when the electrodeposition time is extended to 20 min and 30 min, the micro-nanopores have the tendency to be filled, as evident in Figure 8.1(e & f). The number density of the pores on the surface was found to decrease gradually with the elongation of electrodeposition time It is interesting to note that, seen in the Figure 8.1(a), the reduce rate of current density in electrodeposition process slowed down when the

time is longer than 10 min. It might happen due to the relative thick coating deposited on the anodized surface after 10 min electrodeposition, which prevented the further deposition on the surface with even longer time. Consequently, the resistance of the surface remains similar, so as the current density.

XRD and FTIR have been carried out to determine the composition of the electrodeposited micro-nanostructure thin films on anodized substrate. Figure 8.2(a3) shows four distinct peaks at 4.2°, 6.26°, 8.3° and 10.4° which correspond to the hybrid organic-inorganic ZnSA $(CH_3(CH_2)_{16}COO)_2Zn$ [20]. The possible mechanism of the formation of ZnSA has been presented as follows:

$$CH_3(CH_2)_{16}COOH + Zn^{2+} \rightarrow (CH_3(CH_2)_{16}COO)_2Zn + H^+ \quad \text{(Equation 8. 1)}$$

This reaction mechanism is very similar as mentioned by Liu *et al.* for the electrodeposition of cerium myristate by electrodeposition on magnesium substrates to obtain superhydrophobicity [21]. It is noted that the as-received aluminum alloy and

anodized substrates don't show any characteristic peaks. The inset of Figure 8.2 shows the high angle of XRD patterns of (a11) as-received aluminum alloy, (a12) anodized surface and (a13) electrodeposited anodized surface. The characteristic peaks appeared at 38.47°, 44.72° and 65.1° are in good agreement of Al (111), (200) and (220), respectively, arising from the substrate of aluminum alloy.

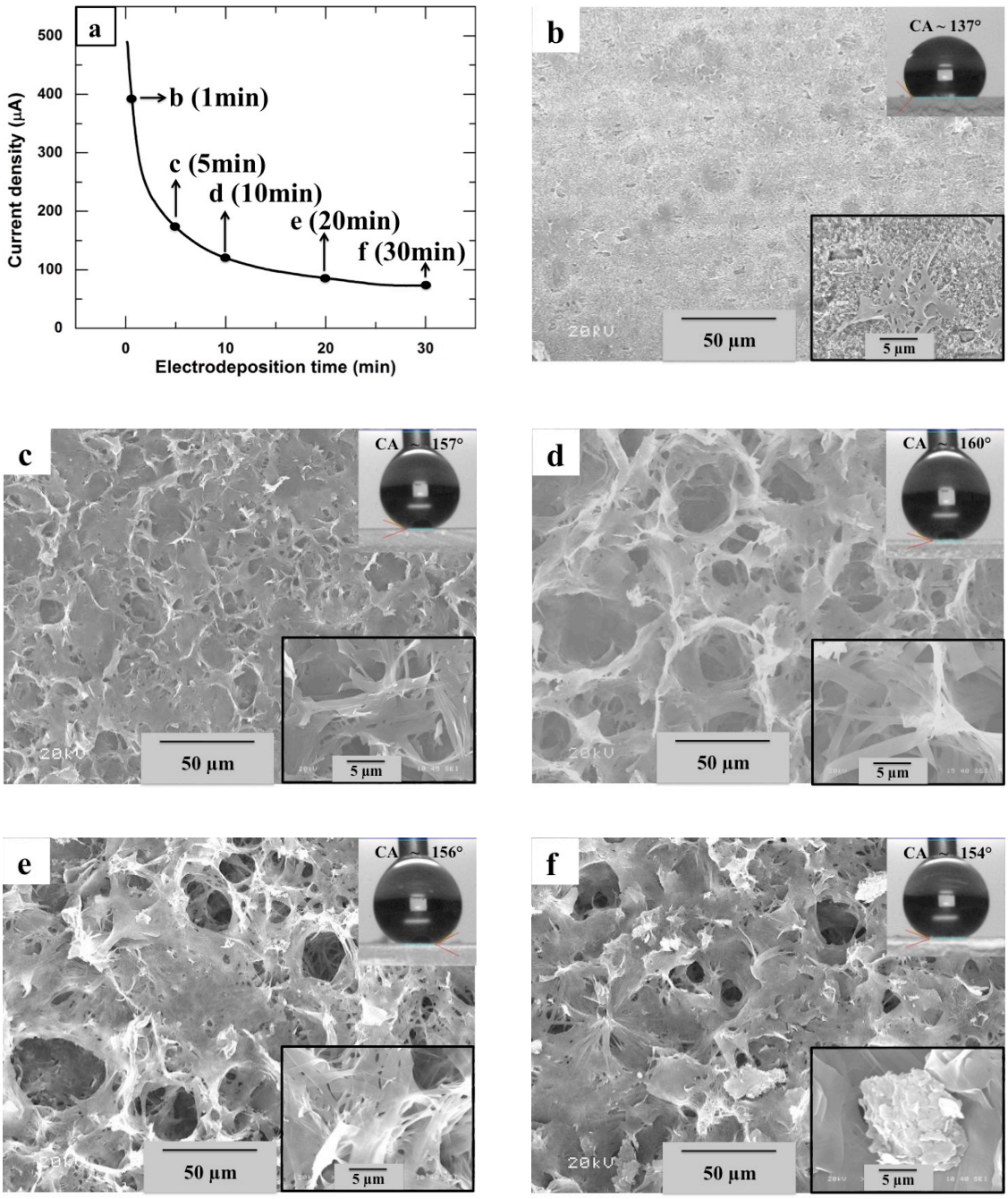

Figure 8. 1(a) Variation of current density in the electrodeposition process with electrolytic solution containing SA and $Zn(NO_3)_2$. SEM images of (b-f) the modified anodized aluminum alloy surfaces for 1 min, 5 min, 10 min, 20 min and 30 min electrodeposition, respectively. The inset images present the higher magnified images and the water drops on respective surfaces.

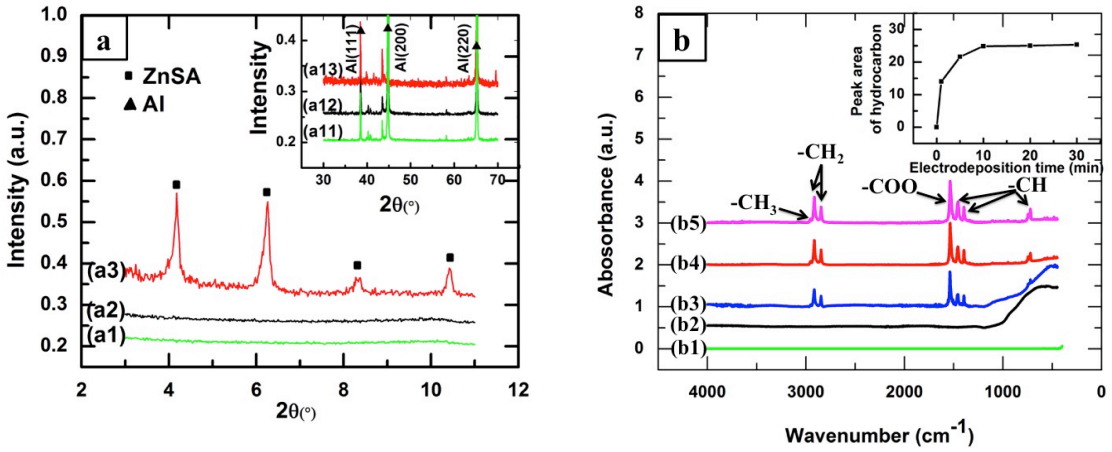

Figure 8. 2 XRD patterns of (a1 & a11) as-received aluminum alloy, (a2 & a12) anodized substrate and (a3 & a13) electrodeposited anodized substrate at the scan range of 3-11° (a1, a2 and a3) and 30-70° (a11, a12 and a13), respectively. (b) FTIR spectra of (b1) as-received aluminum alloy substrate, (b2) anodized substrate, (b3-b5) electrodeposited anodized substrates for 1 min, 10 min and 30 min, respectively. The inset image of Figure 8.2(b) shows the peak area of hydrocarbon as a function of electrodeposition time.

In the FTIR spectra of electrodeposited hybrid organic-inorganic anodized substrates (Figure 8.2(b)), the appearance of –CH group (CH_3 and CH_2) as well as –COO indicated the formation of ZnSA thin films [18], which is in good agreement with XRD results. These results support the presence of low surface energy methylated (CH_3 and CH_2) components in the electrodeposited ZnSA thin films on AAO substrates that effectively leads the superhydrophobicity. Moreover, the peak area of hydrocarbon was found to

increase sharply at the initial electrodeposition process but slow down after 10 min (inset of Figure 8.2(b)). It is complementary with the variation of current density as well as the evolution of surface morphologies by SEM, that the amount of ZnSA electrodeposited on anodized surfaces increased quickly initially but slowed down with longer than 10 min electrodeposition.

Figure 8.3 illustrates the variation of (a) the surface roughness, (b) water contact angle and (c) contact angle hysteresis as a function of the electrodeposition time. The surface roughness and contact angle of anodized surface was found to be 0.68 ± 0.01 μm and 8 ± 2°. The surface roughness and the contact angle are found to increase with increase in the electrodeposition time, from 1.7± 0.01 μm and 137 ± 2° for 1 min electrodeposition of ZnSA, up to 6.85 ± 1.02 μm and 160 ± 1° for 10 min electrodeposition, respectively. It happened due to the formation of micro-nanoporous structures of low surface energy ZnSA on the anodized surfaces.

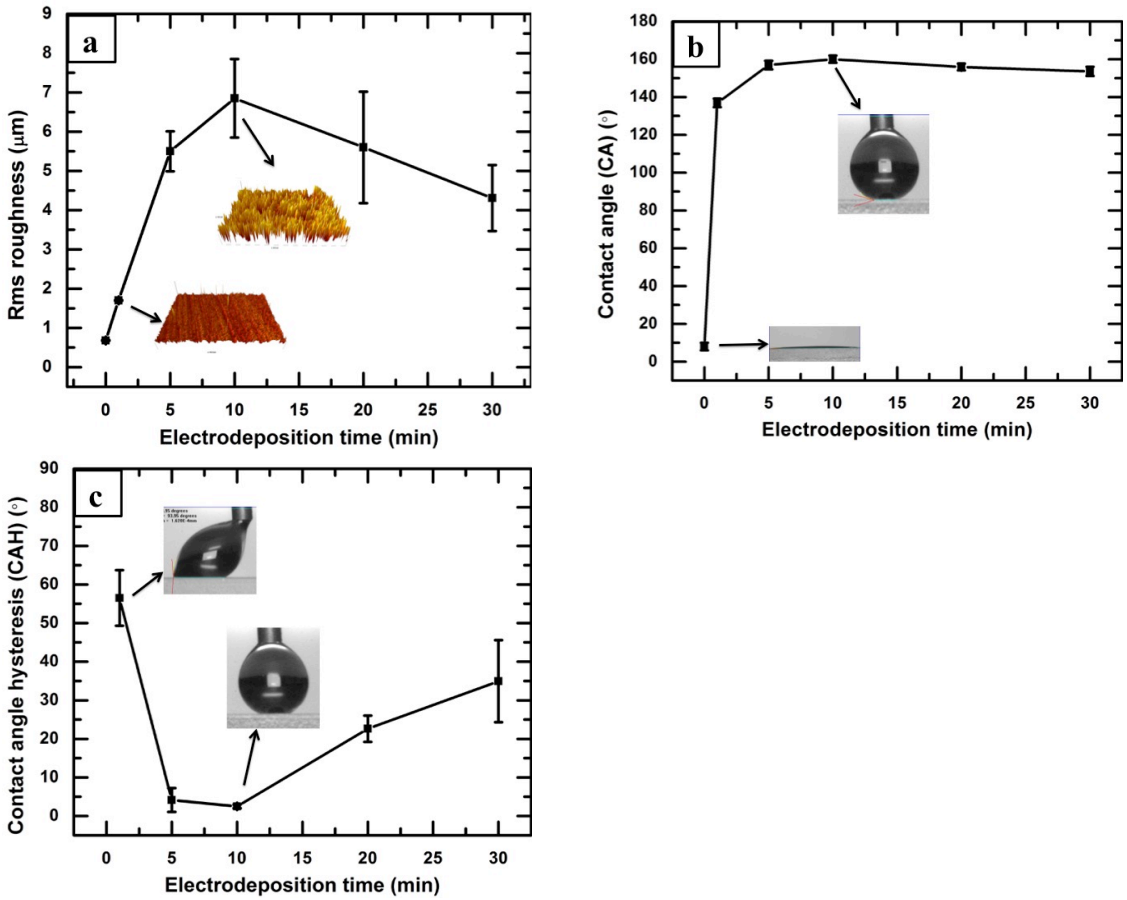

Figure 8. 3(a) Surface roughness, (b) contact angle (CA) and (c) contact angle hysteresis (CAH) of the anodized aluminum alloy surface and the modified anodized surfaces for a range of electrodeposition time.

However, the micro-nanopores were gradually filled with the further elongation of electrodeposition time evident from Figure 8.1(e & f). Consequently, the surface roughness and water contact angle decreased to 5.60 ± 1.42 μm and 156 ± 2° for 20 min electrodeposition, respectively, and further reduced to 4.31 ± 0.84 μm and 154 ± 2° for 30 min electrodeposition, respectively. On the contrary, the contact angle hysteresis of

the modified anodized surfaces decrease from 57 ± 7° to 2 ± 1° when the electrodeposition time increased from 1 min to 10 min, and then reduced gradually with further prolongation of time.

8.3.2 Corrosion resistance of superhydrophobic anodized substrates

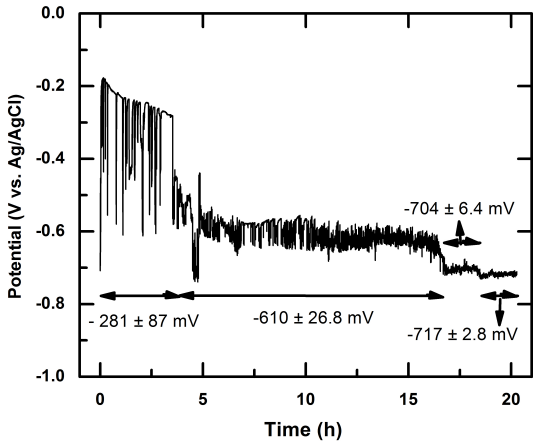

Figure 8. 4 The variation of open circuit potential (OCP) with time on the superhydrophobic AAO (SHAAO) surface prepared by electrodeposition for 10 min.

Figure 8.4 illustrates the variation of open circuit potential (OCP) on superhydrophobic AAO (SHAAO) surface. The OCP value shifted from -177 mV to -708 mV with an average of - 281 ± 87 mV into 5 h immersion time in the salt solution. It is

quite unstable during this period. From 5 to 16 h of immersion time, the OCP value varied from -533 mV to -686 mV with an average of -610 ± 26.8 mV. With the prolongation of immersion time to 20 h, the OCP value varied from -708 mV to -730 mV, average of -717 ± 2.8 mV. It can be seen that the fluctuation of OCP voltage reduces with time and stabilized nearly after 20 h. In contrast, the surface of aluminum alloy substrate gets stabilized within 30 minutes of immersion time in the salt solution. The OCP fluctuations of SHAAO substrate may be due to the poor wetting as well as protective properties of the SHAAO surface with the salt solution. Therefore, The EIS and polarization experiments were performed after 20 h of immersion of the superhydrophobic surface in the salt solution while monitoring the OCP continuously.

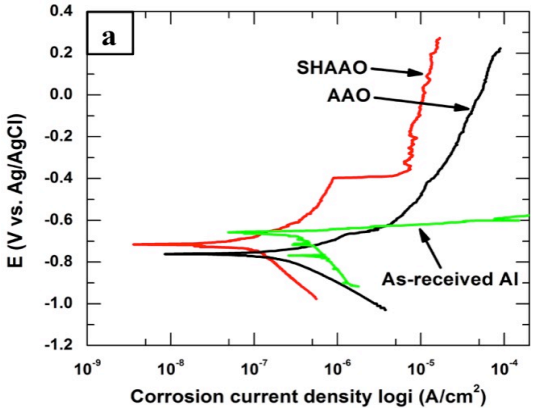
a
SHAAO
AAO
As-received Al
E (V vs. Ag/AgCl)
Corrosion current density logi (A/cm2)

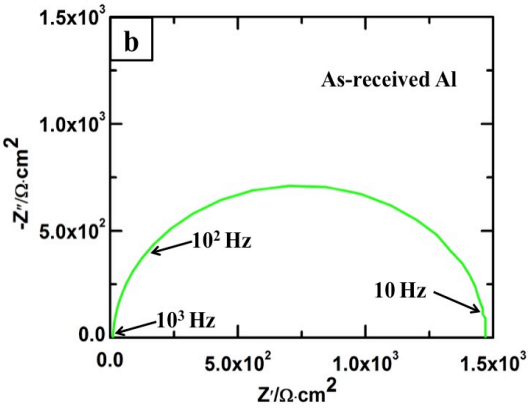
b
As-received Al
-Z''/Ω·cm2
Z'/Ω·cm2
10² Hz
10³ Hz
10 Hz

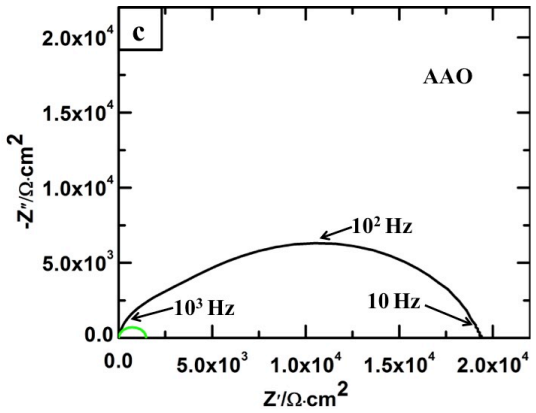
c
AAO
-Z''/Ω·cm2
Z'/Ω·cm2
10² Hz
10³ Hz
10 Hz

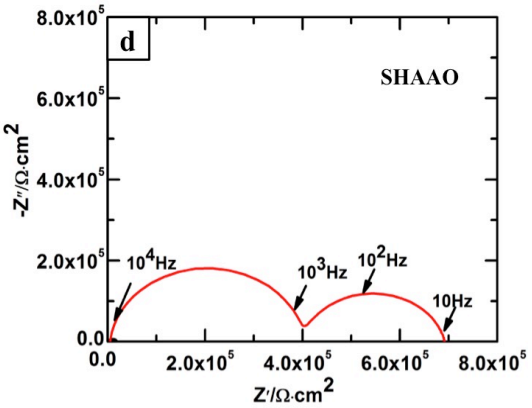
d
SHAAO
-Z''/Ω·cm2
Z'/Ω·cm2
10⁴Hz
10³Hz
10²Hz
10Hz

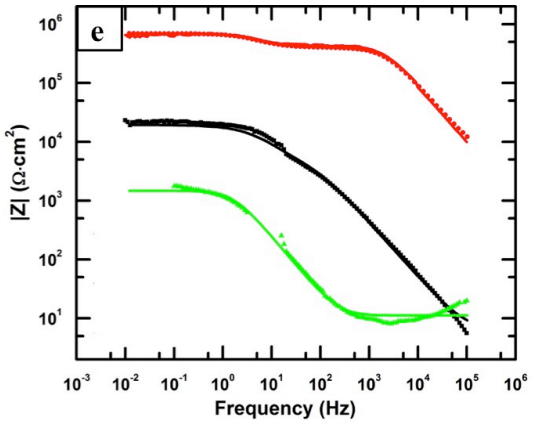
e
|Z| (Ω·cm2)
Frequency (Hz)

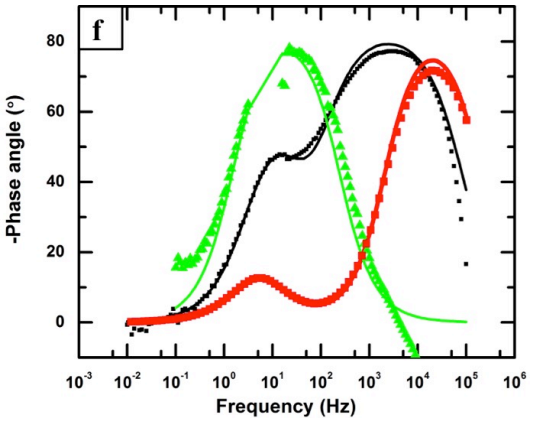
f
-Phase angle (°)
Frequency (Hz)

Figure 8. 5 (a)Polarization curves of the as-received aluminum alloy, AAO and SHAAO substrates in 3 wt.% NaCl corrosive solution. (b-d) shows the Nyquist plots of (b) as-received aluminum alloy, (c) AAO (as-received aluminum alloy (a small semicircle in green close to the origin of the) also shown for comparison) and (d) SHAAO substrate (as-received aluminum alloy and AAO also shown inside for comparison, very small semicircle, nearly visible, close to the origin).

To evaluate corrosion resistance performance of the fabricated as-received aluminum alloy substrate, anodized substrate and SHAAO substrates, potentiodynamic polarization and electrochemical impedance spectroscopy (EIS) tests were carried out. Figure 8.5(a) shows polarization curves of the as-received aluminum alloy, anodized and SHAAO substrates, respectively. The as-received aluminum alloy substrate exhibited a corrosion current density (I_{corr}) of 400 nA/cm^2 and polarization resistance (R_p) of 50 kΩ·cm^2. The R_p value was calculated by Stern-Geary equation, as shown in Equation 8.2.

$$R_p = \frac{\beta_a \beta_c}{2.3 I_{corr}(\beta_a + \beta_c)} \qquad \text{(Equation 8. 2)}$$

When the aluminum alloy substrate was anodized, the I_{corr} was reduced to 200

nA/cm^2 and R_p increased to 87 kΩ·cm^2, indicating an improved corrosion resistance compared with the as-received substrate. This was due to a barrier layer formed on the anodized surface. On the other hand, the I_{corr} of the hybrid organic-inorganic SHAAO substrate decreased remarkably to 88 nA/cm^2, while the R_p increased up to 441 kΩ·cm^2. This shows an even better anti-corrosion performance of the SHAAO substrate relative to the anodized substrate, likely attributed to the superhydrophobic ZnSA coating formed on the surface.

The I_{corr} of the electrodeposited cerium stearate superhydrophobic Mg surfaces was reported to be 142 nA/cm^2 with 30 minutes immersion to perform OCP [21]. Experiments performed by Vengatesh and Kulandainathan with 30 min immersion before polarization, show that the corrosion currents varies between 2-1050 nA/cm^2 depending on the passivated molecules [13]. Moreover, in the study of He et al., 1 hour immersion time is used for the stabilization [22]. In our experiment, the samples were exposed in NaCl solution for 20 h to stabilize under OCP. This indicates our superhydrophobic film displays a better stability and durability in the corrosion test as compared to the reported

values in the literatures.

To get a better understanding of the mechanism of corrosion protection, EIS measurement was also employed to analyze the corrosion behavior of the samples. Nyquist plots of as-received aluminum alloy substrate, AAO substrate and SHAAO substrate are presented in Figure 8.5(b). The working electrode of as-received aluminum alloy substrate comprised a circuit that incorporated resistors and capacitors, as shown in the equivalent electrical circuit (Figure 8.6(a)). In the diagram, R_s is the resistance of the electrolyte, and R_{ct} is the charge transfer resistance, describing the difficulty for corrosion occurred on the substrate. R_{ct} of as-received aluminum alloy substrate is found to be 1.46 $k\Omega \cdot cm^2$. *CPE* is the electric double-layer capacitor, resulting from the charge accumulation at the interface between the substrate and the electrolytic solution.

However, barrier and porous layers are separated into two oxide phases and are considered independent of each other. Figure 8.6(b) shows the equivalent circuit model of AAO substrate. The AAO substrate consists of an inner thin barrier layer and a thick outer porous layer. Also, the porous part is composed of pores and walls of hexagonal

cells. In the circuit, R_s is the electrolyte resistance; R_w and C_w represent the hexagonal cells resistance and hexagonal cells capacitance, respectively, which can be eliminated from the circuit due to the passage of electrical current is prevented through the wall of hexagonal cells. R_p and C_p represent the electrolyte resistance and capacitance through pores, respectively; R_b and C_b are the barrier layer resistance and capacitance, respectively. R_p is 5.51 kΩ·cm^2 and R_b is found to be 13.89 kΩ·cm^2.

The Nyquist plot of the SHAAO alloy substrate displays two capacitive loops in both high and low frequencies. Therefore, two time constants should be considered in the equivalent circuit, as shown in Figure 8.6(c). In the equivalent circuit, R_s is the solution resistance, R_{SH} is found to be 405 kΩ·cm^2, associated with the impedance of the superhydrophobic film, while its capacitance is CPE_{SH}. R_{ctSH} is found to be 284 kΩ·cm^2, refered to the charge transfer resistance, and electrical double layer capacitance is represented by CPE_{ctSH}. The SHAAO substrate exhibits higher impedance as compared with AAO substrate, indicating a significant enhancement of corrosion resistance. It is complementary with the result from the polarization curves, where the polarization

resistance of SHAAO substrate is higher than AAO substrate. It is well known that, the areas covered by the superhydrophobic film are electrochemically inert and all the current is passed via pinholes on the electrode, coverage of film on aluminum surfaces is given by

$$1 - \theta = \frac{R_{t0}}{R_t} \qquad \text{(Equation 8. 3)}$$

where θ is the fraction of film coverage, and 1- θ is the total fraction of pinholes. Rt is the charge transfer resistance of the SHAAO and R_{t0} represents the resistance of the as-received aluminum alloy substrate. The coverage of SHAAO is calculated to be 99.79%, much higher than that of 97% on the superhydrophobic anodized aluminum alloy substrate, prepared by He et al. [22], via melting myristic acid on AAO substrate. Combined with their smaller impedance values, it indicated that our AAO substrate with higher coverage of superhydrophobic film exhibits a better prevention from the corrosive environment.

Figure 8.5(e) shows the Bode plots, representing modulus (|Z|) as a function of

frequency. It is evident that |Z| value of SHAAO substrate are generally higher than that of the AAO and as-received aluminum alloy substrate at any given frequencies. The |Z| value of SHAAO substrate was found to be 656 kΩ·cm^2, much higher than that of 316 kΩ·cm^2 that we calculated from their Bode plot of SHAAO substrate prepared by melting AAO substrate in myristic acid solution [22]. It is well known that, |Z| is defined by the equation 8.4.

$$|Z| = \sqrt{(Z_{real}, Z')^2 + (Z_{imaginary}, Z'')^2} \qquad \text{(Equation 8. 4)}$$

where Z' is the real impedance and Z'' is the imaginary impedance. Z'' is the inversely proportional to the capacitance, which is defined by

$$C = \varepsilon_r \varepsilon_0 \frac{A}{d} \qquad \text{(Equation 8. 5)}$$

where C is the capacitance, ε_r is the dielectric constant of the material between the plates, ε_0 is the electric constant, A is the area of overlap of the two plates and d is the separation between the plates. The thicker superhydrophobic film on our AAO substrate

increased the distance and reduced the capacitance, which might be the reason leading to a higher |Z| value as compared with He's superhydrophobic sample.

Furthermore, the two phase maxima in the phase angle plot of SHAAO substrate indicate the presence of two time constants, as shown in Figure 8.5(f). It is complementary with the discussion for the Nyquist plots, where two semicircles appeared on the Nyquist plot of SHAAO substrate. Furthermore, the phase angle plot of SHAAO substrate shifts towards the higher frequency, indicated the better corrosion resistance property.

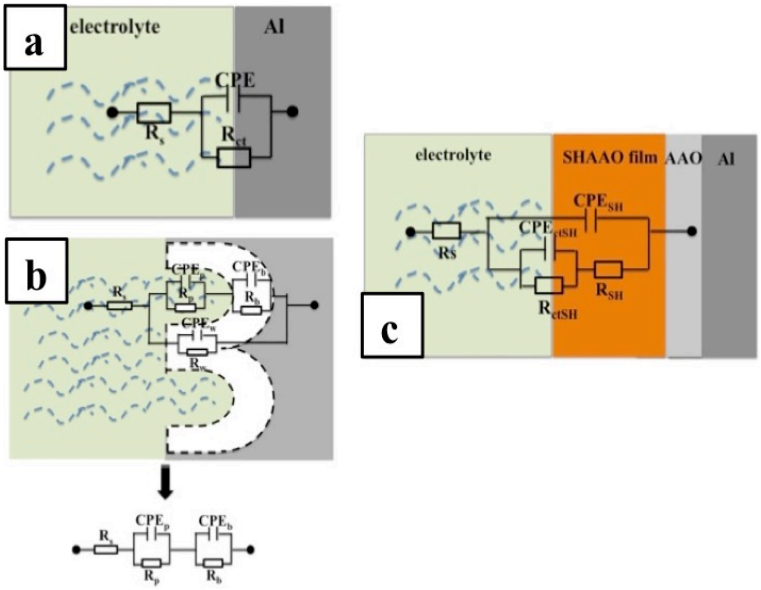

Figure 8. 6 Electrical equivalent circuits of (a) as-received aluminum alloy substrate, (b) AAO substrate and (c) SHAAO substrate, respectively.

8.4 Summary

Superhydrophobic anodic aluminum oxide (SHAAO) surface is prepared by electrodeposition process using ethanolic solution of stearic acid (SA) mixing with zinc nitrate ($Zn(NO_3)_2$) at a constant voltage of 20 V. The hybrid organic-inorganic SHAAO surface having micro-nanoporous structure low surface energy zinc stearate (ZnSA) exhibits a water contact angle (CA) of 160 ± 1°. The SHAAO substrate, having a polarization resistance (R_p) and charge transfer resistance (R_{ct}) of 441 and 284 kΩ·cm^2, respectively, much higher than that of as-received aluminum (R_p of 50 kΩ·cm^2 and R_{ct} of 1.46 kΩ·cm^2) and anodized aluminum substrate (R_p of 87 kΩ·cm^2 and R_{ct} of 14 kΩ·cm^2) in the corrosion. It indicates that the SHAAO substrate displays a much better corrosion resistance property as compared to as-received aluminum alloy substrate as well as anodic aluminum oxide (AAO) substrate.

References

(1) Dotzauer, D.M.; Dai, J.; Sun, L.; Bruening, M.L. *Nano Letters* **2006**, *6*, 2268-2272.

(2) Simovic, S.; Losic, D.; Vasilev, K. *Chemical Communications* **2010**, *46*, 1317-1319.

(3) Wang, M.; Meng, G.; Huang, Q.; Xu, Q.; Chu, Z.; Zhu, C. *Chemical Communications* **2011**, *47*, 3808-3810.

(4) Liu, Y.; Goebl, J.; Yin, Y. *Chemical Society Reviews* **2013**, *42*, 2610-2653.

(5) Mutalib Md Jani, A.; Anglin, E.J.; McInnes, S.J.P.; Losic, D.; Shapter, J.G.; Voelcker, N.H. *Chemical Communications* **2009**, 3062-3064.

(6) Bouchama, L.; Azzouz, N.; Boukmouche, N.; Chopart, J.P.; Daltin, A.L.; Bouznit, Y. *Surface and Coatings Technology* **2013**, *235*, 676-684.

(7) Huang, Y.; Sarkar, D.K.; Chen, X.G. *Materials Letters* **2010**, *64*, 2722-2724.

(8) Ciasca, G.; Papi, M.; Chiarpotto, M.; De Ninno, A.; Giovine, E.; Campi, G.; Gerardino, A.; De Spirito, M.; Businaro, L. *Nano-Micro Letters* **2014**, *6*, 280-286.

(9) Zhang, F.; Chen, S.; Dong, L.; Lei, Y.; Liu, T.; Yin, Y. *Applied Surface Science* **2011**, *257*, 2587-2591.

(10) Yin, B.; Fang, L.; Tang, A.-q.; Huang, Q.-l.; Hu, J.; Mao, J.-h.; Bai, G.; Bai, H. *Applied Surface Science* **2011**, *258*, 580-585.

(11) Huang, Y.; Sarkar, D.K.; Grant Chen, X. *Applied Surface Science* **2015**, *356*, 1012-1024.

(12) Huang, Y.; Sarkar, D.K.; Gallant, D.; Chen, X.G. *Applied Surface Science* **2013**, *282*, 689-694.

(13) Zuo, Z.; Liao, R.; Guo, C.; Yuan, Y.; Zhao, X.; Zhuang, A.; Zhang, Y. *Applied Surface Science* **2015**, *331*, 132-139.

(14) Watson, G.S.; Green, D.W.; Schwarzkopf, L.; Li, X.; Cribb, B.W.; Myhra, S.; Watson, J.A. *Acta Biomaterialia* **2015**, *21*, 109-122.

(15) Vengatesh, P.; Kulandainathan, M.A. *ACS Applied Materials & Interfaces* **2015**, *7*, 1516-1526.

(16) Li, Y.; Li, S.; Zhang, Y.; Yu, M.; Liu, J. *Materials Letters* **2015**, *142*, 137-140.

(17) Liu, W.; Luo, Y.; Sun, L.; Wu, R.; Jiang, H.; Liu, Y. *Applied Surface Science* **2013**,

264, 872-878.

(18) Fujii, T.; Aoki, Y.; Habazaki, H. *Applied Surface Science* **2011**, *257*, 8282-8288.

(19) Zinc stearate JCPDS # [00-055-1618].

(20) Liu, Q.; Kang, Z. *Materials Letters* **2014**, *137*, 210-213.

(21) Huang, Y.; Sarkar, D.K.; Chen, X.G. *Applied Surface Science* **2015**, *327*, 327-334.

(22) He, T.; Wang, Y.; Zhang, Y.; lv, Q.; Xu, T.; Liu, T. *Corrosion Science* **2009**, *51*, 1757-1761.

CHAPTER 9 CONCLUSIONS

The conclusions have been categories in three parts:

In the understanding of electrophoretic deposition:

- The one-step electrophoretic deposition (EPD) process has been developed to prepare superhydrophobic stearic acid functionalized ZnO nanoparticle thin films on aluminum alloy surfaces. The thickness of the thin films increased with the increase of the EPD bath temperature. XRD and IR studies confirmed the presence of stearic-acid-functionalized ZnO particles in the thin films. The surface morphology of the thin film is characterized by a large number of micro-nanorough clusters of ZnO nanoparticles. The water contact angle of 155° with roll-off property has been observed on the film. Furthermore, the activation energy for electrophoretic deposition of SA-functionalized ZnO nanoparticle is calculated to be 0.50 eV.
- The corrosion resistance property of the superhydrophobic surface prepared by electrophoretic deposition slightly increased as compared with as-received aluminum alloy substrate.

In the understanding of electrodeposition,

- The deposition of zinc stearate (ZnSA) was found to increase with an increasing molar ratio (Zn^{2+}/SA) from 0.015 to 0.225, but slightly decrease at the molar ratio of 0.5. The rms roughness as well as contact angle (CA) was consequently increased up to the optimum (Zn^{2+}/SA) of 0.225. The flower-like micro-nanostructures were observed at the molar ratio (Zn^{2+}/SA) of 0.225, which provides a high surface rms roughness of 7.11 ± 0.42 μm and CA of 159 ± 1°. The anticorrosion resistance of the modified aluminum alloy substrates at different molar ratio (Zn^{2+}/SA) was estimated by polarization experiment and EIS measurement. The polarization curves showed that the modified aluminum alloy substrates exhibited a higher corrosion resistance property as compared with as-received aluminum alloy substrate. Among them, the superhydrophobic aluminum alloy substrate having an optimum CA of 159 ± 1° displayed a lowest I_{corr} and highest R_p of 2.5E-03 μA/cm^2 and 7.72E06 Ω·cm^2, respectively. The EIS measurement revealed that the impedance of the modified aluminum alloy substrates was higher than that of as-received aluminum alloy

substrate (1.47E03 $\Omega \cdot cm^2$). The optimum superhydrophobic aluminum alloy substrate was found to be 6.3E07 $\Omega \cdot cm^2$, more than 4 orders of magnitudes higher than that of as-received aluminum alloy substrates. It is in good agreement with the result of polarization experiments, which indicated the superhydrophobic aluminum alloy substrates have a better corrosion resistance property as compared with as-received aluminum alloy substrates.

In the understanding of anodizing,

- The potential was found to increase with higher applied DC current during anodizing process at 10°C for 2 h.
- The porous size was found to increase from ~100 nm at 10 mA/cm^2 to ~200 nm at 10 mA/cm^2 after anodizing process at 10°C for 2 h.

In the study of the incorporation of electrodeposition in the anodized pore to obtain superhydrophobic surfaces,

Superhydrophobic anodic aluminum oxide (SHAAO) surface is prepared by electrodeposition process using ethanolic solution of stearic acid (SA) mixing with zinc nitrate ($Zn(NO_3)_2$) at a constant voltage of 20 V. The low surface energy micro-nanoporous structure zinc stearate (ZnSA) electrodeposited on the surface was found to increase with the increasing time. Furthermore, the surface roughness and contact angle of was found to increase and then decrease with time, and an optimum roughness and contact angle value of 6.85 ± 1.02 μm and 160 ± 1° was found in 10 min electrodeposition. The corrosion experiments via potentiodynamic polarization and electrochemical impedance spectroscopy (EIS) indicated that the SHAAO substrate displays a much better corrosion resistance property as compared with as-received aluminum alloy substrate as well as anodic aluminum oxide (AAO) substrate.

Global conclusions

In this project, superhydrophobic aluminum alloy substrates have been fabricated by electrophoretic deposition (EPD) and electrodeposition. Further, the anodized surfaces

are then transferred to superhydrophobic by EPD and electrodeposition processes. Both EPD and electrodeposition techniques have the advantage of easy to operation and not expensive to fabricate superhydrophobicity. However, as illustrated in chapter 5 and 7, the superhydrophobic surfaces prepared by electrodeposition have a thicker coating and better anticorrosion resistance property as compared by EPD process. However, when electrodeposition process was applied on the anodized surfaces, the corrosion resistance of superhydrophobic anodized surfaces was not as good as superhydrophobic aluminum alloy substrates prepared by electrodeposition. It might because the insulating anodized layer formed on the substrate enlarged the resistance of the electrical circle. As a result, the superhydrophobic layer formed on the anodized layer is not as thick as formed on the as-received substrate.

CHAPTER 10 RECOMMENDATIONS

In the present project, the superhydrophobic anodized surfaces were prepared by electrodeposition. The material characterization and the corrosion resistance of superhydrophobic surfaces have been analyzed. Many interesting results have been presented, as shown in the section of results and discussion. However, it still has some results hard to explain or some potential research direction, as shown in follow:

- The variation of DC potential in electrodeposition can be varied for different deposition behavior.
- The different electrolytic solution ($Zn(NO_3)_2$) can be varied, such as $Ni(NO_3)_2$, $Co(NO_3)_2$ et al..
- The reason of the formation of the porous morphology appeared on the anodized surface after electrodeposition process is not clear so far.
- The size of the anodized pore can be enlarged by varying the temperature, DC current and time et al.

The micro-nanosized ZnSA has not been deposited into the anodized pore. It might

be solved by enlarging the anodized pore size as well as decreasing the deposited particle size.

My list of publications

Journal articles:

- Y. Huang, D.K. Sarkar, Danick Gallant and X.-Grant Chen, Corrosion resistance properties of superhydrophobic copper surfaces fabricated by one-step electrochemical modification process, applied surface science, 2013, 289:689-694.
- Y. Huang, D.K. Sarkar and X.-Grant Chen, Superhydrophobic nanostructured ZnO thin films on aluminum alloy substrates by electrophoretic deposition process, Applied Surface Science, 2015, 327:327-334.
- Y. Huang, D.K. Sarkar and X.-Grant Chen, Superhydrophobic aluminum alloy surfaces prepared by chemical etching process and their corrosion resistance properties, applied surface science, 2015, 356:1012-1024.
- Y. Huang, D.K. Sarkar and X.-Grant Chen, Electrodeposited hybrid organic-inorganic micro-nanostructured superhydrophobic anodized aluminum with enhanced corrosion resistance, metals, 2016, 6: 47.

Conference articles:

- Y. Huang, D.K. Sarkar and X.-Grant Chen, Fabrication of superhydrophobic aluminum surfaces by chemical etching and electrophoretic deposition processes for corrosion application, Conference proceeding of COM (conference of metallurgist) 2013, Oct.27-31, 2014, Montreal, Canada.
- Y. Huang, D.K. Sarkar and X.-Grant Chen, Studies of compositional and corrosion properties of nanostructured superhydrophobic thin films on aluminum substrates, Conference procedding of COM (conference of metallurgist) 2016, September 11-19, 2016, Quebec city, Canada.

Posters:

- Y. Huang, D.K. Sarkar and X.-Grant Chen, Electrophoretic deposition of functionalized ZnO nanoparticle to fabricate superhydrophobic aluminum alloy surfaces, poster in REGAL 2012.
- Y. Huang, D.K. Sarkar and X.-Grant Chen, Superhydrophobic aluminum alloy surfaces by electrophoretic deposition process and their corrosion resistance

properties, poster in REGAL 2013 (rewards of Association of aluminum in Canada & rio tinto alcan).

- Y. Huang, D.K. Sarkar and X.-Grant Chen, Corrosion resistant superhydrophobic nanoparticles-incorporated-anodized aluminum alloys surfaces, poster in REGAL 2014.

Publications cited in this article

- Y. Huang, D.K. Sarkar and X.-Grant Chen, A one-step process to engineer superhydrophobic copper surfaces, Materials Letters 2010, 64: 2722.
- Y. Huang, D.K. Sarkar and X.-Grant Chen, Fabrication of superhydrophobic surfaces on aluminum alloy via electrodeposition of copper followed by electrochemical modification, Nano-micro letters 2011, *3(3)*:160.
- Y. Huang, D.K. Sarkar, Danick Gallant and X.-Grant Chen, Corrosion resistance properties of superhydrophobic copper surfaces fabricated by one-step electrochemical modification process, applied surface science, 2013, 289:689-694.
- Y. Huang, D.K. Sarkar and X.-Grant Chen, Superhydrophobic nanostructured ZnO thin films on aluminum alloy substrates by electrophoretic deposition process, Applied Surface Science, 2015, 327:327-334.
- Y. Huang, D.K. Sarkar and X.-Grant Chen, Superhydrophobic aluminum alloy surfaces prepared by chemical etching process and their corrosion resistance

properties, applied surface science, 2015, 356:1012-1024.